



The
University
Of
Sheffield.

The Application of Halloysite Nanotubes in Epoxy Resin Nanocomposites

R. J. Williams

Thesis submitted in partial fulfillment for the degree of Doctor
of Philosophy

The University of Sheffield,
Faculty of Engineering,
Department of Mechanical Engineering

September 2019

Acknowledgements

Firstly, I would like to thank my supervisor, Prof. Patrick Fairclough. I have learned a huge amount from him over the last four years, not only about science and engineering, but also about being a more effective critical thinker in general. I'd also like to thank the various other academic and post-doctoral staff who have supported me along the way, not least: Dr. Candice Majewski, who always made it clear that her door was open for a chat; Dr. Joel Foreman, for always being generous with the use of his lab and equipment; Dr. Christine Fernyhough, for chats, jam, and expert advice on practical chemistry; and Dr. Mike Weir, and Dr. Dan Toolan, who both repeatedly helped me out with the collection of X-ray scattering data.

Similarly, I should mention some of the fantastic technicians who have supported my work. In no particular order, I'd like to thank Rob Hanson, Christopher Hill, Dr. Debbie Hammond, and Dr. Lisa Hollands for their endless patience and advice when I used their equipment. I'd also like to thank Jack, Kurt and Wendy for the general camaraderie around the lab and office.

Thanks also go to the CDT in Polymers, Soft Matter and Colloids, and FaraPack Polymers, not least for providing me with the opportunity to take on the project in the first place. In particular, I am grateful for the many opportunities for personal and professional development provided by the CDT, which were in no small part due to the tireless work of Dr. Joe Gaunt and Prof. Steve Armes. At FaraPack, I am grateful to Chris Saywell for his enthusiastic advice at the start of the project, and to Babs and Prykey for always being helpful and accommodating on the numerous occasions I popped up in their lab unannounced.

Without the friends I've made in the Fairclough group, in the Garden Street office, and as part of the Polymer CDT, the last four years would have been much less enjoyable. While there are too many to name here, I should give a shout out to some of the friends I made when I first started Garden Street, with whom I've spent four years developing a myriad of office sports. More specifically, I'd like to thank Ste Knox for the several years worth of chats and advice, and for being a constant source of positive perspective on work and life in general. Big shout out to Alex Shackleford (aka Sickelford OG, aka The Bread King, aka The Best Keeper in the League), for generally being sick, and for always reminding us that we don't live in, and never have lived in, if-land. Ryan Seabright is acknowledged for always being right about technical matters, as well as having great stories, giving us constant lifts, and crying and rolling under the table during the speeches at Ste's wedding. Outside the Fairclough group, Luke Fox was invaluable for his unnecessarily obscure sports knowledge, and Ryan Brown put in some of the finest work as Fire Marshal that the University of Sheffield has ever seen. At this point, I would also like to take a moment to remember Ryan Seabright's Ford KA (RIP), which took us all on many adventures: *goodnight, sweet prince; and flights of angels sing thee to thy rest.*

Finally, I'd like to thank my family for their support. Most of all, I need to thank my amazing girlfriend, Siân; she always put up with my complaining with a smile, and without coming home to her love and encouragement every day, I might never have made it this far.

Abstract

Halloysite nanotubes are a type of naturally occurring clay nanoparticle which have attracted increasing research interest as reinforcing fillers in polymer nanocomposites. This thesis investigates some fundamental, but often overlooked, considerations for their application in epoxy resin nanocomposites specifically, with a view to moving towards the eventual scale-up of the production of such materials.

Firstly, some chemical and physical properties of halloysite nanotubes were characterised, and the results compared to supplier and literature data. Measured values were frequently found to differ from those that were expected. Significant attention is paid to the challenges associated with measuring nanotube size and shape, and it is concluded that neither light scattering nor electron microscopy can be used to reliably find these values. However, automated computational analysis of electron micrographs is highlighted as a promising avenue for further work.

Several methods for dispersing halloysite nanotubes into epoxy resin were assessed in terms of the degree of dispersion of the nanotubes, whether any damage had occurred during mixing, and the mechanical properties of the final nanocomposites. It was concluded that the use of a three-roll mill in force mode was the most effective mixing method, as it produced nanocomposites containing individually dispersed nanotubes which had an increased flexural modulus compared to pure epoxy resin. It was also found that several methods could be used to measure the filler content in these samples, including helium pycnometry and burning off the resin in air.

Finally, coating of the nanotubes with alkoxysilane coupling agents was shown to be successful, but it was also found to be variable in terms of the grafted amounts and the wettabilities of the coated samples. Nonetheless, scaling the process up to tens of grams produced coated samples with similar properties to those made on the scale of grams. In addition, piranha solution pre-treatment of the nanotubes was demonstrated to not to be an effective means of increasing the grafted amount of alkoxysilane on the surface, in contradiction to previous literature.

Contents

1	Introduction and Literature Review	1
1.1	Introduction to polymer nanocomposites	2
1.1.1	Introduction to polymers	2
1.1.2	Introduction to polymer composites	2
1.1.3	Introduction to nanocomposites	6
1.2	Introduction to halloysite nanotubes	8
1.2.1	Chemistry and structure of halloysite	8
1.2.2	Geological occurrence and morphology of halloysite	9
1.2.3	Halloysite and kaolinite	9
1.2.4	Formation of the halloysite nanotube	12
1.2.5	The mechanical properties of halloysite nanotubes	13
1.2.6	Biocompatibility of halloysite nanotubes	14
1.2.7	Overview of possible applications for halloysite nanotubes	15
1.2.8	Commercial availability of halloysite nanotubes	17
1.3	Halloysite nanotubes in polymer nanocomposites	17
1.3.1	Halloysite nanotubes in thermoplastics	19
1.3.2	Halloysite nanotubes in epoxy resin nanocomposites	22
1.4	Thesis structure	31
1.4.1	General aims	31
1.4.2	Summaries of chapter contents	31
2	Characterisation of Halloysite Nanotubes	33

2.1	Introduction	34
2.2	Aims of chapter	35
2.3	Supplier data for halloysite nanotubes	37
2.4	Basic physical properties of halloysite nanotubes	38
2.4.1	Physical appearance and handling of halloysite nanotubes	38
2.4.2	Solvents for halloysite nanotubes	40
2.4.3	The surface potential of halloysite nanotubes	44
2.5	Characterising the chemical properties of halloysite nanotubes	46
2.5.1	Elemental analysis of halloysite nanotubes using ICP-MS	46
2.5.2	Phase analysis of halloysite nanotubes using X-ray diffraction	48
2.5.3	Infrared spectroscopy measurements of halloysite nanotubes	51
2.5.4	Thermal decomposition of halloysite nanotubes	52
2.6	Measuring the size and morphology of halloysite nanotubes	54
2.6.1	Measurement of halloysite nanotube dimensions from transmission electron microscope images	54
2.6.2	Quantifying morphological impurities in halloysite samples using TEM images	55
2.6.3	Measuring halloysite nanotube dimensions by hand	56
2.6.4	Automated image analysis to determine halloysite nanotube dimensions	60
2.6.5	Small-angle X-ray scattering measurements of halloysite nanotubes	87
2.6.6	Dynamic Light Scattering	92
2.7	Conclusions and future work	96
2.8	Materials and methods	98
2.8.1	Materials	98
2.8.2	Methods	98
3	A Comparison of Mixing Methods for Dispersing Halloysite Nanotubes into Epoxy Resin	102
3.1	Introduction	103
3.2	Results and discussion	108

3.2.1	The epoxy resin system	108
3.2.2	The use of ultrasonication to disperse HNTs into epoxy resin . . .	109
3.2.3	The use of a three-roll mill to disperse HNTs into epoxy resin . .	115
3.2.4	Issues experienced with processing organo-montmorillonite into epoxy resin	120
3.2.5	Sample labelling	123
3.2.6	Using TEM to study the degree of dispersion and size of halloysite nanotubes in epoxy/HNT nanocomposites	123
3.2.7	Investigating rheometry as a means for determining the degree of dispersion of halloysite nanotubes	134
3.2.8	Determining HNT content in epoxy/HNT nanocomposites	139
3.2.9	The glass transition temperatures of epoxy/HNT nanocomposites	151
3.2.10	The effect of mixing method on the mechanical properties of the obtained composites	152
3.3	Conclusions and future work	160
3.4	Materials and methods	161
3.4.1	Materials	161
3.4.2	Synthetic methods	161
3.4.3	Characterisation	163
4	Functionalisation of Halloysite Nanotubes with Alkoxysilane and Activation with Piranha Solution	167
4.1	Introduction	168
4.1.1	Justification for alkoxysilane coating	168
4.1.2	Introduction to alkoxysilane chemistry	168
4.1.3	Alkoxysilane coating in practice	172
4.1.4	Piranha solution pretreatments	173
4.1.5	Aims of chapter	175
4.2	Results and discussion	177
4.2.1	Initial investigation of silane coating of HNTs	177
4.2.2	Coating HNTs with APTES	185

4.2.3	Piranha solution treatment of HNTs	202
4.2.4	Summary of the effect of piranha solution treatment on HNTs . . .	223
4.2.5	APTES coating of piranha-solution-treated HNTs	223
4.3	Conclusions and future work	225
4.4	Materials and methods	227
4.4.1	Materials	227
4.4.2	Synthetic methods	227
4.4.3	Characterisation	230
5	Conclusions and Future Work	232
5.1	Introduction	233
5.2	Summary of conclusions of each chapter	233
5.2.1	Chapter 2 - Characterisation of Halloysite Nanotubes	233
5.2.2	Chapter 3 - A Comparison of Mixing Methods for Dispersing Halloysite Nanotubes into an Epoxy Resin	233
5.2.3	Chapter 4 - Functionalisation of Halloysite Nanotubes with Alkoxy- silane and Activation with Piranha Solution Pre-treatment	234
5.3	General conclusions	236
5.4	Future Work	237
5.4.1	Chapter 2	237
5.4.2	Chapter 3	237
5.4.3	Chapter 4	238
A		239
A.1	Appendix to Chapter 2	239
A.1.1	Supplier data sheet for HNTs	239
A.1.2	Comparison of all size data for HNTs	241
A.1.3	MATLAB code	241
A.2	Appendix to Chapter 3	248
A.2.1	General propagation of uncertainties	248
A.2.2	Uncertainty in filler content determined by He pycnometry	248

A.2.3 Uncertainty in filler content determined by burn-off in a furnace . 249

Bibliography

251

List of abbreviations

1PF	One peak fit
2PF	Two peak fit
3RM	Three-roll mill
90p-HNT	Halloysite nanotube heated in pre-made piranha solution at 90 °C for 1 h.
ABS	Acrylonitrile butadiene styrene
AEAPS	3-(2-aminoethyl)-aminopropyltrimethoxysilane
AFM	Atomic force microscopy
a-HNT	Alkali treated halloysite nanotube
AS	Ultrasonication in epoxy/acetone solution.
AP	Agglomerated particle
APTES	(3-aminopropyl)triethoxysilane
BL	Beer-Lambert
CNT	Carbon nanotube
DGEBA	Difunctional diglycidyl ether of bisphenol A
DLS	Dynamic light scattering
DMA	Dynamic mechanical analysis
DS	DropSnake
DTG	Differential thermogravimetry
F	Three-roll mill in force mode.
FH	Freehand
FWHM	Full width at half maximum
G	Three-roll mill in gap mode.
GPTMS	(3-glycidyloxypropyl)-trimethoxysilane
HNT	Halloysite nanotube
HSP	Hansen solubility parameter
HT	Halpin-Tsai
ICP-MS	Inductively-coupled plasma mass spectrometry
IR	Infrared
LOI	Loss on ignition
MMT	Montmorillonite
MSE	Mean squared error
MXDA	meta-xylylenediamine
N	Nanocomposite sample imaged by TEM.
NH2-HNT	APTES-coated halloysite nanotube
NTP	Non-tubular particle
oMMT	Organo-modified montmorillonite
OTES	Octyltriethoxysilane
PAA	Poly(amidoamine)
PCS	Photon correlation spectroscopy
PDA	Poly(dopamine)
PDF	Probability density function
PE	Poly(ethylene)
pH1-HNT	Halloysite nanotube dried from water at pH 1
p-HNT	Halloysite nanotube treated with piranha solution made in situ.
PLA	Poly(lactic acid)
PMMA	Poly(methyl methacrylate)

PP	Poly(propylene)
PPA	Phenylphosphonic acid
PTFE	Poly(tetrafluorethylene)
R²	Coefficient of determination
RMSE	Root mean squared error
S	Ultrasonication in pure epoxy resin.
SANS	Small-angle neutron scattering
SAXS	Small-angle X-ray scattering
SEM	Scanning electron microscopy
Si-NP	Silica nanoparticle
SPP	Sodium poly(phosphate)
SSE	Sum of squared residuals
SST	Total sum of squared errors
TEM	Transmission electron microscopy
TEOS	Tetraethyl orthosilicate
T_g	Glass transition temperature
TGA	Thermogravimetric analysis
TMPM	(Trimethoxysilyl)propyl methacrylate
W	Sample washed from epoxy/HNT mixture then imaged with TEM.
WAXS	Wide-angle X-ray scattering
XPS	X-ray photoelectron spectroscopy
XRD	X-ray diffraction

List of Figures

1.1	The skeletal structure of the difunctional diglycidyl ether of Bisphenol A (DGEBA), a commonly-used epoxy resin monomer.	5
1.2	The opening of the epoxide ring by nucleophilic attack, in this case by a primary amine.	5
1.3	The number of publications about halloysite in general per year from 1995 to 2018, and about halloysite nanocomposites specifically from 2008 to 2018. The last decade has seen a huge increase in research interest in HNTs and HNT nanocomposites. This data was generated on Web of Science by finding the number of search results per year matching the key search terms shown.	8
1.4	The unit cell of halloysite with Al, Si and O atoms labelled (a), and a 2 x 2 matrix of halloysite unit cells which illustrates the layered structure of the mineral (b). The distance between the 001 planes, d_{001} , i.e. the interlayer distance, is illustrated in the bottom image. Missing from the images are hydrogen atoms, which are present in hydroxyl groups found on the alumina surface and at edges and defects on the silica surface. . . .	10
1.5	TEM image of HNTs from Idaho, which were used in this work. The image shows the wide variety of tube dimensions, as well as the presence of some morphological impurities (i.e. the flat sheets).	11
1.6	A scanning electron microscope image of a kaolinite particle. The structure of stacked aluminosilicate platelets can clearly be seen	11
1.7	AFM images of HNTs on a microporous membrane. The image is reproduced with permission from work by Lecouvet <i>et al.</i> , who used the AFM tip to perform 3-point bending tests on any nanotubes observed to be correctly bridging the pores. ¹	13
1.8	A comparison of the specific prices of several different types of filler particles, specifically: Talc, kaolinite (K), organo-modified MMT clay (oMMT), halloysite nanotubes (HNT), graphene oxide (GO), multi-walled carbon nanotubes (MWCNT), graphene (G), and single-walled carbon nanotubes (SWCNT). The prices are for the largest quantities of each that were available from Sigma-Aldrich in July 2019.	18

1.9	A TEM image taken from work by Lecouvet <i>et al.</i> , which illustrates how HNTs align in the direction of flow during twin-screw extrusion. ² Image adapted with permission.	21
2.1	A flowchart illustrating the structure of the chapter “Characterisation of Halloysite Nanotubes”	36
2.2	A concentration series of HNTs in water (HNT concentration from left to right: 0.1 wt%, 1 wt%, 5 wt%, 9 wt%, 17 wt%, 31 wt%, 50 wt%, and 100 wt%). Turning the sample vials upside down (bottom) illustrates the increasing dispersion viscosity with increasing HNT loading, as well as the gel-like behaviour of samples with high HNT loadings.	38
2.3	Washing HNTs with water at pH 12 produces pale, brown washings (left). The colour is thought to be due to formation of colloidal iron oxide or iron hydroxide particles. These particles can be measured by DLS (right), which indicates a particle diameter of approximately 105 nm.	39
2.4	Example images of HNTs as they sediment out of toluene, which were taken using time-lapse photography. Image (a) was taken just after stirring was switched off (i.e. 0 s), image (b) shows the HNTs during sedimentation (after 5 s), and the final image (c) is the first frame in which the HNTs are considered to have fully settled out of the liquid (after 10 s). . .	41
2.5	A graph of pH versus zeta potential for HNTs. The nanoparticles have the highest zeta potential at high pH, and go through an isoelectric point at around pH 2. The error bars are the zeta deviation of each measurement.	45
2.6	Bragg’s law of diffraction illustrated using the example of diffraction by the interlayer in halloysite.	49
2.7	Powder XRD pattern of HNTs from I-Minerals Inc.. All of the peaks can be assigned to those expected for halloysite and kaolinite. Peak A was also measured on an instrument which was calibrated for lower angle scattering; it corresponds to a distance of 7.09 Å, which is the width of a single aluminosilicate layer.	50
2.8	The IR absorption spectrum of pure HNTs.	52
2.9	Mass loss and derivative mass versus temperature for pure HNTs. Two mass loss events occur, one as soon as heating begins, and the other around 200 - 400 °C. These correspond to the loss of physisorbed and chemisorbed water, respectively.	53
2.10	TEM image of pure HNTs. The length, external diameter, and internal diameter are indicated in yellow, red, and blue, respectively.	54
2.11	SEM image of pure HNTs.	55

2.12	An example image where the numbers of tubular and non-tubular particles have been counted. In this image, there are 26 tubular particles, and 16 non-tubular particles. Features A, B and C are possible sources of ambiguity, as explained in the text.	56
2.13	A representative TEM image of HNTs which shows how the tubular particles tend to be much larger than non-tubular particles. Despite non-tubular particles having a relatively high number concentration (about 40%), it would be expected that their mass and volume fractions would be significantly lower.	57
2.14	A plot of internal diameter of HNTs versus external diameter of HNTs does not seem to show a trend, hence the fact that the internal diameters of the largest HNTs cannot be measured by TEM is not taken to be an issue.	58
2.15	A histogram of the measured external diameters of the HNTs alongside a log-normal PDF plotted with the log-normal parameters estimated from the raw data using MATLAB.	58
2.16	TEM images of HNTs before (a) and after (b) the image has been converted to a binary matrix using a user-defined threshold, and then inverted. In binary images, APs appear as a single object, and it is difficult to distinguish between HNTs and NTPs of a similar size and shape. It should be noted that inversion (i.e. transformation of dark pixels in binary from 0 to 1, and vice versa) is required for the operation of MATLAB's edge finding algorithms.	61
2.17	A flowchart illustrating a simplified version of the general logic behind the image processing carried out in MATLAB.	63
2.18	Images of successive steps in the MATLAB image processing algorithm used to automate measurement of HNT dimensions: (a) the original image; (b) the image after binary conversion and clearing of border objects; (c) the image after removal of objects with a size-and-shape-based filter; and (d) the image after the indexing of and fitting of ellipses to the remaining objects.	64
2.19	An example of a TEM image of HNTs analysed automatically using MATLAB.	65
2.20	A graph illustrating how the values for width and eccentricity overlap for all of HNTs, NTPs, and APs. The columns are average values, and the error bars represent the ranges of each value.	65
2.21	An example of a HNT which has been fitted with an ellipse by MATLAB. The ellipse appears to approximate the dimensions of the HNT well. . . .	66
2.22	The average ratios of the external diameters and lengths of the HNTs calculated by MATLAB versus those measured in ImageJ. MATLAB overestimates the dimensions because it approximates the shape of the nanotubes using ellipses. The error bars represent standard deviation.	67

2.23	Plots of the HNT dimensions measured by ImageJ against the ratio of the value measured by MATLAB to the value measured by ImageJ for each dimension. There does not seem to be a trend, which suggests that the degree to which the MATLAB value differs from the ImageJ (i.e. true) value does not depend on the size or shape of tube being measured.	68
2.24	A comparison of the areas of the objects and corresponding fitted ellipses for all of HNTs, NTP, and AP. The error bars represent the ranges of each value.	68
2.25	The mean circularities for the various types of particle found in TEM images of HNTs. The error bars show the range of values. The ranges overlap for all three types of particle.	69
2.26	Pixel intensity against distance for a line drawn across the width of a HNT in a TEM image. The intensity varies almost symmetrically across the tube; this feature is unique to the HNTs in the images.	70
2.27	An example of a Euclidean distance transform for a simple matrix. The value of each pixel is changed to the straight line distance between it and its nearest non-zero pixel neighbour in the original binary matrix.	70
2.28	An example of a Euclidean distance transform for an isolated HNT.	70
2.29	The intensity profile across a HNT as found by hand across one width of the HNT in ImageJ, and by carrying out a distance transform in one direction on the same HNT using MATLAB. This distance transform returns a scalar value of distance, so the right-hand graph contains intensities from both directions away from the centre of the nanotube, which cannot be separated.	71
2.30	The skeleton of a binary image of an isolated HNT (top), and the intensity profile across the same HNT as found by hand in ImageJ, and by carrying out a distance transform in two directions from the image skeleton using MATLAB (bottom).	72
2.31	The intensity profiles for three further examples of isolated HNTs. The two translucent HNTs (a), both show a similar intensity profile to the first HNT analysed, but the opaque HNT (b) does not have an intensity rise across its centre.	73
2.32	Examples of an AP (a) and an NTP (b) alongside their corresponding intensity profiles found using a Euclidean distance transform.	74
2.33	Gommes <i>et al.</i> used the BL law to model the absorption of electrons of their CNTs in TEM images, and could use this to fit the intensity profiles found using distance transforms of the nanotubes. ³	75

2.34	The actual pixel intensity across a HNT in a TEM image plotted alongside a) the theoretical intensity calculated using first estimates of its radii and absorption coefficient, and b) the result of fitting equations 2.15 and 2.16 to the data using nonlinear least squares regression, including the fit residuals.	78
2.35	A flowchart indicating the general logic of how objects in TEM images of HNTs could be filtered in MATLAB using the goodness of fit of the BL law to their edges.	80
2.36	The results of fitting equation 2.15 to the pixel intensity across several isolated HNTs in a TEM image versus NTPs and APs. The dark red dashed line is at the minimum R^2 found for an isolated HNT (0.87), and the dark blue dashed line is at the maximum RMSE seen for an isolated HNT (4.55). It can be seen that there is one NTP with both an R^2 close to the minimum for HNTs, and an RMSE below the maximum of HNTs. This suggests that these goodness of fit criteria cannot be used to distinguish isolated HNTs from NTPs.	81
2.37	Fits of the intensity profiles at the edges of an example of either an NTP or AP using the BL model for a cylinder and the corresponding residuals. Note that the the fit is only applied at distance greater than the value of R_i , which is determined from the distance at which intensity is a minimum.	82
2.38	An NTP for which the BL model produced a comparable fit to HNTs alongside its fitted intensity profile and corresponding fit residuals.	82
2.39	An SEM image adapted with permission from work by Hillier <i>et al.</i> ⁴ They used a dispersing agent when preparing samples of HNTs, and the particles subsequently appear well separated in their electron micrographs.	83
2.40	A TEM image of HNTs dried in a desiccator from a concentration of about 0.008 wt% in pH 7 water. Significant agglomeration still occurs.	84
2.41	A TEM image of HNTs dried in a desiccator from a concentration of about 0.008 wt% in pH 12 water. Agglomeration still occurs, but many of the smaller particles appear well separated from one another.	85
2.42	A TEM image of HNTs dried in a desiccator from a concentration of about 0.008 wt% in water containing 0.05 wt% SPP as a dispersant. Not only does agglomeration occur, but the particles appear to be coated in a thick layer of polymer.	85
2.43	TEM images of HNTs dried using the procedure inspired by Hillier <i>et al.</i> , ⁴ but at a lower concentration of around 0.0008 wt%. Agglomeration still occurs for all samples, and a layer of polymer is still apparent around the particles where SPP was used as a dispersant (i.e. c and d).	86
2.44	Graphs showing a) SAXS by HNTs in water, and b) the first derivative of this data at low q	89

2.45	Graphs showing simulated SAXS by cylinders of different sizes, and an illustration of how averaging this scattering can start to approximate the actual scattering by HNTs. The featureless SAXS seen for HNTs is therefore explained as a consequence of the polydispersity of their dimensions.	90
2.46	A graph of X-ray intensity as a function of scattering vector, q , for 0.1 wt% HNTs in water. This data was obtained using a shorter sample-to-detector distance than in figure 2.44 in order to reduce noise in the higher q -range.	91
2.47	The raw correlation data for HNTs in water at pH 12 (a), and the same data fitted with three multiple exponential decay functions (representing different particle populations) using the CONTIN algorithm (b). Fitting this way does achieve a close fit to the data, but yields some nonsensical size values.	95
3.1	An example of a 3RM (a), and a diagram showing how material is fed through the rollers of the mill during processing (b).	106
3.2	A flowchart illustrating the structure of the chapter “A Comparison of Mixing Methods for Dispersing Halloysite Nanotubes into Epoxy Resin”	107
3.3	The chemical structure of DGEBA.	108
3.4	The reaction of bisphenol A with epichlorohydrin under alkali conditions produces DGEBA monomer (i.e. $n = 0$), as well as oligomeric species (i.e. $n > 0$).	108
3.5	The chemical structure of MXDA.	109
3.6	A graph showing the temperature rise of the mixing vessel during continuous ultrasonication of an epoxy/HNT mixture (left), and a comparison of resin/HNT mixtures which have and have not undergone ultrasonication (right). The mixture treated with ultrasonication (US) is much darker than the other (non-US), which suggests that oxidation of the resin has occurred.	110
3.7	An optical microscope image of a sample of HNTs in epoxy which was treated to 25 min of continuous ultrasonication. There are still relatively large (tens of μm in diameter) agglomerates of HNTs visible, some examples of which are indicated by the yellow arrows. This shows that complete dispersion of the particles was not achieved.	111
3.8	Optical microscope images taken at different times during continuous ultrasonication of an epoxy/HNT mixture. The agglomerates decrease significantly in size and number the longer ultrasonication proceeds.	112

3.9	The temperature of the vessel exterior during continuous ultrasonication of an undiluted resin/HNT mixture with no cooling (red), compared to pulsed ultrasonication of a resin/HNT mixture diluted with acetone which was cooled with an ice bath (blue). With pulsed ultrasonication and external cooling, the temperature of the mixture could be kept low throughout processing.	113
3.10	The size of HNTs during ultrasonication in epoxy diluted with acetone, as measured by DLS. The size at each time is an average of three measurements, and the error bars are the standard deviation in this average. The average size is seen to decrease as ultrasonication proceeds, until a plateau is reached after about 45 min.	113
3.11	Optical microscope images taken during pulsed ultrasonication of an epoxy/HNT mixture diluted with acetone. The agglomerates decrease significantly in size and number the longer ultrasonication proceeds. However, even after 80 min, large agglomerates (an example is indicated with the red arrow) can still be found in the samples. The worm-like features in one of the images are motes of dust caught in the resin.	114
3.12	An optical microscope image taken of an approximately 5 wt% epoxy/HNT nanocomposite made by passing the epoxy/HNT mixture 5 times through the 3RM at a 5 μm gap setting. Many large agglomerates (an example is indicated with a yellow arrow) are still visible, suggesting that this was a poor mixing technique.	116
3.13	An illustration of a simple possible explanation for why agglomerates much larger than 5 μm remain in epoxy/HNT mixtures after several passes through a 5 μm gap width. Essentially, it is feasible that a particle can pass through the gap with a large size in one or two dimensions, so long as it has at least one dimension of 5 μm or less.	117
3.14	An optical microscope image taken of an approximately 2 wt% epoxy/HNT nanocomposite made by passing the epoxy/HNT mixture 15 times through the 3RM at a 5 μm gap setting. Many agglomerates are still visible (two examples are indicated with yellow arrows), suggesting that this was a poor mixing technique, but they are typically much smaller (about half the size) than the agglomerates seen after 5 passes through the mill at this gap width. This suggests that increasing the number of passes through the 3RM in gap mode can increase the level of dispersion of the particles. . .	118
3.15	A graph showing how the mean force between the front 3RM rollers decreased as a mixture was repeatedly passed through it in force mode. Heating of the mixture reduces its viscosity, reducing the forces experienced between the rollers. The error bars are half the range of observed values.	119

3.16	An optical microscope image taken of an approximately 2 wt% epoxy/HNT nanocomposite made by passing the epoxy/HNT mixture 10 times through the 3RM at the maximum force setting. Visible agglomerates are rare (an example is indicated with a yellow arrow), suggesting that this was a good mixing technique.	119
3.17	A mixture of oMMT and epoxy resin which is opaque because of the degree of foaming which occurs upon mixing.	120
3.18	Images illustrating the rapid expansion of gas in an epoxy/oMMT mixture as vacuum is applied (in this case using a rotary evaporator).	121
3.19	Mixtures of 1 and 2 wt% epoxy/oMMT after around one hour of treatment in an ultrasonic bath at 40 °C. The 1 wt% sample has almost been fully degassed, although longer treatment times are needed for mixtures with a higher oMMT content than this.	121
3.20	A sample of epoxy/oMMT nanocomposite which had been cured after extensive degassing using an ultrasonic bath. The sample has been backlit to illustrate the large number of bubbles that remain throughout the material after curing.	122
3.21	TEM images of nanocomposites of HNTs and epoxy made by different mixing methods. Large agglomerates of several μm were visible for the S and G samples, whereas most of the HNTs seemed to be individually dispersed in images of the AS and F samples.	124
3.22	TEM images of nanocomposites of HNTs and epoxy made using the 3RM in gap mode. A large agglomerate of several μm is visible in image (a), but not image (b). This illustrates the potential for incorrect conclusions to be drawn from TEM images if only a small area/number of images is considered in isolation.	125
3.23	An illustration of how both cutting of the nanotubes by the microtome knife during sample preparation, and rotation of nanotubes out of the plane of the TEM image, could make HNTs in TEM images of nanocomposites appear shorter than they truly are.	126
3.24	A plot of length versus angle of rotation calculated using equation 3.3. This gives an idea of how only a small rotation of a nanotube out of the plane of a TEM image is needed before it will look significantly shorter than it truly is.	127
3.25	A TEM image of a sample made by dropping an acetone-diluted mixture of HNTs in epoxy onto a carbon-coated copper TEM grid. The epoxy forms a film impenetrable to the electron beam, meaning epoxy/HNT mixtures cannot be imaged in this way.	128
3.26	TEM images of HNTs washed from epoxy/HNT mixtures made by different mixing methods.	129

3.27	Close-up images of HNTs in the WS and WF samples which appeared to have a coating. The red arrows indicate features which are thought to be a coating of epoxy, possibly formed due to heating of the epoxy/HNT dispersion during mixing.	129
3.28	A comparison of the mode values of the log-normal probability density functions of HNT length found for pure HNTs and both N and W samples. All of the samples bar WS seem to have overlapping uncertainties, suggesting that they are probably all following the same size distribution. The uncertainties are the mode values calculated using the 95% confidence intervals of the log-normal parameters μ and σ fitted to the data using MATLAB.	131
3.29	DLS measurements of S HNTs in an epoxy/acetone solution at different centrifugation times (at 3000 rpm). By 20 min of centrifugation, the measured 'size' of the S sample is the same as that of a pure epoxy + acetone solution, and this does not change after 30 min. Therefore, it is concluded that all of the HNTs have been retrieved from solution by 30 min of centrifugation. The error bars are the standard deviation of three size measurements.	132
3.30	A comparison of the percentages of HNTs over certain lengths found for pure HNTs and the W samples. The W samples actually seem to have a larger proportion of longer tubes than the pure sample, which suggests that the mixing techniques used did not damage the HNTs (i.e. did not reduce their length).	133
3.31	The moisture uptake of a cellulose soxhlet thimble which had been soaked in acetone then completely dried.	136
3.32	Viscosity plotted against shear rate for pure epoxy and the epoxy/HNT samples made by different mixing methods. Up and down refer to measurements made during an initial increase of shear rate from 0 s ⁻¹ (up), and subsequent measurements made as the shear rate was decreased from 1000 s ⁻¹ (down).	137
3.33	A photo of the bottom of the mixing vessel for an S sample after sonication and decanting of most of the mixture. There are clearly many large agglomerates remaining in the vessel (highlighted with the red arrow), so the filler content in the decanted mixture must be lower than that which was originally added before mixing.	139
3.34	TGA of pure cured epoxy under different atmospheres. Only heating under air leads to complete combustion and no mass remaining at the end of the run. The dotted line is at y = 0 wt%.	142
3.35	A comparison of the filler content measured for the S1 and S5 samples using TGA in air and He pycnometry. The values measured by both techniques are similar, suggesting that both are accurate. The uncertainties in the TGA measurements are a standard deviation of three measurements, while the instrumental uncertainties are given for He pycnometry.	145

3.36	A comparison of the filler content measured for the 15G samples using densities found via He pycnometry and bulk measurements. The bulk measurement gives filler content close to that found via pycnometry for the 15G5 sample, but the bulk measurements give very different filler contents to the pycnometry values for 15G2 and 15G1. The error bars associated with He pycnometry values are instrumental uncertainties. . . .	145
3.37	A comparison of filler contents found for three samples via He pycnometry and burn-off in a furnace. The two measurements seem to be in good agreement with one another.	149
3.38	A comparison of actual filler contents found for the nanocomposite samples versus the expected filler contents calculated from the amount added to the resin before mixing.	150
3.39	The flexural moduli relative to that of pure epoxy for samples of different filler content made by different mixing methods. The uncertainty in filler content is that found in section 3.2.8, and the uncertainty in relative flexural modulus is propagated from the standard error of several nanocomposite and pure epoxy samples.	155
3.40	The DMA trace for the AS5 sample. A low temperature peak is observed, which is not seen for the other samples (e.g. the pure epoxy sample also shown here). This suggests that the sample is being plasticised to some degree by solvent remaining from the mixing step.	156
3.41	The flexural strength relative to that of pure epoxy for samples of different filler content made by different mixing methods. The uncertainty in filler content is that found in section 3.2.8, and the uncertainty in relative flexural strength is propagated from the standard error of several nanocomposite and pure epoxy samples.	157
3.42	A plot of modulus versus oMMT content for a series of epoxy/oMMT nanocomposites, adapted with permission from work by Yasmin <i>et al.</i> ⁵ The improvements in modulus are much greater than those seen for the epoxy/HNT nanocomposites made here.	159
3.43	A plot of tensile strength versus clay content for a series of epoxy/oMMT nanocomposites, adapted with permission from work by Yasmin <i>et al.</i> ⁵ The strength is seen to drop significantly upon the addition of oMMT, which they attribute to the formation of difficult-to-remove bubbles during processing. ⁵	159
4.1	The structure of a generic trialkoxysilane.	168
4.2	A reaction scheme showing the hydrolysis of a trialkoxysilane followed by subsequent condensation, in this case with another a silanol, but which can also take place with hydroxyl groups on a surface to form a coating. .	169
4.3	The different transition states which occur during the hydrolysis of alkoxysilanes under acidic (left) and basic (right) conditions.	170

4.4	Simple 2D representations of the types of structures obtained from diffusion limited (left) and reaction limited (right) growth. In the context of silane coatings, diffusion and reaction limited structures are obtained when hydrolysis is disfavoured and favoured respectively.	171
4.5	Some examples of the complex structures that amine-functional alkoxy-silanes (in this case APTES) can form on silica surfaces via various means of inter- and intramolecular bonding.	172
4.6	Upon mixing, sulfuric acid and hydrogen peroxide react to form Caro's acid, a powerful oxidising agent. ⁶	174
4.7	A hypothetical mechanism for the acid-catalysed hydrolysis of silica. . . .	174
4.8	An example of HNTs which have been damaged during treatment with aqueous acid (a), compared to pristine, untreated HNTs (b). The damage manifests itself as enlargement and roughening of the nanotube interior as the alumina surface is removed (some examples in (a) are indicated with yellow arrows), which is accompanied by the formation of Si-NPs (some examples are indicated with purple arrows in the inset image in (a), which shows a zoomed-in view of part of the same TEM image).	176
4.9	A flowchart illustrating the structure of the chapter "Functionalisation of Halloysite Nanotubes with Alkoxy-silane and Activation with Piranha Solution"	178
4.10	The structure of 3-(trimethoxysilyl)propyl methacrylate (TMPM).	179
4.11	A greater mass loss is seen for TMPM-coated HNTs than for untreated HNTs, and this mass loss occurs at a lower onset temperature. This suggests that an organic coating is present, i.e. that the reaction was successful. 179	179
4.12	The IR spectra of HNTs and TMPM-HNTs. After silane coating, new absorption peaks can be seen, which are associated with various organic functional groups on the coating molecule. However, no absorption peaks associated with the C=C bond can be identified.	180
4.13	A side-by-side comparison of a water droplet on TMPM coated HNTs and unmodified HNTs. The coated HNTs appear to have a relatively high water contact angle, while the untreated HNTs have a much lower contact angle, that quickly recedes to 0 as the water is absorbed by the HNT pellet. 180	180
4.14	A TEM image of TMPM coated HNTs. The yellow arrows indicate features which are thought to be the silane coating, as they are not seen in TEM images of pure HNTs. In places, these features extend many nanometres away from the HNT surface, indicating a multilayer coating of silane.	181
4.15	TGA of the same TMPM-HNT sample, half of which was washed using soxhlet extraction, the other half by hand (as described in the text). The higher mass remaining for the soxhlet extracted sample indicates that this was the better method for washing non-grafted species away from the HNTs. 183	183

4.16	TGA for TMPM-HNTs coated using toluene and ethanol. Coating in ethanol with a high TMPM concentration (P2) led to a much lower grafted amount than using toluene. Coating in ethanol with the same TMPM concentration as was used in P1, i.e. P3, led to different thermal degradation behaviour, and a somewhat lower grafted amount.	184
4.17	A side-by-side comparison of the water contact angles of TMPM coated HNT samples made by reaction in toluene or ethanol (i.e. by using P1 or P3, respectively).	184
4.18	The structure of (3-aminopropyl)triethoxysilane (APTES).	185
4.19	A greater mass loss is seen for NH ₂ -HNTs than for untreated HNTs, which suggests that the APTES coating reaction was successful.	186
4.20	The IR spectrum of a sample of NH ₂ -HNTs compared to that of unmodified HNTs. The presence of a C-H stretching absorption suggests that APTES grafting has been successful, but the signature vibrations of the amine group cannot be seen, presumably due to their low concentration and relatively low absorption coefficient.	186
4.21	There is a peak for the N 1s electron orbital in XPS of NH ₂ -HNTs, but not in the spectra of HNTs. This can be taken as proof that APTES has been grafted onto the surface of the HNTs.	187
4.22	TEM images of a sample of NH ₂ -HNTs. In some areas, there appears to be a multilayer coating of APTES on the nanotubes (indicated with yellow arrows), but these features are rare.	188
4.23	The mass remaining at 800 °C for NH ₂ -HNTs extracted with toluene and NH ₂ -HNTs extracted with toluene followed by ethanol is virtually identical. This suggests that the toluene wash removes all non-grafted silane species, and further washing with a more polar solvent is unnecessary.	189
4.24	The amount of grafted APTES found on HNTs by TGA plotted against several variables. There does not seem to be any correlation between the grafted amount of APTES, and any of the variables listed here.	190
4.25	The relative humidity in our lab measured between March and May, and over one week in April (note that these dates do not overlap with the APTES coatings reported here). It can be seen that ambient humidity varies significantly (within a range of 42%), even over the course of a few days.	190
4.26	In a system consisting of two fluid phases (B and C), and a solid surface, a droplet can form on the surface provided that the energetic interaction between the surface and the fluid phases is intermediate between the interactions between the two fluid phases. The angle, θ , between the surface and the edge of the adhered droplet is known as the contact angle.	191

4.27	An example of a contact angle being measured using the analogue goniometer (not a sample from this work). The sample height, the viewfinder focus, and the goniometer must all be adjusted manually in order to take a measurement.	192
4.28	The set-up that was constructed to allow measurement of the water contact angle of HNT samples immediately after delivery of the water droplet.	193
4.29	An example image of a droplet taken using the digital microscope set-up shown in figure 4.28.	194
4.30	The contact angle of a water droplet on a surface can be measured by drawing freehand lines in ImageJ and evaluating the angle between them (the contact angle is 180° - this angle). However, the relatively poor resolution at small scales means that there is some uncertainty over exactly where the edge of the droplet is.	195
4.31	An example use of the DropSnake plug-in for ImageJ to evaluate contact angles. The software uses the droplet shape as defined by the user (the blue points) to calculate the contact angle. The red line/dots are part of a fitting feature which was not used, but could not be turned off, and should be ignored.	195
4.32	A comparison of the mean water contact angle for a sample of I.44P organoclay found in the literature to those measured using the analogue goniometer, the digital USB microscope and freehand line drawing (USBM-FH), and the microscope and DropSnake software (USBM-DS). The contact angle found using the USBM-DS method was closest to the literature value.	196
4.33	A figure illustrating how absorption of a water droplet by a pressed pellet of HNTs causes the pellet to undergo stresses which eventually lead to it breaking. This means that each sample can only be measured once.	197
4.34	The water contact angle against time for three individual samples of HNTs, and the average of all three samples at these times. The contact angle appears to decrease linearly with time, which is consistent with Lucas-Washburn flow. Indeed, the change in average contact angle over time can be well-fitted with a straight line.	198
4.35	The water contact angle against time for three separate pellets of the same NH ₂ -HNTs. The behaviour of each sample is different, but an average across all three discs still seems to show a reasonable trend, with the contact angle starting to decrease linearly with time after about 30 s.	199
4.36	The contact angle versus time for several pellets of two different samples of NH ₂ -HNTs. The rate of absorption was seen to vary significantly even between pellets of the same sample, suggesting that the previous observation of a well-defined linear regime of water absorption by NH ₂ -HNTs may have been a coincidence.	199

4.37	Absorption time (i.e. the amount of time for the water droplet to be fully absorbed) versus pellet thickness. Identical symbols indicate different pellets of the same sample. There was no clear trend between the speed of droplet absorption and disc thickness, so the differences in absorption time seen for discs of the same sample must be due to some other factor.	200
4.38	The mean initial water contact angles for all samples of NH ₂ -HNTs compared to untreated HNTs. All of the NH ₂ -HNTs show an increased contact angle in comparison to HNTs, but surprisingly the contact angle appears to decrease with a greater degree of coating. The solid red line is the initial water contact angle of untreated HNTs, and the dotted red lines are its associated uncertainty.	201
4.39	The temperature change seen when sulfuric acid is added to HNTs, followed by hydrogen peroxide to make piranha solution. The x axis is time from the addition of the sulfuric acid to the HNTs.	203
4.40	Pictures taken of the HNTs during the p and 90p piranha solution treatment processes. In both cases, the clay dispersion formed a foam, which is potentially hazardous as it could lead to spills of piranha solution.	204
4.41	The correlation data from DLS for a dispersion of filtered p-HNTs vs filtered HNTs. Fitting the correlation data does not reveal a new population of smaller particles for the p-HNTs, which would be evidence of the small particles suspected to cause inaccurate pH meter readings in the dispersions of p-HNTs. Instead, the correlation data shows increased signal at longer times for the p-HNTs, suggesting the presence of larger particles, which are probably flocs of HNTs.	205
4.42	A side-by-side comparison of samples of untreated and piranha solution treated HNTs. Piranha solution treatment causes a colour change from light brown to white, which is thought to arise from dissolution and removal of iron oxide in the low pH solution.	206
4.43	TEM images of piranha solution treated HNTs. There appear to be some initial signs of acid-damage having occurred to the p-HNTs and 90p-HNTs, which manifests as roughening of the interior surfaces of the nanotubes. Examples of these features are highlighted with yellow arrows.	208
4.44	A magnified TEM image of untreated HNTs which illustrates the relatively smooth surface of the nanotube interiors.	209
4.45	DTG curves for the various HNT and piranha-treated HNT samples. The data are noisy, but appear to show similar thermal decomposition behaviour (i.e. a similarly shaped peak) for all samples, at least superficially. The peak heights and centres differ, but these are influenced by the amount of sample used, so cannot be used to draw conclusions.	210

4.46	A close-up of the low frequency region of the IR spectra of HNTs, acid-etched HNTs, and piranha treated HNTs. The shoulder at about 1200 cm^{-1} is indicative of acid-etching of the nanotubes, and this has started to appear for both piranha-solution treated samples. The dotted lines are at 100% transmission for each sample.	211
4.47	A close-up of the high frequency region of the IR spectra of HNTs and piranha treated HNTs. Sun <i>et al.</i> reported a new peak at 3450 cm^{-1} after piranha solution treatment, which they suggest is evidence of formation of new Si-OH groups. ⁷ A broad absorption peak in this region was also found here, but it was found for untreated HNTs as well as piranha-treated HNTs, so it is not evidence of a change in the chemistry of the material. The dotted lines are at 100% transmission for each sample.	212
4.48	A close-up of the high frequency region of the IR spectra of p-HNTs that had and had not been dried immediately prior to measurement. Drying the samples reduces the intensity of the broad peak, suggesting that this peak is due to physisorbed water. To allow for comparison, the spectra have been adjusted using the ratio of the peak heights of the highest frequency Al-OH absorption (i.e. the peak at about 3700 cm^{-1})	213
4.49	The C 1s region of HNTs, pH1-HNTs, and piranha-solution treated HNTs. The signal-to-noise ratio is poor for samples other than the pure HNTs, so it could not be used for calibration. The left-hand image illustrates the relative peak intensities when the background is adjusted to be the same for all four samples, while the right-hand image illustrates the absolute count rates for each sample.	215
4.50	The concentration of elements in HNTs and piranha-solution treated HNTs relative to the concentration of silicon.	217
4.51	XPS data for the Si 2p region of HNTs and piranha solution treated HNTs, taken from work by Sun <i>et al.</i> (adapted with permission from The Royal Society of Chemistry). ⁷ They fit the Si 2p region of their piranha solution treated HNTs with two peaks, and suggest that this is evidence of an increased concentration of silanol functional groups.	218
4.52	A comparison of one and two peak fits for XPS data in the Si 2p region of HNTs and treated HNTs. The black line is the data, the red dashed line is the 1PF, and the blue dotted lines represent the 2PF.	219
4.53	XPS data for the O 1s region of HNTs, adapted from work by Kloprogge and Wood. ⁸ They fit the O 1s region of HNTs with three peaks, and suggest that the two largest peaks correspond to either Si-O-Si/Si-O-Al, or -O-H environments. Image adapted with permission.	220
4.54	The O 1s region in XPS spectra of p-HNTs and 90p-HNTs. Between different samples, there was a lot of variation in how the O 1s peak could be fitted. It is therefore difficult to ascribe any physical meaning to the fitted curves.	221

4.55	The raw data (black, solid lines) for the O 1s region of XPS spectra of HNTs can be fitted with one, two or three peaks (dashed lines). One peak clearly does not fit the edges of the peak, whereas two peaks produces a fit which is much closer to the raw data. Only using three peaks matches the data closely, but the three peaks do not match those described for halloysite by Kloprogge and Wood. ⁸	221
4.56	The water contact angle of untreated HNTs versus p-HNTs and 90p-HNTs. The HNTs and the p-HNTs have the same water contact angle, so it is concluded that the p-treatment does not change the HNT surface. However, the 90p-HNTs were measurably more hydrophilic; it is unknown why this is the case.	222
4.57	The water contact angles of all the APTES coated samples. None of the pre-treatments had an effect on the water contact angle of the obtained APTES-coated samples.	224
A.1	TEM images of and size data for ULTRA HalloPure HNTs provided by I-Minerals Inc.	239
A.2	Trace elements in ULTRA HalloPure HNTs provided by I-Minerals Inc.	240
A.3	The standalone data sheet for the properties of ULTRA HalloPure HNTs provided by I-Minerals Inc.	240
A.4	Histograms and PDFs for the internal and external diameters (a), and lengths and aspect ratios (b) of HNTs measured in TEM images from the first (i.e. old) and second (i.e. new) sets of measurements	242

List of Tables

1.1	The typical ranges of some of the physical properties of glass and carbon fibre fillers. The listed densities are relative to that of poly(ethylene). ⁹ . . .	3
1.2	The changes in mechanical properties of an epoxy resin seen by Deng <i>et al.</i> after inclusion of HNTs.	23
1.3	A summary of the effect of mixing method seen by Vahedi <i>et al.</i> on the impact properties of epoxy/HNT nanocomposites. ¹⁰	24
1.4	A table summarising the work of Sun <i>et al.</i> , who found that coating HNTs with different alkoxy silanes allowed them to reinforce an amine-cured epoxy resin to different degrees. ¹¹	25
1.5	A table summarising the changes in the mechanical properties of an epoxy resin after addition of HNTs or sodium-hydroxide-treated HNTs (a-HNTs).	26
1.6	The changes in mechanical properties for epoxy resin nanocomposites (10 wt% filler) relative to the pure epoxy seen by Tang <i>et al.</i> ¹² They compared the effects of different treatment times of HNTs with aqueous PPA (0 h = untreated HNTs)	27
1.7	A summary of the changes in mechanical properties of an epoxy resin seen by Vijayan <i>et al.</i> upon the addition of either HNTs or a HNTs/TiO ₂ hybrid at 5 wt% loading.	27
1.8	A summary of the changes in mechanical properties of an epoxy resin seen by Li <i>et al.</i> upon the addition of HNTs, PDA-modified, or Fe(OH) ₃ - and PDA-modified HNTs.	27
1.9	A summary of the reports on epoxy/HNT nanocomposites, as described in the main text. Refer to the text for more details regarding functionalisation. The mechanical properties are abbreviated as follows: FM (Flexural Modulus), FS (Flexural Strength), IS (Impact Strength), YM (Young's Modulus), TS (Tensile Strength), FT (Fracture Toughness), T (Toughness). For degree of dispersion: *imaged by TEM, **imaged by SEM. . .	30
2.1	“Typical Tube Dimensions” from the supplier data sheet.	37
2.2	“Typical Chemical Analyses” from the supplier data sheet (measured by X-ray fluorescence).	37

2.3	“Typical Trace Elements” from the supplier data sheet.	37
2.4	“Typical Mineralogy by XRD” from the supplier data sheet.	38
2.5	The approximate time taken for HNTs to completely sediment out of the groups of solvents described in the text.	42
2.6	The distance in solvent parameter space from water for all the solvents screened in this work, and that calculated using a literature value for the HSPs of a bisphenol-derived epoxy resin ¹³ (highlighted green).	44
2.7	The concentrations of the most abundant elements in HNTs as found by ICP-MS	46
2.8	The concentration of the most abundant elements in HNTs as found by ICP-MS converted to hypothetical concentrations of the oxides listed in the supplier data sheet.	47
2.9	A comparison of trace elements in HNTs from I-Minerals Inc. found by ICP-MS in this work, versus those listed in the supplier data sheet. Also included is the percentage difference between the supplier data and that found here.	48
2.10	A summary of peak positions and assignments in a powder XRD pattern of HNTs	49
2.11	A summary of peak positions in the IR absorption spectrum of HNTs, and the bonds and, where possible, specific vibrational modes they are assigned to.	51
2.12	The mode values of the HNT dimensions and their 95% confidence intervals, found from the peaks of log-normal PDFs fitted to measurements of particles in TEM images.	59
2.13	The initial and final variables from fitting an isolated HNT in a TEM image using the BL law.	79
2.14	A list of the materials used in this chapter.	98
3.1	The ultrasonication powers used by Vahedi <i>et al.</i> ¹⁰ versus this work. . . .	110
3.2	A summary of the abbreviations used to label samples in this chapter. The suffixes 1, 2 and 5, which are later used with these abbreviations, refer to the approximate amount of HNTs which were added to the epoxy resin before mixing (in wt%).	123
3.3	The mode lengths of the log-normal distributions fitted to the HNTs seen in TEM images of the N samples, and the maximum length of tube measured for each sample.	126

3.4	The mode lengths of the log-normal distributions fitted to the HNTs seen in TEM images of the N and W samples, and the maximum length of tube measured for each sample.	130
3.5	Filler content for uncured epoxy/HNT mixtures made by different mixing techniques, as found by washing away the resin through repeated rinsing, and weighing the resulting solid. The instrumental uncertainty in filler content is low, but values are only given to 1 d.p. in recognition of the fact that the uncertainty is unknown and probably much larger than the instrumental uncertainty (e.g. due to loss of sample during washing). . . .	136
3.6	Explanation of the variables used in equation 3.5	140
3.7	The filler contents of various epoxy/HNT samples as found by TGA in different atmospheres. Only TGA in air does not give nonsensical, negative values.	141
3.8	The densities of HNTs and cured epoxy (with no filler).	144
3.9	Values of filler content found via He pycnometry.	144
3.10	Explanation of the variables used in equation 3.10	147
3.11	The filler content of various epoxy/HNT samples as found by heating in a furnace. Asterisks indicate samples with particularly large uncertainties in filler content (arising from a low sample mass and/or an imprecise balance being used).	148
3.12	The filler content of various epoxy/HNT samples found by either TGA in air, He pycnometry, or burn-off in a furnace. These are compared to the expected filler contents calculated from the amount added to the resin before mixing.	149
3.13	The T_g s of pure cured epoxy and all of the epoxy/HNT nanocomposites made by different mixing methods, as found using DMA.	152
3.14	The results of flexural testing of the nanocomposite samples. Because of problems with the tensometer, samples were essentially measured in two different set-ups (original and changed), and the flexural moduli are normalised using that of a pure epoxy measured in each set-up. The error in flexural modulus is the standard error of several measurements, and the error in relative flexural modulus is that error for each nanocomposite propagated with the standard error in the epoxy measurement.	154
3.15	A list of the materials used in this chapter.	161
3.16	The 3RM parameters used to process the epoxy/HNT mixtures in gap mode.	162
3.17	The 3RM parameters used to process the epoxy/HNT mixtures in force mode.	162
4.1	The concentration of iron in HNTs and p-HNTs as found by ICP-MS . . .	206

4.2	The masses lost by treated and untreated samples of HNTs by 800 °C during TGA.	207
4.3	The temperatures at the onset of alumina decomposition for HNTs and treated HNTs.	210
4.4	The position of the Si 2p peak when binding energy is calibrated using either the C 1s peak or Al 2p as a reference. Using the Al 2p produces much less variation, and so is preferred.	215
4.5	The binding energies for the peaks fitted to XPS spectra of the HNTs and piranha-solution treated HNTs (calibrated by setting the Al 2p binding energy to 78.4 eV ⁸).	215
4.6	The concentrations of surface atoms as found in XPS spectra of the HNTs and piranha solution treated HNTs. The units are the percentage of total atoms, At%.	216
4.7	The relative (to Si) concentrations of surface atoms as found in XPS spectra of the HNTs and piranha-solution treated HNTs.	216
4.8	A comparison of the peak positions and residuals found when fitting the Si 2p of the HNT and piranha-solution treated HNTs with either one peak (1PF) or two peaks (2PF).	220
4.9	The grafted amounts of APTES on HNTs and pre-treated HNTs.	223
4.10	The relative (to Si) concentrations of surface atoms as found in XPS spectra of uncoated and APTES-coated HNT samples.	224
4.11	A list of the materials used in this chapter.	227
A.1	Explanation of the variables contained in equations A.1 and A.2	249
A.2	Explanation of the variables used in equation A.7	250

Chapter 1

Introduction and Literature Review

1.1 Introduction to polymer nanocomposites

1.1.1 Introduction to polymers

A polymer is a large molecule (or macromolecule) made up of a chain or 3D network of covalently bonded small molecules. These small molecules are known individually as monomers, and the process of converting monomer to polymer through a chemical reaction is known as polymerisation.¹⁴ Polymers can have dramatically different chemical and physical properties than their monomer analogues, for example in their reactivity, solubility, and rheology.¹⁴

Polymers can be broadly divided into two categories: thermoplastics, and thermosets.¹⁵ A thermoplastic is made up of discrete polymer chains, which can interact through intermolecular forces and physical chain entanglements to form solid networks. In contrast, thermosets consist of various complex 3D networks of monomers, oligomers (i.e. very short polymers), or polymer chains, which are connected to one other with strong chemical or physical bonds (known as cross-links), essentially forming a single macromolecule which spans the full extent of the material.¹⁵ An important practical distinction between the two classes of polymer is their behaviour upon heating or exposure to a compatible solvent: thermoplastics will eventually melt and flow as they are heated, while thermosets will only soften and eventually start to burn; and thermoplastics can fully dissolve in a compatible solvent, whereas thermosets can only swell.¹⁵ In terms of processing, thermoplastics are often easy to shape using formative manufacturing processes such as injection molding. In contrast, thermosets are often used as liquid resins in which the reactive monomers are mixed, then applied or poured into a mold before the application of an appropriate stimulus to cause or accelerate polymerisation (for example, light or, more commonly, heat). In some cases, thermosets can be made by cross-linking a thermoplastic after it has already been molded into shape, e.g. the vulcanisation of rubber. Excluding the obvious example of vulcanised rubber, most common, commercially utilised thermoset polymers tend to be stiffer and stronger than commercial thermoplastics, but are also much less ductile.¹⁶

In general, polymers are chemically unreactive, lightweight solids, which are stable under ambient conditions. These properties, as well as the relative ease of their processing, and the fact that many can be derived cheaply as a by-product of crude oil, mean that polymers have become ubiquitous in modern life. Their low density and chemical inertness in particular mean that polymers have attracted interest as engineering materials, for example for reducing the weight of automotive and aerospace parts, thereby increasing the fuel efficiency of the vehicle. However, polymers still do not have sufficiently robust mechanical and thermal properties to replace traditional engineering materials like steel in these high-performance applications.¹⁷

1.1.2 Introduction to polymer composites

One way of improving the engineering properties of polymers is by adding a second solid component to the polymer to make a reinforced polymer composite. The basic principle of

reinforcement is to add a relatively stiff and strong material to the bulk polymer to obtain a material with mechanical properties which are a combination of those of the two phases.¹⁸ When a load is applied to the composite, the stress is transferred from the bulk matrix to the more robust filler phase, leading to an increase in the Young's modulus (i.e. stiffness) and strength of the composite relative to the pure bulk material.¹⁸ The filler phase is often a substance which itself is also limited as a bulk engineering material, for example by its brittleness (e.g. glass), so the properties of the composite can be considered to be a synergistic combination of bulk and filler. That is to say, while the filler phase allows the useful transfer of load from the polymer, the polymer also provides a useful means of binding the otherwise difficult-to-use filler into a cohesive material.¹⁸ Where the filler is very brittle specifically, the polymer phase provides a means of dissipating stress build-up through plastic deformation.¹⁸ However, the opposite can also be true; if the filler is a particle of the right size, and the polymer is relatively brittle, then the presence of a hard filler can improve the toughness of the polymer by limiting crack propagation through a variety of mechanisms.^{19,20} Some of the most important fillers in traditional polymer composites are continuous carbon and glass fibres, as well as various other types of glass particles.¹⁸ Some of the typical ranges of properties of glass and carbon fibres specifically are listed in table 1.1, where they are also compared to the properties of high-density poly(ethylene), an important commercial thermoplastic.^{9,21}

Table 1.1: The typical ranges of some of the physical properties of glass and carbon fibre fillers. The listed densities are relative to that of poly(ethylene).⁹

Filler type	Relative density	Young's modulus/GPa	Tensile strength/GPa
Glass fibre ⁹	2.5	72	1.5 - 4.0
Carbon fibre ⁹	1.8 - 2.0	200 - 350	1.5 - 4.0
High-density poly(ethylene) ²¹	1	0.8 - 1.4	0.019 - 0.030

Fillers are not only added to polymers to provide mechanical reinforcement. For example, fillers are often included in polymers to improve their thermal stability. Organic polymers typically start to undergo thermal decomposition and ignition at relatively low temperatures, and can burn rapidly, often releasing large amounts of hazardous fumes and smoke.²² This means that they can be significant safety concerns in some applications.²² Particulate mineral fillers, such as aluminium hydroxide, can be added to combat this problem. Such fillers endothermically decompose at temperatures similar to the onset of polymer decomposition, meaning they can absorb some of the heat given out by the burning material, and they present a physical barrier for the diffusion of volatile gases within the polymer.²³ Some fillers also release water vapour upon thermal decomposition, which dilutes and cools the volatile organics being released from the material.²³ All of these effects serve to limit the self-perpetuation of combustion.²³ Appropriate fillers can also be added to change the thermal and electrical conducting properties of the polymer.¹⁸ It is also worth noting that cheap inorganic fillers are often added to polymers simply to allow the production of an increased volume of material for a lower cost (such fillers are known as extenders).^{18,24} However, for high-performance applications (e.g. aerospace and automotive), producing polymer composite materials with improved mechanical properties relative to the individual components is the main goal.

Where fillers are used to reinforce polymer materials, the importance of the interface and the interphase region between the filler and the bulk has long been recognised.²⁵ The interface is the 2D region at the surface of the filler, and the interphase is a 3D region starting at the edge of the filler and extending over the volume in which the properties of the local network gradually become those of the bulk.²⁵ Stress concentrations are thought to develop in the interphase region not only when a load is applied to the material, but also because of differences between thermal expansion coefficients between filler and bulk, as well as shrinkage of the bulk polymer due to curing or crystallisation.²⁶ The nature of this region is therefore considered crucial to the overall performance of the composite.²⁵⁻²⁷

In practice, the interface is engineered by adding a coating (often called a sizing) to the filler. This coating serves to change the chemical nature of the interface to make it more compatible with the bulk, thereby allowing more complete coverage of the filler surface, and reducing the number of voids caused by poor wetting, which would otherwise reduce the strength of the composite. It has also long been understood that the best coating agents are those which not only promote energetically favourable, physical interactions between the phases (i.e. promote wetting), but can also form covalent chemical bonds with both the filler surface and the bulk network.²⁸ Such species are often referred to as coupling-agents.

Commercial sizings are typically complex formulations containing not only coupling-agents, but also various components less important for adhesion (e.g. film-formers to enhance scratch resistance).²⁹ For glass fillers in particular, sizings normally contain some kind of alkoxy silane molecule as a coupling-agent.²⁹ Alkoxy silanes contain hydrolysable alkoxy groups which allows them to react with the hydroxyl groups present on many types of surface (e.g. silanol groups on glass surfaces), as well as an additional organic functional group, which can be chosen so that it is both compatible with, and able to react into, the appropriate polymer network. While current sizing technologies give good results, it is also widely acknowledged that improving the understanding of and the ability to engineer the composite interface is important for the ongoing improvement of composite performance.³⁰

Epoxy resin composites

Epoxy resins are often the preferred bulk component for making polymer composites. Epoxy resin is the generic name given both to organic monomers containing two or more epoxide groups, and to thermoset polymers derived from such epoxy monomers.³¹ A common example of an epoxy resin monomer, the difunctional diglycidyl ether of Bisphenol A (DGEBA), is shown in figure 1.1. Epoxide groups are highly reactive to nucleophilic attack (figure 1.2), which opens the strained epoxide ring to produce a new covalent bond and a pendant alcohol group.³¹ This means epoxies will readily react with dinucleophiles such as diamines to form thermoset polymer networks via step-growth polymerisation.³² However, this is an oversimplification of the process, as the alcohol groups produced by ring opening can both catalyse further ring opening, and act as nucleophiles themselves (in a process known as homopolymerisation). As network development proceeds, the viscosity of the mixture increases as increasingly large polymer networks are created, and eventually these large polymer networks join to form a continuous polymer that spans the extent of the material (i.e. a gel).³² During the reaction, the material also shrinks be-

cause of conversion of the relatively long intermolecular bonds to shorter covalent bonds. Eventually, an amorphous solid is produced, which is typically glassy at ambient temperature, and has significant hydrophilic character because of the high concentration of alcohol groups. The polymerisation process is known as curing, and while reaction occurs immediately upon mixing of the epoxy monomer and the dinucleophile, the mixture is normally heated to ensure that the optimum rate and extent of reaction is achieved.³²

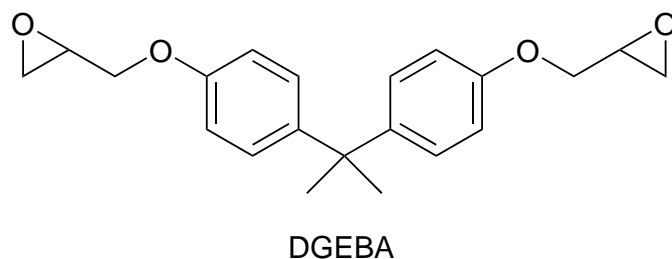


Figure 1.1: The skeletal structure of the difunctional diglycidyl ether of Bisphenol A (DGEBA), a commonly-used epoxy resin monomer.

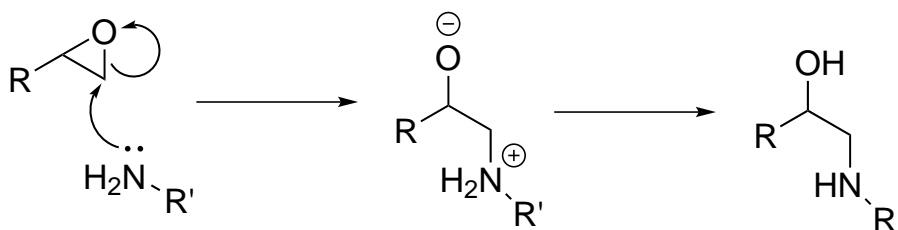


Figure 1.2: The opening of the epoxide ring by nucleophilic attack, in this case by a primary amine.

Epoxy resins are used in composites for a number of reasons: they have a relatively low viscosity, which allows easy processing and impregnation inbetween the filler phase; they are very reactive upon curing; their curing can be controlled without producing volatiles; and they have sufficiently robust mechanical properties, yet low enough density to be useful in high-performance applications.³³ It is also easy to promote good adhesion between an epoxy resin and various filler phases, since many types of alkoxy silane are available with nucleophilic functional groups that will readily react into the epoxy network during cure (e.g. the amine-functional molecule, (3-aminopropyl)triethoxy silane (APTES)). However, the use of epoxy resins has several potential drawbacks. Firstly, they are significantly more expensive than many types of polymer, particularly those thermoplastics which are produced in high volumes, e.g. poly(styrene) and poly(ethylene).³⁴ However, in high-performance applications, the additional cost can often be justified if sufficient improvements in performance are gained. More importantly, while the mechanical properties of cured epoxy resins are good relative to many other polymers, they are still not ideal; not only do they have a relatively low modulus compared to other engineering materials (e.g. metals), they are also quite brittle and hence can undergo fracture and catastrophic failure at high loads or under impact.³⁵ Epoxy resins also retain many of the engineering disadvantages of polymers in general, notably flammability and permeability (with water uptake into the hydrophilic network being a particular cause for concern³⁶). Therefore, while epoxy resins remain widely used in composites, research continues into methods to improve their engineering properties. This includes the addition of particulate fillers to the resin.³⁷

1.1.3 Introduction to nanocomposites

The degree of mechanical reinforcement provided by a filler in a polymer composite increases as the surface area for load transfer between the two phases increases. Increasing the amount of surface area of filler obviously requires the addition of a greater volume of filler, which necessarily also increases the mass of the composite because fillers (e.g. glass and carbon fibre) are usually denser than polymer resins. For example, the densities of typical polymer resins are about 1.1 - 1.5 gcm⁻³, whereas the densities of glass and carbon fibres can be anywhere from 2 to 2.5 gcm⁻³. In traditional polymer composites, a substantial volume fraction (typically over 10 vol%) is required for effective reinforcement,¹⁸ which amounts to a significant increase in mass relative to the pure polymer. In addition, since load transfer between the bulk and reinforcing phases only occurs in the interphase, much of the volume of each individual filler unit is essentially “dead weight” since it is unnecessary for effective reinforcement. The use of nanoparticles rather than micro- or macroparticles can avoid this problem.

A nanoparticle is generally defined as any particle which has at least one dimension in the range of 1-100 nm, and the term encompasses particles of many different shapes, including spheres, tubes/fibres, and plates.³⁸ Because of their small size, nanoparticles have a very high surface-area-to-volume ratio, and those with high aspect ratio morphologies like nanotubes and nanoplates have particularly high surface areas. This means that when nanoparticles are used as fillers in polymer composites (i.e. to make a polymer nanocomposite), there is a much higher area for interaction between filler and bulk compared to the same mass loading of traditional micro- or macrofillers. That is to say, a much lower mass of nanofiller should need to be added for the same reinforcing effect to be achieved, so nanoparticles should be more desirable for composites than traditional fillers.³⁹

However, it is not easy to replace traditional fillers with nanofillers, as there are a number of unique challenges associated with making effective nanocomposites. For example, while the high specific surface area of nanoparticles makes them effective reinforcing agents, it also means that there is a high surface area for interaction of the particles with one another. In cases where the energetic interaction between the particle and bulk is significantly less favourable than that between the particles, there can be a large thermodynamic barrier to dispersion of the nanoparticles.⁴⁰ Agglomeration of particles in these cases hinders the mechanical reinforcement of the polymer, or even reduces the mechanical properties of the nanocomposite in comparison to the pure polymer.⁴¹ In addition, their small size means that nanoparticles begin to percolate in bulk media at low weight concentrations. This can lead to significant increases in mixture viscosity,⁴⁰ which may represent a serious hindrance to processing. Issues like these mean that the replacement of traditional composites with nanocomposites has not been realised in many applications; doing so remains the focus of much research.

Many different types of nanoparticle have been researched as fillers for polymer composites. These include advanced carbon nanomaterials like carbon nanotubes (CNTs) and graphene, metallic nanoparticles (e.g. gold and silver), and various types of other inorganic nanoparticles (e.g. metal oxides), including several which are naturally occurring.⁴² Much of the research on nanocomposites is not focused on mechanical reinforcement, but rather on other applications that can utilise the high specific surface area of nanoparticles, including in electronics, environmental remediation, and biomedical applications.⁴²

For example, silver nanoparticles are often used as antimicrobial agents,⁴² since their higher specific surface area means that the active antibacterial ions (i.e. Ag^+) diffuse faster from the surface of a sample of silver nanoparticles compared to the same amount of bulk metal.⁴³ This allows less of the expensive precious metal to be used to achieve the same effect. Perhaps the most widely studied nanoparticles for mechanical reinforcement specifically are the advanced carbon nanomaterials (CNTs and graphenes), and nanoparticles derived from naturally occurring clay minerals. Accordingly, these two classes will be discussed in more detail.

Because of their conjugated networks of sp^2 electron orbitals, both CNTs and graphenes have unique electrical and structural properties, and they are predicted to have tensile strengths on the order of 100 GPa, and Young's moduli on the order of 1 TPa.^{44,45} These impressive mechanical properties mean that they have long been considered promising as reinforcing fillers for polymers. However, their potential as reinforcements in polymer nanocomposites has still not been fully realised, not least because their surface chemistry makes them incompatible with many solvents and polymers.⁴⁶ As such, commercial applications of CNTs in particular have mainly taken advantage of their electrical properties,⁴⁴ where good dispersion is not as important. In addition, it can be hard to justify their use in many applications because of their high cost⁴⁴ and potential hazard.⁴⁷

Of the clays used in polymer nanocomposites, montmorillonite (MMT) is arguably the most important. MMT is an aluminosilicate consisting of rigid plates each made from an alumina sheet sandwiched between two silica sheets. The isolated sheets have a modulus of around 180 GPa,⁴⁸ making them suitably stiff to be able to reinforce polymers. The silica faces of each plate have a net negative charge, and small cations (e.g. sodium) occupy charged sites on the surfaces. These cations are able to act as bridges between charged sites on opposing surfaces, which causes the individual plates to stack and form particles. The particles are on the order of microns in size, but the individual sheets have a thickness of about a nanometre, and can be separated from one another to produce plate-like nanoparticles in a process known as exfoliation. To exfoliate the particles into polymers or pre-polymer resins to make nanocomposites, the interlayer gallery between the sheets (which is inherently hydrophilic because of the charged species present) must be made more compatible with the bulk to allow diffusion of the bulk material therein. Fortunately, this is easy to do: the interlayer cations in MMT can readily be exchanged with cationic organic surfactants like alkyl ammonium species, which have a cationic end with which to adhere to the negatively-charged clay surface via Coulomb forces, and a hydrophobic organic end with which to interact with the bulk.⁴⁹ However, even with organic modification, high-shear and extended processing times are needed to disperse the platelets.^{50,51} Nonetheless, such organically modified MMT clays (organoclays/oMMT) have found widespread use in nanocomposites for many years, for example in automotive parts (e.g. timing belts).³⁸ In particular, they are valued for their barrier properties, i.e. their ability to decrease the rate of gas diffusion through the polymer by presenting an impermeable, physical barrier which increases the diffusion path length for the gases within the network.⁵² As previously mentioned, this increases the flame retardancy of the polymer,²³ but is also desirable in applications where any gas diffusion through the polymer should be avoided, e.g. in rubber car tyres.³⁸ As well as being useful as nanofillers in polymers, since MMTs are naturally occurring, they are widely available, cheap, and environmentally and biologically benign (at least in their native state).⁵³

However, MMT is not the only type of clay to attract research interest as a nanofiller: other clays that have been used include sepiolite, palygorskite, kaolinite, and halloysite, to name but a few.⁵⁴ These clays all share the benefit of being naturally abundant, but can have significantly different chemical, physical, and morphological properties. In general, they are solids composed of alternating layers of silica bonded to another inorganic oxide, typically alumina or an alkali or alkali earth metal oxide (e.g. sepiolite is a magnesium silicate), and assemble into nano- or microplates or fibres/tubes. Of these, halloysite in particular has been attracting growing research interest, both in general, and in the field of nanocomposites specifically. This can be seen in figure 1.3, which illustrates how the number of publications about halloysite and halloysite nanocomposites has been rising almost exponentially over the last decade. Indeed, the field has grown from a niche area with very little interest to one which attracts hundreds of publications a year (although it should be noted that the search term “halloysite nanocomposite” includes hybrid nanoparticles of halloysite and another material, not just polymer nanocomposites).

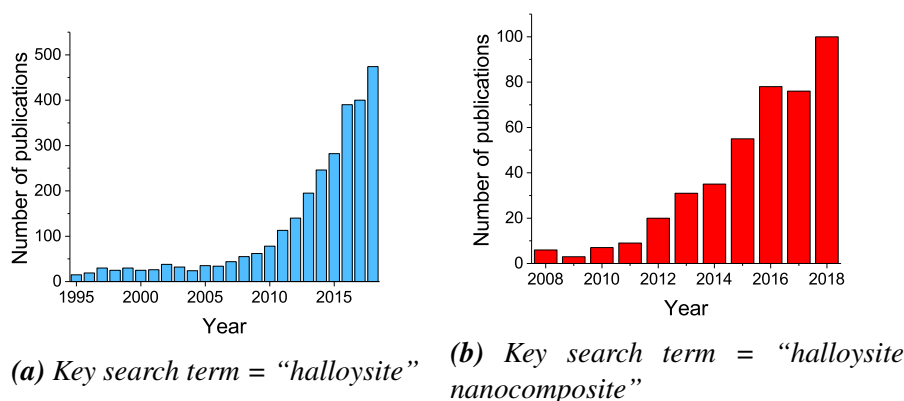


Figure 1.3: The number of publications about halloysite in general per year from 1995 to 2018, and about halloysite nanocomposites specifically from 2008 to 2018. The last decade has seen a huge increase in research interest in HNTs and HNT nanocomposites. This data was generated on Web of Science by finding the number of search results per year matching the key search terms shown.

1.2 Introduction to halloysite nanotubes

1.2.1 Chemistry and structure of halloysite

Halloysite is a clay mineral with the chemical formula $\text{Al}_2\text{Si}_2\text{O}_5(\text{OH})_4 \cdot n\text{H}_2\text{O}$, where n equals 0 or 2 depending on the degree of hydration of the mineral’s environment.⁵⁵ It consists of sheets of tetrahedral silica which corner-share oxygen atoms with aluminium-centred octahedra. The crystal structure of halloysite is illustrated in figure 1.4. One surface of each sheet is mainly siloxane (Si-O-Si), while the other surface consists of aluminol (Al-OH) groups. The silica surface of each sheet bears a net negative charge, whereas the inner alumina surface has a permanent positive charge. There are also silanol (Si-OH) groups present at the edges of the silica surfaces, and at any surface defects.⁵⁶ While these groups are hydrophilic, it is supposed by some that halloysite is “relatively

hydrophobic” compared to other types of clay particle because the surface silanol groups are only present in relatively low concentrations.⁵⁷ This is in turn thought to mean that halloysite should be more readily able to disperse in polymers without modification than other types of nanoclay.⁵⁷

When halloysite is hydrated (i.e. $n = 2$), there is a thin layer of water molecules between each aluminosilicate sheet, and these form hydrogen bonds with one another, with oxygen atoms on the siloxane plane, and with hydroxyl groups on the aluminol plane.⁵⁵ When hydrated, the d_{001} dimension of the mineral, i.e. the distance from the top of one silica layer to the top of another, should be 10 Å (a 7 Å thick aluminosilicate sheet plus a 3 Å layer of water).⁵⁵ However, water is readily lost from halloysite even in ambient conditions, so in most cases halloysite is seen via X-ray diffraction (XRD) to have an interlayer distance closer to 7 Å. Indeed, halloysite has only been measured to have d_{001} of 10 Å when the sample is kept on a damp substrate throughout the acquisition of XRD data.⁵⁵ Preserving an interlayer spacing of 10 Å requires either keeping the halloysite wet, or carefully controlling the humidity conditions in which it is stored.⁵⁵ Dehydration of some halloysites can permanently change the morphology of the nanoparticles.⁵⁸

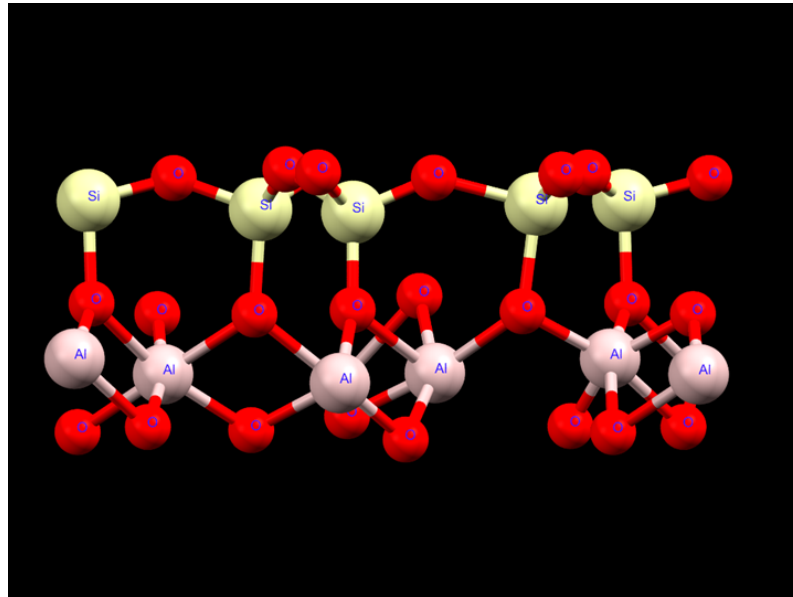
1.2.2 Geological occurrence and morphology of halloysite

Halloysite occurs in a number of locations on several continents, including North America (Idaho, Utah), South America (Brasil, Guatemala), Asia (China, Japan), and Oceania (Australia, New Zealand).⁵⁵ Samples of natural halloysites can contain particles of a number of different morphologies, including tubes, spheres and pseudospheres.⁵⁵ The occurrence of these morphologies is related to local geological and environmental factors, such as soil type and weathering. For example, certain halloysite morphologies can be correlated with the local concentrations of iron, as Fe (III) is able to undergo isomorphic substitution with Al (III) in the mineral’s crystal structure.⁵⁵ The dominant morphology of halloysite is typically a high aspect ratio, hollow tube, with the exact morphologies and size distributions of the tubes depending on the exact geological environment in which they are found.⁵⁵ However, regardless of origin, the tubes’ diameters are typically of the correct size for them to be considered nanotubes. The halloysite nanotubes (HNTs) used in this work are from a site in Idaho which has only recently begun to be commercially utilised. A transmission electron microscope (TEM) image of some of these HNTs is shown in figure 1.5.

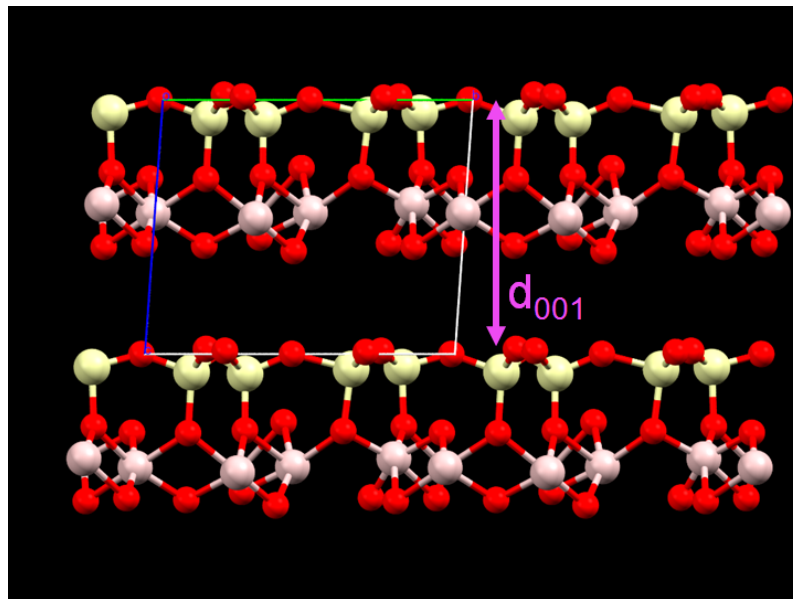
1.2.3 Halloysite and kaolinite

Halloysite is chemically identical to another mineral, kaolinite, and the two are often found in the same deposits.⁵⁵ However, kaolinite particles consist of stacks of aluminosilicate platelets (figure 1.6), rather than the individual particles of rolled (or otherwise deformed) sheets seen for halloysite. In kaolinite, there is no interlayer water, and the sheets are held together by extensive hydrogen bonding between each neighbouring alumina and silica face.⁵⁹

Halloysite and kaolinite form under similar geological conditions, and are usually the re-



(a)



(b)

Figure 1.4: The unit cell of halloysite with Al, Si and O atoms labelled (a), and a 2 x 2 matrix of halloysite unit cells which illustrates the layered structure of the mineral (b). The distance between the 001 planes, d_{001} , i.e. the interlayer distance, is illustrated in the bottom image. Missing from the images are hydrogen atoms, which are present in hydroxyl groups found on the alumina surface and at edges and defects on the silica surface.

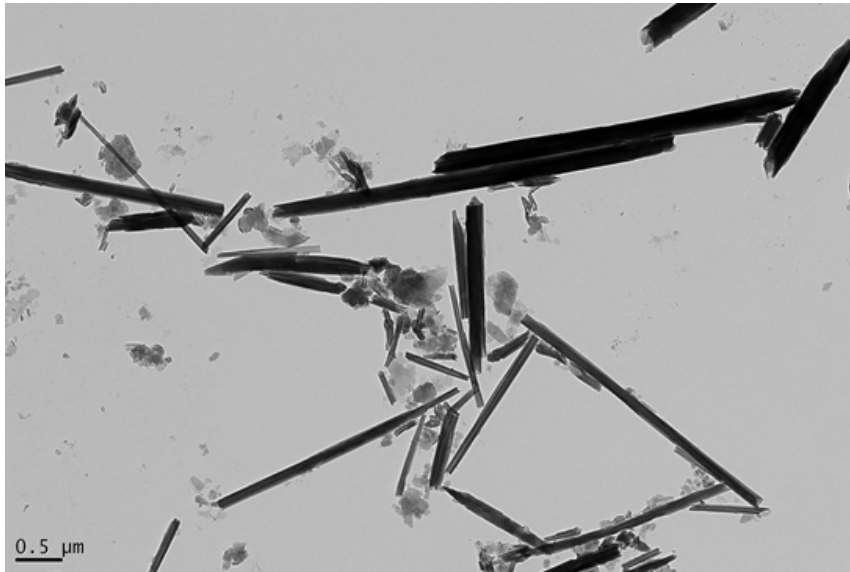


Figure 1.5: TEM image of HNTs from Idaho, which were used in this work. The image shows the wide variety of tube dimensions, as well as the presence of some morphological impurities (i.e. the flat sheets).

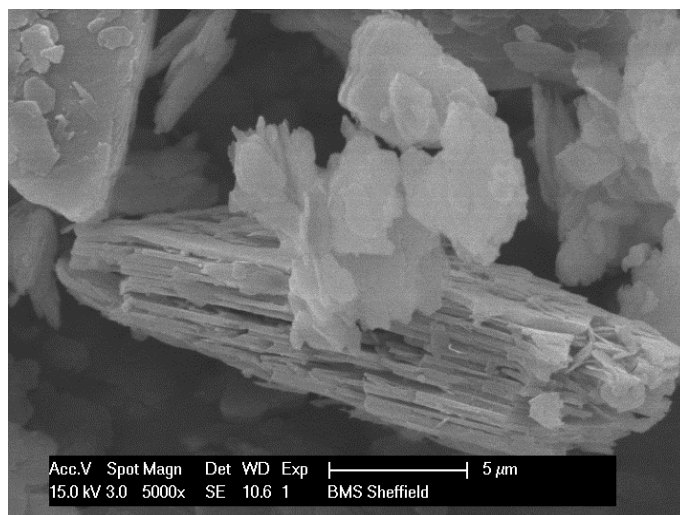


Figure 1.6: A scanning electron microscope image of a kaolinite particle. The structure of stacked aluminosilicate platelets can clearly be seen

sult of weathering of other minerals in warm, wet locations, or by hydrothermal activity.⁶⁰ For example, they may be formed from the interaction of groundwater with silicate minerals or glassy volcanic ash. Kaolinite is also commonly found in secondary sedimentary deposits, but halloysite is mostly authigenic, i.e. deposits of halloysite are usually found in the same place as the mineral was formed.⁶⁰ This is thought to be because halloysite is more easily destroyed under the mechanical stresses exerted during erosion, transport, and deposition.⁶⁰

It is difficult to distinguish between kaolinite and halloysite in mixed samples of the two minerals, although it can be done.⁵⁵ The most effective way is to treat the mixed sample with an organic compound which can intercalate between the aluminosilicate layers in halloysite but not kaolinite.^{55,61} A comparison of the intensities of the d_{001} XRD peaks corresponding to expanded and unchanged interlayer distances can then be used to quantify the relative amounts of halloysite and kaolinite respectively in the sample.⁶¹

1.2.4 Formation of the halloysite nanotube

The tubular structure of halloysite has often been attributed to a mismatch in the size of the bonded silica and alumina units, which have the unit cell parameters $a = 5.02 \text{ \AA}$, $b = 9.164 \text{ \AA}$, and $a = 5.066 \text{ \AA}$, $b = 8.655 \text{ \AA}$, respectively.⁵⁶ This is thought to lead to distortion of the units and subsequent structural stress, which can be compensated for by a rolled, scroll-like structure.^{56,62} Computational modelling studies suggest that any distortion of bond lengths caused by rolling of the sheets is negligible, as the stress is distributed evenly across the whole nanotube.⁶³ Kaolinite does not roll up in this way because of strong hydrogen bonding between different aluminosilicate sheets, which can overcome the stress from the structural distortion.⁶²

In the laboratory, kaolinite plates can be converted into the nanoscrolls typical of halloysite, and vice versa. The former can be achieved by treatment of kaolinite with an ammonium salt in methanol, as the solvent and salt are able to intercalate between the individual sheets and disrupt the hydrogen bonding holding them together.⁶⁴ Conversely, prolonged dehydration or intercalation of the aluminosilicate layers of halloysite with organic molecules can cause the scrolls to unroll into thin sheets.^{12,62}

The preferential formation of halloysite relative to kaolinite in certain deposits is explained by geologists in terms of local environmental conditions. More specifically, the nucleation and growth of halloysite crystallites is thought to be favoured relative to that of kaolinite where groundwater is more acidic, and in sites which remain constantly wet, but have fluctuating concentrations of dissolved ions.⁶⁰ However, there is still some discussion as to whether this is the case, or if halloysite nanotubes actually form when weathering of existing kaolinite particles causes the individual aluminosilicate sheets to roll in a similar mechanism to that which can be achieved experimentally by chemical treatment.^{64,65} The dynamics of this rolling mechanism are still not fully understood.⁶⁵

1.2.5 The mechanical properties of halloysite nanotubes

The measurement of the mechanical properties of nanoparticles like HNTs is not straightforward because of their nanoscale size. Nonetheless, it can be achieved, and values for some flexural properties of HNTs can be found in the literature. For example, Lecouvet *et al.* were able to obtain a value of the flexural modulus of HNTs by using atomic force microscopy (AFM) to carry out a “nanoscale three-point bending test”.¹

They did this by first dispersing the HNTs in ethanol, then filtering the dispersion through a poly(carbonate) membrane containing uniformly sized pores. During filtration, some of the HNTs became positioned such that they lay as bridges across the pores (figure 1.7). The AFM tip was positioned halfway across these tubes, and the test was performed. Measurements were also conducted on HNTs on the membrane, but not suspended across pores, to confirm that the tip did not penetrate the nanotubes i.e. to confirm that any deflection of the cantilever was solely due to bending of the tube.¹ However, they do not comment on whether distortion of the membrane occurs during the measurement, or whether this would significantly affect the measured modulus.

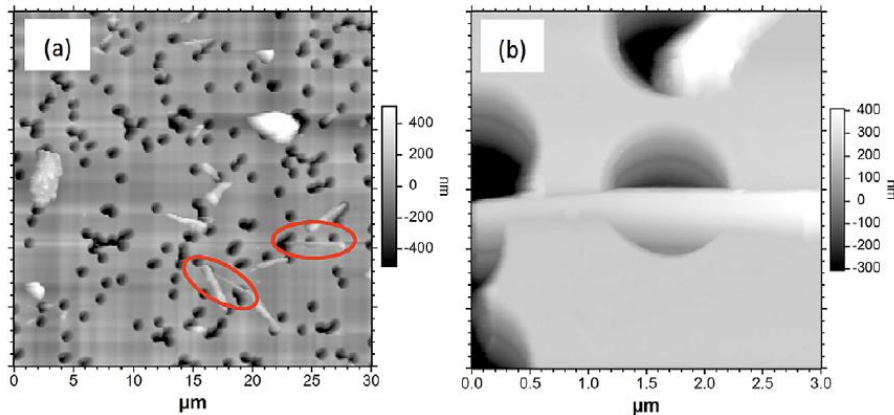


Figure 1.7: AFM images of HNTs on a microporous membrane. The image is reproduced with permission from work by Lecouvet *et al.*, who used the AFM tip to perform 3-point bending tests on any nanotubes observed to be correctly bridging the pores.¹

It was observed that modulus was greatest for the thinnest tubes. They suggest that this is mainly due to surface tension effects, which arise because bending the nanotubes leads to an increase in their length and hence surface area. They justify this in terms of an empirical relationship of surface tension to a nanorod’s dimensions when it is deformed under bending conditions (equation 1.1),¹ which had been observed previously by Cuenot *et al.*⁶⁶ More specifically, when two nanotubes are comparable in length (L), the surface tension is much greater for the nanotube with smaller diameter (D), i.e. it requires more energy to bend a thinner nanotube. This effect was also previously reported for other high aspect ratio nanoparticles, including Ag, Pb and ZnO nanowires.⁶⁶

$$\text{Surface tension} \propto \frac{L^2}{D^3} \quad (1.1)$$

Overall, they tested around 25 nanotubes between 50 and 160 nm in diameter, and the average elastic modulus obtained was 140 GPa. However, the modulus depended signif-

icantly on the diameter of the tube, and the measured values varied from 10 to 460 GPa. The flexural moduli of HNTs with a diameter greater than 160 nm were not measured, because it was thought that the applied load would mainly cause inelastic shear deformations as the individual layers of the tubes slipped over each other, rather than elastic bending of the whole structure. Nonetheless, a modulus of 140 GPa means that HNTs should certainly be stiff enough to be effective reinforcements for polymer materials, and indeed this value is similar to that of the MMTs (ca. 180 GPa)⁴⁸ and glass fibres (ca. 72 GPa)⁹ frequently used in existing polymer composites.

1.2.6 Biocompatibility of halloysite nanotubes

Traditionally, the potential of a particle to be a hazard to human health has been determined from its chemistry.⁶⁷ However, this view is increasingly being recognised as incorrect; the size of a particle is now known to also be a key factor in its potential to cause harm.^{67,68} More specifically, particles on the order of tens to hundreds of nanometres are small enough to be able to penetrate parts of the body not reached by large particles (e.g. the deepest parts of the lungs), but too big to be cleared away by autophagic processes.⁶⁷ An increased particle length and aspect ratio (i.e. the ratio of length and width) is also known to correlate to increased hazard, which can make nanotubes/fibres a particular cause for concern; asbestos is the most famous example of this. Once in the body, nanoparticles can undergo various chemical interactions with biological chemicals, e.g. the generation of free radicals, which can either cause cell death directly, or alternatively lead to a prolonged, harmful immune response.⁶⁷ It is typical for halloysite samples to contain particles with sizes of the right order of magnitude to be hazardous, hence it is important to consider the potential for them to cause harm.

Despite their size and shape, HNTs are generally regarded in the literature as being biocompatible;^{56,57,69} indeed typical safety data sheets for halloysite report no hazard statements. While the absence of evidence for toxicity should not be taken as evidence of absence, especially since research interest in halloysite, and nanotoxicology in general, are in relative infancy, there are several reports that support the view of halloysite being relatively biologically benign. For example, Vergaro *et al.* found that HNTs were only toxic to human cancer cells at relatively high concentrations (above about 7 wt%) and long exposure times; they even conclude that the degree of cytotoxicity of HNTs is lower than that of table salt.⁷⁰ The nanotubes were also found to be non-toxic towards simple aquatic organisms at concentrations up to 0.1 wt%, in contrast to graphene oxide, which was highly toxic.⁷¹ Similarly, it has been shown that ingestion of HNTs by zebrafish⁷² and nematode worms⁷³ does not lead to acute toxicity or significant inhibition of the organisms' growth rates. The body of evidence against the cytotoxicity of HNTs has typically led researchers to the conclusion that HNTs are suitable for use in biomedical applications, at least in non-invasive ones (e.g. cosmetics, wound care etc.), where the lack of a natural excretion pathway of HNTs from the body should not be a concern.⁷⁴

However, despite the general consensus that HNTs are safe, there is also evidence that HNTs can cause inflammation of human intestinal cells *in vitro*,⁷⁵ and inflammation of lung tissue when inhaled by mice.⁷⁶ The latter is of particular concern, since it is well known that chronic exposure to certain respirable dusts, including silica minerals, can not

only lead to a number of different interstitial lung diseases (including cancer),^{77,78} but can also cause damage to various other organs as part of the immune response to the inflammation caused by the particles.⁷⁸ It is also worth noting that when Koivisto *et al.* studied the concentrations of HNTs released as aerosols during mixing into a medium, they found that the potential respiratory exposure level was significantly below the regulatory limit for kaolinite, but it was significantly higher than that for CNTs, which are known to represent a considerable respiratory hazard.⁷⁹ Outside the fumehood in which they performed the mixing, however, the aerosol level remained no higher than the background.⁷⁹ They comment that, in the absence of complete toxicological data, particularly with regards to chronic exposure, HNTs should not be assumed to be safe to handle without appropriate extraction. Nonetheless, while it is clear that they should not be assumed to be completely safe, reviewing the literature suggests that HNTs are at least much less hazardous than many other types of nanoparticle,⁶⁷ especially carbon nanoparticles such as CNTs.⁴⁷ This is often cited as a key advantage of HNTs.^{56,57,69}

1.2.7 Overview of possible applications for halloysite nanotubes

A variety of different applications have been investigated for HNTs. Typically, researchers identify the apparent biocompatibility and/or hollow interior of the nanotubes as key features required for the application, with the abundance and low cost of HNTs being an additional advantage over existing nanoparticles (e.g. synthetic nanoparticles, which may be expensive and/or difficult to produce on a large scale).⁵⁶ Some of the applications discussed in the literature for HNTs include biomedical applications, environmental remediation, catalysis, and as reinforcing fillers in polymer nanocomposites.⁵⁶

Where HNTs have been studied for biomedical applications, their hollow interiors have often been utilised to allow for controlled release of active compounds, e.g. drugs. That is to say, the compound can be loaded into the nanotubes, and will slowly diffuse back out while in situ. This serves to extend the release time of the compound compared to where it is simply mixed into the formulation or applied directly. For example, Levis and Deasy showed that loading HNTs with propranolol (a beta blocker) and coating the nanotubes with a cationic polymer could extend drug release from under 1 h to over 8 h.⁸⁰ Similarly, Tan *et al.* showed that HNTs could be made to release ibuprofen over several days.⁸¹ In some cases, other chemical phenomena have been utilised to allow stimulated release of the compounds from the HNTs. For example, Li *et al.* demonstrated that doxorubicin (an anti-tumour drug) release from HNTs occurred at a much faster rate at pH 5 than at pH 7,⁸² and Cavallaro *et al.* were able to stimulate curcumin release from HNTs using heat by coating the loaded nanotubes with a thermally responsive polymer.⁸³ In some cases, adding antimicrobial-agent-loaded HNTs into a polymer composite intended to adhere to hard tissue has not only improved the antimicrobial functionality of the composite, but also increased the strength of its adhesion to the tissue.^{84,85} It is clear that HNTs do have potential for use in biomedical applications, but the wisdom of actually using them in vivo would depend on further investigation to confirm the exact level of hazard they represent.

The hollow interior of HNTs has not only been taken advantage of for controlled release in biomedical applications. For example, Cavallaro *et al.* suggested that adsorbing anionic, fluorinated surfactants to the positively charged interior surface of HNTs could be a route

for controlled release of oxygen in aqueous media.⁸⁶ Jing *et al.* showed that modification of the HNT interior using octadecylphosphonic acid allowed loading of a hydrophobic flame retardant into HNTs, which could be released (in a solution of THF) over a period of 80 h.⁸⁷ This may be a promising system for improving the flame retardancy of polymer nanocomposites. Owoseni *et al.* showed that HNTs loaded with surfactant could effectively stabilise oil-in-water emulsions through a synergistic combination of the surfactant lowering droplet surface tension, and the HNTs adsorbing at the oil-water interface and providing a steric barrier to droplet coalescence.⁸⁸ Delivering surfactant in this way was suggested as a possible method for oceanic oil spill remediation, since HNTs are environmentally benign.⁸⁸ From these examples alone, it is clear that HNTs have potential for controlled release of a variety of compounds in a variety of different contexts. However, as of yet, none of these appear to have been commercialised.

Another interesting application of HNTs is in environmental remediation. Clays in general have been frequently studied for this application, since they are cheap, inherently environmentally benign (at least when unmodified), have high specific surface areas with which to interact with pollutants, and can easily be chemically modified in a variety of ways.^{53,89} The surfaces of clays also have a spontaneous charge, which facilitates the adsorption of metal ions to them in aqueous solution.⁸⁹ For example, unmodified HNTs have been shown to have a high adsorption capacity for silver ions in water.⁹⁰ However, most studies regarding removal of pollutants from solution using HNTs have also applied some kind of chemical modification to the nanotubes. For instance, He *et al.* coated HNTs with iron oxide nanoparticles to facilitate removal of uranium dioxide from water,⁹¹ and Matusik and Wscisclo showed that modifying HNTs with diethanolamine allowed them to effectively adsorb a variety of potentially hazardous heavy metals, which could subsequently be removed from solution with the HNTs.⁹² Bielska *et al.* adsorbed Rose Bengal dye onto HNTs which, upon irradiation with visible light, generates free radical species, thereby causing the breakdown of phenol-based pesticides.⁹³ However, while it is obvious that HNTs can be effective in various environmental remediation applications, it is probable that using cheaper, more abundant, yet chemically similar clays (e.g. MMT and kaolinite) would be preferable to using high-purity HNTs (excluding cases where the hollow interior of HNTs plays an important role, e.g. Owoseni *et al.*⁸⁸).

HNTs have also been used in catalysis. Pure HNTs can be used directly as catalysts for cracking in the petroleum industry,⁹⁴ but most research using HNTs for catalysis has tended to focus on the immobilisation of metal nanoparticles on the HNT surface, and these metals are the active catalysts. Examples include silver⁹⁵ and gold⁹⁶ for the reduction of nitrobenzenes, and palladium for carbon-carbon cross-coupling reactions.⁹⁷ Some other interesting examples include magnetic iron oxide particles as well as the catalyst particles, which allows the nanotubes to be magnetically retrieved from solution after the reaction has been completed.⁹⁸ Immobilising the metal nanoparticles on a solid support has the advantage of providing a high surface area for catalysis while avoiding agglomeration of the metal particles. However, it is not always clearly explained why HNTs should be used instead of other types of particle with similar chemistry.

While there are obviously a wide variety of potential applications for HNTs, their use as mechanical reinforcements in polymer nanocomposites is possibly one of the most achievable at this point in time. Using HNTs as engineering materials should largely avoid the issue of their potential respiratory hazard, since they will be fully encapsulated

in polymer by the time they reach their end use. That is to say, exposure to the pure nanotubes would only occur during manufacturing, something which can easily be mitigated by engineering controls (e.g. extraction). Using HNTs in polymer nanocomposites also makes use of their high aspect ratio, and good mechanical properties, and it should also be relatively easy to modify them using existing coupling-agents for silica glass fillers given the chemical similarity between glass and HNT surfaces. The natural abundance of HNTs would also be of great benefit, as it would allow for rapid scale-up of any new nanocomposite technology. For these reasons, the use of HNTs in polymer nanocomposites was chosen as the focus of this project.

1.2.8 Commercial availability of halloysite nanotubes

Cost is an important consideration in the development of commercial polymer materials. Due to its association with and similarity to kaolinite, halloysite has long been used as a raw material in the ceramics industry.⁹⁹ As such, it has also long been available in large quantities; in 2008, annual halloysite production was already estimated at >50 kTon per year.¹⁰⁰ For comparison, this is similar to estimates of carbon fibre production at around 40 kTon per year,¹⁰¹ and much greater than CNT production at between 2 - 5 kTon per year⁴⁴ (both estimates are from 2013). This is in turn reflected in the price of HNTs: figure 1.8 shows the specific prices for several different types of commonly used nanoparticles (at least in research), and it can be seen that HNTs are several orders of magnitude cheaper than well-known, carbon-based nanomaterials. However, HNTs are somewhat more expensive than existing, commercially-utilised clay nanomaterials, and much more expensive than inorganic fillers that are commonly used as extenders.

Comparing prices in this way can be used to inform the choice of possible commercial applications for HNTs. More specifically, it illustrates that HNTs are probably too expensive to be economically viable in high volume applications, where polymer products should be produced as cheaply as possible (e.g. packaging for consumer goods). Instead, specialised applications such as high-performance engineering are probably where HNTs would be best used, i.e. applications where increased costs can be justified if performance gains are sufficiently high. In these applications, the main competitor to HNTs would be oMMT, which is both somewhat cheaper and already widely commercially available.

1.3 Halloysite nanotubes in polymer nanocomposites

There have been a number of publications about the application of HNTs in polymer nanocomposites to date. In general, these have justified investigation of HNTs as nanofillers because of their high abundance, low cost, and good biocompatibility, as well as their physical size, high aspect ratio shape, and relatively high Young's Modulus (although the relevance of biocompatibility is not always clear). That is to say, HNTs are expected to have good enough mechanical properties and high enough specific surface area to be able to reinforce polymers at relatively low volume fractions, and are cheap and abundant enough that it should be economically viable to use them on a large scale.

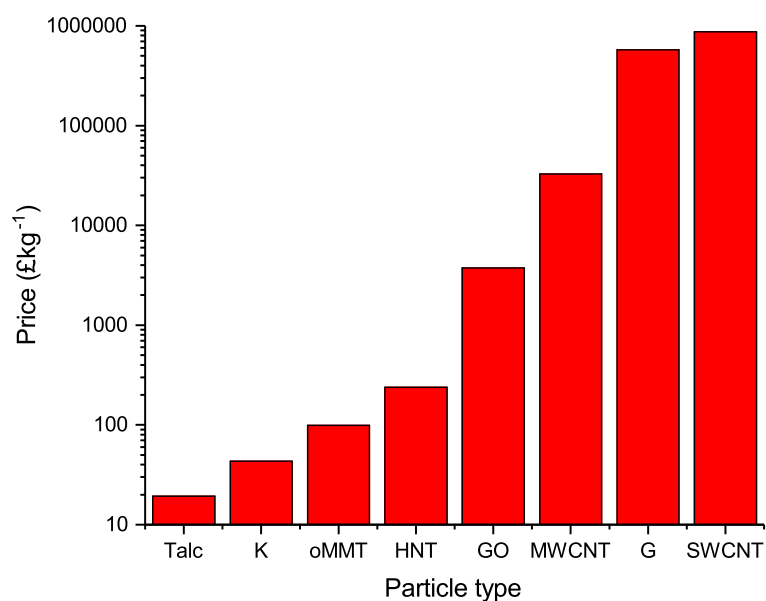


Figure 1.8: A comparison of the specific prices of several different types of filler particles, specifically: Talc, kaolinite (K), organo-modified MMT clay (oMMT), halloysite nanotubes (HNT), graphene oxide (GO), multi-walled carbon nanotubes (MWCNT), graphene (G), and single-walled carbon nanotubes (SWCNT). The prices are for the largest quantities of each that were available from Sigma-Aldrich in July 2019.

Although the justification for investigating HNTs sometimes appears to be simply that many other researchers have been interested in them previously,^{102,103} they are often investigated as alternatives to more well-established nanofillers. For instance, it is common for HNTs to be explicitly investigated as cheap and safe nanotubular alternatives to CNTs,^{10,11,104–112} although the similarity between the two types of nanoparticle is only really superficial, i.e. they are both nanotubes, but have significantly different mechanical, morphological, chemical, and electrical properties. That is to say, HNTs might be expected to behave very differently to CNTs in the same polymer system. Where the relative merits of HNTs versus oMMTs are addressed, the advantage often suggested for HNTs is that they are expected to be easier to disperse into polymers and pre-polymer resins because of their low surface hydroxyl group concentration.^{2,107,113,114} However, this claim is difficult to trace to its origin. Surprisingly, despite the obvious recognition of competition of HNTs with other high-aspect ratio nanofillers, there has been relatively little work where they have been directly compared to another type of particle. That is to say, it is common for publications to compare the performance of polymer/HNT nanocomposites with different loadings and/or surface treatments, but it is unusual for their performance to be directly compared to other nanofillers as part of the same work. Nonetheless, surveying the literature gives a good impression of how HNTs can be used as nanofillers to improve polymer performance.

1.3.1 Halloysite nanotubes in thermoplastics

A polymer in which HNTs have been regularly studied is poly(lactic acid) (PLA), a semi-crystalline thermoplastic used in a number of applications. Krishnaiah *et al.* first modified HNTs with APTES, then compounded them with PLA via melt-mixing then compression molding.¹¹⁵ They found that loading HNTs up to 8 wt% led to an up to 20% increase in Young's Modulus. Adding 6 wt% filler increased impact strength by 30%, but it decreased above this filler loading.¹¹⁵ Dong *et al.* were able to include HNTs in electrospun PLA mats.¹¹⁶ Electrospinning is a technique in which a polymer is cast from solution or melt into very fine fibres by applying a high voltage to the liquid. It produces fibre mats with very high surface areas, which have various applications, for example in drug delivery. They compared unmodified HNTs to those modified with an alkyl ammonium surfactant, which should be able to adhere to the negatively charged HNT outer surface to some degree through Coulomb interactions between the cationic ammonium species and the surface.¹¹⁶ Compared to the pure PLA mats, addition of both unmodified and modified HNTs increased both the tensile modulus and tensile strength of the material by around 200% up to 5 wt% filler loading. At around 10 wt% loading, the tensile modulus of the modified HNT nanocomposite was almost 400% higher than the pure PLA, but that of the unmodified HNTs decreased. This was attributed to poor dispersion of the filler in the case of the unmodified HNT nanocomposite.¹¹⁶ Guo *et al.* studied the addition of HNTs to PLA for packaging applications.¹⁰⁷ Specifically, they compared unmodified HNTs to those which had been treated with aqueous sodium hydroxide to dissolve some of the outer silica surface and generate more hydroxyl groups, which they speculated would be able to hydrogen bond with the PLA and hence increase adhesion in the interphase.¹⁰⁷ The HNTs were melt-compounded with the PLA in a specialist laboratory mixer, and then injection molded. For both modified and unmodified HNTs, inclusion of filler up to 9 wt% led to about a 26% increase in Young's Modulus. Interestingly, inclusion of unmodified HNTs decreased the tensile strength of the material, whereas using hydroxide-treated HNTs led to around a 10% increase at a loading of 9 wt% filler, which suggests that the treatment did lead to increase in the strength of the interaction between the particle and polymer. Both types of HNTs decreased the ductility of the polymer.¹⁰⁷ In all of the above cases, the presence of the HNTs also improved the thermal stability of the polymer, and increased the degree of crystallinity.

Several studies have also investigated HNTs as fillers in thermoplastic Nylon polymers (i.e. poly(amide)s). Handge *et al.* found that the presence of HNTs in Nylon-6 significantly increased the Young's Modulus and yield stress of the material, even at relatively low loadings.¹⁰⁴ For example, at a HNT content of 5 wt%, the nanocomposite had a 30% higher Young's Modulus, and 8% higher yield stress.¹⁰⁴ Similarly, Guo *et al.* added HNTs to Nylon-6, but this time coated the nanotubes with the alkoxysilane (3-trimethoxysilyl)propyl methacrylate to ease HNT dispersion into the polymer and enhance interfacial adhesion.¹⁰³ They found that incorporation of their modified HNTs up to 10 wt% led to increases of tensile strength and flexural strength of up to 20% and 30% respectively, and flexural modulus was found to increase by up to 56%.¹⁰³ They also found an up to 7% increase in impact strength, and a 73% increase in heat distortion temperature. However, they do not compare their modified HNTs to the untreated particles.¹⁰³ Lecouvet *et al.* found that incorporating HNTs into Nylon-12 led to an almost two-fold increase in Young's Modulus and a 28% increase in yield stress at 16 wt% filler loading.²

They also noted an increase in the thermal stability of the nanocomposites.²

Poly(propylene) (PP) is another polymer which is frequently selected for study with the addition of HNTs as a reinforcing agent. Raji *et al.* compared the effect of coating HNTs, MMT and sepiolite clays with either APTES or vinyltrimethoxysilane in terms of their performance as reinforcing fillers in PP.¹¹⁷ It should be noted that this coating is unlikely to have allowed exfoliation of the MMT into individual nanosheets during processing, and they do not show any evidence (e.g. X-ray diffraction data) to illustrate whether or not this happened.¹¹⁷ Nonetheless, they found that adding any of the clays led to an increase in Young's Modulus compared to pure PP. This increase was highest for the APTES-coated particles, with the incorporation APTES coated HNTs causing an increase of 62%. However, adding APTES coated sepiolite led to an even greater increase of 86%. There was only a modest increase in tensile strength for all particles.¹¹⁷ They also found that the addition of HNTs and sepiolite increased the melt viscosity of the PP by a similar amount, with viscosity increasing with increasing clay content. The melt viscosity was lower for MMT, and decreased with increasing MMT content, but it is probable that this is related to poor dispersion of the MMT particles (i.e. a low degree of exfoliation). It was also shown that all of the clays increased the degree of crystallinity of the polymer by acting as sites for the nucleation of crystal growth.¹¹⁷ Kubade *et al.* studied the affect of HNT addition on PP blends with acrylonitrile butadiene styrene (ABS).¹¹⁸ ABS is a rubbery copolymer which can be added to PP to increase toughness. They found that the addition of 1 wt% of HNTs increased Young's Modulus by 26%, increased tensile strength by 30%, and increased impact strength by almost 50%. However, these properties subsequently decreased at filler loadings greater than 1 wt%.¹¹⁸ Jenifer *et al.* made PP composites containing both HNTs and macroscopic glass fibres.¹⁰² With the addition of the PP/maleic anhydride copolymer, PP-g-MA, as a dispersing agent for the glass and HNTs, they found that adding both of the two fillers (at loadings of 2.5 wt% and 20 wt% of HNTs and glass fibre respectively) caused an increase in tensile strength of 71% and an increase in Young's Modulus of 135%. This is much higher than the increases seen when the fillers were used individually; adding 2.5 wt% of HNTs and no glass fibre led to an increase in tensile strength of 14% and an increase in Young's Modulus of 9%.¹⁰² They also found that adding HNTs increased the degree of crystallinity and rate of crystallisation of the polymer.¹⁰² Du *et al.* showed that the addition of HNTs could also dramatically improve the thermal stability of PP, with the addition of around 10 wt% of the nanotubes leading to a 74 °C increase in the temperature at which the maximum rate of thermal decomposition of the material occurred.¹¹⁹

All of the PP and Nylon nanocomposites discussed so far were made by blending in a twin-screw extruder followed by subsequent molding. Twin-screw extrusion subjects the polymer melt to high-shear and highly anisotropic flow, and it is worth noting that where transmission electron micrographs of these nanocomposites have been taken, the HNTs show a high degree of alignment and a good degree of dispersion, i.e. most of the nanotubes appear well separated. An example is shown in figure 1.9. Lecouvet *et al.* in particular were interested in the degree of dispersion of the nanotubes, and they found that water-assisted extrusion was particularly effective at dispersing HNTs;² in water-assisted extrusion, water is injected into the melt at high temperature and pressure, reducing the viscosity as well as increasing the polarity of the mixture, which appears to be beneficial for the dispersion of the HNTs.²

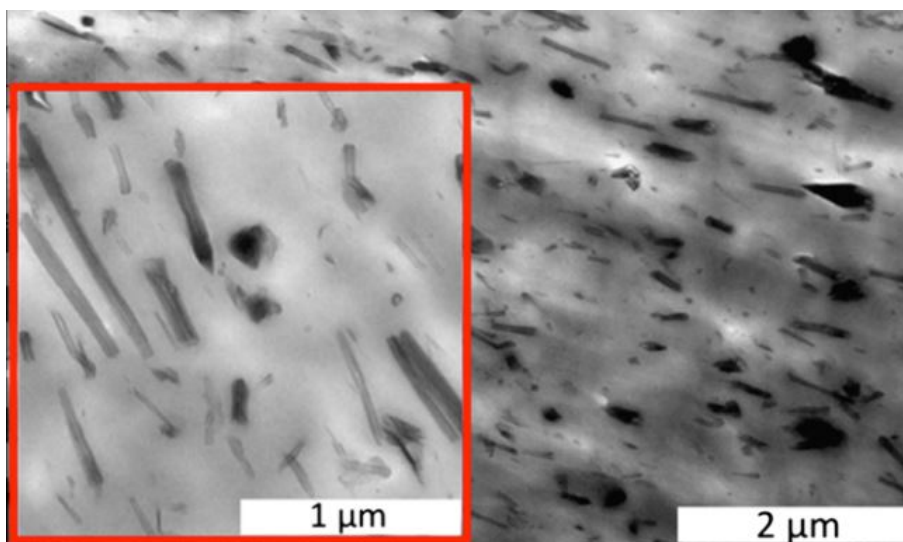


Figure 1.9: A TEM image taken from work by Lecouvet *et al.*, which illustrates how HNTs align in the direction of flow during twin-screw extrusion.² Image adapted with permission.

There are also at least two examples of HNTs being studied as fillers to improve the barrier properties of polymers, which, as mentioned in section 1.1.3, is an important existing application for oMMT. Tas *et al.* made HNT/poly(ethylene) (PE) nanocomposites by twin-screw extrusion, then blowing the composite into films.¹¹⁴ They found that adding HNTs at loadings below 3 wt% could reduce the rate of diffusion of oxygen and water through the films, which in turn prolonged the shelf-life of food products packaged in the nanocomposite film versus the pure PE. Interestingly, they also found that the HNTs could “scavenge” ethylene and reduce its concentration within the packaging, which allowed fruit to be kept in the nanocomposite packaging for longer without ripening compared to the pure polymer. However, they did not compare these effects to oMMT, and they also found no change in either the Young’s Modulus or tensile strength of the nanocomposite films versus the pure polymer, regardless of filler loading. This is possibly due to poor dispersion of the HNTs in the polymer, which is a parameter they did not assess.¹¹⁴ Yang *et al.* also studied HNTs for improving the gas permeability of polymer packaging, but in this case they did compare them to oMMT.¹²⁰ More specifically, they modified HNTs with resorcinol di(phenyl phosphate) and compared their performance to a commercially available oMMT. The moduli and strength of nanocomposites containing modified HNTs and oMMT were comparable, although the HNTs had better impact strength. Importantly, the oMMT was much better barrier for gas diffusion than the HNTs; at a volume fraction of 0.08, the rate of oxygen diffusion through the HNT nanocomposite decreased by only 10% compared to the pure polymer, whereas in the oMMT nanocomposite it had decreased by around 60%.¹²⁰ The poor performance of the HNTs relative to the oMMT is justified in terms of the nanoparticles’ geometries. Specifically, they demonstrated theoretically that an array of impermeable plates randomly oriented in space will cause a bigger increase in diffusion path length than the same volume of tubes.¹²⁰ These results are important as they demonstrate that, although incorporation of HNTs in polymers can have beneficial effects on permeability, it is unlikely that they can be used in this application as a replacement for oMMT nanoparticles, which are also already cheaper and widely commercially available.

As well as those already mentioned, HNTs have been studied in a variety of other thermoplastics on a less regular basis. For example, Wu *et al.* combined HNTs into poly(vinylidene fluoride) using water-assisted twin screw extrusion, and found an increase in Young's Modulus of 60% at 7 vol% of filler.¹²¹ Lin *et al.* treated HNTs with the anionic surfactant, sodium dodecyl sulfate, and added these to styrene which was then converted to poly(styrene) (PS) using bulk free radical polymerisation.¹⁰⁵ They found that the nanocomposites had a 200% larger impact strength compared to PS at a filler loading of 5 wt%, although this dropped to a 75% increase at a loading of 10 wt%.¹⁰⁵ Vuluga *et al.* extruded poly(methyl methacrylate) (PMMA) with HNTs and a stearamide dispersing agent.¹¹³ They found no improvement in strength or modulus at a loading of 2 wt%, but they did find that the HNTs improved scratch resistance compared to pure PMMA.¹¹³ This is important since PMMA is often used for its good optical properties (i.e. its transparency).

The examples of HNTs being used in thermoplastic nanocomposites given here are not exhaustive, but they do give a sense of the general trends seen in such nanocomposites. Specifically, the addition of HNTs often (but not always) leads to significant improvement in mechanical properties compared to the pure polymer, especially when the HNTs have been modified to increase dispersion into the polymer matrix. The addition of HNTs also tends to improve the thermal stability of the polymers, and has been shown to increase the crystallinity of several semi-crystalline thermoplastics. However, it is hard to get a sense of how significant these improvements are because, as previously noted, the performance of HNT nanocomposites is not often directly compared those using other types of nanoparticle. Importantly, where the barrier properties of a HNT nanocomposite was compared to one using commercially available oMMT, it was shown to be less effective at inhibiting gas diffusion. There is also limited consistency in the surface treatments used for HNTs for dispersion into the same polymer, which may be a product of the research area being relatively young. It would be fair to say that the field of HNTs in thermoplastic nanocomposites would benefit in future from increased consistency in HNT surface treatments between publications, as well as direct comparison to its main nanofiller competitors.

1.3.2 Halloysite nanotubes in epoxy resin nanocomposites

Using HNTs as a nanofiller in epoxy resins should have several benefits. Firstly, the nanotubes are clearly of an appropriate size and high enough stiffness to be able to reinforce epoxy at low volume fractions. The surface chemistry of HNTs, which is similar to glass (i.e. siloxane plus silanol groups), means that HNTs should be easy to functionalise with the kind of alkoxy silane coupling agents commonly utilised in commercial sizings for glass fibres, either to aid dispersion of the HNTs into the resin (if necessary), or to increase the strength of the resulting nanocomposite. In addition, epoxy resins are high value polymers used in a variety of high-performance chemical and engineering applications, so the addition of the relatively expensive HNTs to the resin would be easy to justify upon sufficient improvements in performance. Finally, on a more practical note, there are a variety of different potential strategies for mixing HNTs into liquid epoxy monomer while under a high degree of extraction (i.e. in a fumehood), such as ultrasonication, or three-roll milling. This is in contrast to twin-screw extrusion, which would

probably be necessary for processing HNTs into thermoplastics, and which, in our lab, cannot be done under extraction. That is to say, as long as the exact respiratory hazard posed by HNTs remained unclear,⁷⁹ we could not justify handling the nanotubes outside a fumehood, which ruled out several common polymer processing techniques. For all of the above reasons, epoxy resin/HNT nanocomposites were chosen as the specific subject of focus in this thesis.

Mechanical reinforcement of epoxy resins by halloysite nanotubes

In an early example of using HNTs in epoxy resin, Ye *et al.* dispersed the nanotubes into a solution of acetone and epoxy using “mechanical mixing” and then removed the solvent. Perhaps unsurprisingly, since they only used a very low shear mixing technique and no surface modification to aid dispersion of the HNTs into the mixture, they found no increase in the strength or stiffness of the nanocomposites up to a filler loading of 2.3 wt%; indeed, they note a high degree of agglomeration of the HNTs in electron micrographs.¹¹² However, an increase in impact strength of 400% was observed.¹¹² In addition, the presence of HNTs at 1.6 wt% loading increased the onset of thermal decomposition of the epoxy by over 20 °C. This was one of the first indications of the potential of HNTs as beneficial fillers in epoxy resins.

Deng *et al.* subsequently also investigated the effect of HNTs on the toughness of epoxy resins. They also only used mechanical mixing, this time simply with the pure resin as it was heated to reduce its viscosity (i.e. with no diluant).¹²² The mechanical properties of their nanocomposites compared to the pure resin are summarised in table 1.2. Notably, the fracture toughness of the nanocomposites was significantly higher than the pure resin. The improvements in strength and stiffness were more modest, but this could be related to the fact that the HNTs were not fully dispersed in the resin; electron micrographs showed the presence of large agglomerates of nanotubes, and they explicitly note that samples were polished in order to remove large agglomerates of HNTs which had sunk to the bottom of the mixture during cure.¹²² It is also surprising that significant differences were seen in the relative improvement of the material under tension and flexure. The specimens for each test were made separately, possibly using a different batch of material, so this might be an indication of a lack of repeatability in their manufacture of the nanocomposites.

Table 1.2: The changes in mechanical properties of an epoxy resin seen by Deng *et al.* after inclusion of HNTs.

Filler content/wt%	Young's Modulus	Tensile Strength	Flexural Modulus	Flexural Strength	Fracture Toughness
5	Unchanged	+8%	+11%	+5%	+40%
10	Unchanged	+8%	+18%	+8%	+50%

Vahedi *et al.* were interested in the effects of the addition of HNTs via different mixing methods on the viscosity of uncured resin mixtures and the impact strengths of the nanocomposites obtained upon curing.¹⁰ Resin viscosity can be an important parameter in some processing techniques, e.g. resin transfer molding.¹⁰ They compared low-shear, mechanical mixing to ultrasonication, and found that addition of 10 wt% HNTs to the

resin led to increases in viscosity of about 33% for mechanical mixing, and 66% for ultrasonication, suggesting that ultrasonication had led to more complete dispersion of the nanoparticles.¹⁰ Using different mixing methods also led to different impact properties in the final nanocomposites, as summarised in table 1.3. It was found that the changes in impact properties seen also depended on the amine curing agent used; when diethylene-triamine was used, addition of any HNTs led to a decrease in impact strength, whereas using a diamine (4,4'-diaminodiphenylmethane) led to the improvements summarised in the table.¹⁰ They also compared HNTs from different sources, and found that the maximum increase in relative impact strength varied from 30% to 230%.¹⁰ Their work not only serves to highlight the importance of mixing method in the manufacture of epoxy/HNT nanocomposites, but also illustrates the potential for significant variation in reinforcement by HNTs from different sources in different resin systems.¹⁰

Table 1.3: A summary of the effect of mixing method seen by Vahedi *et al.* on the impact properties of epoxy/HNT nanocomposites.¹⁰

Mixing method	Filler content/wt%	Impact Strength
Ultrasonication	2.5	+34%
Ultrasonication	5	+105%
Ultrasonication	10	+142%
Ultrasonication	15	+50%
Mechanical	2.5	Unchanged
Mechanical	5	+80%
Mechanical	10	+48%

More recently, Brantseva *et al.* also studied the effect of mixing method on the properties of an epoxy/HNT nanocomposite, this time in terms of its application as an adhesive.¹⁰⁸ Importantly, they compared the performance of HNTs to that of oMMT. They found that the lap-shear strengths of joints bonded with the nanocomposites were greater than when pure epoxy was used, and that the oMMT produced stronger joints than the HNTs. Strangely, they report that ultrasonication led to poorer particle dispersion, and that it had no effect on the joint strength in comparison to mechanical mixing.¹⁰⁸ They also report that the ultrasonication process broke the nanotubes into smaller pieces, although their evidence for this is not convincing.¹⁰⁸

Sun *et al.* compared different alkoxy-silanes as coupling agents for HNTs in amine-cured epoxy resins, specifically 3-(2-aminoethyl)-aminopropyltrimethoxysilane (AEAPS), (3-glycidyloxypropyl)-trimethoxysilane (GPTMS), and octyltriethoxysilane (OTES).¹¹ The amine groups on AEAPS and the epoxide group on GPTMS should allow reaction of the alkoxy-silane into the resin network as it cures, thereby increasing adhesion between the HNT surface and the polymer network. They mixed the HNTs into a solution of epoxy resin and chloroform using 45 min of ultrasonication with a 250 W probe, before evaporation of the solvent. Without any surface modification, the HNTs increased the Young's Modulus of the epoxy by 3% and 7% at filler contents of 2.5 wt% and 5 wt%, respectively, but led to no change in the tensile strength, impact strength, or toughness of the material. Applying alkoxy-silanes to the HNTs as coupling agents led to a greater degree of improvement in the resins' mechanical properties, which are summarised in table 1.4. All of the HNTs apart from those coated with OTES also increased the impact strength

of the material by about 50-60%. It is clear that the exact type of surface modification used can have significant impact on the performance of HNTs as reinforcing fillers in epoxy nanocomposites, with using an amine-functional silane coupling appearing to be the most effective.¹¹ They also found that the addition of any type of HNT at 5 wt% reduced the thermal stability of the nanocomposites relative to the pure epoxy, with the AEAPS and GPTMS coated HNTs doing so to a lesser degree than the pure or OTES treated HNTs.¹¹ However, it should be noted that they do see some differences between the amount of GPTMS grafted onto the surface compared to AEAPS and OTES, and that their assessment of the level of dispersion of each HNT sample in the epoxy is only qualitative. Therefore, it is difficult to determine whether the difference in performance seen is due to a difference in the reactivity of the alkoxy silane with the epoxy, a difference in the degree of dispersion of each type of particle, or a difference in the exact network structure of the alkoxy silane layer formed on the HNT surface.

Table 1.4: A table summarising the work of Sun *et al.*, who found that coating HNTs with different alkoxy silanes allowed them to reinforce an amine-cured epoxy resin to different degrees.¹¹

Alkoxy silane	Filler content/wt%	Young's Modulus	Tensile Strength	Toughness
AEAPS	2.5	+6%	+8%	+27%
AEAPS	5	+11%	+21%	+80%
GPTMS	2.5	+5%	+6%	+14%
GPTMS	5	+9%	+14%	+36%
OTES	2.5	+5%	+15%	+49%
OTES	5	+10%	+9%	+7%

Zhang *et al.* compared the affect of coating HNTs with APTES versus coating with a dendritic poly(amidoamine) (PAA).¹²³ The HNT samples were dispersed in the resin by 2 h of ball milling. At a filler loading of 1 wt%, they found no change in flexural strength for any of the samples, but flexural modulus was found to increase. Specifically, an increase in flexural modulus of 44% was seen for the PAA modified HNTs, compared to 22% for the APTES modified HNTs, and 13% for the unmodified HNTs. There were also significant improvements in impact strength compared to the pure resin; at 1 wt% filler, impact strength was over 1000% greater for the PAA modified HNTs, but more modest at around 400% for the unmodified and APTES modified samples. This example again highlights the significant reinforcing effects HNTs can have on epoxy resin even at low filler contents, especially if the surface is modified with an amine coupling agent.¹²³

Zeng *et al.* took a different approach to surface modification of HNTs for dispersion in epoxy resin. More specifically, rather than using an alkoxy silane coupling agent, they treated the HNTs with a solution of sodium hydroxide to dissolve some of the outer silica and expose more silanol groups (a-HNTs). It was speculated that these groups would increase interfacial adhesion between the HNT surface and the epoxy by promoting hydrogen bonding, and possibly also reacting directly with the epoxide in the resin.¹¹¹ The HNTs were mixed into a solution of epoxy resin and acetone with 20 min of ultrasonication. The mechanical properties of the nanocomposites relative to the pure epoxy are summarised in table 1.5. At low filler loadings, the unmodified HNTs had minor effects on

the strength and stiffness of the material, and while increased filler loading led to a higher modulus, it may have also been detrimental to strength. The a-HNTs showed better performance, notably increasing fracture toughness by 43% at a 4.8 wt% filler loading.¹¹¹ However, it is difficult to say whether these improvements were due to better dispersion of the HNTs in the epoxy or better adhesion between the two phases due to the surface modification.

Table 1.5: A table summarising the changes in the mechanical properties of an epoxy resin after addition of HNTs or sodium-hydroxide-treated HNTs (a-HNTs).

Sample	Filler content wt%	Young's Modulus	Tensile Strength	Fracture Toughness
HNTs	1.0	Unchanged	Unchanged	+11%
HNTs	4.8	+11%	-14%	+16%
a-HNTs	1.0	+11%	+5%	+11%
a-HNTs	4.8	+18%	Unchanged	+43%

Kim *et al.* also used an unusual surface treatment to modify HNTs for use in an epoxy resin.¹⁰⁹ They reacted HNTs with tetraethyl orthosilicate (TEOS), which polymerised to form a thick, amorphous siloxane coating around the nanotubes. Treated and untreated HNTs were mixed into epoxy resin using a three-roll mill before curing. Both fillers increased the flexural strength of the resin up to 16% at filler contents up to 15 wt%. However, while strength decreased above this concentration of unmodified HNTs, a 20 wt% loading of coated HNTs led to an increase in flexural strength of 20%.¹⁰⁹

In another interesting example of HNT treatment, Tang *et al.* compared untreated HNTs to those heated to reflux in an aqueous solution of phenyl phosphonic acid (PPA).¹² The PPA molecule is able to intercalate between the halloysite layers, causing the tubes to begin to unroll, which was evidenced by a change in the d_{001} peak in XRD data, as well as direct imaging with electron microscopy.¹² Nanocomposites were made by mechanical mixing for 5 h, and there was obvious agglomeration of the filler particles in electron micrographs of the nanocomposites. The changes in mechanical properties observed for the nanocomposites (at a 10 wt% filler loading) are summarised in table 1.6.¹² The surface treatment of the HNTs was not effective at improving strength and stiffness compared to the pure HNTs, especially at short treatment times. However, extended treatment times produced a marked increase in the fracture toughness of the nanocomposites compared to both the pure epoxy, and the nanocomposite made using untreated HNTs.¹² They found the 78% improvement seen for the 100 h PPA HNTs to be comparable to a literature value¹²⁴ of +80% for an epoxy/oMMT nanocomposite,¹² although this reinforcement was achieved at a much lower filler loading of 2.5 wt% of oMMT (possibly due to a more effective mixing strategy¹²⁴).

Vijayan *et al.* made nanocomposites using a hybrid nanomaterial of HNTs coated in TiO₂ nanoparticles, with the aim of using the HNTs as supports to allow the dispersion of the TiO₂ without the need for surface modification.¹²⁵ Particles were dispersed into the epoxy resin using 30 min of ultrasonication. The changes in the mechanical properties of the epoxy resin seen upon the addition of filler are summarised in table 1.7. They also found that both pure HNTs and the hybrid material reduced the thermal stability of the epoxy.

Table 1.6: The changes in mechanical properties for epoxy resin nanocomposites (10 wt% filler) relative to the pure epoxy seen by Tang et al..¹² They compared the effects of different treatment times of HNTs with aqueous PPA (0 h = untreated HNTs)

PPA treatment time/h	Young's Modulus	Tensile Strength	Fracture Toughness
0	+17%	+3%	+25%
25	+9%	Unchanged	+24%
50	+8%	+2%	+42%
100	+15%	Unchanged	+78%

Table 1.7: A summary of the changes in mechanical properties of an epoxy resin seen by Vijayan et al. upon the addition of either HNTs or a HNTs/TiO₂ hybrid at 5 wt% loading.

Sample	Young's Modulus	Tensile Strength	Toughness
HNTs	Unchanged	+56%	+293%
HNTs/TiO ₂ hybrid	+44%	+40%	+157%

Li et al. also made a hybrid material for use in epoxy resins. Specifically, they coated HNTs with poly(dopamine) (PDA), onto which they subsequently deposited iron hydroxide (Fe(OH)₃) nanoparticles.¹²⁶ These particles were dispersed into the resin using a three-roll mill, and the mechanical properties of the nanocomposites are summarised in table 1.8. In terms of thermal properties, they noted a slight decrease in thermal stability of the epoxy/HNT nanocomposite, but a significant increase in the char yield. A similar effect was seen for the Fe(OH)₃-PDA-coated HNTs, except the increase in char yield seen was much greater. In contrast, the PDA-coated HNTs slightly increased the thermal stability.¹²⁶ They were principally interested in the combustion behaviour of the materials, and concluded that the Fe(OH)₃-PDA-coated HNTs were better than the other HNTs or a simple mixture of HNTs and Fe(OH)₃, which they attribute to a high degree of catalytic degradation of combustion products occurring at the hybrid nanoparticle surface during combustion. This increased the degree of charring and breakdown of volatile combustion products, enhancing the flame retardance of the material.¹²⁶

Table 1.8: A summary of the changes in mechanical properties of an epoxy resin seen by Li et al. upon the addition of HNTs, PDA-modified, or Fe(OH)₃- and PDA-modified HNTs.

Sample	Young's Modulus	Tensile Strength
HNTs	+4%	+7%
PDA-HNTs	+8%	+20%
Fe(OH) ₃ -PDA-HNTs	+20%	+12%

Summary

After reviewing the literature concerning epoxy/HNT nanocomposites, it is clear that a variety of mixing and HNT surface modification strategies have been attempted for making these materials. For ease of reference, the literature discussed thus far is summarised in table 1.9. The general trend is for HNT addition to improve the mechanical properties of epoxy resins, particularly their toughness, although the extent to which reinforcement is seen does seem to vary significantly between authors. Often, surface modification of the nanotubes improves the mechanical properties of the nanocomposite relative to using pure HNTs. On the basis of the literature, HNTs would indeed appear to be promising nanofillers for reinforcing epoxy resins. However, there are some key issues which still have not adequately been addressed.

Firstly, the importance of effective mixing to achieve a material with individually dispersed nanotubes is often overlooked. Sometimes very low energy mixing techniques (e.g. mechanical stirring) are used, and often significant agglomeration of the nanoparticles is observed. Table 1.9 contains comments on the degree of dispersion of HNTs seen in epoxy/HNT nanocomposites in the literature; it is labelled 'Poor' if there obvious agglomerates of HNTs were observed, or 'Good' if there were no obvious agglomerates. The reporting of mixing parameters (e.g. mixer power) is also normally only vague. This is problematic, since unless an author is sure that they have achieved a mixture containing individually dispersed HNTs, the properties of the obtained nanocomposites cannot be assumed to be the optimum properties of an epoxy/HNT nanocomposite with that filler loading. Indeed, the amount of filler interacting with the epoxy cannot be known since the quantity of HNTs in agglomerates versus those individually dispersed will be unknown. This makes it difficult to make fair comparisons between different publications. In addition, the effect of the mixing technique on the structure of the nanotubes (i.e. whether they are damaged by certain mixing techniques) has never been adequately addressed. Further progress in the field therefore requires the establishment of a means of consistently producing samples with well-dispersed nanotubes.

On a related note, the measurement of filler content has, as far as I am aware, always been neglected when producing epoxy/HNT nanocomposites; the filler contents of the nanocomposite samples were not measured in any of the examples cited. Instead, it is presumably calculated from the amount of HNTs added to the resin at the beginning of the mixing process, or approximated from this amount (i.e. is essentially nominal). This is also highlighted in table 1.9. It may be that most of the HNTs remain in the material throughout processing, and this is a good approximation. However, this cannot simply assumed to be the case, and, as such, uncertainty in the exact filler content in each sample may serve to undermine comparisons between different samples, and indeed between different publications.

In addition, the aim of many researchers seems to be to develop new surface modification strategies for HNTs in epoxy nanocomposites, rather than improve on existing ones, as is illustrated by the wide variety of functionalisation strategies reported in table 1.9. While this is not inherently a problem, it does make it difficult to get an idea of how repeatably surface-modification of HNTs can be carried out, and how repeatable the effect of the surface modification of the HNTs on the properties of any subsequent nanocomposite is. This knowledge would be vital for the commercial application of HNTs in epoxy nanocom-

posites, where performance would need to be consistent and predictable between batches. Similarly, surface modification of HNTs for epoxy/HNT nanocomposites has normally been undertaken on the scale of a few grams at a time,^{11,109,123,126} whereas industrial scale processes would require kilogram batches at least. Therefore, the production of surface-modified HNTs which can be made repeatably in large batches is probably as important for future applications of epoxy/HNT nanocomposites as the development of new types of surface modifications.

In conclusion, the variation seen in the literature makes it difficult for a researcher entering the field to define a single, “state-of-the-art” method for producing epoxy resin/HNT nanocomposite materials with improved mechanical properties. However, it can generally be concluded that the best improvements in mechanical properties have been obtained in reports where high-shear mixing techniques were used, and/or surface modifications of the HNTs were carried out. More specifically, ultrasonication, three-roll milling, and ball milling all appear to be effective mixing techniques for dispersing HNTs into epoxy resin, and functionalisation with appropriate amine-bearing molecules seems to improve mechanical properties relative to using unmodified HNTs. Appropriate molecules include APTES and related species, which are already widely-used in composite materials. These general conclusions provide a starting point for producing epoxy resin/HNT nanocomposites, from which more incremental progress can be made towards optimising their properties, as well as understanding how to make them repeatably and on larger scales.

Table 1.9: A summary of the reports on epoxy/HNT nanocomposites, as described in the main text. Refer to the text for more details regarding functionalisation. The mechanical properties are abbreviated as follows: FM (Flexural Modulus), FS (Flexural Strength), IS (Impact Strength), YM (Young's Modulus), TS (Tensile Strength), FT (Fracture Toughness), T (Toughness). For degree of dispersion: *imaged by TEM, **imaged by SEM.

Reference	Mixing technique	HNT functionalisation?	Measured mechanical properties	Maximum change	Reported filler content?	Degree of dispersion
Ye <i>et al.</i> ¹¹²	Mechanical	None	FM, FS, IS	0%, 0%, +400% (at 2.3 wt%)	Calculated	Poor*
Deng <i>et al.</i> ¹²²	Mechanical	None	YM, TS, FM, FS, FT	0%, +8%, +18%, +8%, +50% (at 10 wt%)	Nominal	Poor*
Yahedi <i>et al.</i> ¹⁰	Mechanical, Ultrasonication	None	IS	+80% (at 5 wt%), +142% (at 10 wt%) +7%, 0%, 0%, +11%, +21%, +80%, +9%, +14%, +36% +10%, +9%, +7% (all 5 wt%)	Nominal	Poor**
Sun <i>et al.</i> ¹¹	Ultrasonication	None, AEAPS , GPTMS , OTES	YM, TS, T	+13%, 0%, +400% +44%, 0%, +1000% +22%, 0%, +400% (all at 1 wt%)	Nominal	Poor*
Zhang <i>et al.</i> ¹²³	Ball milling	None, PAA APTES	FM, FS, IS	+11%, -14%, +16% +18%, 0%, +43% (all at 4.8 wt%)	Nominal	Good*
Zeng <i>et al.</i> ¹¹¹	Ultrasonication	None, Alkali	YM, TS, FT	+16% (at 15 wt%), +20% (at 20 wt%)	Calculated	Poor**, Good**
Kim <i>et al.</i> ¹⁰⁹	Three-roll mill	None, TEOS	FS	+17%, +3%, +25%, +15%, 0%, +78% (all at 10 wt%)	Nominal	Poor**
Tang <i>et al.</i> ¹²	Mechanical	None, PPA (100 h)	YM, TS, FT	0%, +56%, +293%, +44%, +40%, +157% (all at 5 wt%)	Nominal	Poor**
Vijayan <i>et al.</i> ¹²⁵	Ultrasonication	None, TiO₂	YM, TS, T	+4%, +7%, +8%, +20%, +20%, +12% (all at 5 wt%)	Nominal	Not measured
Li <i>et al.</i> ¹²⁶	Three-roll mill	None, PDA , PDA-Fe(OH)₃	YM, TS		Nominal	Not measured

1.4 Thesis structure

1.4.1 General aims

The general aim of this thesis was to conduct a fundamental study on the use of HNTs in epoxy resin nanocomposites. Particular attention was to be paid to parameters that would be relevant to the commercial development of these materials (such as repeatability and scale-up), as well as certain important aspects of nanocomposite research that have generally been overlooked in the literature regarding epoxy/HNT nanocomposites thus far (such as the effect of mixing method, and the measurement of HNT content in the final material). The initial intention was also to critically compare the properties of epoxy/HNT nanocomposites to those of oMMT analogues, which has particular significance since oMMT would be expected to be the main commercial competitor to HNTs as a nanofiller in this application.

1.4.2 Summaries of chapter contents

Chapter 2: Characterisation of halloysite nanotubes

This chapter provides an in-depth study of the chemical, physical, and morphological properties of HNTs provided by I-Minerals Inc. from their source in Idaho, and compares the measured properties of these HNTs to those reported by the supplier. Particular attention is paid to challenges associated with measuring the size and shape of HNTs, and methods for automated analysis of HNTs in electron microscope images are discussed in detail.

Chapter 3: A comparison of mixing methods for dispersing halloysite nanotubes into epoxy resin

This chapter compares the effectiveness of two different high-shear mixing methods for making epoxy/HNT nanocomposites, namely ultrasonication and the use of a three-roll mill. The effect of using different mixing parameters in each technique is also investigated. Attention is paid to the degree of dispersion of the HNTs in the resulting nanocomposites, as well as to whether mixing caused any destruction of the particles. The viscosities of the resulting mixtures are compared, as are the flexural properties of the cured nanocomposites. Importantly, methods are developed for the accurate determination of HNT filler content in these nanocomposites. Using the three-roll mill in force mode was identified as the best way for producing epoxy/HNT nanocomposites with well dispersed HNTs and improvements to flexural modulus. It is also shown that oMMT is difficult to process into epoxy resin to produce satisfactory nanocomposite parts, but the flexural properties of epoxy/HNT nanocomposites obtained here are nonetheless compared oMMT examples by using literature values.

Chapter 4: Functionalisation of halloysite nanotubes with alkoxy silanes and activation with piranha solution

In this chapter, a literature method for coating HNTs with APTES is repeated several times and scaled up from a few grams to tens of grams. It is shown that scale-up does not appear to change the results of the coating reaction, which is promising for the use of this coating process on scales applicable to commercial utilisation of such coated HNTs. However, the reaction is also shown to give different grafted amounts of coating with no apparent correlation to reactant concentrations. The degree of variation seen is in turn shown to affect the wettability of the resulting coated HNTs, which may have implications for the repeatability of their use as reinforcing fillers in epoxy/HNT nanocomposites (i.e. if it causes significantly different interphase structures). Unfortunately, the three-roll mill broke before these nanocomposites could be made, with repair beyond the remaining timescale and budget for the project.

Also investigated is the use of a piranha solution pre-treatment to generate an increased number of surface silanol groups on the HNTs and hence improve the grafted amount of APTES in subsequent coating reactions, as was suggested to be possible in previous literature.⁷ It is shown in this chapter that piranha solution treatment does cause acid-catalysed etching of the HNTs, but there is no evidence for new silanol groups on the HNT surface. In turn, there is no difference in grafted amount of APTES or the wettability of coated HNTs when piranha solution pre-treatment is used versus when it is not used, which directly contradicts previous literature.⁷

Chapter 5: Conclusions and future work

This chapter contains a final summary of the conclusions and suggestions for future work that were outcomes from the previous results chapters.

Chapter 2

Characterisation of Halloysite Nanotubes

2.1 Introduction

As discussed in Chapter 1, the natural, geological origin of halloysite formation means that the properties of the particles can vary significantly from source to source. For example, local chemical and weathering conditions can lead to a wide variety of morphologies, including spheres, pseudospheres and fibres, as well as the nanoscroll typical of HNTs.⁵⁵ The exact morphology distribution influences the physical properties of particles, including their surface areas, and even mechanical properties; for instance, thin HNTs have been found to have higher flexural moduli than thick HNTs.¹ Halloysites from different sources are also often associated with differing concentrations of chemical impurities, such as metal oxides and various other alumina or silicate minerals (including the closely related kaolinite).⁵⁵ A good reference for highlighting the degree of variation between halloysites is the work of Pasbakhsh *et al.*, who compared HNTs from six different sources and found significant variations in tube dimensions, surface and pore areas, and cation exchange capacities.¹²⁷

In their work, Pasbakhsh *et al.* note the importance of taking into account the variations in the properties of HNTs from different sources.¹²⁷ For instance, one might want to choose the HNT with the largest pore volume when designing HNTs for controlled release applications, or one would want to choose the nanotubes with the lowest length and aspect ratio to reduce the potential for respiratory hazard if the HNTs were to be released into the environment.⁷⁹ The presence of impurities may be also an important factor to consider for any chemical applications. For application as reinforcing fillers in polymer nanocomposites, the most desirable HNTs for mechanical reinforcement are those with the smallest diameters¹ and highest aspect ratios,¹²⁸ i.e. the HNTs with the highest flexural moduli, and highest surface specific areas for stress transfer from the polymer under load. It is therefore clear that the chemical and morphological properties of any sample of halloysite must be studied to understand how it will behave in a particular application.

Despite the well-known potential for significant variation between HNT samples, it is common in the literature for no or only limited characterisation to be carried out on HNT samples. For example, some reports rely only on data from the supplier,^{109,129,130} while others use data from previous literature.^{116,123} Focusing on HNT dimensions specifically, when characterisation is carried out, it is often vague and limited to relatively few particles; it is common for values to be given as a range of typical values estimated from a small number of particles in TEM images.^{131–134}

The work of Silva *et al.* can be used as an example of why relying on such “typical” values can be problematic. They were interested in modelling the reinforcing effect of HNTs in poly(lactic acid) nanocomposites using three methods: firstly, by using the empirical Halpin-Tsai (HT) model and a single, typical HNT dimension; secondly, by computing stress distributions in a voxel unit-cell containing randomly-oriented HNTs all of the same size, specifically the mode of the distribution measured from TEM images (the “ideal model”); and, finally, by studying a voxel unit cell, this time containing HNTs with the whole range of sizes measured for the HNTs in TEM images (the “real model”).¹³⁵ At about a 10 wt% loading of HNTs, they found that the HT model overestimated the experimental composite modulus by 30%, the ideal model overestimated by 18%, and the real model overestimated by only 6%. The remaining discrepancy between the real model and experimental data could be due to various factors, including incomplete dispersion of

the nanofiller, inaccuracies in their HNT size data since they only measured a small number of particles (50), or because they did not take non-HNT impurities into account.¹³⁵ In any case, their work is a good illustration of why thorough characterisation of HNT morphology is important for predicting and understanding their behaviour, particularly in composite applications.

2.2 Aims of chapter

The aim of this chapter was to perform chemical and physical characterisation of HNTs provided by I-Minerals Inc. from their source in Idaho. Where possible, this data could then be compared to both literature data and that from the supplier data sheet in order to comment on the wisdom of relying on such data when using HNTs, rather than performing independent characterisation. In addition, the data gathered here could be used as a baseline for future work (e.g. when considering the success of chemical functionalisation of the nanotubes). To aid navigation, a flowchart illustrating the structure of the chapter is given in figure 2.1.

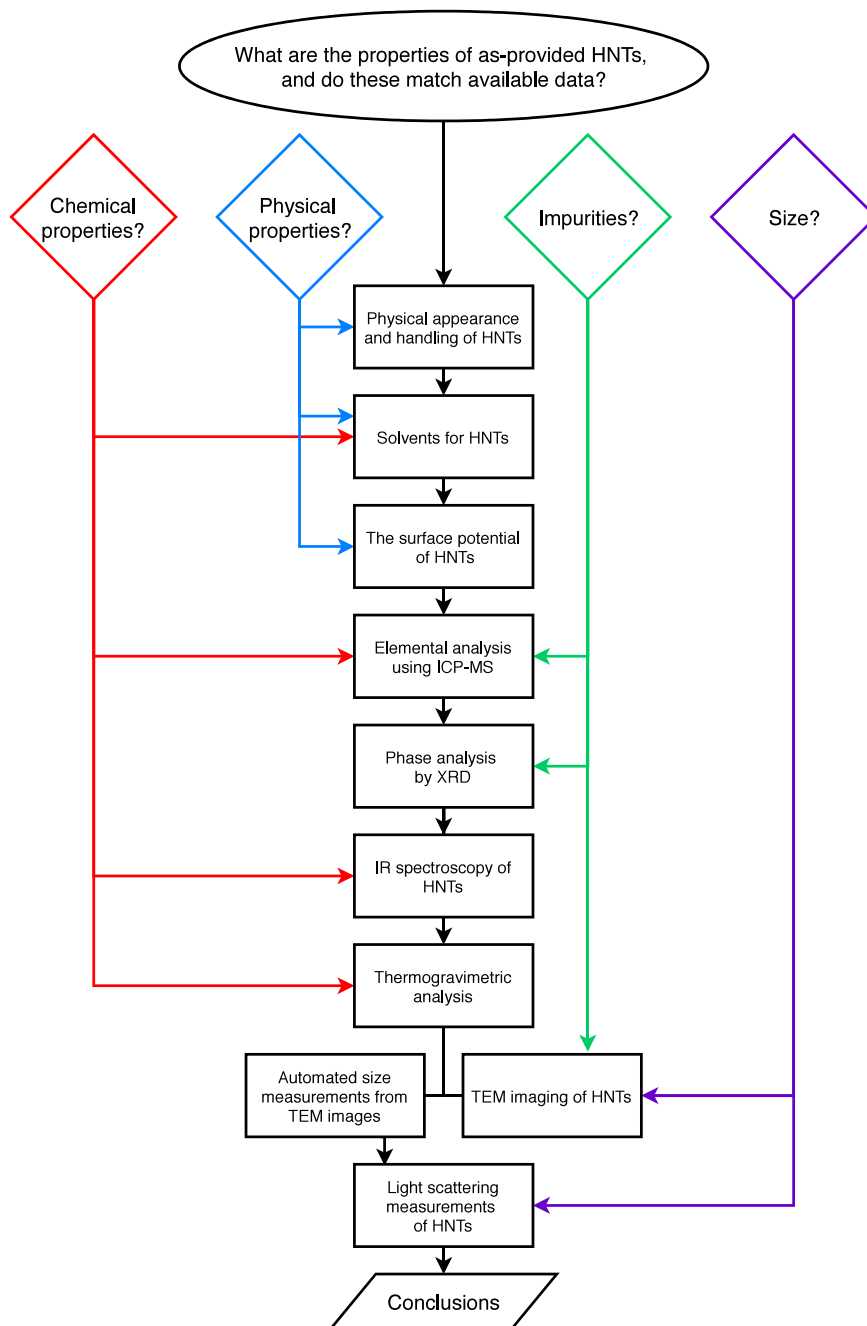


Figure 2.1: A flowchart illustrating the structure of the chapter “Characterisation of Halloysite Nanotubes”

2.3 Supplier data for halloysite nanotubes

The HNTs used in this work are from a batch of ULTRA HalloPure Halloysite provided by I-Minerals Inc. (Idaho, US). A data sheet for this material can be obtained directly from the company, and this is included in full in the appendix. Some key details from this data sheet are summarised in tables 2.1 to 2.4, and will be referred to throughout this chapter.

Table 2.1: “Typical Tube Dimensions” from the supplier data sheet.

Dimension	“Typical” value
Length	2000 nm
External diameter	200 nm
Internal diameter	20 nm
Aspect ratio	10

Table 2.2: “Typical Chemical Analyses” from the supplier data sheet (measured by X-ray fluorescence).

Compound	Content in sample/wt%
SiO ₂	46.00
Al ₂ O ₃	37.80
Fe ₂ O ₃	0.72
K ₂ O	0.30
MgO	0.13
TiO ₂	0.07
CaO	0.07
Na ₂ O	0.01

Table 2.3: “Typical Trace Elements” from the supplier data sheet.

Element	Concentration in sample/ppm
Ba	115.6
Zn	15.4
Pb	12.8
Cu	7.66
Cr	7.08
Ni	2.28
As	1.03
Mo	0.10
Hg	0.10
Se	<0.10
Ta	<0.10
Ag	<0.02
Cd	<0.003

Table 2.4: “Typical Mineralogy by XRD” from the supplier data sheet.

Mineral	Content in sample/%
Halloysite	90.0
Kaolinite	9.5
Quartz	0.5

2.4 Basic physical properties of halloysite nanotubes

2.4.1 Physical appearance and handling of halloysite nanotubes

The as-provided HNTs were in the form of a soft, light brown powder. A concentration series of these HNTs in water is shown in figure 2.2. Dispersions of HNTs in water increase in viscosity with increasing HNT concentration, until they eventually form a gel.



Figure 2.2: A concentration series of HNTs in water (HNT concentration from left to right: 0.1 wt%, 1 wt%, 5 wt%, 9 wt%, 17 wt%, 31 wt%, 50 wt%, and 100 wt%). Turning the sample vials upside down (bottom) illustrates the increasing dispersion viscosity with increasing HNT loading, as well as the gel-like behaviour of samples with high HNT loadings.

It is clear from figure 2.2 that gelation occurs somewhere between a 30 wt% and 50 wt% loading of the clay, and indeed Luo *et al.* observed an aqueous HNT gel at a HNT loading of 40 wt%.¹³⁶ They also showed that the HNT concentration at which gelation of these dispersions occurs depends significantly on the pH of the solution, with gelation occurring at a lower HNT concentration at low pH, and a higher HNT concentration at high pH.¹³⁶ This is explained in terms of the nanoparticles’ surface charge, i.e. increasing $[H^+]$ leads to increased screening of the HNTs’ negative surface charges and subsequently lower electrostatic repulsion between particles, and vice versa (see section 2.4.3).¹³⁶ They also suggest that H^+ ions act as cross-linkers between silanol groups on the HNT surfaces.¹³⁶

Making a concentration series in this way can be used to inform certain aspects of processing and using HNTs. For example, it is clear that there is a maximum loading of HNTs in aqueous solution above which the mixture becomes difficult to stir or otherwise

process, which is useful to know when designing reactions. It also shows that any dispersion of HNTs above about 1 wt% is likely to be translucent or opaque, which makes high HNT loadings undesirable for applications where optical clarity is important (unless the bulk material has a refractive index similar to that of halloysite). However, it should be noted that to make the samples in figure 2.2, the HNTs were only dispersed into solution by shaking the vials by hand, so the opacity of the dispersions could be due to light scattering by agglomerates of HNTs rather than individually dispersed nanoparticles.

The origin of colour in halloysite

The brown colour of the as-provided HNTs is probably due to the presence of iron oxide impurities, which supplier data lists as making up 0.7 wt% of this grade of HNT (see section 2.3). This is confirmed by ICP-MS (see section 2.5.1), and is also supported by two experimental observations when washing the HNTs at different pH:

1. The brown colour disappears upon washing the HNTs with concentrated acid (this is discussed in more detail in Chapter 4).
2. Washings appear brown when the HNTs are washed with water at pH 12 (figure 2.3), and an additional dark brown sediment is observed on top of the HNTs upon centrifugation of the sample.

Observation 1 is explained by dissolution of any solid iron oxide in the extremely low pH solution, which is subsequently washed away with the acid.¹³⁷ Observation 2 is explained by the formation of some variety of colloidal iron oxide or iron hydroxide nanoparticles in the high pH solution,^{137,138} which, while stable in solution, can be retrieved to some extent using a centrifuge. As shown in figure 2.3, particles of around 105 nm in size can be observed in the washings by Dynamic Light Scattering (DLS) (see section 2.6.6), which confirms that the colour seen in observation 2 is due to colloidal particles rather than a dissolved ligand/metal complex.

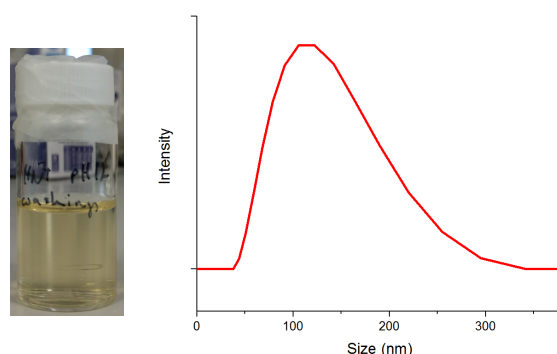


Figure 2.3: Washing HNTs with water at pH 12 produces pale, brown washings (left). The colour is thought to be due to formation of colloidal iron oxide or iron hydroxide particles. These particles can be measured by DLS (right), which indicates a particle diameter of approximately 105 nm.

2.4.2 Solvents for halloysite nanotubes

Basic theory of mixing

The mixing of two components is spontaneous if the change in the Gibbs free energy of mixing is negative. The change in Gibbs free energy upon mixing (ΔG_{mix}) is described by equation 2.1, where H_{mix} , S_{mix} , and T are the enthalpy of mixing, entropy of mixing, and temperature, respectively. For nanotubes, ΔS_{mix} is relatively small because of their relatively large size and rigidity.⁴⁶ This means that ΔH_{mix} must either also be small, or be negative (i.e. exothermic) if mixing is to be spontaneous. The mixing of nanotubes into a solvent is hence dominated by the energetics of the interaction between the solvent and nanotube surface.⁴⁶

$$\Delta G_{\text{mix}} = \Delta H_{\text{mix}} - T\Delta S_{\text{mix}} \quad (2.1)$$

The importance of understanding the compatibility halloysite with different solvents

Understanding how readily HNTs will disperse into different kinds of solvents, and the stability of these suspensions, can be useful for designing chemical reactions and predicting the nanotubes' behaviour in certain applications. For example, were they to be used as part of a liquid formulation, it would be necessary to be able to predict under what conditions the HNTs might flocculate. Understanding the nanotubes' behaviour in small molecular solvents also gives an insight into how readily the nanoparticles would be expected to disperse when mixed into polymers to produce a polymer nanocomposite.¹³⁹ Most relevant to this work, exploring the stability of HNTs in a variety of solvents should allow the prediction of the compatibility between the as-provided HNTs and epoxy resin when they are mixed to make a nanocomposite.

As discussed in Chapter 1, the outer surface of HNTs largely consists of Si-O-Si, with Si-OH groups found at surface defects and edges. The Si-O-Si are relatively hydrophobic, and the silanol groups are relatively polar, and can form hydrogen bonds. Therefore, the concentration of silanols on the nanotube surface relative to Si-O-Si would be expected to influence the energetic interaction between the HNT and a solvent. In addition, HNTs from different sources often have different surface structures, and hence the dispersability of the particles might be expected to differ from sample to sample. Indeed, when Pasbakhsh *et al.* studied HNTs from various sources, they found that some halloysites would disperse readily into deionised water, while others flocculated.¹²⁷ Because of this variability in surface properties, it was deemed important to independently study the ability of the HNTs used here to disperse into different solvents rather than rely on literature data or make assumptions based on generic HNT surface chemistry.

Using sedimentation time to rank solvent performance

A simple experiment to explore the compatibility of HNTs with different solvents is to disperse them into a variety of solvents and observe how long it takes for the HNTs to sed-

iment out. The longer it takes for the HNTs to sediment out of a dispersion in a particular compound/mixture of compounds, the better a solvent for HNTs the compound/mixture is considered to be. The difference in sedimentation speed in different solvents is due to the presence of larger agglomerates of particles in poor solvents and vice versa. More specifically, in poor solvents, ΔH_{mix} is low, and the nanotubes tend to stick together rather than disperse into solution; these relatively large agglomerates have greater gravitational momentum relative to viscous drag, and hence settle more quickly out of solution. However, linking sedimentation speed solely to compatibility between solvent and particle is incorrect, as it also depends on the viscosity of the liquid, and relative densities of the particle and the liquid.¹⁴⁰ As such, this experiment is not taken to give any quantitative information about the energetic interaction between the HNTs and solvents, but ranking the performance of different solvents can nonetheless reveal useful trends. The dependence on solvent viscosity in particular makes this experiment unsuitable for exploring the compatibility of HNTs and epoxy resin directly, since epoxy resins are especially viscous liquids.

To measure sedimentation time in practice, dispersions of HNTs in various solvents were filmed using time-lapse photography. The time between the first frame after stirring was switched off, and the first frame in which the HNTs could be considered to have fully settled out of the liquid, was taken to be the sedimentation time, and this value was used to rank the performance of each solvent. A measurement of sedimentation time is illustrated for the example of toluene in figure 2.4.

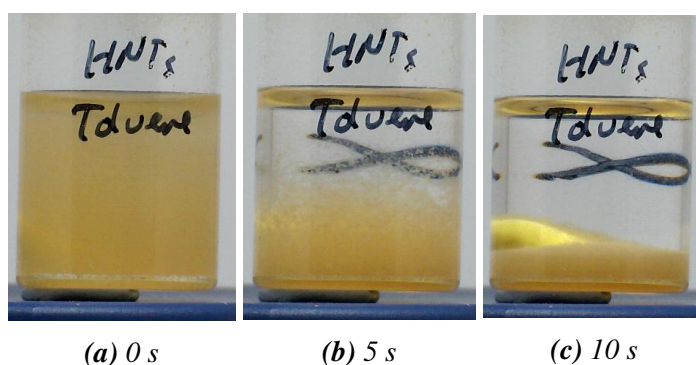


Figure 2.4: Example images of HNTs as they sediment out of toluene, which were taken using time-lapse photography. Image (a) was taken just after stirring was switched off (i.e. 0 s), image (b) shows the HNTs during sedimentation (after 5 s), and the final image (c) is the first frame in which the HNTs are considered to have fully settled out of the liquid (after 10 s).

There is obviously a lot of room for error with this method, mainly because subjective judgement is required to identify when the HNTs have fully sedimented from dispersion. However, the difference in sedimentation time was sometimes so large that this was not an issue. For solvents where there was some uncertainty, they are grouped together to indicate them being equally good. Using this method, the following solvents were ranked in order of increasing sedimentation time (i.e. from “worst” solvent for HNTs to “best” solvent for HNTs):

A: Toluene, Diethyl Ether, Cyclohexane << B: Xylenes, Chloroform, Ethyl Acetate <

C: Methyl Methacrylate, Acetone < D: Tetrahydrofuran < E: 2-Propanol, Butan-2-one, 1-Heptanol, Methanol, Ethanol << F: Water

Approximate sedimentation times for each group of solvents (indexed by letter) are given in table 2.5. It is clear that a dispersion of HNTs is only briefly stable in most solvents. This might limit their potential for use in certain applications, at least without some kind of surface modification of the nanotubes to change the energetic interaction with the solvent. It also has implications for performing certain measurements; for example, some light scattering measurements take several minutes, and so would not be able to be performed for HNTs in many solvents. Nonetheless, relative compatibilities between the solvents and HNTs can be described using table 2.5: compounds in groups A and B are bad solvents for HNTs; compounds in groups C and D are moderately good solvents for HNTs; solvents in group E are relatively good solvents for HNTs; and water (the sole member of group F) is a very good solvent for HNTs.

Table 2.5: *The approximate time taken for HNTs to completely sediment out of the groups of solvents described in the text.*

Group	Approximate sedimentation time
A	10 s
B	30 s
C	45 - 60 s
D	1 - 2 min
E	Several min
F	1 day

Applying Hansen solubility parameters to solvent performance results

A more thorough way of exploring the energetic interactions between the nanotubes and the different solvents is by applying Hansen solubility parameters (HSPs). In the HSP model, every molecule has a total solubility parameter (δ_{TOT}), which is a combination of three parameters representing dispersion (i.e. van der Waals) forces (δ_D), dipole-dipole interactions (δ_p), and hydrogen bonding (δ_H).¹⁴¹ This is expressed mathematically in equation 2.2.

$$\delta_{TOT}^2 = \delta_D^2 + \delta_p^2 + \delta_H^2 \quad (2.2)$$

To put it another way, every solvent occupies a specific point on a 3D plot where the axes are the three solubility parameters.¹⁴¹ The distance between molecules on this plot can then be used as a guide to predict how compatible they are with one another, with a short point-to-point distance suggesting good solubility/miscibility, and vice versa.¹⁴¹ The distance, R , between two solvents in solvent parameter space can be calculated as shown in equation 2.3.

$$R = \sqrt{4(\delta_{D1} - \delta_{D2})^2 + (\delta_{p1} - \delta_{p2})^2 + (\delta_{H1} - \delta_{H2})^2} \quad (2.3)$$

Although HSPs were originally devised for small molecules and polymers,¹⁴¹ they are also frequently applied to particles. Colloidal particles are by definition insoluble in the liquid in which they are dispersed, but HSPs can nonetheless give some insight into the chemical nature of the particle surface. As previously mentioned, good mixing of a particle with a solvent requires energetically favourable interactions between the solvent and particle surface (i.e. negative ΔH_{mix}), hence the surface of a particle that disperses readily in a given liquid is likely to be chemically similar to that liquid. This means that HSPs are often used experimentally to aid the choice or design of solvents or surfactants for a particle in order to maximise its colloidal stability. For example: Bergin *et al.* screened solvents in order to estimate the HSPs of single-walled carbon nanotubes, which allowed them to identify the best solvent in which to disperse the agglomerated nanoparticles;⁴⁶ Petersen *et al.* estimated HSPs for surfactant-capped silver nanoparticles, and used them to optimise the manufacture of a polymer nanocomposite film;¹⁴² and Wang *et al.* used HSPs to explain the colloidal stability of zirconia nanoparticles coated with a variety of carboxylic-acid-functional compounds.¹⁴³

In the case of pure, unmodified HNTs, the closest solvents in solvent parameter space are water, and short chain alcohols (e.g. ethanol and 2-Propanol), i.e. solvents with high δ_{H} and δ_{p} , and relatively low δ_{D} . Hence a generalisation can be made: HNTs disperse more readily in polar solvents in which hydrogen bonding occurs. That is to say, the surfaces of the HNTs used in this work are considerably hydrophilic in nature. Indeed, water was by far the best solvent for the HNTs, with a sedimentation time several orders of magnitude longer than the next closest solvents.

However, the conclusion that HNTs are hydrophilic can also be reached simply from brief inspection of the experimental trend in sedimentation time. For unmodified HNTs at least, HSPs are therefore of limited value. HSPs may be useful for evaluating HNTs with functionalised or otherwise chemically treated surfaces, but it should also be noted that evaluating solvent compatibility via solvent screening and HSPs can be time and labour intensive.

Nonetheless, the results gathered from sedimentation time experiments do allow prediction of the compatibility between the HNTs and epoxy resin. More specifically, one can compare the positions of the solvents in solvent parameter space by using equation 2.3 to calculate the distance from a set reference point. Water was used as a reference point, since it was by far the best solvent for HNTs, and indeed it can be seen in table 2.6 that ranking the solvents in terms of distance from water in solvent parameter space gives a similar trend as found by measuring sedimentation time. The exception to this is butan-2-one, which is further from water than would be expected from its sedimentation time; the reason for this unknown, since it has a lower viscosity than, and similar density to, solvents with similar sedimentation time. In any case, using literature values for the HSPs of a bisphenol diglycidyl ether,¹³ epoxy resins can be placed in the ranking in terms of their distance from water in solvent parameter space, as is shown in table 2.6. Doing so reveals that epoxy resins are probably moderately good solvents for unmodified HNTs (i.e. would belong in group C or D in table 2.5).

Table 2.6: The distance in solvent parameter space from water for all the solvents screened in this work, and that calculated using a literature value for the HSPs of a bisphenol-derived epoxy resin¹³ (highlighted green).

Solvent	Distance from water in solvent space/MPa ^{1/2}	Sedimentation time group
Water	0	F
Methanol	20.4	E
Ethanol	24.0	E
2-Propanol	27.7	E
1-Heptanol	32.4	E
Acetone	35.7	C
Tetrahydrofuran	35.9	D
Epoxy resin	36.0	n/a
Ethyl acetate	36.7	B
Butan-2-one	37.9	E
Methyl methacrylate	38.1	C
Chloroform	39.1	B
Diethyl ether	40.0	A
Toluene	43.2	A
Cyclohexane	45.1	A

2.4.3 The surface potential of halloysite nanotubes

It is clear that the behaviour of HNTs in solution is dictated by hydrogen bonding and dipole-dipole interactions at the particle/solvent interface. When particles are dispersed in water specifically, the surface charge of the particles is an important indicator of how likely the individual particles are to either remain dispersed, or flocculate and settle out. Measuring the surface potential of particles is also necessary to be able to predict how the particle surface would interact with specific functional groups (e.g. ions or polar molecules).

In water containing dissolved electrolyte, ions on a particle surface dissociate and mix with those in solution to form a diffuse layer of anions and cations known as an electrical double layer.¹⁴⁴ In the undisturbed double layer, the ions maximise their configurational entropy.¹⁴⁴ However, bringing two surfaces together compresses the ion layer and forces the ions away from their preferred equilibrium state, which causes a repulsive force between the particles.¹⁴⁵ This repulsive force is in balance with an attractive van der Waals force which becomes increasingly large at short surface separations.¹⁴⁶ The consequence of the combination of these two forces is the existence of an energy barrier at a certain particle separation distance, which must be overcome if the particles are to flocculate together.¹⁴⁶ Increasing the surface charge of a particle increases the height of this energy barrier, and makes the particles more likely to remain individually dispersed.¹⁴⁶ Some common surface functional groups have labile protons, notably hydroxyls (i.e. -OH). When such functional groups are present, the surface charge and hence stability of the particles in electrolytic solutions is dependent on pH.¹⁴⁷

In practise, the zeta potential of particles in water is measured rather than their actual surface charge.¹⁴⁸ The zeta potential of a particle is the potential at the outer edge of the electrical double layer, and it gives an indication of the size of the surface charge. A particle's zeta potential can be calculated from measurements of the velocity of the particles in solution upon application of an electric field (i.e. electrophoresis).

The zeta potentials of HNTs in distilled water were measured over a range of pH, and are shown in figure 2.5. At high pH, the HNTs have large negative zeta potentials. Despite the large standard deviations associated with high pH measurements, these results suggest that HNTs are most well-dispersed in water at pH 12 and above. Decreasing pH led to an increasingly positive zeta potential, until the isoelectric point (i.e. a zeta potential of zero) was reached at around pH 2. At the isoelectric point, the repulsive force between particles is minimised and hence the particles flocculate the most readily at this pH.

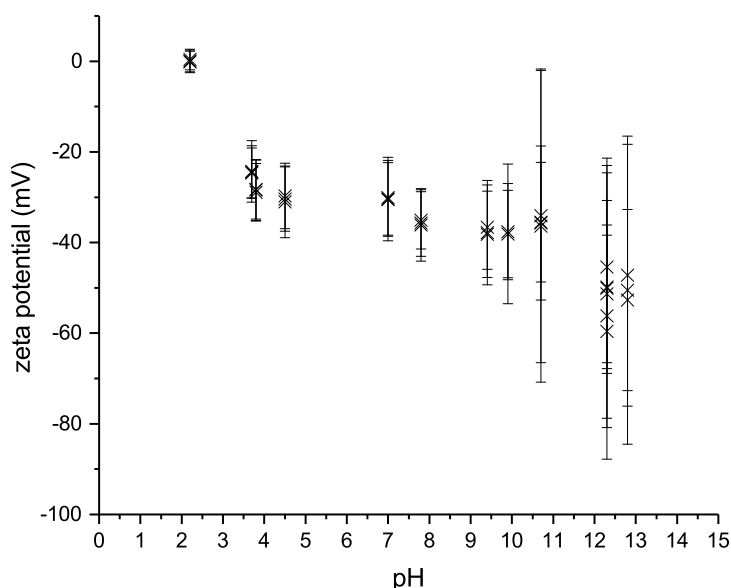


Figure 2.5: A graph of pH versus zeta potential for HNTs. The nanoparticles have the highest zeta potential at high pH, and go through an isoelectric point at around pH 2. The error bars are the zeta deviation of each measurement.

These results generally match published values of HNT zeta potentials in water,^{136,149} and indeed are consistent with those found for silica surfaces in general.¹⁵⁰ However, Joo *et al.* also describe positive zeta potentials for the nanotubes in water below pH 2.¹⁴⁹ Values for HNT zeta potentials below pH 2 are omitted here, as they were measured to be on the order of -20 mV, which does not make sense considering the higher cation concentrations in lower pH solutions, which should screen any negative surface charges. This was the case even after more or less exact replication of the method published by Joo *et al.*¹⁴⁹ It is unclear why negative zeta potentials were seen in low pH solutions, but it may be related to the increased conductivity of aqueous solutions with high $[H^+]$ causing problems for either the electrodes in the measurement cell, or the instrument itself. The results here are also slightly different to those found by Pasbakhsh *et al.*, who found that HNTs had no isoelectric point at pH 2, but rather had a negative zeta potential even at

pH as low as 1.5 (below -10 mV).¹²⁷ These differences once again serve to highlight the fact that literature data for HNTs should not be taken to be 100% transferable between different samples/batches, and characterisation of the nanotubes should hence be carried out independently.

2.5 Characterising the chemical properties of halloysite nanotubes

2.5.1 Elemental analysis of halloysite nanotubes using ICP-MS

The composition of the as-provided HNTs was analysed using inductively-coupled-plasma mass spectrometry (ICP-MS). ICP-MS is a mass spectrometry technique which uses a high-temperature plasma to ionise aqueous samples before they enter a mass spectrometer. It is useful for the detection of elements with high first-ionisation energies which are difficult to ionise by other techniques. ICP-MS also allows the detection of very low elemental concentrations in a sample.

The concentrations of the most abundant elements in the HNTs as found by ICP-MS are given in table 2.7. From the empirical formula for dehydrated halloysite ($\text{Al}_2\text{Si}_2\text{O}_5(\text{OH})_4$), one would expect Al and Si to represent 20.9 and 21.8 wt% of the sample, respectively. The higher-than-expected amount of Si relative to Al indicates the presence of other silica minerals as impurities, probably the quartz impurity listed in the supplier data sheet. Excluding the small contribution from trace elements, the rest of the mass not accounted for by the elements listed in table 2.7 is presumably oxygen, which is not detected by ICP-MS.

Table 2.7: The concentrations of the most abundant elements in HNTs as found by ICP-MS

Element	Concentration/wt%
Si	22.1
Al	16.0
Fe	1.0
K	0.3
Ti	0.2
Mg	0.1
Ca	0.04
Na	0.02

The values of elemental concentrations from ICP-MS found here had to be converted to a concentration of the corresponding oxide to allow for comparison with the chemical composition described in the supplier data sheet (i.e. table 2.2). First, it was assumed that the signal for each element in ICP-MS only came from the oxides described by the supplier. The mass fraction that each element contributes to the corresponding oxide can then be described using equation 2.4, where ϕ_E is the mass fraction of the element, M_E is

the relative atomic mass of the element, $M_{E_xO_y}$ is the relative molecular mass of the oxide, and x and y are the stoichiometric numbers of the element and oxygen, respectively. The elemental concentration can subsequently be converted to an oxide concentration using equation 2.5, where C_E is the concentration of the element in the sample, and $C_{E_xO_y}$ is the hypothetical concentration of the oxide.

$$\phi_E = \frac{xM_E}{M_{E_xO_y}} \quad (2.4)$$

$$C_{E_xO_y} = \frac{C_E}{\phi_E} \quad (2.5)$$

The results of converting elemental concentrations from ICP-MS to oxide concentrations are given in table 2.8, where they are also compared to values from the supplier data sheet. Most significantly, there appears to more SiO_2 , more Fe_2O_3 , and less Al_2O_3 in the sample than described by the supplier. This is evidence for an increased number of silicate and iron impurities in the sample versus that reported by the supplier.

Table 2.8: The concentration of the most abundant elements in HNTs as found by ICP-MS converted to hypothetical concentrations of the oxides listed in the supplier data sheet.

Compound	Concentration (supplier data)/wt%	Concentration (this work)/wt%	Difference
SiO_2	46.00	47.28	+3%
Al_2O_3	37.80	30.23	-20%
Fe_2O_3	0.72	1.43	+99%
K_2O	0.30	0.36	+20%
MgO	0.13	0.17	+30%
TiO_2	0.07	0.33	+371%
CaO	0.07	0.008	-89%
Na_2O	0.01	0.008	-20%

Not included in this table are other elements that were present in concentrations below 0.1 wt%, namely S, Ba, Mn, P, Ce, Zn, La, Zr, Sr, Y, Li, V, Cr and Cu. Combined, the trace elements make up about 0.2 wt% of the HNT sample. Of these, the following were not mentioned in the supplier data sheet: S, Mn, P, Ce, La, Zr, Sr, Y, Li, and V. The concentrations of trace elements are given in table 2.9, and, where possible, compared to values given in the supplier data sheet. As well as differences being seen in which elements were present, where the same impurities have been found, they are all present in significantly larger quantities than reported by the supplier.

The low concentration of the trace elements means that they probably have a small effect on the behaviour of the sample overall. However, there are clearly discrepancies between the data in this work and the supplier data concerning the trace element concentration in HNTs, in addition to the discrepancies in the oxide composition of the HNTs already discussed. This once again highlights the fact that independent characterisation of samples of these HNTs should be carried out rather than relying on existing data.

Table 2.9: A comparison of trace elements in HNTs from I-Minerals Inc. found by ICP-MS in this work, versus those listed in the supplier data sheet. Also included is the percentage difference between the supplier data and that found here.

Element	Concentration (supplier data)/ppm	Concentration (this work)/ppm	Difference
Ba	115.6	232	+102%
Zn	15.4	24.8	+61%
Pb	12.8	not found	
Cu	7.66	9.6	+25%
Cr	7.08	10.4	+47%
Ni	2.28	not found	
As	1.03	not found	
Mo	0.10	not found	
Hg	0.10	not found	
Se	<0.10	not found	
Ta	<0.10	not found	
Ag	<0.02	not found	
Cd	<0.003	not found	
S	not found	480	
Mn	not found	107	
P	not found	96	
Ce	not found	32	
La	not found	23	
Zr	not found	19	
Sr	not found	18	
Y	not found	14	
Li	not found	13	
V	not found	13	

2.5.2 Phase analysis of halloysite nanotubes using X-ray diffraction

X-ray diffraction (XRD), which is also sometimes referred to wide-angle X-ray scattering (WAXS), is a technique which can be used to study very small structural features in a compound. X-rays have wavelengths on the order of 10^{-10} m, which is in the region of typical chemical bond lengths.¹⁵¹ Constructive and destructive interference of X-rays diffracted by a particular lattice plane means that a reflection from that plane will only be observed at positions where Bragg's law is satisfied (equation 2.6).¹⁵¹ More specifically, constructive interference occurs when the glancing angle of incident X-ray radiation is such that the difference in the distance travelled by two photons reflected off neighbouring lattice planes is equal to an integer multiplied by the photons' wavelength, meaning the two are in-phase.¹⁵¹ This glancing angle is the θ described in Bragg's law. The wavelength of the photons is λ , and d is the distance between neighbouring lattice planes.¹⁵¹ These are illustrated in figure 2.6. While XRD can be used to accurately determine inter-atomic distances in crystalline compounds, it was used here simply to perform phase analysis, i.e. to identify the various mineral components of the sample by reference to an existing database of XRD data for samples of known composition.¹⁵²

$$\lambda = 2d\sin\theta \quad (2.6)$$

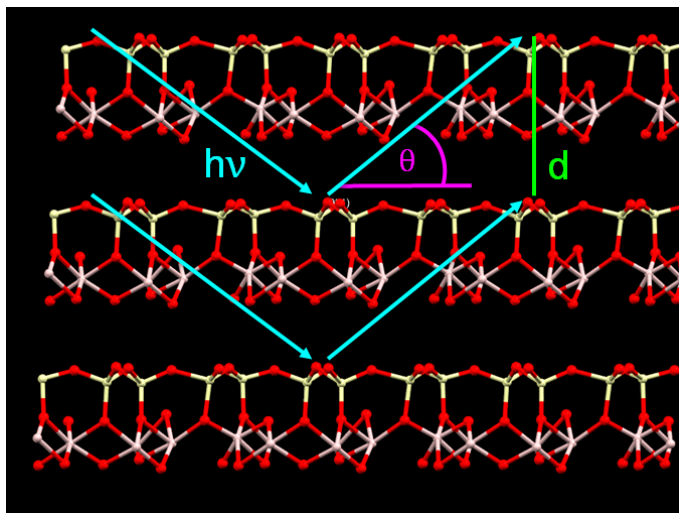


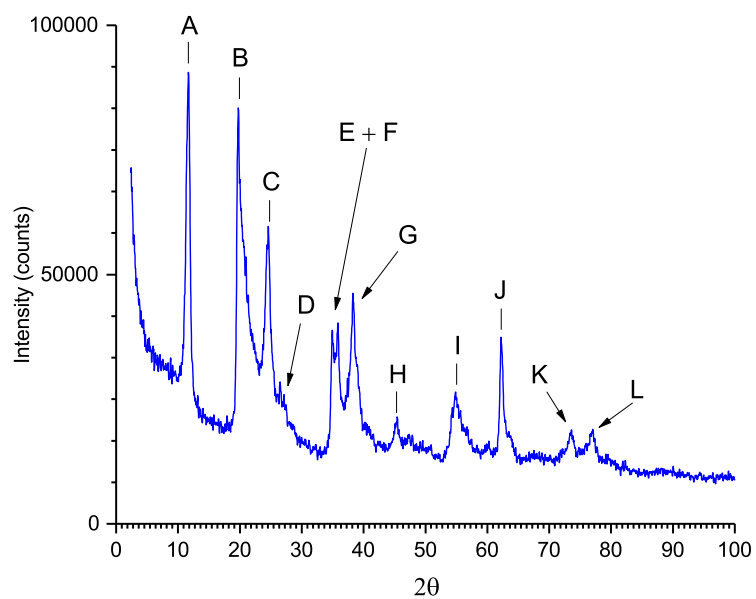
Figure 2.6: Bragg's law of diffraction illustrated using the example of diffraction by the interlayer in halloysite.

The XRD of pure HNTs is shown in figure 2.7. The data shown in figure 2.7a was calibrated using a Si standard, which gives an effective calibration for peaks of around $28^\circ 2\theta$ and above. To find accurate values for the important d_{001} plane, this peak was measured separately on a different instrument where calibration for low angle reflections had been done using a silver behenate standard (figure 2.7b), but which could not measure as high values of θ .

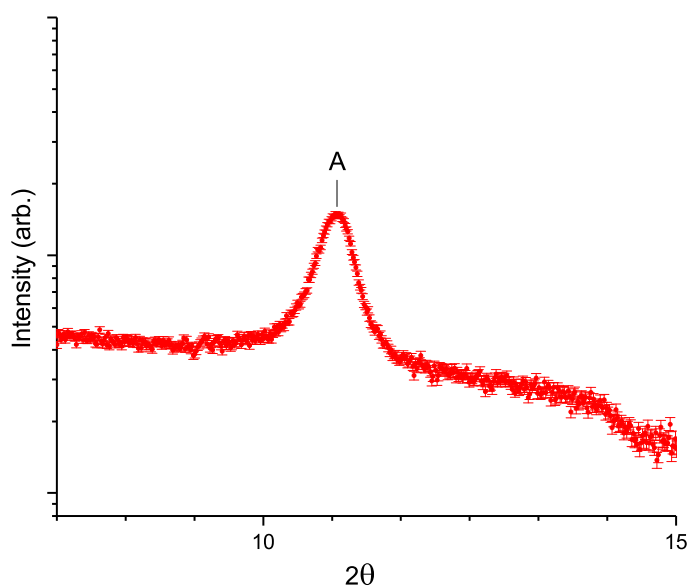
Table 2.10: A summary of peak positions and assignments in a powder XRD pattern of HNTs

Peak	$2\theta/^\circ$	Miller index	Mineral
A	10.87	001	Halloysite
B	19.76	110	Halloysite (shoulder is kaolinite)
C	24.59	002	Halloysite (shoulder is kaolinite)
D	26.51		Kaolinite
E	34.94	200	Halloysite
F	35.84	200	Halloysite + kaolinite
G	38.27		Halloysite + kaolinite
H	45.44		Kaolinite
I	54.86		Kaolinite + halloysite
J	62.21		Halloysite + kaolinite
K	73.58		Halloysite + kaolinite
L	77.03		Kaolinite

Peak A represents the d_{001} lattice plane of the HNTs. Using equation 2.6, a distance of 7.09 \AA can be calculated. This is the width of a single aluminosilicate layer, and is indicative of halloysite in a relatively dry environment, i.e. one in which most of the interlayer water has left the structure.⁵⁵ An increase of this distance after chemical treatment of the



(a)



(b)

Figure 2.7: Powder XRD pattern of HNTs from I-Minerals Inc.. All of the peaks can be assigned to those expected for halloysite and kaolinite. Peak A was also measured on an instrument which was calibrated for lower angle scattering; it corresponds to a distance of 7.09 Å, which is the width of a single aluminosilicate layer.

HNTs would imply that molecules other than water have intercalated into the nanoscrolls and expanded the interlayer region.¹⁵³

As would be expected, matching the peaks to a database reveals that the sample appears to consist largely of halloysite, with some kaolinite impurities. Metallic impurities (e.g. iron), known to be in the sample via ICP-MS, are present at concentrations below the detection limit of the diffractometer. The halloysite peaks were matched to a reference pattern for HNTs from the Dragon Mine in Utah,¹⁵² which is another important commercial source of HNTs. However, peaks D, H, K, and L were not present in the reference. This confirms the information given in the supplier data sheet, i.e. that the HNTs are almost completely free from mineral impurities (other than kaolinite), at least at levels detectable by XRD. The absence of signature peaks for quartz may be due to a combination of the quartz concentration being too low to be detected by the instrument, and/or the peaks corresponding to quartz being swamped by peaks from halloysite and kaolinite.

2.5.3 Infrared spectroscopy measurements of halloysite nanotubes

Photons with wavelengths in the infrared (IR) region can be absorbed by many types of covalent bonds within molecules. These bonds transition to higher energy vibrational and rotational states upon absorption of an incident photon, provided that this transition leads to a change in the dipole moment of the bond.¹⁵⁴ The energy of this transition is dependent on the strength of the bond between the atoms, the masses of the atoms involved in the vibrational motion, and the specific type of vibrational movement involved (e.g. stretching of the bond, ‘wagging’ of the bond from side-to-side, etc.).¹⁵⁴ Because of this, the transition between any two vibrations involving covalently bonded atoms, or groups of atoms, has a unique energy, and hence a unique frequency of IR photon is required in order for the transition to occur. The study of the wavelengths of IR absorbed by a sample can therefore be used to infer the presence of specific types of chemical bonds in the sample.¹⁵⁴ The IR absorption spectrum of pure HNTs is shown in figure 2.8, and a summary of the peak positions and the specific chemical bonds they are assigned to is given in table 2.11. Some peaks and peak shoulders found here were also found in literature, but not assigned, and hence are also not assigned here.

Table 2.11: A summary of peak positions in the IR absorption spectrum of HNTs, and the bonds and, where possible, specific vibrational modes they are assigned to.

Peaks	Wavenumber/cm ⁻¹	Bond
A	3696, 3621	Al-O-H (stretch) ^{7, 155, 156}
B	1655	H-O-H (wag)
C	1029, 467	Si-O-Si (stretch) ^{156, 157}
D	912	Al-OH ⁷
E	751, 532	Al-O-Si (stretch) ^{155, 156}
F	688	Si-O ^{156, 157}

The majority of the peaks seen are associated with vibrations of silica, alumina and aluminol functional groups, which would be expected considering the chemistry of halloysite. There is also a peak associated with water at around 1655 cm⁻¹, despite the fact that the

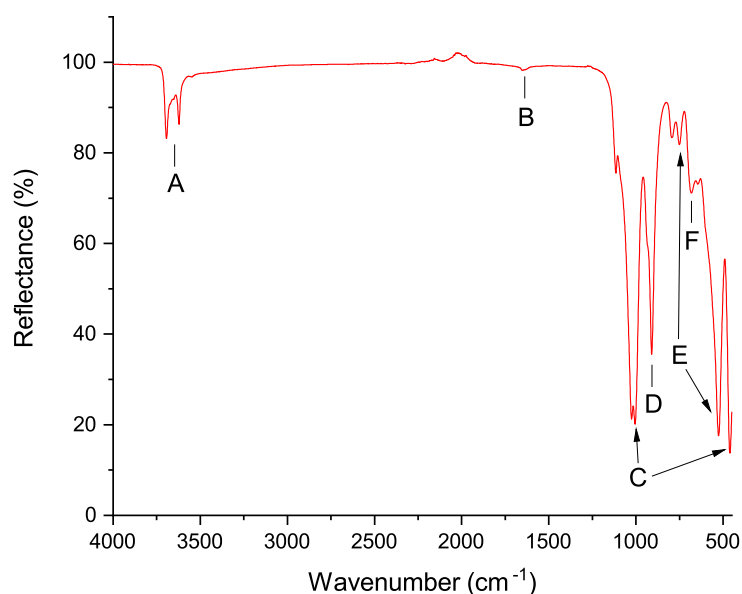


Figure 2.8: The IR absorption spectrum of pure HNTs.

sample had been dried in an oven prior to measurement, which shows that the HNTs are readily hydrated under ambient conditions. The small bump on the shoulder of peak A is associated with the water trapped in the interlayers of the nanoscrolls.⁴

2.5.4 Thermal decomposition of halloysite nanotubes

The decomposition of HNTs upon heating can be studied using thermogravimetric analysis (TGA), a straightforward technique in which the mass of a sample is measured to high precision as it is heated. Upon heating under inert atmosphere, HNTs should undergo two endothermic events which can be seen using TGA. Firstly, any water which is physisorbed to the clay's surface should be lost. This should occur between around 50 °C and 150 °C.⁵⁵ Between around 300 °C and 600 °C, there should be significant mass loss as the alumina structure in the HNTs undergoes dehydroxylation.⁵⁵ This is essentially the loss of chemisorbed water, i.e. loss of hydrogen and oxygen which were part of the mineral's original structure at lower temperature. Above around 835 °C, the HNTs would also be expected to undergo exothermic structural changes.⁵⁵ However, these do not correspond to any mass loss, and hence would not be seen using TGA. This is also above the maximum operating temperature of many differential scanning calorimeters, which would be able to study such an exotherm.

The result of TGA on HNTs is shown in figure 2.9. On the main graph, mass loss is plotted against temperature, while the inset graph shows the derivative mass (i.e. $d(\text{mass})/d(\text{time})$). The loss of physisorbed water appears to occur immediately upon exposure of the sample to the dry, nitrogen atmosphere of the TGA, and appears to be complete by the time the sample has reached 100 °C. The onset of mass loss due to dehydroxylation appears to occur between 200 - 400 °C, although noise in the derivative data makes this difficult to

precisely determine. Overall, the HNTs lost 14.4% of their mass when the loss of physisorbed water is taken into account, and 13.9% of their mass when only mass loss due to dehydroxylation (i.e. decomposition of the mineral's structure) is taken into account. The latter total mass loss is found by plotting mass as a percentage of the sample mass at 100 °C against temperature, rather than using the initial mass of the sample at ambient temperature. A total mass loss of 14.4% is similar to the loss on ignition (LOI) of 14.9% reported by I-Minerals Inc. for these HNTs (see appendix).

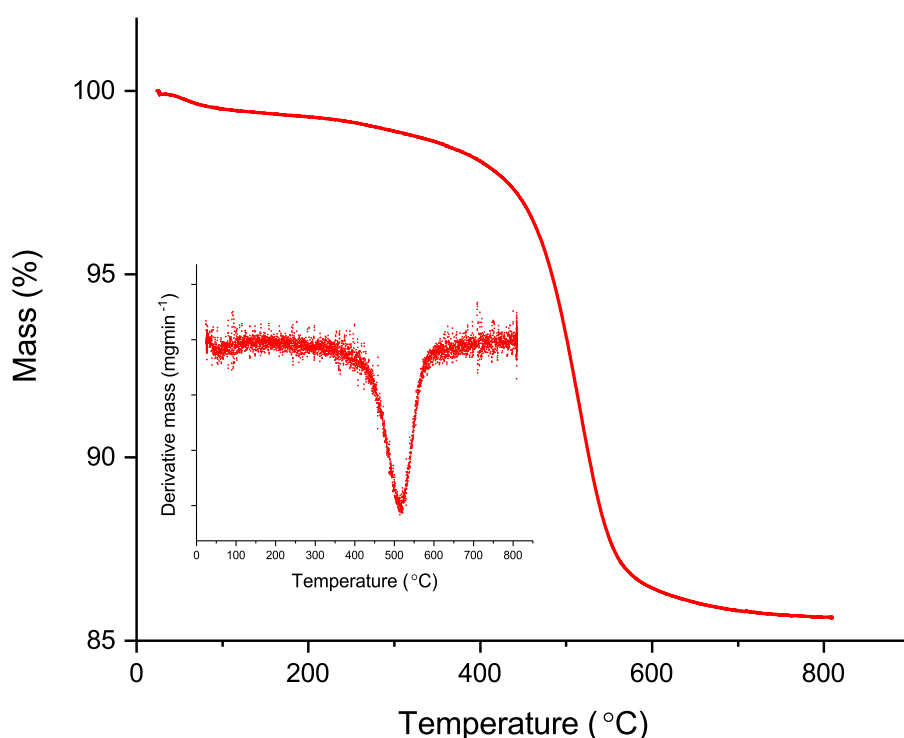


Figure 2.9: Mass loss and derivative mass versus temperature for pure HNTs. Two mass loss events occur, one as soon as heating begins, and the other around 200 - 400 °C. These correspond to the loss of physisorbed and chemisorbed water, respectively.

The most useful information that can be drawn from the results of TGA on HNTs is that they should be expected to contain a reasonable amount of physisorbed water under ambient conditions, and that heating them above around 300 °C will lead to irreversible chemical damage to the nanotubes. This means that they will have to be dried before they can be used in any water-sensitive processes, and they should ideally not be taken above 300 °C during processing.

2.6 Measuring the size and morphology of halloysite nanotubes

2.6.1 Measurement of halloysite nanotube dimensions from transmission electron microscope images

In transmission electron microscopy (TEM), an electron beam is fired through a thin layer of sample (typically suspended on a carbon-coated, copper grid), before being focused onto an imaging device, e.g. a digital camera. This provides very high magnification images of a 2D cross-section of a sample, and as such can be used to visualise HNTs in real space. Providing that the scale of the image is known, image analysis software such as ImageJ can be used to measure the lengths, internal diameters, and external diameters of the HNTs. These dimensions are indicated in figure 2.10 for the sake of clarity.

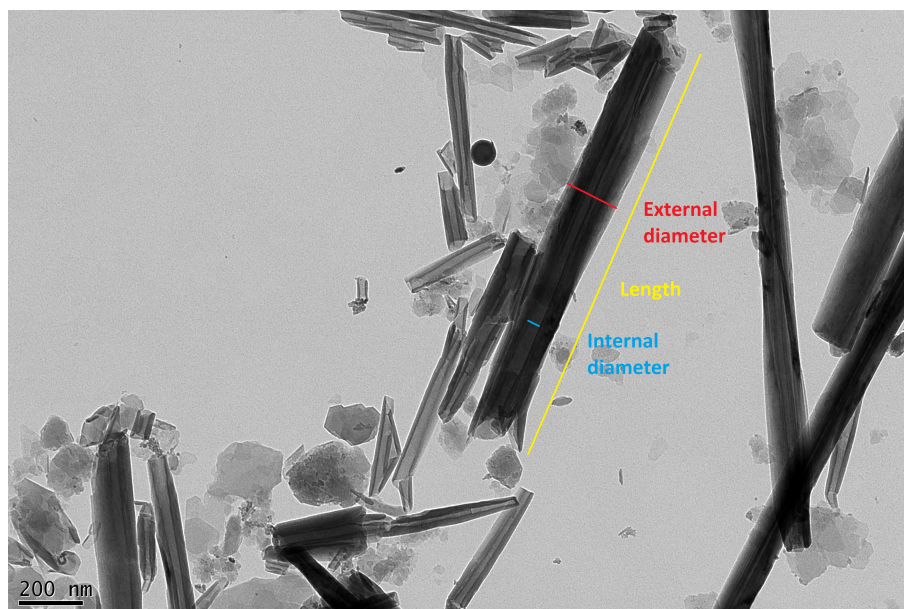


Figure 2.10: TEM image of pure HNTs. The length, external diameter, and internal diameter are indicated in yellow, red, and blue, respectively.

Scanning electron microscopy (SEM) can also be used to image HNTs. In contrast to TEM, SEM uses the interaction of a metallic or metal-coated sample with an electron beam to produce an image with a relatively large depth of field (i.e. objects are shown with three dimensions). An SEM image of HNTs is shown in figure 2.11. The main reason TEM was chosen over SEM to measure the HNTs was because the metal-coated HNTs are opaque in SEM images, which does not allow measurement of their internal diameter.

Even from first inspection of a small number of the particles in electron micrographs of HNTs such as those shown in figures 2.10 and 2.11, the number of clearly non-tubular particles present as impurities is readily apparent, as is the polydispersity of the nanotubes; there is a significant degree of variation in the size and shape of the HNTs, sometimes even along a single nanotube, and some nanotubes appear cracked or otherwise damaged. The supplier data sheet for the HNTs states simply that they have a typical length of 2 μm , a

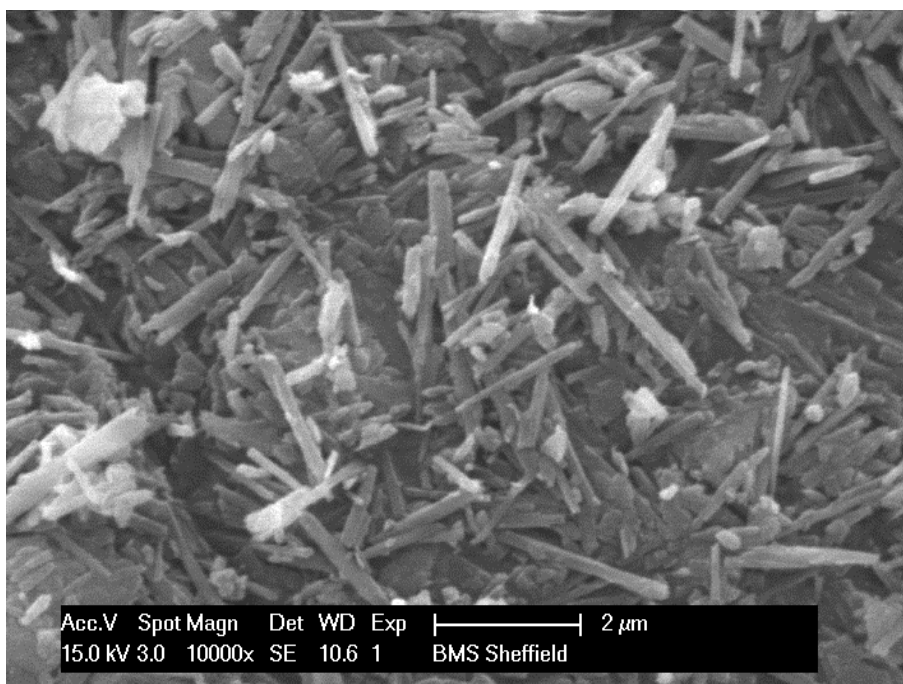


Figure 2.11: SEM image of pure HNTs.

typical external diameter of 200 nm, and a typical internal diameter of 20 nm, and that the sample is 90.0% halloysite as measured by XRD. However, it is clear from qualitative inspection of the micrographs that this specification should not be relied upon on its own, and the dimensions and purity of the sample should instead be quantified independently.

2.6.2 Quantifying morphological impurities in halloysite samples using TEM images

Using TEM images, one can estimate a number concentration of non-tubular particles versus tubular particles (i.e. a number concentration of morphological impurities) in a sample of halloysite. This is done simply by performing a count of the different particles in the images. As Joussein *et al.* point out, this is not necessarily a reflection of the number of halloysite particles versus those of kaolin or other minerals, as some halloysites can adopt several non-tubular morphologies.⁵⁵ However, this distinction is irrelevant if one is only concerned with the relative size of the population of nanotubes compared to other particles. An example count is shown in figure 2.12 (although it should be noted that this image contains fewer particles overall than many of the images, and as such may not be representative of the sample as a whole). While performing such a count is straightforward, it can also be quite subjective when deciding which particles/features to include in each population. Some examples of possible sources of ambiguity are also shown in figure 2.12: it was unclear whether feature A was a non-tubular particle, or an artefact from the TEM grid, so it was not counted; it was unclear whether particles B were tubes or not, so they were not counted; and it was unclear how many constituent particles made up particle C. Nonetheless, it is presumed that over a large enough count, the effect of such sources of bias are minimised, and an accurate number concentration of non-tubular particles can be obtained.

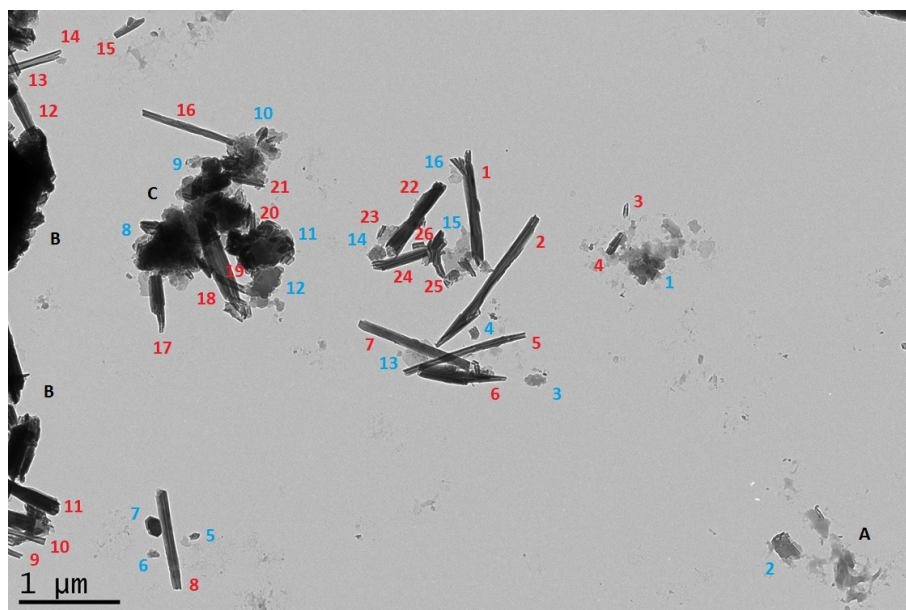


Figure 2.12: An example image where the numbers of tubular and non-tubular particles have been counted. In this image, there are 26 tubular particles, and 16 non-tubular particles. Features A, B and C are possible sources of ambiguity, as explained in the text.

Overall, 800 particles were counted in a total of 16 separate TEM images. About 40% of that number were found to be non-tubular. This is a large proportion of the total number of particles, however it does not necessarily represent how much of the sample non-tubular particles make up by mass or by volume. By qualitative inspection of the size of the different types of particle in the images, it seems reasonable to assume that the mass and volume fractions of non-tubular particles is significantly smaller than their number fraction. This is illustrated in figure 2.13, where it can be seen that most of the HNTs are much larger than the non-tubular particles.

2.6.3 Measuring halloysite nanotube dimensions by hand

In order to obtain dimensions for the HNTs, ImageJ was used to measure several hundred nanotubes by hand across a number of different TEM images. More specifically, measurements were made of the nanotubes' external diameters, internal diameters, lengths, and aspect ratios. The aspect ratios of the nanotubes were calculated as shown in equation 2.7. Aspect ratios were only calculated for nanotubes with both known external diameter and length, but they could also feasibly be obtained from a convolution of the probability density functions (PDFs) for external diameter and length.

$$\text{Nanotube aspect ratio} = \frac{\text{Nanotube length}}{\text{Nanotube external diameter}} \quad (2.7)$$

It should be noted that the nanotubes with the largest external diameters were often opaque to the electron beam, which means their internal diameters could not be measured by analysing TEM images. However, it is shown in figure 2.14 that the external and internal diameters of the nanotubes do not seem to be correlated, and hence ignoring the internal

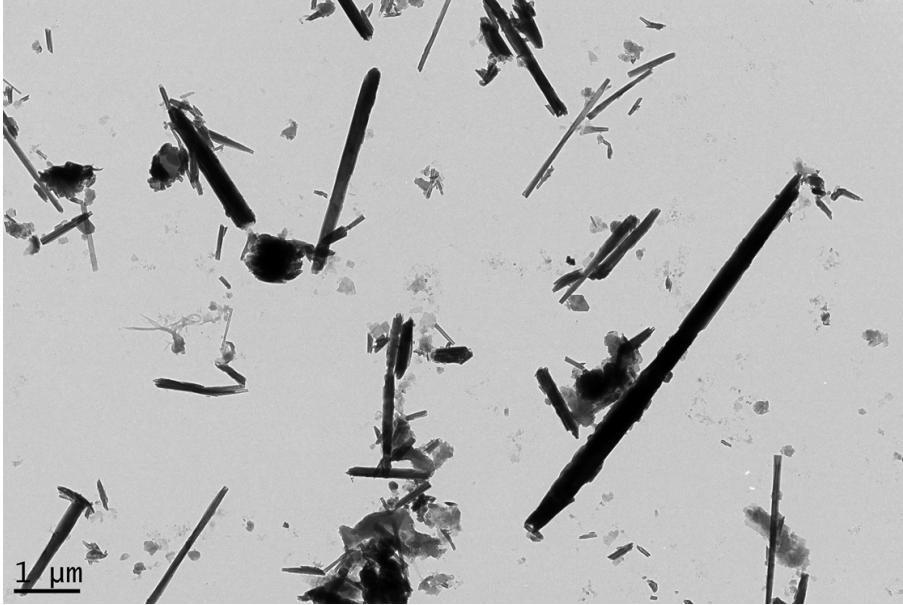


Figure 2.13: A representative TEM image of HNTs which shows how the tubular particles tend to be much larger than non-tubular particles. Despite non-tubular particles having a relatively high number concentration (about 40%), it would be expected that their mass and volume fractions would be significantly lower.

diameters of the thickest nanotubes can be assumed not to skew the measured distribution of the internal diameters.

All of the measured HNT dimensions appear to fit a log-normal distribution, with the example of the external diameter shown in figure 2.15. A set of measurements of quantity x are said to be distributed log-normally if $\log(x)$ follow a normal distribution.¹⁵⁸ Log-normal distributions are common in nature, including in chemistry and geology.¹⁵⁸ The PDF for a lognormal distribution of quantity x is given by equation 2.8.¹⁵⁸ The constants μ and σ represent the mean and standard deviation of the normal distribution of $\log(x)$, respectively. The x coordinate at the centre of the peak in the PDF is the mode (i.e. the most probable value of x), and is given by equation 2.9.

$$f(x) = \frac{1}{x\sigma\sqrt{2\pi}} \exp\left(-\frac{1}{2\sigma^2}(\log(x) - \mu)^2\right) \quad (2.8)$$

$$\text{Mode} = \exp(\mu - \sigma^2) \quad (2.9)$$

Log-normal distributions can be fit to the size data using MATLAB, which can estimate the log-normal parameters μ and σ for each data set. These can be used to plot the PDFs corresponding to each dimension, and to calculate the most probable value of each dimension directly using equation 2.9. MATLAB can also return confidence intervals for these parameters, which allows uncertainties to be added to the calculated mode values (i.e. by using the largest and smallest values of μ and σ respectively to calculate the upper bound, and vice versa).

Initially, around 450, 250, and 190 measurements were made of the external diameter,

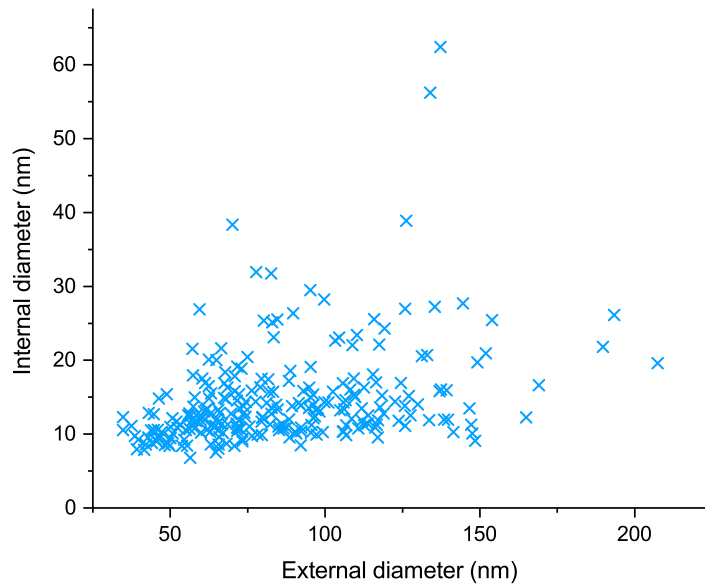


Figure 2.14: A plot of internal diameter of HNTs versus external diameter of HNTs does not seem to show a trend, hence the fact that the internal diameters of the largest HNTs cannot be measured by TEM is not taken to be an issue.

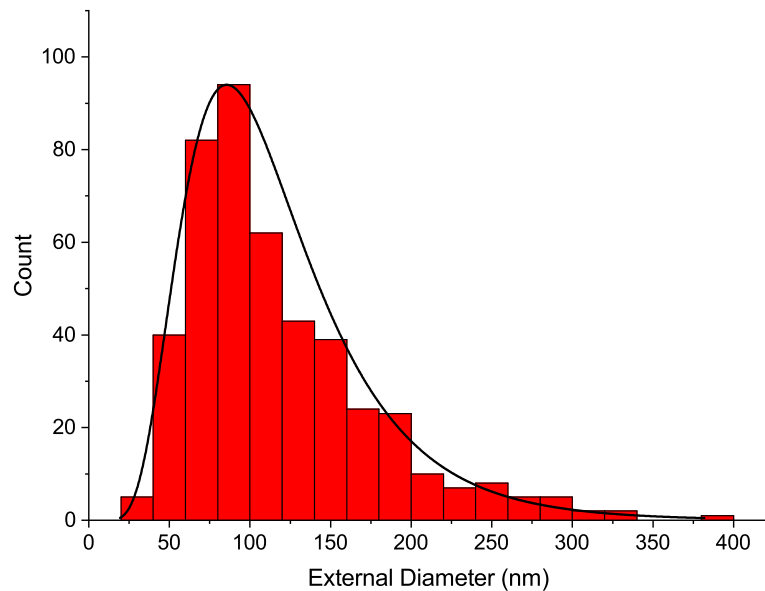


Figure 2.15: A histogram of the measured external diameters of the HNTs alongside a log-normal PDF plotted with the log-normal parameters estimated from the raw data using MATLAB.

internal diameter, and length and aspect ratio, respectively. Every attempt was made to avoid bias when selecting the nanotubes to be measured, for example by trying to make sure every discernible nanotube in an image was measured, and by keeping careful track of nanotubes which had already been measured to prevent duplicate data. However, when the nanotubes in the exact same images were measured again some time later, the obtained mode dimensions for the length, external diameter, and aspect ratio were significantly different than the original values (the reasons for re-measuring the nanotubes are discussed in Chapter 3). The internal diameter was an exception, as it was found to be similar in both measurements, which suggests that measuring this dimension is less susceptible to bias, possibly because the distribution is less broad, so it is less important if certain particles are left out. The mode dimensions and 95% confidence intervals from both sets of measurements are compared in table 2.12. From inspection of the raw length and external diameter data and the corresponding histograms (shown in the appendix), there is no obvious indication as to which set of measurements is correct. These differences illustrate how even unconscious bias can have a dramatic and unpredictable affect on the measured values of size of HNTs when measurements are carried out by hand.

Table 2.12: The mode values of the HNT dimensions and their 95% confidence intervals, found from the peaks of log-normal PDFs fitted to measurements of particles in TEM images.

Dimension	Set of measurements	Mode	Lower 95% confidence	Upper 95% confidence
Internal diameter	Old	12.1 nm	11.3 nm	12.9 nm
Internal diameter	New	11.6 nm	11.1 nm	12.1 nm
External diameter	Old	85.6 nm	79.5 nm	91.5 nm
External diameter	New	59.8 nm	55.5 nm	64.1 nm
Length	Old	486 nm	377 nm	602 nm
Length	New	164 nm	134 nm	197 nm
Aspect Ratio	Old	5.71	4.85	6.58
Aspect Ratio	New	3.42	3.04	3.81

Despite it being difficult to determine which of these two data sets is accurate, the second set of measurements (i.e. those performed later) are taken to be correct. As will be shown in Chapter 3, the second length measurement was repeatable for HNTs in several samples. In addition, more particles were measured in the second set: over 550 measurements were made of length, external diameter, and aspect ratio, and over 350 measurements were made of the internal diameter. Therefore, in the absence of an infallible means of determining the dimensions of the HNTs, the values found by hand on the second attempt using ImageJ are taken to be accurate.

The most probable values of the dimensions found for the HNTs are significantly different to the typical values for the dimensions reported by the supplier on their data sheet, i.e. a typical nanotube length of 2 μm , a typical diameter of 200 nm, a subsequent typical aspect ratio of 10, and a typical internal diameter of 20 nm. Indeed, the values found in this work make these HNTs less attractive for polymer nanocomposite applications than would be expected from the supplier data. More specifically, lower aspect ratio HNTs have a lower specific surface area for interaction with the polymer than those with a higher aspect

ratio. The large discrepancy between the sizes found in this work and the supplier data demonstrates the importance of performing independent morphological characterisation of halloysites.

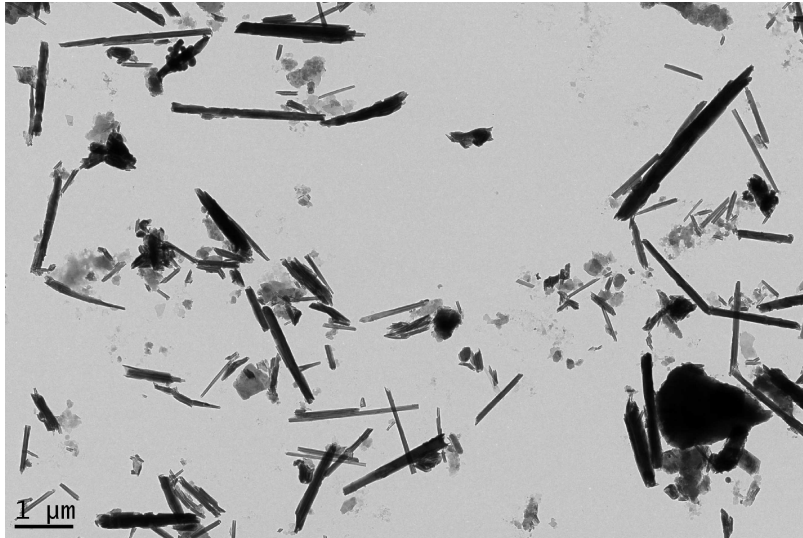
2.6.4 Automated image analysis to determine halloysite nanotube dimensions

The only solution for avoiding bias on behalf of the operator when measuring HNTs in TEM images is by automating the image analysis process. However, there are several challenges involved with automating image analysis of HNTs, namely: their polydispersity of size and shape; particle aggregation; and the presence of many non-tubular, morphological impurities. Agglomerates of particles and non-tubular particles in the TEM images will be referred to in this section as APs and NTPs, respectively.

In automated image analysis, the image is typically converted to 8-bit greyscale and then into a binary matrix using a set threshold, i.e. pixels in the image above the threshold intensity are set to 1, and vice versa. Edge finding algorithms are then able to detect objects in the image by identifying regions of connected pixels of the same values. Once objects have been identified, various object properties, including dimensions and areas, can be rapidly computed. While these operations can easily be applied to TEM images of HNTs, problems arise as soon as the images have been converted to binary. Specifically, in binary images, individual HNTs cannot be separated from APs, and it can be difficult to distinguish between HNTs and NTPs of a similar size and shape. This is illustrated in figure 2.16. Extensive filtering of the objects is necessary to minimise the number of NTPs and APs measured. However, care has to be taken to avoid applying too much filtering and artificially altering the measured size distributions of the HNTs, which would defeat the purpose of automating the image analysis process in the first place.

Despite these difficulties, there are at least two examples in the literature of automated size measurements of HNTs being attempted; Hillier *et al.* used ImageJ to semi-automate the process of analysing HNT lengths and diameters in SEM images,⁴ and, more recently, Koivisto *et al.* used a python-based automated image analysis toolbox to ascertain the number of HNTs released as an aerosol during sample processing which were above a length and aspect ratio deemed to be critical for predicting their potential respiratory hazard.⁷⁹ Examining their methods can be used as a starting point for automating the process of analysing images of HNTs.

Koivisto *et al.* chose a global threshold value for their images, and used this to automatically convert them to binary.⁷⁹ Objects with an area smaller than 10 pixels were deemed to be noise, and were removed. Particles in the images were then identified, and fitted with a bounding box (i.e. the smallest rectangle that can fully contain the object). The lengths and aspect ratios of these bounding boxes were taken to be those of the HNTs. This may be inaccurate as a measure of the HNTs dimensions, since a rectangular bounding box is only a crude approximation of the shape of a HNT. In addition, and more significantly, this does not serve to distinguish APs or NTPs from the HNTs. However, they were only concerned with the length and aspect ratio of the aerosol particles as they pertained to hazard. That is to say, they were concerned with the number of aerosol particles that had length and aspect ratio above the critical values for respiratory hazard ($2 \mu\text{m}$ and 3,



(a)



(b)

Figure 2.16: TEM images of HNTs before (a) and after (b) the image has been converted to a binary matrix using a user-defined threshold, and then inverted. In binary images, APs appear as a single object, and it is difficult to distinguish between HNTs and NTPs of a similar size and shape. It should be noted that inversion (i.e. transformation of dark pixels in binary from 0 to 1, and vice versa) is required for the operation of MATLAB's edge finding algorithms.

respectively), and these were few enough in number to allow for individual inspection of each one to identify what type of particle they were.⁷⁹

In a somewhat different approach, Hillier *et al.* manually adjusted the threshold on each image in ImageJ, before converting it to binary and fitting ellipses to the HNTs.⁴ The obtained width and length distributions of the HNTs were simply taken as those of the fitted ellipses. For each image, they conducted a manual survey to identify the largest and smallest HNTs, and used the dimensions of these as limits to filter the objects detected by the software. The upper size limit served to filter out APs, and the lower limit filtered out both noise and NTPs. They also removed any objects with an aspect ratio less than 1.5, however it is feasible that this filter erroneously removed HNTs; for example, about 3% of the HNTs measured in section 2.6.3 had an aspect ratio lower than this. Using their semi-automated method, they were able to measure a large number of nanotubes in several different HNT samples. However, they do not discuss the error inherent in approximating the shape of the HNTs to ellipses, and they do not discuss whether ignoring nanotubes in APs could have skewed the measured distributions; this is feasible, since the largest nanotubes would be expected to be more likely to form part of an AP simply because they have a larger area, and would statistically have a higher chance of colliding with other particles. Nonetheless, their work⁴ was taken as a starting point for the automated image analysis of HNTs carried out here.

Basic image analysis using MATLAB

While Hillier *et al.* used ImageJ to perform particle size analysis,⁴ MATLAB was used here. MATLAB has a variety of image processing tools which are relatively straightforward to use, and has the advantage of being quicker than ImageJ since it requires less user input for each image. It also has increased reproducibility compared to ImageJ, as there may be differences in the judgement of two different operators who are applying manual processing steps to images in ImageJ (e.g. manual thresholding). The general logic of the MATLAB image processing algorithm is outlined in figure 2.17, and images illustrating several of the intermediate processing steps are shown in figure 2.18. It should be noted that the scale bar has been left in these images, and hence has been identified/measured as an object, but it can easily be removed or masked.

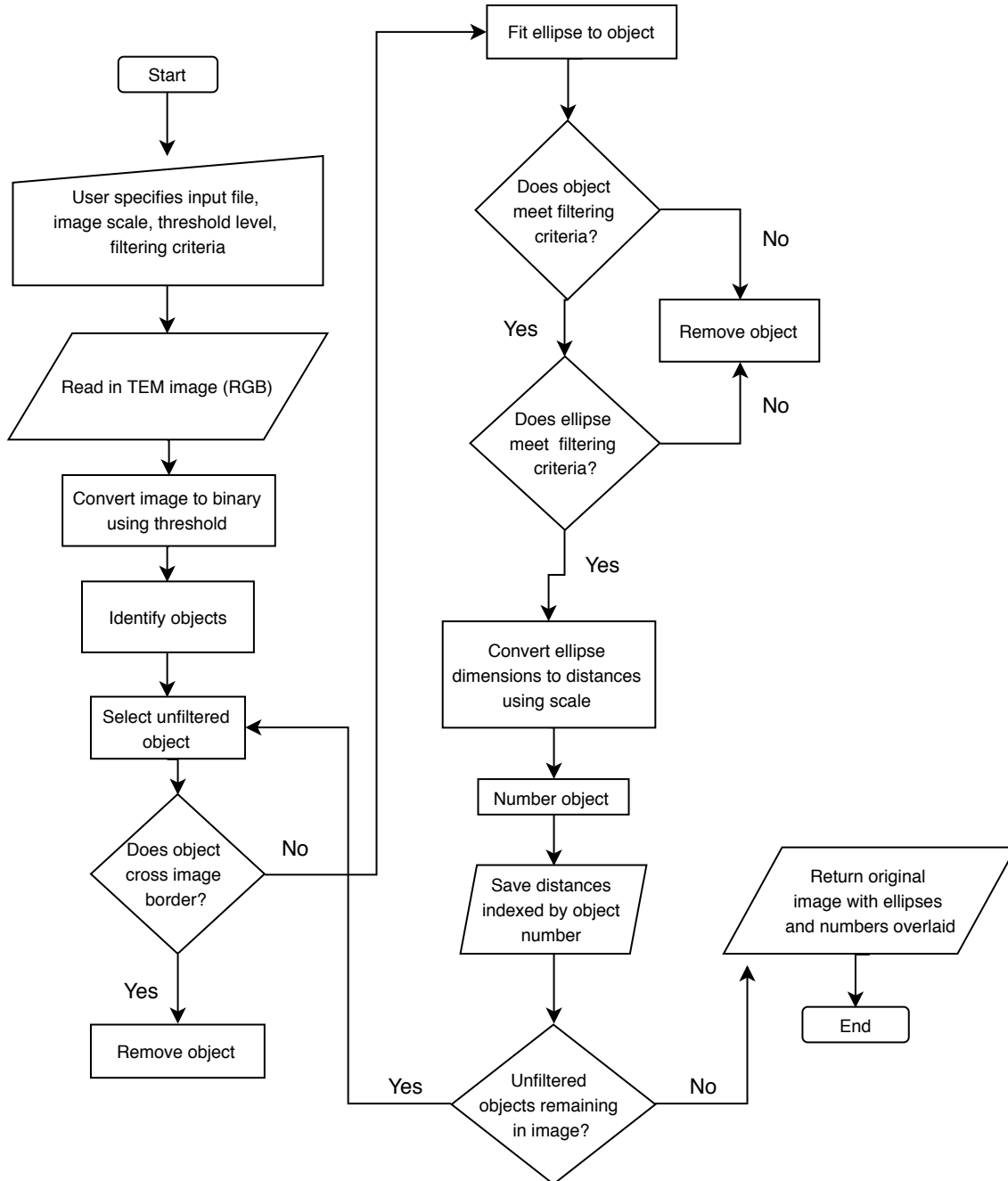


Figure 2.17: A flowchart illustrating a simplified version of the general logic behind the image processing carried out in MATLAB.

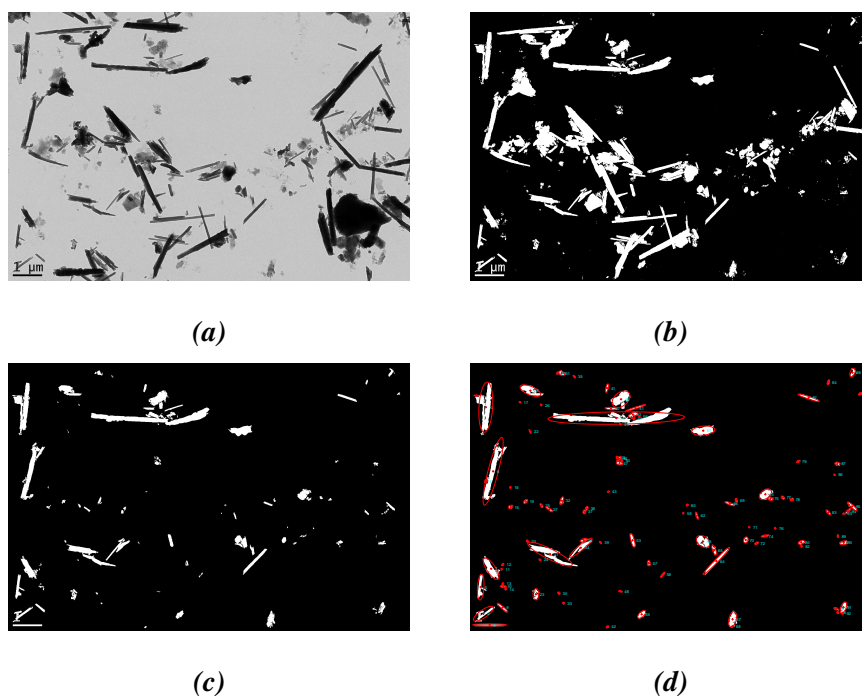


Figure 2.18: Images of successive steps in the MATLAB image processing algorithm used to automate measurement of HNT dimensions: (a) the original image; (b) the image after binary conversion and clearing of border objects; (c) the image after removal of objects with a size-and-shape-based filter; and (d) the image after the indexing of and fitting of ellipses to the remaining objects.

An example of a final image output from this process is shown in figure 2.19. The objects in this image were filtered such that those that remained had a minimum area of 100 pixels, a width of between 20 and 500 nm, and a fitted ellipse with a minimum eccentricity of 0.7. The eccentricity of an ellipse is the ratio of the distance between its foci and its length (equation 2.10); for a circle, this value is 0, and it approaches 1 as the ellipse becomes increasingly elongated, i.e. it is a similar measure to aspect ratio. Applying a filter based on object eccentricity can therefore remove spherical objects (which will not be nanotubes). Applying a minimum area filter serves to remove noise and smaller artefacts on the TEM grid. The width restriction is based on the fact that the maximum width of a nanotube measured in any of the images was around 370 nm, and the minimum was 21 nm (which is also close to the internal diameter of the nanotubes). It can be seen in figure 2.19 that filtering based on these criteria does remove many of the large APs and NTPs, as well as many of the background artefacts. However, many APs (e.g. objects 4, 6, and 28 etc.), and NTPs (e.g. 55, 70 etc.), remain in the image. In fact, for the example of the image shown in figure 2.19, 97 objects remain after the filtering criteria have been applied, of which 28% are APs, 53% are isolated NTPs, and only 19% are isolated HNTs. In addition, the range of widths and eccentricities for the remaining objects all overlap, as shown in figure 2.20. It is therefore clear that using object sizes and aspect ratios as filtering criteria is not suitable for automatically identifying isolated HNTs in TEM images.

$$\text{Eccentricity} = \frac{\text{Distance between ellipse foci}}{\text{Ellipse length}} \quad (2.10)$$

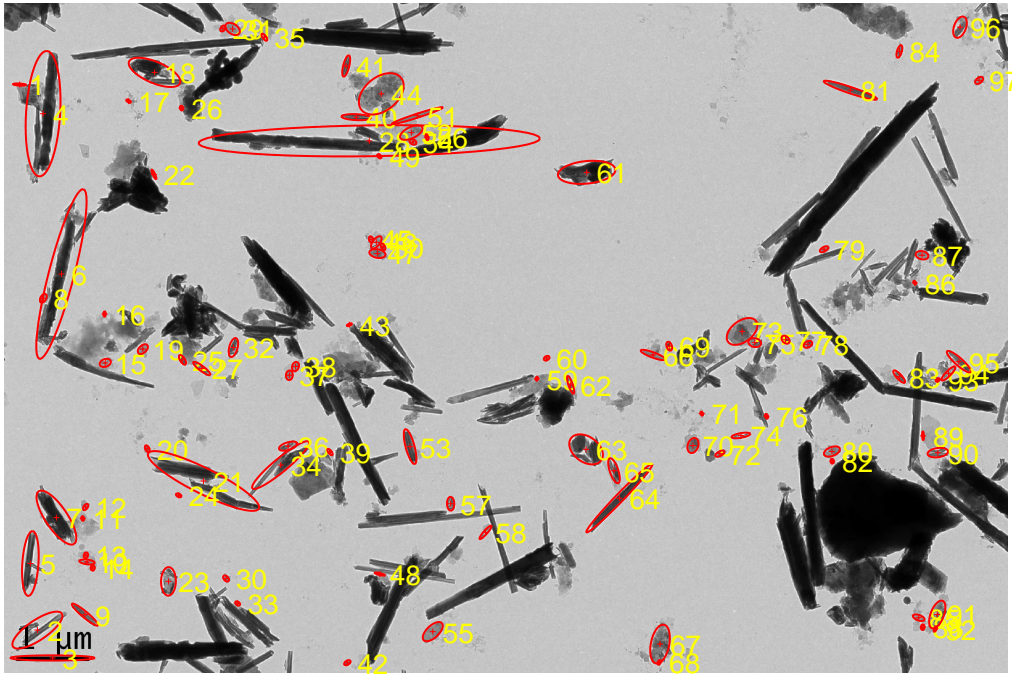


Figure 2.19: An example of a TEM image of HNTs analysed automatically using MATLAB.

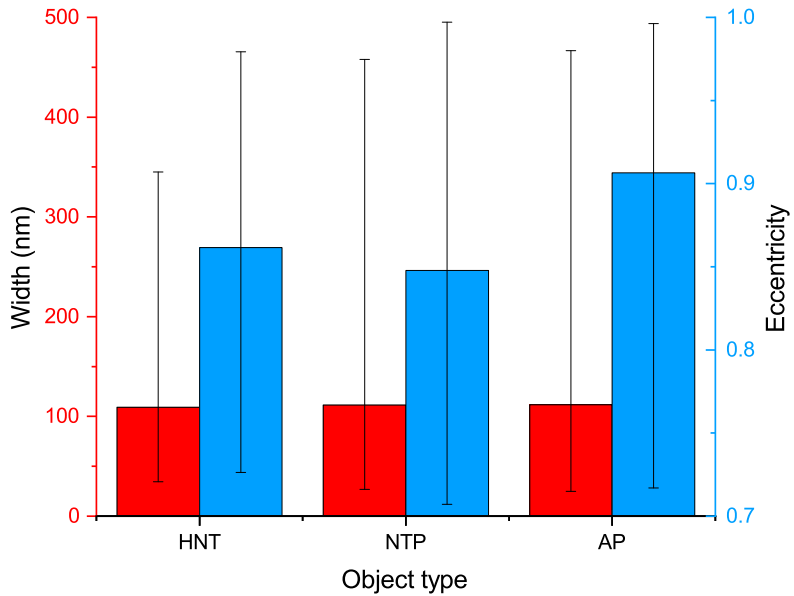


Figure 2.20: A graph illustrating how the values for width and eccentricity overlap for all of HNTs, NTPs, and APs. The columns are average values, and the error bars represent the ranges of each value.

Despite the algorithm's inability to automatically identify isolated HNTs, where there are such particles, it has detected them and appeared to fit them well with ellipses (e.g. objects 9, 64, 81 etc. in figure 2.19). A magnified image of object 81 is shown in figure 2.21 as an example of a HNT which has been well-fitted with an ellipse.

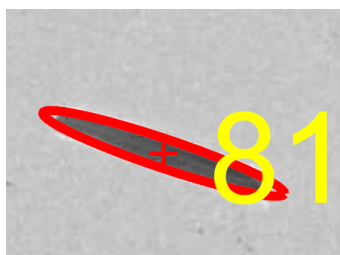


Figure 2.21: An example of a HNT which has been fitted with an ellipse by MATLAB. The ellipse appears to approximate the dimensions of the HNT well.

The dimensions of the ellipses fitted to the isolated HNTs by MATLAB can be compared to those found by hand in ImageJ for the same nanotubes (i.e. the true values). Doing so across all of the TEM images reveals that the dimensions of the ellipses are almost always an overestimate of the true dimensions of the nanotubes (figure 2.22). However, when the true value is plotted against the ratio of the ellipse value to the true value for each dimension, it can be seen that there is no apparent trend (figure 2.23). In practical terms, this suggests that it would be reasonable to adjust the dimensions of a nanotube of any size by the average overestimation, propagating the associated uncertainty when necessary. An example for nanotube length is given in equation 2.11, where the length of a single tube found by MATLAB is adjusted by the average overestimation of length by MATLAB (i.e. $(8 \pm 4)\%$). Were a large enough number of nanotubes well separated from other particles, then it should therefore be easy to accurately find their dimensions by fitting ellipses to them in MATLAB and adjusting the ellipse dimensions to account for the overestimation of nanotube size.

$$\text{True nanotube length} = \frac{\text{Length found by MATLAB}}{(1.08 \pm 0.04)} \quad (2.11)$$

Advanced filtering criteria for identifying HNTs

As discussed, the simple filtering criteria outlined thus far serve to remove many of the larger APs and NTPs from TEM images of HNTs, but many smaller APs and NTPs remain in the images. More advanced filtering criteria are clearly required to remove these objects from the TEM images.

Since the ellipses fitted to the APs seem to contain more empty space than those fitted to single particles (e.g. object 6 in figure 2.19), it was thought that this might provide useful criteria for at least removing APs from the images. However, while both the difference between ellipse area and object area and the ratio of ellipse area to object area are generally smaller for isolated HNTs than APs and NTPs, the ranges of these values for all types of object overlap (figure 2.24). That is to say, were objects filtered using a minimum value of either of these quantities, some isolated HNTs might be erroneously removed.

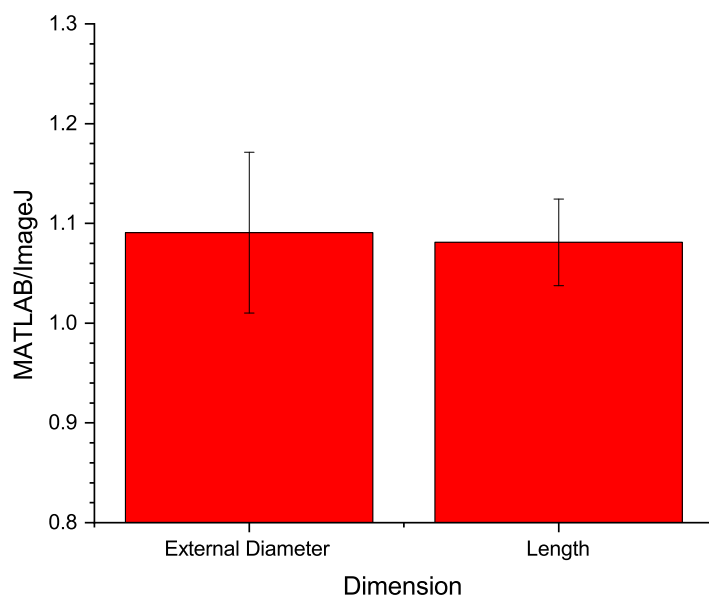


Figure 2.22: The average ratios of the external diameters and lengths of the HNTs calculated by MATLAB versus those measured in ImageJ. MATLAB overestimates the dimensions because it approximates the shape of the nanotubes using ellipses. The error bars represent standard deviation.

Therefore, comparing the areas of the objects versus those of their fitted ellipses cannot be used as a filtering criteria for identifying isolated HNTs.

Similarly, the circularity of the objects in the images cannot be used to distinguish between HNTs, NTPs, and APs. Circularity is a measure of a 2D shape's compactness, and is computed for an object by MATLAB using equation 2.12, where A and P are the object's area and perimeter, respectively. For a perfect circle, this value is 1, and it approaches 0 with decreasing compactness (i.e. the less 'circular' the object is). Since APs in particular appear to have larger perimeters relative to their areas, it was thought that filtering objects by circularity might be a useful way to at least remove these from the images. Figure 2.25 shows the mean circularities of all of the types of objects remaining in the TEM image after filtering (i.e. all of the indexed objects in figure 2.19). It can be seen that these are similar for all types of object, and their ranges overlap to a significant degree. Therefore, any filtering based on circularity would either leave unwanted objects in the image, or erroneously remove isolated HNTs.

$$\text{Circularity} = \frac{4\pi A}{P^2} \quad (2.12)$$

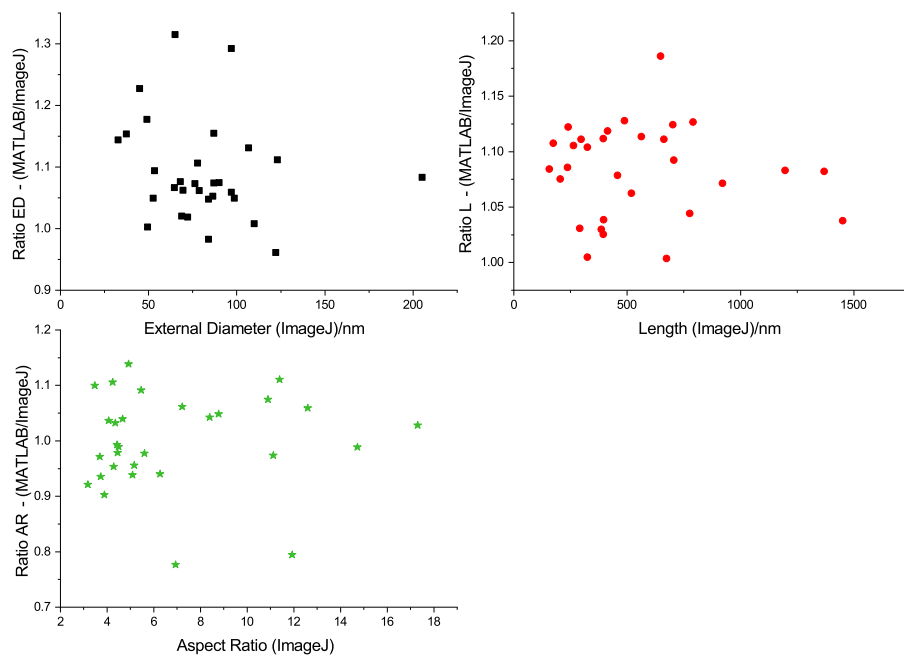


Figure 2.23: Plots of the HNT dimensions measured by ImageJ against the ratio of the value measured by MATLAB to the value measured by ImageJ for each dimension. There does not seem to be a trend, which suggests that the degree to which the MATLAB value differs from the ImageJ (i.e. true) value does not depend on the size or shape of tube being measured.

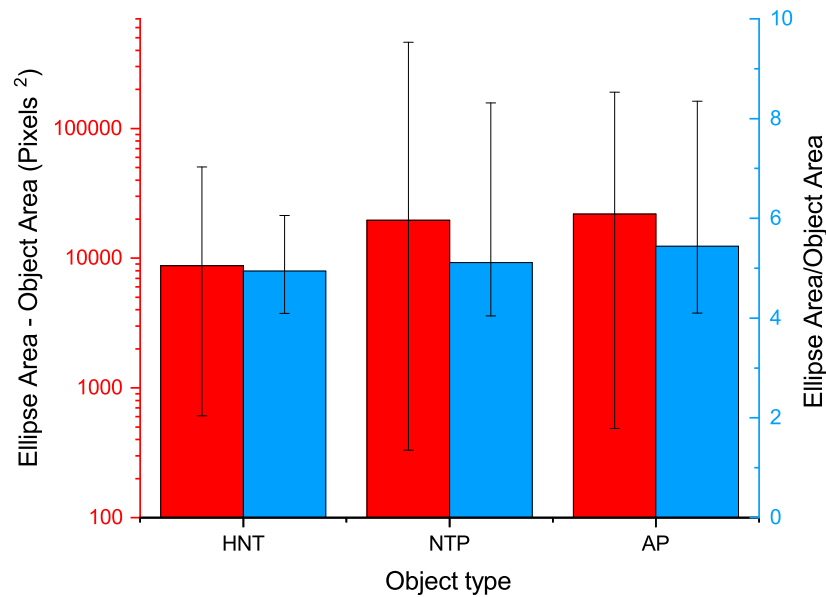


Figure 2.24: A comparison of the areas of the objects and corresponding fitted ellipses for all of HNTs, NTP, and AP. The error bars represent the ranges of each value.

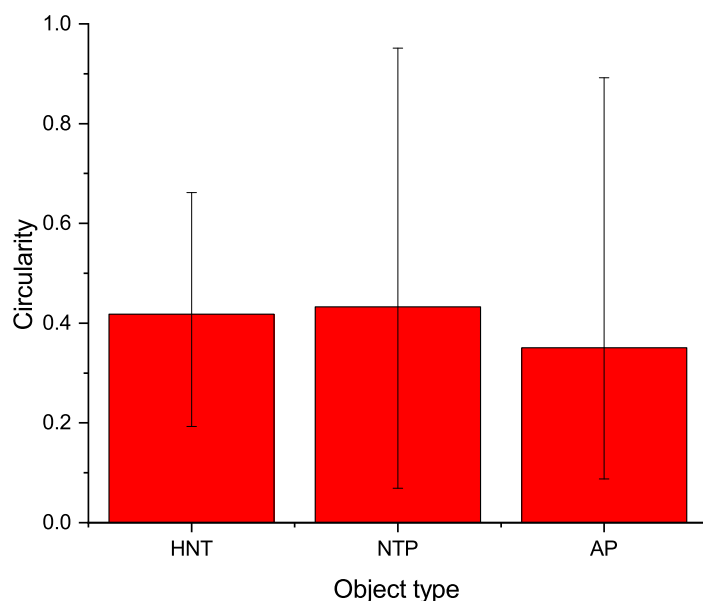


Figure 2.25: The mean circularities for the various types of particle found in TEM images of HNTs. The error bars show the range of values. The ranges overlap for all three types of particle.

The applicability of the Beer-Lambert law to HNTs in TEM images

It is clear that there is no simple, geometrical property which can be used to automatically distinguish isolated HNTs from the other types of objects in TEM images. However, there is one feature in the TEM images that is unique to the isolated HNTs: if a line is drawn across a HNT perpendicular to its length, the pixel intensity along the line rises and falls almost symmetrically as the line crosses the tube walls and internal diameter. This is illustrated in figure 2.26. Indeed, this type of intensity profile was used by Gommès *et al.* to fit the internal and external diameters of multi-walled carbon nanotubes (CNTs) in TEM images.³ In doing so, they were able to not only measure the diameters of their nanotubes, but also identify when a ‘parasitic’ object was present and had affected the object measurement; these objects could subsequently be discarded. The existence of this type of intensity profile for the HNTs therefore appeared promising for removing all objects apart from isolated HNTs from the TEM images.

To find the pixel intensity across the whole width of a nanotube, a Euclidean distance transform must first be applied. A Euclidean distance transform of a binary image calculates the Euclidean (i.e. straight line) distance from every dark (i.e. 0) pixel to its nearest bright (i.e. 1) pixel. This process is illustrated for a simple matrix in figure 2.27. In a binary image where objects are represented by dark pixels (e.g. after conversion of the initial TEM image to binary, but before it has been inverted to allow for edge detection), the distance transform can be used to assign each pixel in the object a distance to the edge of the object. When such a matrix is displayed as an image, the centre of the object appears brightest, and pixels become progressively darker towards its edge. An example of a distance transform carried out on an isolated HNT is shown in figure 2.28. It should

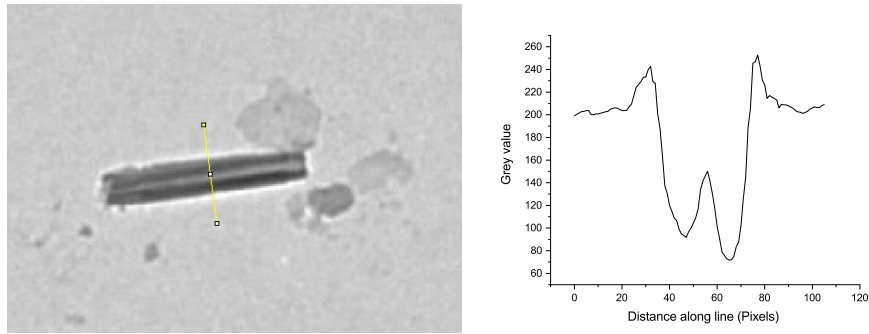


Figure 2.26: Pixel intensity against distance for a line drawn across the width of a HNT in a TEM image. The intensity varies almost symmetrically across the tube; this feature is unique to the HNTs in the images.

be noted that the distance transform method only works for images containing a single object, but it is relatively straightforward to split an image containing many objects into a series of images containing only one object each using MATLAB's image processing toolbox.

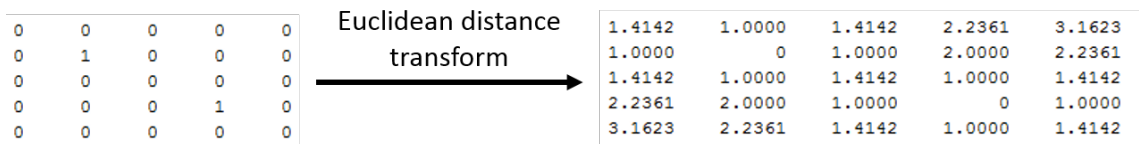


Figure 2.27: An example of a Euclidean distance transform for a simple matrix. The value of each pixel is changed to the straight line distance between it and its nearest non-zero pixel neighbour in the original binary matrix.

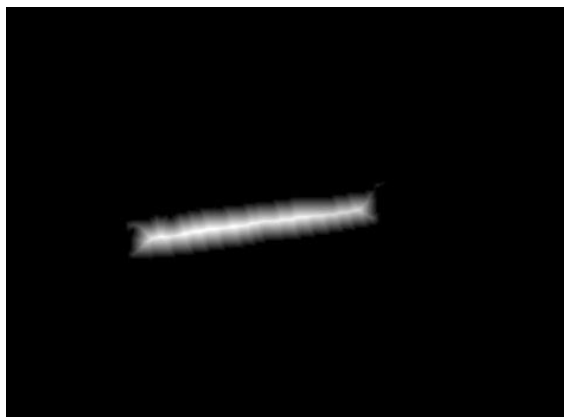


Figure 2.28: An example of a Euclidean distance transform for an isolated HNT.

After a distance transform has been applied to the image, sets of pixels with unique distance values can be identified, and their corresponding grey values can be retrieved from the original image. Averaging the pixel intensities for each unique distance then allows intensity to be found as a function of distance from the centre of the object. The distance can easily be converted from pixels to nm using the image scale, but it was left in pixels here since cropping and enlarging the particles from the original TEM images for

individual analysis changed the scale of each image by an unknown degree. It should be noted that the distance transform returns a scalar value for each pixel, which means that the outcome of this process is an average of pixel intensities in both directions away from the centre of the object. This is problematic when the intensity profile across the tube is not perfectly symmetrical (e.g. in figure 2.26). Figure 2.29 compares the intensity profile across the same HNT found by hand in ImageJ, and by carrying out a distance transform in one direction using MATLAB.

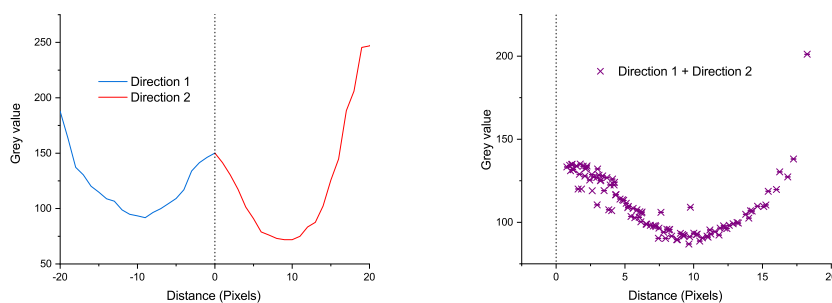


Figure 2.29: *The intensity profile across a HNT as found by hand across one width of the HNT in ImageJ, and by carrying out a distance transform in one direction on the same HNT using MATLAB. This distance transform returns a scalar value of distance, so the right-hand graph contains intensities from both directions away from the centre of the nanotube, which cannot be separated.*

To find the pixel intensity as a function of distance in both directions from the centre of a HNT, the image skeleton must be found. For a HNT, this is essentially a straight line, one pixel in diameter, running down the centre of the tube (figure 2.30). MATLAB’s ‘imgradient’ function can be used to assign a positive value to all pixels on one side of this line, and a negative value to those on the other side. Separately retrieving pixels with negative and positive gradients in the imgradient matrix from the distance-transformed matrix then allows pixel intensity versus distance to be plotted in both directions away from the centre of the nanotube. An example of this plot is also shown in figure 2.30. The intensity profile found using a distance transform in two directions from the HNT skeleton is similar to that found by hand in ImageJ, but it is a better representation of the nanotube as a whole as it takes into account the full length of the nanotube.

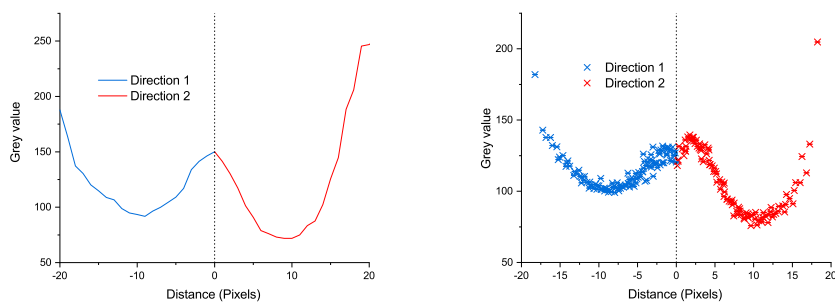
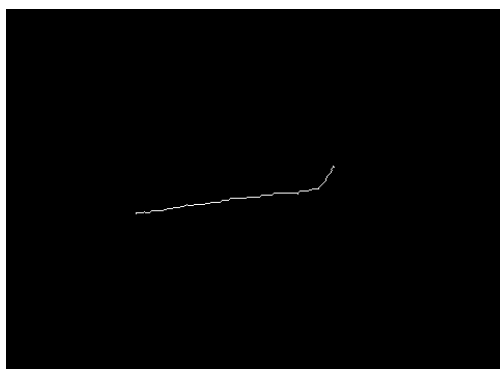


Figure 2.30: The skeleton of a binary image of an isolated HNT (top), and the intensity profile across the same HNT as found by hand in ImageJ, and by carrying out a distance transform in two directions from the image skeleton using MATLAB (bottom).

This process was carried out for three additional isolated HNTs. It can be seen in figure 2.31a that the two which were translucent to the electron beam had similarly shaped intensity profiles across their diameters. However, for an isolated HNT which is so thick that it is opaque to the electron beam across its internal diameter (figure 2.31b), the intensity profile across its width is slightly different to translucent HNTs; there is no peak in intensity at the centre of the tube. When the process is applied to an isolated NTP or an AP, the resulting intensity profiles are significantly different to those observed for both translucent and opaque HNTs. Two examples are shown in figure 2.32. This suggests that the shape of the intensity profiles found via distance transforms of the objects in the images might be able to be used to distinguish isolated HNTs from NTPs and APs.

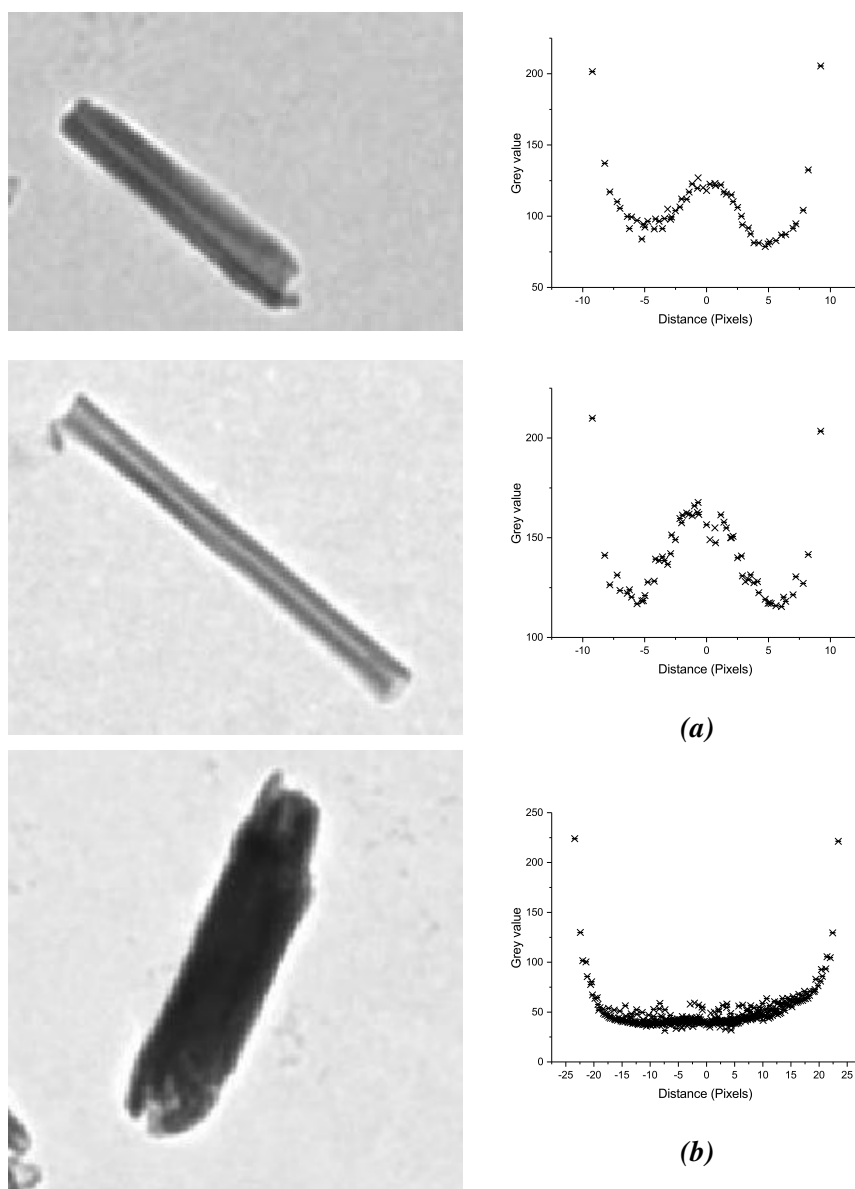
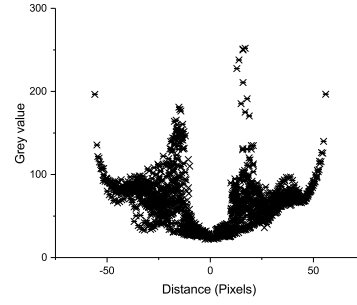
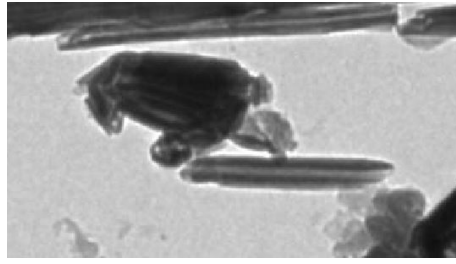
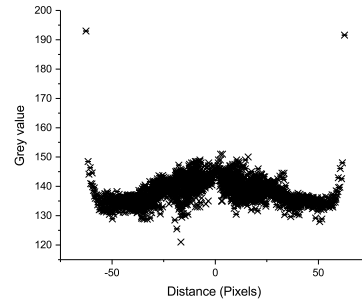
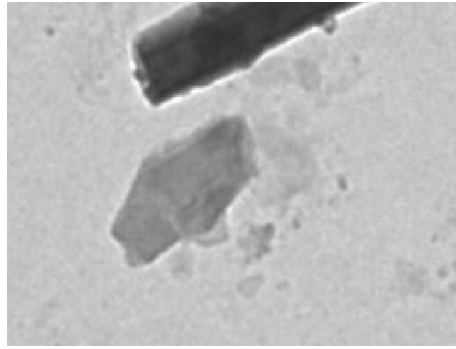


Figure 2.31: The intensity profiles for three further examples of isolated HNTs. The two translucent HNTs (a), both show a similar intensity profile to the first HNT analysed, but the opaque HNT (b) does not have an intensity rise across its centre.



(a)



(b)

Figure 2.32: Examples of an AP (a) and an NTP (b) alongside their corresponding intensity profiles found using a Euclidean distance transform.

In their work, Gommès *et al.* fitted the intensity profile of the CNTs by using the Beer-Lambert (BL) law to model the absorption of electrons by a hollow, cylindrical tube.³ The BL law describes the attenuation of incident radiation (in this case electrons) by a medium. For a single particle, the degree of attenuation of the radiation can be given by equation 2.13, where I is the intensity of the transmitted radiation, I_0 is the intensity of the incident radiation, l is the thickness of the particle over which the radiation has travelled, and k is a material-specific constant (the absorption coefficient).³

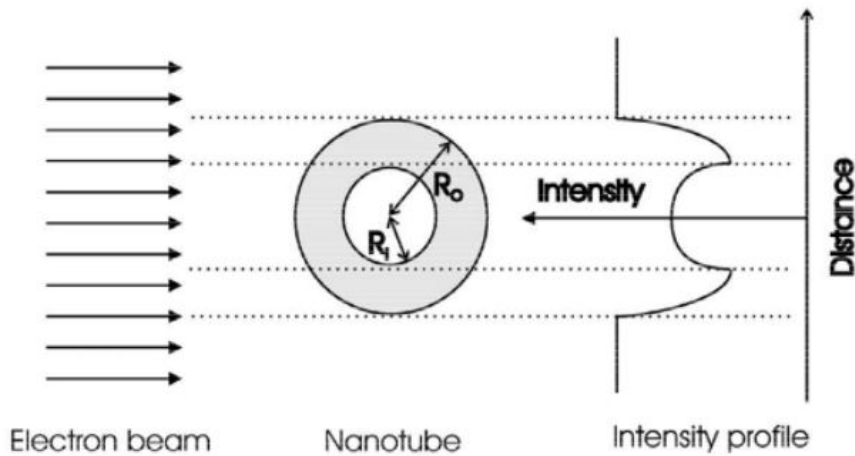
$$\log\left(\frac{I}{I_0}\right) = -kl \quad (2.13)$$

To fit the BL law to their data, Gommès *et al.* calculated l as a function of the distance from the nanotube centre (d), and the nanotube's internal (R_i) and external (R_o) radii, and substituted this into equation 2.13. More specifically, they describe the variation in intensity of the transmitted electron beam across the nanotube using equations 2.14, 2.15, and 2.16. The shape of these functions is illustrated in figure 2.33a. In figure 2.33a, there is a sharp transition in the intensity gradient at the edge of the hollow interior. However, in experimental data, this transition is blurred, presumably by gaussian noise, giving rise to smoother intensity changes. Despite this, Gommès *et al.* found the model sufficient to fit the intensity profiles across their CNTs, as shown in figure 2.33b.³

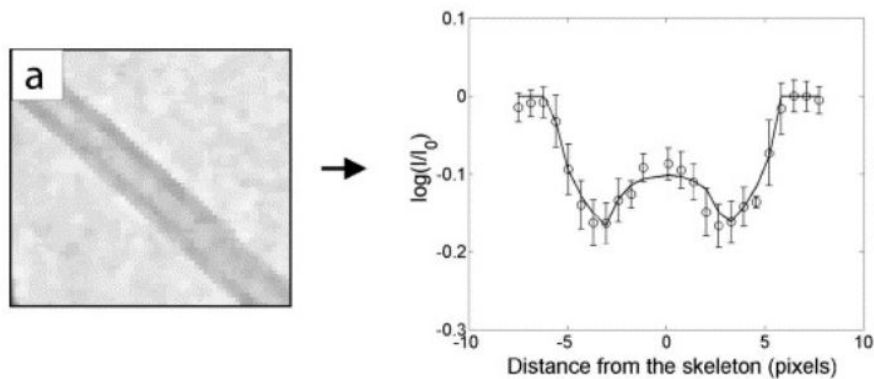
$$-\log\left(\frac{I}{I_0}\right) = 0 \quad \text{if } d > R_o \quad (2.14)$$

$$-\log\left(\frac{I}{I_0}\right) = 2kR_o\sqrt{1 - \left(\frac{d}{R_o}\right)^2} \text{ if } R_o \geq d \geq R_i \quad (2.15)$$

$$-\log\left(\frac{I}{I_0}\right) = 2k\left(R_o\sqrt{1 - \left(\frac{d}{R_o}\right)^2} - R_i\sqrt{1 - \left(\frac{d}{R_i}\right)^2}\right) \text{ if } R_i > d \quad (2.16)$$



(a) A cartoon illustration of the absorption of an electron beam by a hollow cylinder. Image reproduced with permission.³



(b) An example of the model used by Gommes et al. fitted to data from an image of a CNT.³ Image adapted with permission.³

Figure 2.33: Gommes et al. used the BL law to model the absorption of electrons of their CNTs in TEM images, and could use this to fit the intensity profiles found using distance transforms of the nanotubes.³

It should be possible to carry out a similar fitting process for isolated HNTs, but this model would clearly not be a good fit for APs or NTPs. Therefore, fitting this model to the intensity profiles of each object in a TEM image of HNTs might be a suitable way for discriminating isolated HNTs from other objects, i.e. objects could be discarded if the quality of this fit was too poor.

Fitting the Beer-Lambert law to HNTs in TEM images using nonlinear least squares regression

Gommes *et al.* fitted equations 2.15 and 2.16 to their data using nonlinear least squares regression carried out in MATLAB.³ Nonlinear least squares regression is a computational technique which aims to produce the best fit of a nonlinear mathematical model to experimental data. More specifically, the regression algorithm seeks to minimise the sum of squared residuals (SSE) of the fit in successive iterations until either a minimum is found (i.e. the fit converges), or the maximum allowable number of iterations is reached.¹⁵⁹ The residuals of the fit are the differences between the data (y) and the fit (\hat{y}) at each value of x , i.e. equation 2.17.¹⁶⁰ The SSE is then given by equation 2.18.¹⁶¹ To some extent, the goodness of the resulting fit (i.e. how closely the model matches the data) can be determined by inspection of the fitted function in comparison to the data, and/or inspection of a plot of the residuals against x . If the model is a good fit, the fitted function should be close to most of the data points, and the residuals should be randomly distributed around zero.¹⁶²

$$\text{Residual} = y - \hat{y} \quad (2.17)$$

$$\text{SSE} = \sum_{i=1}^n (y_i - \hat{y}_i)^2 \quad (2.18)$$

The goodness of a fit can be quantified using its root mean squared error (RMSE). The RMSE is the square root of the mean squared error (MSE), which is calculated as shown in equation 2.19.¹⁶¹ The ν in this equation is the residual degrees of freedom, which is calculated as shown in equation 2.20, where n is the number of data points, and m is the number of coefficients being fitted to the data.¹⁶¹ The closer the RMSE is to 0, the better a fit the model can be concluded to be for the data. An alternative measure of goodness of fit is the coefficient of determination, or R^2 . To find this value, the total sum of squared errors of the fit (SST) must first be calculated using equation 2.21, where \bar{y} is the mean of all of the values of y .¹⁶¹ R^2 is then obtained using equation 2.22.¹⁶¹ R^2 is a value between 0 and 1, and, in general, the closer it is to 1, the better the model fits the experimental data. However, it must be acknowledged that R^2 values for nonlinear models are known to not always be valid,¹⁶⁰ so they are reported here with the caveat that they are not necessarily the most reliable indicator of goodness of fit. Nonetheless, reporting R^2 alongside RMSE should allow for the comparison of the quality of the BL law fit to the intensity profile in TEM images of different particles. The values of both the R^2 and RMSE of a fit are obtainable using MATLAB.

$$\text{RMSE} = (\text{MSE})^{\frac{1}{2}} = \left(\frac{\text{SSE}}{\nu}\right)^{\frac{1}{2}} \quad (2.19)$$

$$\nu = n - m \quad (2.20)$$

$$\text{SST} = \sum_{i=1}^n (y_i - \bar{y})^2 \quad (2.21)$$

$$R^2 = 1 - \frac{SSE}{SST} \quad (2.22)$$

Nonlinear regression algorithms require the input of first estimates of the to-be-fitted variables in order to provide the computer a point from which to start iteration. These estimates need to be reasonably accurate, otherwise the algorithm can arrive at a local rather than global error minimum, and subsequently output incorrect values.¹⁵⁹ In this case, estimates are required for the variables k , R_o , and R_i . Gommel *et al.* suggested determining these estimates in the following ways: for R_o , the first estimate should be half the ratio of the object area to its length; for R_i , the first estimate should be the distance at which the minimum intensity (I_{\min}) is observed; and for k , the first estimate should be calculated using equation 2.23, which is obtained from equation 2.16 by setting $d = R_i$ and $I = I_{\min}$. For the incident intensity, I_0 , the average intensity of the background pixels is used.

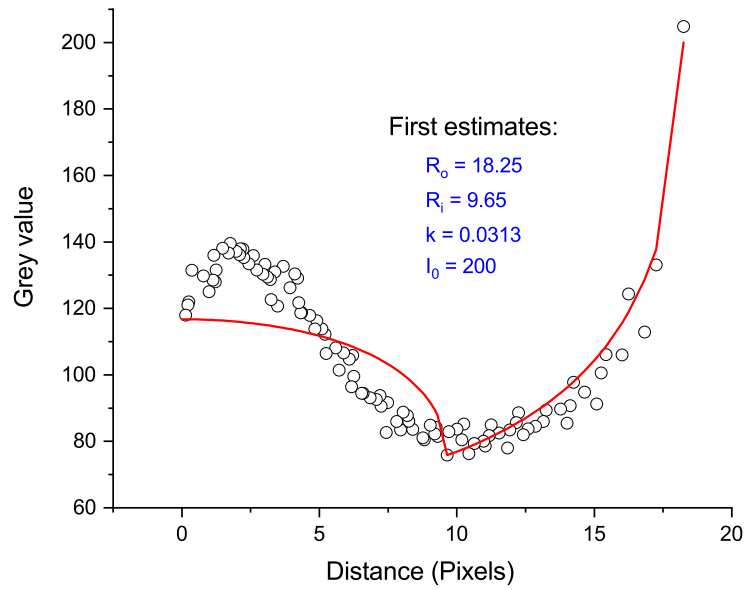
$$k = -\frac{\log\left(\frac{I_{\min}}{I_0}\right)}{2\sqrt{R_o^2 - R_i^2}} \quad (2.23)$$

For the HNTs, estimates of R_i and k were found as suggested by Gommel *et al.*³ However, the first estimate of R_o was taken simply as the maximum value of the distance transform in the relevant direction. After manual inspection of background pixels in ImageJ, the value of I_0 was taken to be 200. For the intensity profile of the HNT shown in figure 2.26, figure 2.34a shows how well equations 2.15 and 2.16 fit the data when these first estimates of the variables are used. It can be seen by inspection that the equations give a reasonable approximation of the data, especially towards the tube exterior.

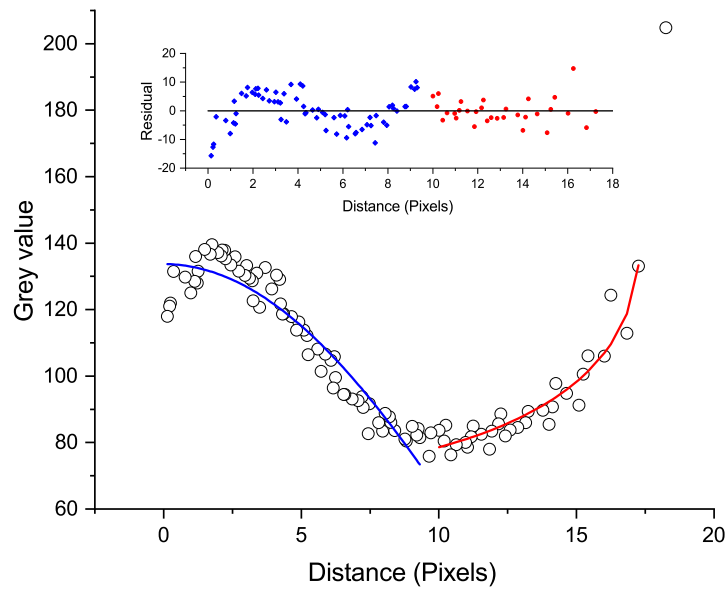
Using these estimates as starting parameters, equations 2.15 and 2.16 were then fit to the same data using nonlinear least squares regression in MATLAB's curve fitting app. Each equation is fit separately to the other over the appropriate distance range. It should also be noted that I_0 was fitted as an additional variable (with a first estimate of 200), rather than kept constant as was done by Gommel *et al.*³ This is because the intensity of the incident electron beam was unknown, and because it was also unknown whether the electron beam intensity was uniform or whether the carbon coating on the grid was uniformly thick. The results of the fit are shown in figure 2.34b.

From simple inspection of the fits and their corresponding residuals in figure 2.34b, it appears that the model fits the tube walls (i.e. $R_i \leq \text{distance} \leq R_o$) well, and the tube interior (i.e. $\text{distance} \leq R_i$) less well. Indeed, the fit for the tube interior does not converge even over 10,000 iterations, whereas the fit for the wall region converges within 400 iterations. In addition, while the fits for the separate distance regions have comparable R^2 and RMSE, they return very different values for the variables, which are given in table 2.13. The fit for the tube interior in particular returns values which are far from the starting estimates.

Based on table 2.13, inspection of the fit and its residuals, and the fact that the fit did not converge, it is clear that the model described by Gommel *et al.* is not a good fit for pixel intensity across the hollow interior of HNTs in TEM images. This could be due to the fact that the internal diameter of the tube varies too significantly across its length, or because Gaussian noise (overlooked by Gommel *et al.*³) has too large an effect on the



(a)



(b)

Figure 2.34: The actual pixel intensity across a HNT in a TEM image plotted alongside a) the theoretical intensity calculated using first estimates of its radii and absorption coefficient, and b) the result of fitting equations 2.15 and 2.16 to the data using nonlinear least squares regression, including the fit residuals.

Table 2.13: The initial and final variables from fitting an isolated HNT in a TEM image using the BL law.

Variable	First estimate	Fit: Distance $\leq R_i$	Fit: $R_i \leq$ Distance $\leq R_o$
R^2	n/a	0.91	0.89
RMSE	n/a	5.20	4.55
R_i	9.65 pixels	14.36 pixels	n/a
R_o	18.25 pixels	35.31 pixels	17.28 pixels
I_0	200	43380	139.1
k	0.03	0.14	0.02

shape of the function to be ignored. However, the variables found by fitting their model³ to the nanotube's walls were close to both the initial parameter estimates, and the actual values; for comparison, the R_o found for the tube in the image using ImageJ was 20.32 pixel, which was close to the value of 17.28 pixel found by fitting. Therefore, this model can be concluded to at least be a good fit for the transmitted intensity across the nanotube walls.

Initially, it was thought that the unique intensity peak across the centre of the HNTs could be used as a criterion for distinguishing isolated HNTs from other particles. However, as has been shown, this region is difficult to fit satisfactorily. Nonetheless, the model for the tube walls might still be expected to be a better fit for tubular particles than NTPs and APs, so it was thought that the goodness of this fit might still be a useful criterion for differentiating the different classes of particle. For example, the logic of the algorithm shown in figure 2.17 could be altered with the insertion of the routine outlined in figure 2.35 (i.e. after the image borders have been cleared, but before ellipses have been fitted). To explore this possibility, the model for the tube walls was first applied to the additional isolated HNTs shown in figure 2.31, before being applied to the NTP and AP shown in figure 2.32, as well as two further examples of each. The R^2 and RMSE values for the isolated HNTs versus those the other types of particle are shown in figure 2.36.

In general, the R^2 values for fitting the BL model are much lower for APs and NTPs, and the RMSE values are much higher, meaning that the model fits these particles much more poorly than isolated HNTs. Two examples of poor fits for the NTPs and APs are shown in figure 2.37 to illustrate where the cylinder model deviates from their intensity data. However, while the model produced a poor fit for all of APs, it managed to fit the intensity data for one of the NTPs with an R^2 of 0.86, which is very close to that of the HNTs (the lowest for a HNT was 0.87), and an RMSE of 3.76, which is lower than that for all but one of the HNTs. This NTP alongside its fitted intensity profile is shown in figure 2.38. The fact that one of the NTPs could be fitted with the BL model with comparable values of R^2 and RMSE to the HNTs means that these values cannot be used as criteria to automatically remove all NTPs from the images: if the threshold values were too restrictive, one would risk erroneously omitting isolated HNTs, and if they were too inclusive, one might erroneously include some NTPs.

While it is clear that filtering objects in TEM images based on the goodness of the BL fit cannot get rid of all of the NTPs, it should not be ruled out completely as a filtering method. This is because it is unknown how many NTPs would be left in the image after

filtering; if it were relatively few, it might be the case that they only have a small influence on the overall size distribution found for the HNTs. In order to examine this further, new TEM images would be required in which there were enough isolated HNT and NTPs (rather than APs) that their populations could be studied using MATLAB. In addition, even were a perfectly functional automated measurement algorithm developed, there are so many APs in the TEM images discussed thus far that there may not be enough isolated HNTs for a useful statistical distribution to be found. This distribution might also be skewed towards smaller sizes if, as suspected, larger nanotubes are more prone to agglomeration. Making progress towards automated analysis of TEM images from this point was therefore a sample preparation issue, i.e. a method needed to be developed to prevent agglomeration of the particles on the TEM grid.

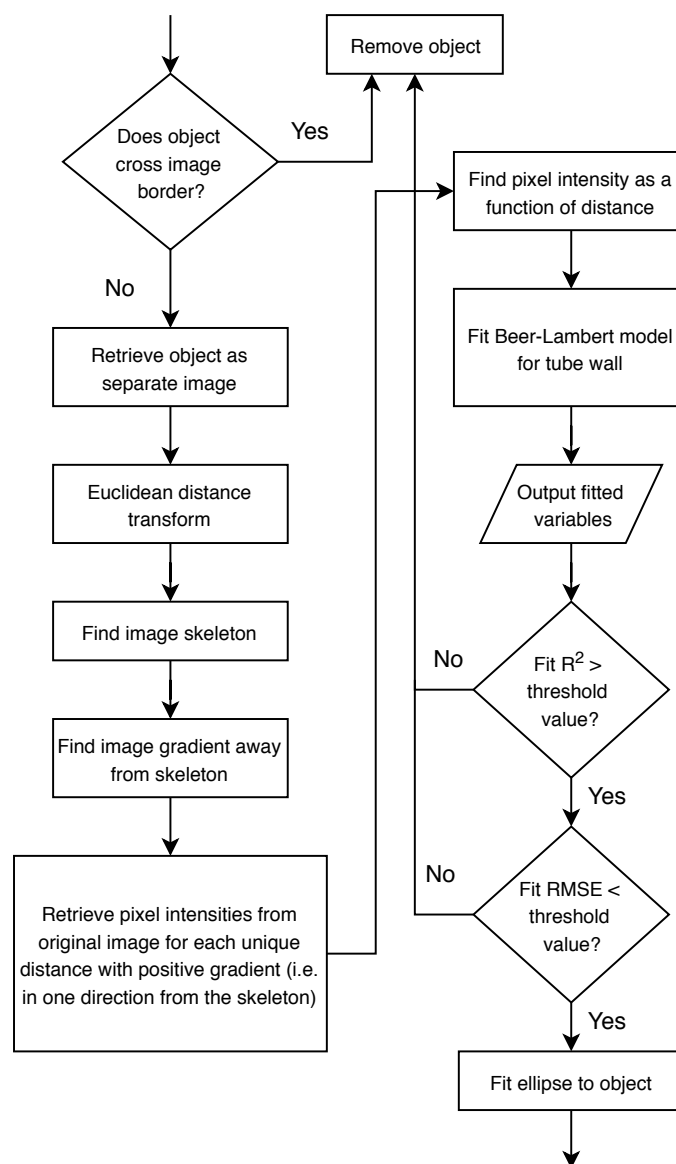


Figure 2.35: A flowchart indicating the general logic of how objects in TEM images of HNTs could be filtered in MATLAB using the goodness of fit of the BL law to their edges.

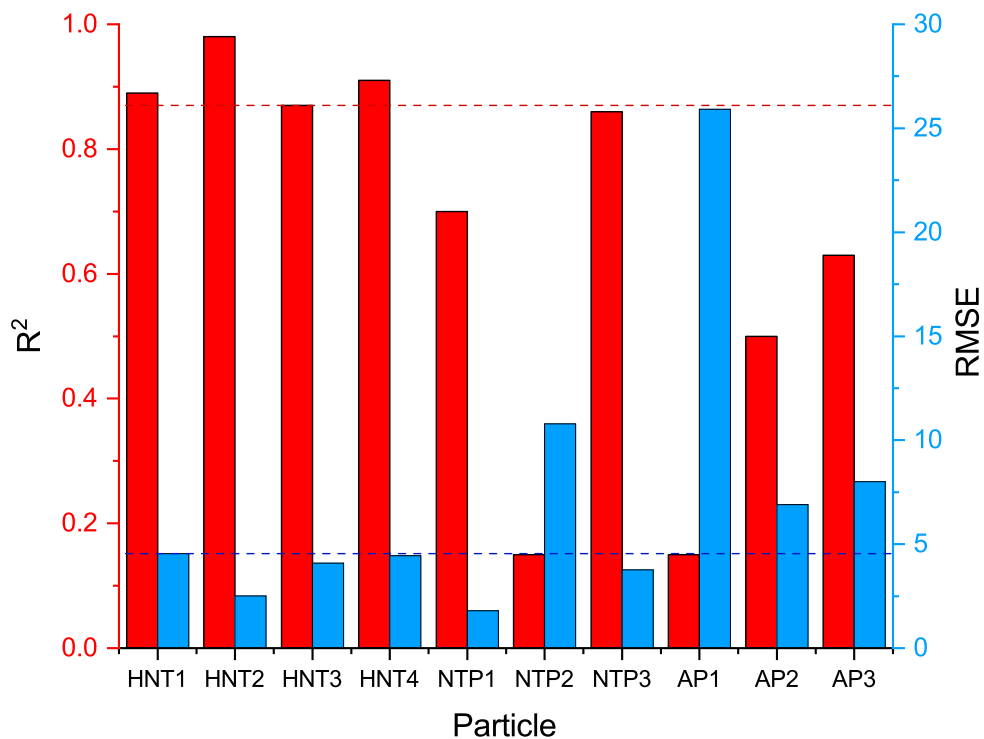


Figure 2.36: The results of fitting equation 2.15 to the pixel intensity across several isolated HNTs in a TEM image versus NTPs and APs. The dark red dashed line is at the minimum R^2 found for an isolated HNT (0.87), and the dark blue dashed line is at the maximum RMSE seen for an isolated HNT (4.55). It can be seen that there is one NTP with both an R^2 close to the minimum for HNTs, and an RMSE below the maximum of HNTs. This suggests that these goodness of fit criteria cannot be used to distinguish isolated HNTs from NTPs.

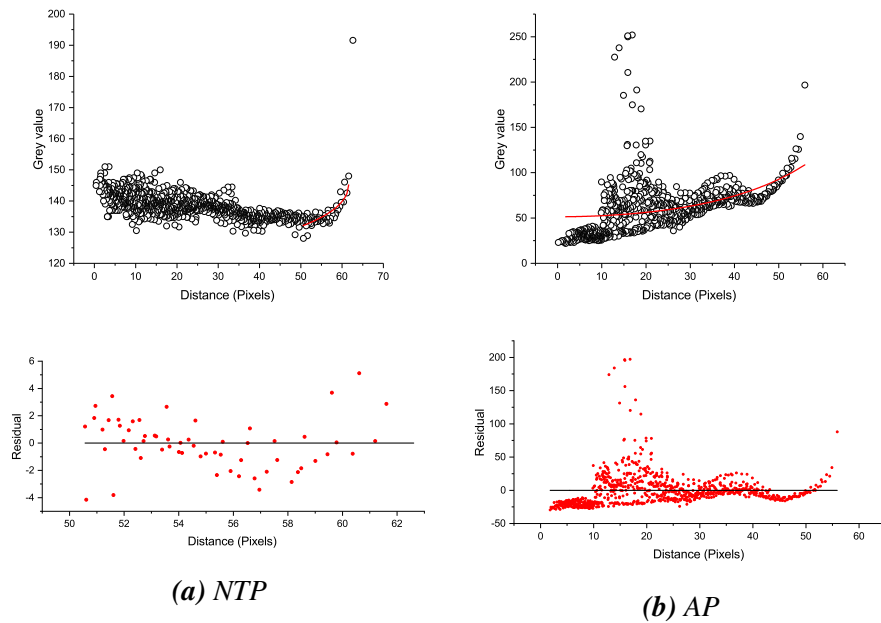


Figure 2.37: Fits of the intensity profiles at the edges of an example of either an NTP or AP using the BL model for a cylinder and the corresponding residuals. Note that the fit is only applied at distance greater than the value of R_i , which is determined from the distance at which intensity is a minimum.

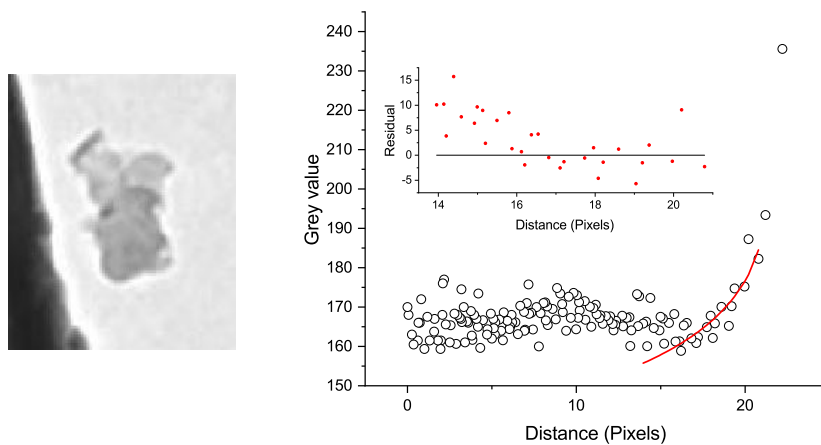


Figure 2.38: An NTP for which the BL model produced a comparable fit to HNTs alongside its fitted intensity profile and corresponding fit residuals.

Changing TEM sample preparation method to improve particle separation

It was thought that the problematic agglomeration of the particles seen in TEM images might be able to be overcome by promoting repulsive interactions between the nanotubes in the dispersion dropped onto the grid during sample preparation. For example, the pH of the solution could be increased to increase the zeta potential of the HNTs (see section 2.4.3), or a dispersing agent could be added. Indeed, to their samples, Hillier *et al.*⁴ added a solution of Calgon (sodium poly(phosphate) (SPP)), a widely used dispersing agent for clay particles, and the nanotubes were dispersed into the solution via ultrasonication in an attempt to break up existing agglomerates. In addition, in the sample preparation described here, a solution with a relatively high HNT content (1 wt%) was used, with the dispersion dried on the TEM grid by wicking away excess liquid with paper, whereas Hillier *et al.* used a relatively low concentration of HNTs (on the order of 0.001 wt%), and left their samples to dry over a longer period of time in a desiccator.⁴ Presumably as a consequence of these differences, the HNTs in their images (e.g. figure 2.39) appear better separated than those shown so far in this work. Therefore, the next step taken towards developing automated size measurement of HNTs was changing the dispersant solution used to transfer the HNTs to the grid, and changing the way in which the dispersion was dried once on the grid.

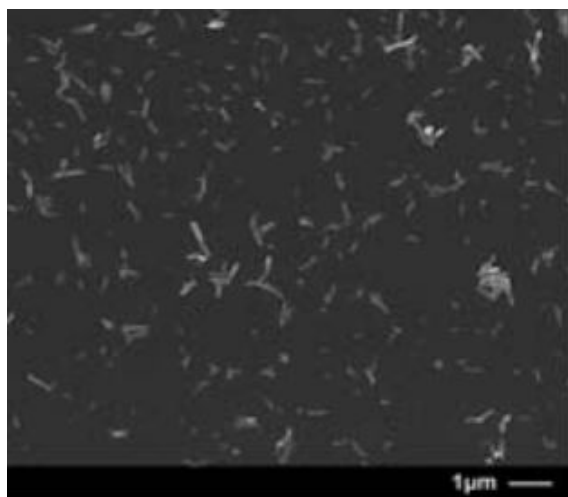


Figure 2.39: An SEM image adapted with permission from work by Hillier *et al.*⁴ They used a dispersing agent when preparing samples of HNTs, and the particles subsequently appear well separated in their electron micrographs.

A similar procedure to that described by Hillier *et al.* was used for making new samples of HNTs for TEM imaging.⁴ More specifically, three samples were made which each contained a much lower concentration of HNTs than used previously (about 0.008 wt% versus 1 wt%), but which each also contained different aqueous solutions: one contained deionised water adjusted to pH 12 to maximise the particles' zeta potentials; one contained SPP at a concentration of around 0.05 wt% (a similar concentration to literature examples);^{7,163} and the remaining one was a control sample containing pure, deionised water. These samples were ultrasonicated, then 10 μL of each was dropped onto a TEM sample grid. These were then placed in a desiccator over phosphorus pentoxide to allow the liquid to dry before being imaged by TEM.

Images of the control sample (figure 2.40) show a significant degree of agglomeration, so it is clear that the physical aspects of the new procedure (i.e. lower concentration, better mixing, and slower drying) are not sufficient on their own to produce TEM sample grids with well-separated HNTs. Similarly, agglomeration is seen in the pH 12 sample (figure 2.41), especially of the largest particles. However, the smaller particles do appear to be much more evenly spread out than in previous images, which suggests that the high pH of the solution has been at least somewhat successful for improving particle separation. There is also a hazy layer around many of the bigger particles; it is unknown whether this is an actual chemical feature of the sample, or an unfortunate artefact. For the sample containing SPP (figure 2.42), not only is agglomeration still present, but there is also clearly a thick polymer layer over all of the particles, which would cause multiple issues with automated image analysis (e.g. problems with setting the correct threshold). This is probably due to too high a concentration of SPP being used: in the literature examples where SPP was used as a dispersant^{7,163} a much greater amount of HNTs was also used. Indeed, any excess SPP is likely to cause problems when this drying procedure is used; the polymer will not evaporate under these conditions, and so will always remain on the sample grid. It is concluded that changing the drying procedure and dispersant solution is not effective for producing TEM images of HNTs where every particle is well separated from the rest, at least not at the HNT concentrations described by Hillier *et al.*⁴

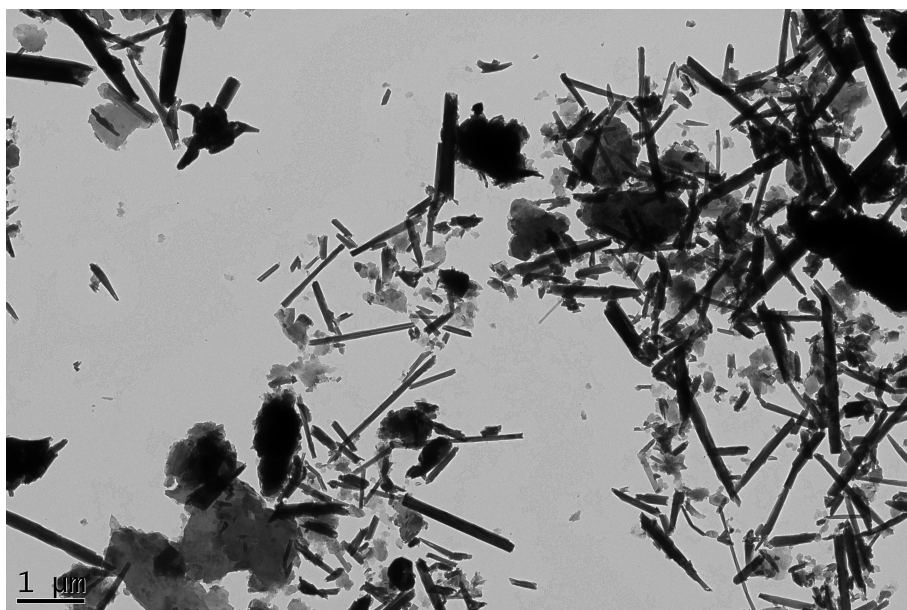


Figure 2.40: A TEM image of HNTs dried in a desiccator from a concentration of about 0.008 wt% in pH 7 water. Significant agglomeration still occurs.

To investigate the importance of HNT concentration on particle separation in TEM images, the samples described above were diluted by about a factor of ten with deionised water (i.e. producing samples of around 0.0008 wt% HNTs) and re-imaged (figure 2.43). However, in all cases, agglomeration is still apparent, and the dilution only appeared to achieve a reduction in the HNT number concentration in the images. This reduction happened to the extent that it would become time-consuming to take pictures of enough HNTs to allow for a reasonable statistical distribution of sizes to be obtained (i.e. because they are too far apart for many to be captured per image). In addition, a polymer layer is still apparent around the particles in the SPP sample. The procedure inspired by Hillier

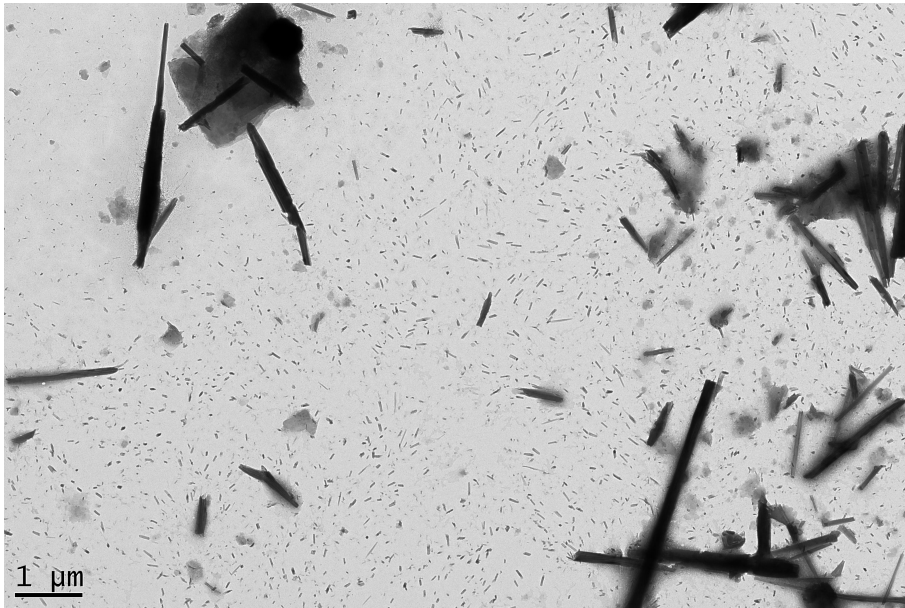


Figure 2.41: A TEM image of HNTs dried in a desiccator from a concentration of about 0.008 wt% in pH 12 water. Agglomeration still occurs, but many of the smaller particles appear well separated from one another.

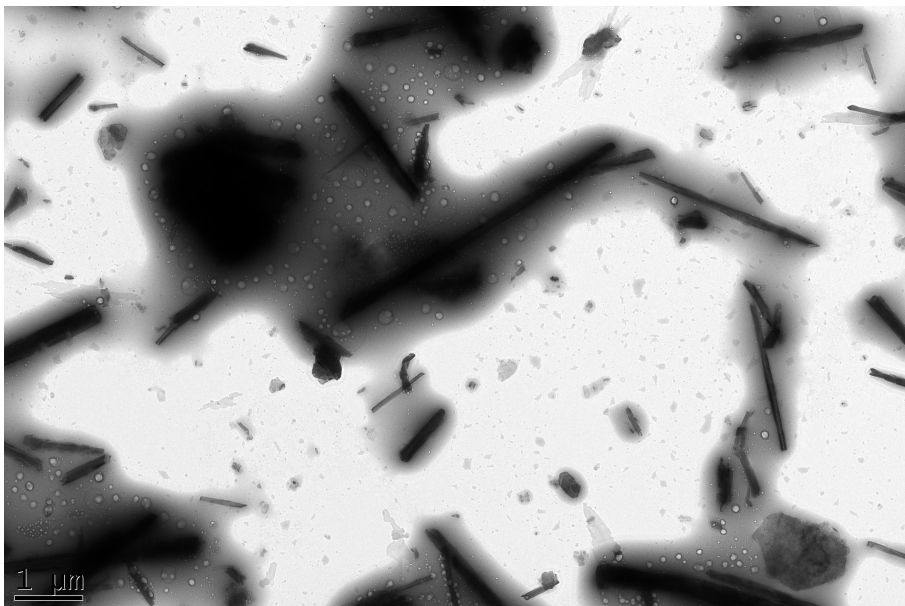


Figure 2.42: A TEM image of HNTs dried in a desiccator from a concentration of about 0.008 wt% in water containing 0.05 wt% SPP as a dispersant. Not only does agglomeration occur, but the particles appear to be coated in a thick layer of polymer.

*et al.*⁴ was therefore concluded to be unsuitable for producing TEM images of HNTs suitable for automatic image analysis. The reason Hillier *et al.* may have found their procedure to be effective could be because they actually dried their samples on uncoated copper TEM grids (rather than carbon-film coated), and noted that they believe the holes in the grid to play a role in breaking the droplet up, and changing the way the sample dries. Unfortunately, while they were able to use such grids for their SEM measurements, this method is not suitable for TEM imaging, which requires the grid to be covered with a film. Indeed, it might be the case that any method of preparing HNT samples for TEM imaging by drying of liquid water will lead to agglomeration of the particles. The next step in obtaining TEM of HNTs with no agglomeration might be to use cryo-TEM. In cryo-TEM, the sample is flash-frozen, rather than dried, which might allow the particles to be imaged essentially as they were when suspended in the liquid (although blotting of water from the the sample is sometimes also required in this technique).¹⁶⁴ From the results found here, it is suggested that cryo-TEM be carried out on suspensions of HNTs in water at pH 12.

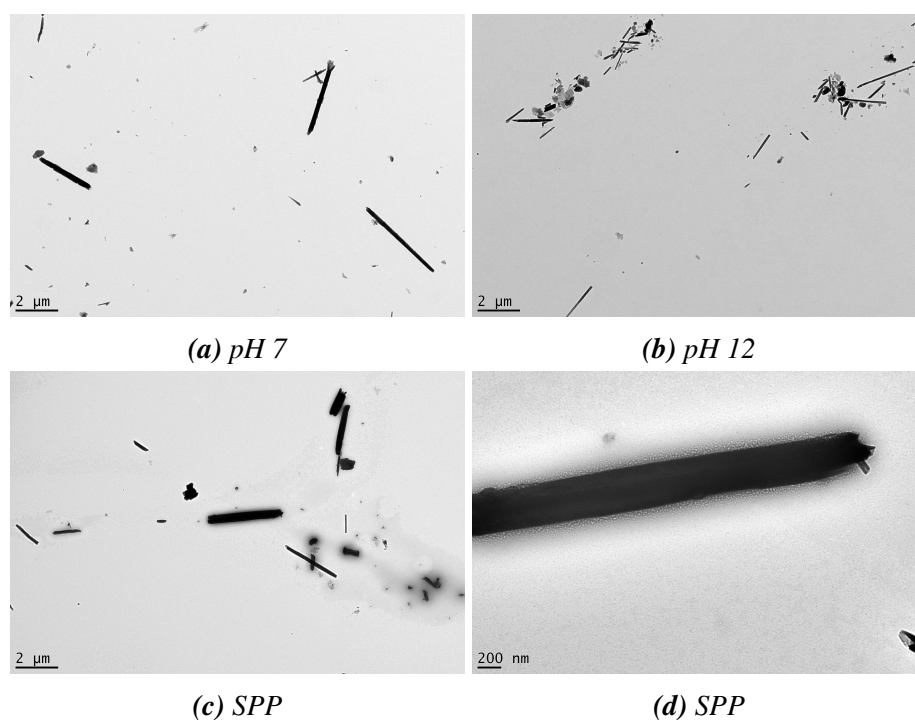


Figure 2.43: TEM images of HNTs dried using the procedure inspired by Hillier *et al.*,⁴ but at a lower concentration of around 0.0008 wt%. Agglomeration still occurs for all samples, and a layer of polymer is still apparent around the particles where SPP was used as a dispersant (i.e. c and d).

2.6.5 Small-angle X-ray scattering measurements of halloysite nanotubes

Introduction to SAXS

In contrast to WAXS (see section 2.5.2) where the scattering features are similar in size to the wavelength of the incident X-rays, small-angle scattering of X-rays (SAXS) by a particle occurs when the particle is large in comparison to the wavelength of the X-rays.¹⁶⁵ More specifically, photons scattered from two positions which are relatively far away from another in a large particle become out of phase and begin to interfere destructively more quickly with increasing 2θ than those scattered from two positions which are relatively close together (e.g. in a small particle, or atomic lattice).¹⁶⁵ This is also evident from Bragg's law (equation 2.6); if λ is constant, then θ must decrease as d increases.

In a SAXS experiment, the intensity of scattered X-rays (I) is typically measured as a function of q , which is the scattering vector. As shown in equation 2.24, q is calculated from the scattering angle, which is 2θ , and the wavelength of the incident radiation, λ , and it has units of reciprocal length.¹⁶⁶ Length, L , can be calculated from q using equation 2.25.¹⁶⁷ Intensity as a function of q can be described by the relationship in equation 2.26. The term $\langle \eta^2 \rangle$ contains the number and volume of the particles, and the contrast (i.e. difference in electron density) between the particles and bulk medium.¹⁶⁸ The functions $P(q)$ and $S(q)$ are known as the form and structure factors, respectively. The form factor is characteristic of the shape of the particle, while the structure factor relates to the particle positions relative to one another. In a dilute system, $S(q)$ can be approximated to 1, i.e. multiple scattering of X-rays by different particles can be neglected.¹⁶⁸ It should also be noted that scattering scales with particle size as per the relationship shown in equation 2.27 (where V is particle volume),¹⁶⁸ so larger particles will contribute more to the scattered intensity per particle than smaller ones.

$$q = \frac{4\pi \sin \theta}{\lambda} \quad (2.24)$$

$$L = \frac{2\pi}{q} \quad (2.25)$$

$$I(q) = \langle \eta^2 \rangle P(q)S(q) \quad (2.26)$$

$$I(q) \propto V^2 \quad (2.27)$$

The length scales which can be measured by SAXS instruments generally range from tens to hundreds of nm, although this depends on the exact instrument being used. Specifically, the length scales available for measurement depend on the distance between the sample and the detector, with scattering by larger colloidal/nanoparticles (i.e. at increasingly small angles) only able to be sufficiently resolved by instruments where this distance can be set to be relatively long (several m). The ability to measure dimensions at these length

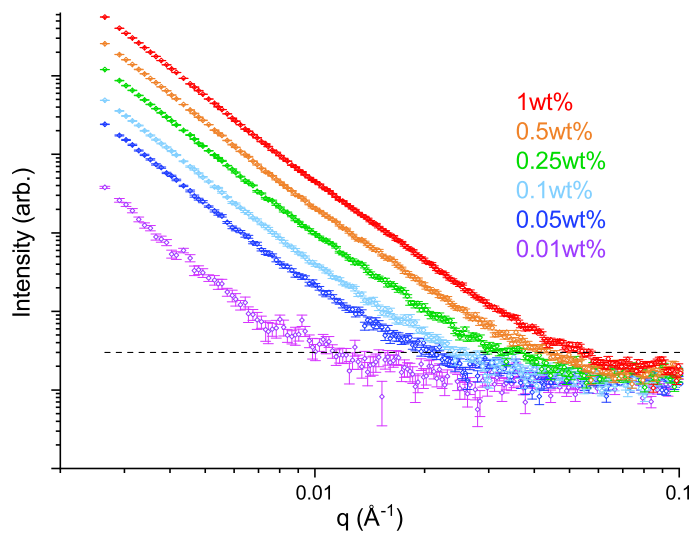
scales makes the technique useful for the characterisation of both organic and inorganic colloids and nanoparticles.¹⁶⁵ In contrast to microscopy, the technique produces data through interactions with a large number of particles, and suffers few issues with regards to operator bias.¹⁶⁹ However, interpreting scattering data to reach meaningful conclusions about particle size and shape can be challenging.

Scattering by HNTs

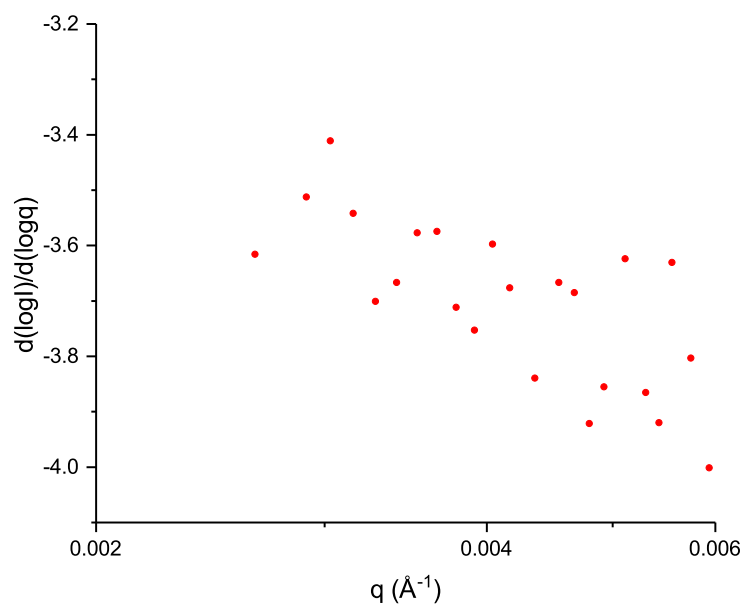
SAXS analysis was carried out on a series of dispersions of HNTs in water at increasing concentration, and the results are shown in figure 2.44a. Since low HNT concentrations were measured, and the shape of the scattering patterns does not seem to change with increasing concentration, measurements are assumed to be in the dilute regime (i.e. $S(q) = 1$). Therefore, the small-angle scattering pattern should be described solely by the form factor of the particles. The intensity of the scattered X-rays increases roughly proportionally to the concentration of HNTs, which is consistent with the introduction of an increasing number of interfaces which can scatter the radiation. Plotting intensity versus q on a logarithmic scale gives smooth, straight lines which with gradients between about -3.4 and -4.0 from $q = 0.002 \text{ \AA}^{-1}$ to 0.02 \AA^{-1} , i.e. between around 300 nm and 30 nm. The gradient appears to increase with decreasing q , as shown in figure 2.44b, but the scattering patterns are otherwise featureless.

However, featureless SAXS patterns would not be expected for a cylinder. Figure 2.45a shows intensity versus q which has been simulated for different cylinder sizes using SASfit software and a cylindrical form factor. The dimensions of the cylinders are taken from examples of HNTs seen in TEM images, and it can be seen that each one produces a distinct, oscillating scattering pattern. However, the polydispersity of the HNT dimensions, and the external diameter in particular, causes these scattering patterns to average out. Figure 2.45b shows the scattering patterns of several different cylinder sizes, and the result of averaging these patterns (after weighting each one by their relative populations from the PDFs described in section 2.6.1). It can be seen that the average scattering pattern is much closer to a straight line than that from individual cylinders. The actual SAXS data for HNTs is plotted over this average; it is apparent that a straight line similar to that of the real data would eventually be obtained by continuing to average the simulated scattering of cylinders representing all of the different nanotube sizes. This smoothing of the SAXS pattern due to polydispersity of size is exacerbated by the scattering contributions of the various non-tubular impurities in the samples.

No conclusions about the size or shape of the HNTs can be made from the SAXS data shown in figure 2.44a, but it could be argued from that there may be features at higher q (i.e. $q = 0.04 \text{ \AA}^{-1}$ and higher) that are indecipherable at long sample-to-detector lengths due to noise on the detector. This corresponds to a distance of around 15 nm, and so the internal diameters of the tubes would be expected to be seen in this region. However, when a shorter sample-to-detector distance was used to reduce noise in the higher q -range (i.e. by collecting data over a smaller number of pixels), the scattering pattern was equally featureless. This data is shown in figure 2.46.

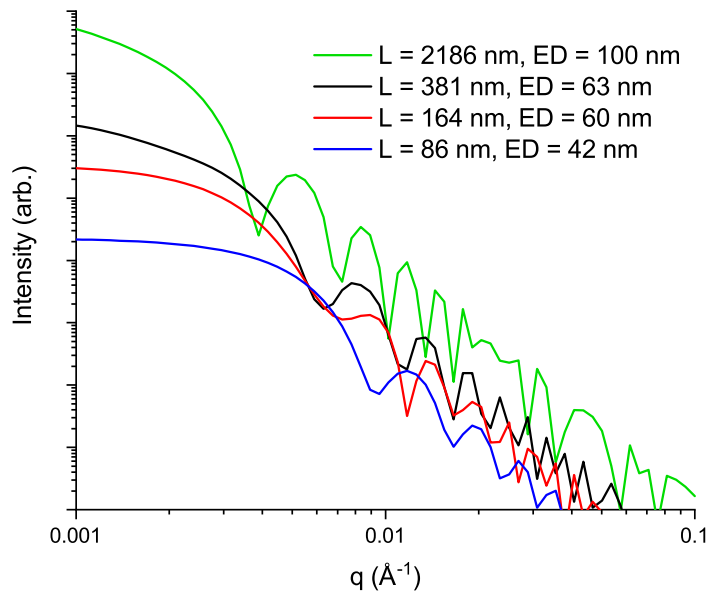


(a) X-ray intensity as a function of scattering vector, q , for a concentration series of HNTs in water (the signal-to-noise ratio becomes problematically low at intensities below the dotted line).

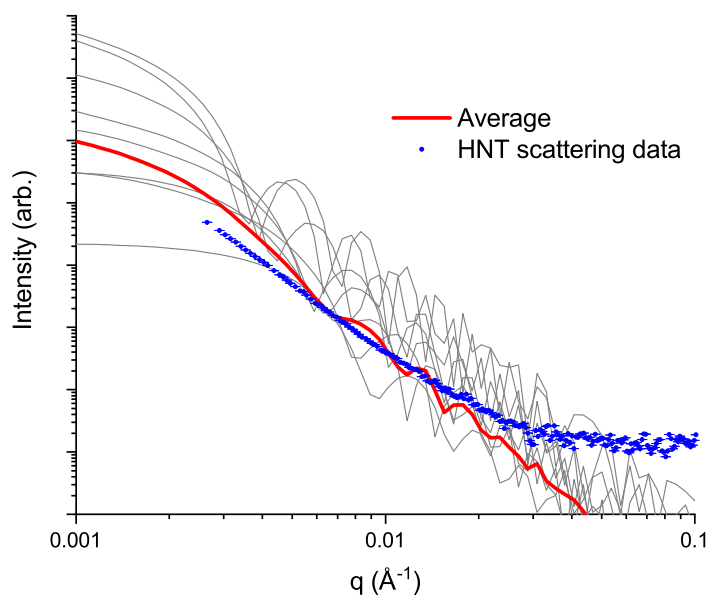


(b) The gradient of $\log(I)$ decreases at low q . The derivative data above 0.006 \AA^{-1} is increasingly noisy, and so is omitted. This is because, in Origin analysis software, the derivative of discrete data is calculated by taking the average of the slopes between that point and its nearest two neighbours.

Figure 2.44: Graphs showing a) SAXS by HNTs in water, and b) the first derivative of this data at low q .



(a) Simulated SAXS data for cylinders with lengths (L) and external diameters (ED) taken from examples of real HNTs in TEM images



(b) Simulated SAXS data for several of these cylinders, and the result of averaging this data compared to real SAXS data for HNTs.

Figure 2.45: Graphs showing simulated SAXS by cylinders of different sizes, and an illustration of how averaging this scattering can start to approximate the actual scattering by HNTs. The featureless SAXS seen for HNTs is therefore explained as a consequence of the polydispersity of their dimensions.

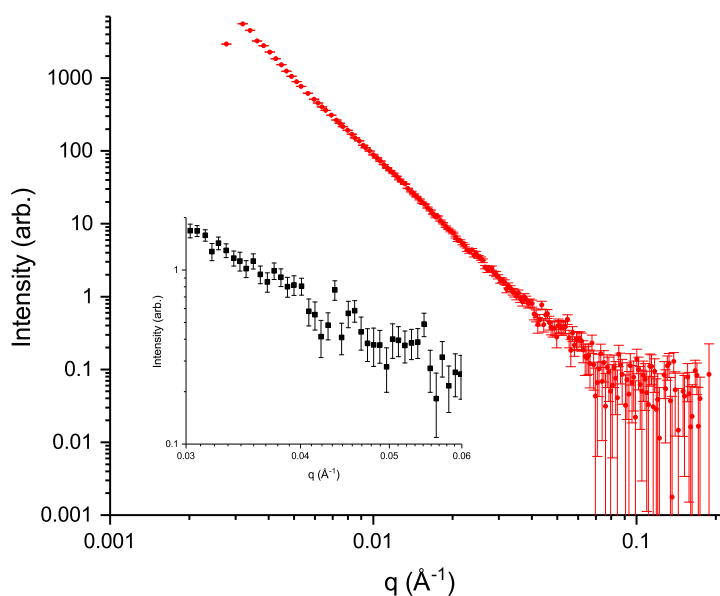


Figure 2.46: A graph of X-ray intensity as a function of scattering vector, q , for 0.1 wt% HNTs in water. This data was obtained using a shorter sample-to-detector distance than in figure 2.44 in order to reduce noise in the higher q -range.

Small-angle scattering analysis of HNTs in literature

There have been few studies of halloysite by small-angle scattering. The most recent, and comprehensive, was by Cavallaro *et al.* in 2017,¹⁷⁰ who used small-angle neutron scattering (SANS) to study four halloysites from different sources across the globe. While a similar to a technique to SAXS in terms of the data produced and types of features studied, SANS measures the scattering of neutron radiation by atomic nuclei rather than the scattering of electromagnetic radiation by electrons. Typically, SANS is used where the phases being studied do not have significantly different refractive indices (i.e. they have similar electron density), but do have different tendencies to scatter neutrons, e.g. normal alkanes versus those enriched with deuterium. However, HNTs in H₂O or D₂O have good contrast for both X-ray and neutron scattering, respectively, so similar results can be obtained from either technique.

HNTs from the Dragon Mine gave featureless SANS patterns,¹⁷⁰ similar to the SAXS patterns reported in this work. HNTs from the Dragon Mine are perhaps the most similar to those used in this work, as the two sources are relatively geographically close (Utah and Idaho), and XRD data for HNTs from I-Minerals Inc. in section 2.5.2 could be matched to many of the scattering features in a reference for those from the Dragon Mine. Cavallaro *et al.* did find oscillations in scattering by HNTs from a different origin (specifically from Western Australia), and they were able to fit this data with a theoretical model for scattering by a hollow, tubular particle.¹⁷⁰ However, the same model did not provide a good fit for the HNTs from the Dragon Mine. They concluded that this was due to the relative lack of homogeneity of size and shape for these HNTs, especially in comparison to those from Australia.¹⁷⁰

From the SAXS data found here, and other scattering data in the literature, it is reasonable to conclude that static light-scattering techniques are probably unable to provide any useful morphological information about the HNTs provided by I-Minerals Inc..

2.6.6 Dynamic Light Scattering

Dynamic light scattering (DLS) refers to a range of light-scattering measurement techniques which can be used to find information about the size of colloidal particles.¹⁷¹ More specifically, experimental data from DLS measurements can be fitted with theoretical models of particle diffusion in order to quantify the hydrodynamic properties of particles suspended in solution, usually their translational and/or rotational diffusion coefficients.¹⁷¹ Photon Correlation Spectroscopy (PCS) is a type of DLS technique.

Introduction to Photon Correlation Spectroscopy

When a beam of light passes through a colloidal suspension, it is scattered by the suspended particles. The intensity of light measured at any given scattering angle is dependent on the size and positions of the particles.¹⁷¹ Because the particles' positions are constantly changing due to Brownian (i.e. thermal) motion, the total scattered intensity measured at a constant angle from the incident light fluctuates. The fluctuations occur on the same time scale that it takes the particles to move a significant fraction of the wavelength of the incident light. This means that the rate of fluctuation of scattered intensity at a given angle is related to the rate of diffusion of the particles in solution. More specifically, the faster the rate of diffusion of the particles, the faster the rate of change of the scattered light intensity at a constant angle.¹⁷¹ For the simple example of a spherical particle of radius R , the translational self-diffusion coefficient, D , in a liquid with viscosity η , at temperature, T , is given by the Stokes-Einstein equation (equation 2.28), where k_B is the Boltzmann constant.¹⁷¹

$$D = \frac{k_B T}{6\pi\eta R} \quad (2.28)$$

In a typical PCS instrument, the sample is irradiated with a laser beam, the light-scattering from the sample is measured over time by one or more detectors at set angles to the incident beam, and the signal is digitised. A laser must be used, as the incident light needs to be coherent and high intensity. Using the digital signal, a component known as an autocorrelator computes an intensity time correlation function, which can be expressed as an integral of the products of intensity at time t , and the intensity at time t plus a delay time τ (equation 2.29).¹⁷¹

$$f(\tau) = \langle I(t)I(t + \tau) \rangle \quad (2.29)$$

The obtained correlation function is then processed mathematically by using one of either the CONTIN algorithm or Cumulant method to yield a value for the apparent diffusion coefficient of the particles in solution.¹⁷² For spherical particles, which are isotropic, this

diffusion coefficient is a direct measure of their centre of mass diffusion.¹⁷² This can be input into Stokes-Einstein equation (equation 2.28) in order to find a value for particle hydrodynamic radius, which is close to the true radius of the particles.¹⁷¹

PCS measurements of rigid rods

For anisotropic particles such as rods, the situation is more complicated.¹⁷² For rods specifically, this is because they diffuse more quickly in the longitudinal direction than the transverse direction, and because their translational diffusion is coupled with their rotational motion.¹⁷² The separate diffusion coefficients which must be taken into account for rigid rods are:

1. The centre-of-mass diffusion coefficient.
2. The longitudinal diffusion coefficient, i.e. motion in the direction of the rod's length.
3. The transverse diffusion coefficient, i.e. motion perpendicular to the rod's length.
4. The rotational diffusion coefficient.

The apparent diffusion coefficient, (D), which is measured for rigid rods has a contribution from all of these modes of movement.

Indeed, the difficulty associated with calculating rod dimensions from PCS measurements means that there has been relatively little work concerning the subject. The most recent attempt to model DLS by rigid rods appears to be the work of Liu *et al.* in 2012, who described a theoretical model for calculation of the length (but not width) of rods from PCS measurements.¹⁷² However, their model has not been verified experimentally, and, more importantly, is only valid for rods with an aspect ratio greater than six. For the HNTs measured in section 2.6.3, 56% of the particles were found to have an aspect ratio lower than six. Therefore, even were the HNT sample made up purely of nanotubes, PCS would not be a good technique for determining their lengths.

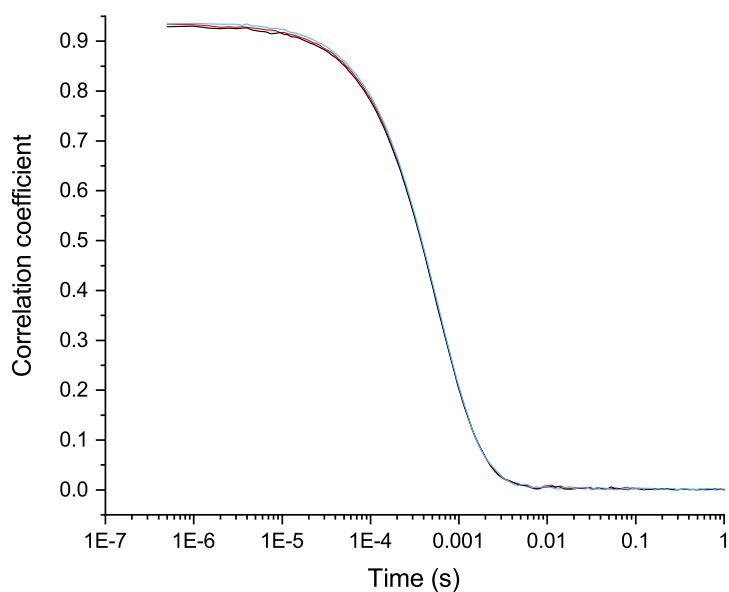
Practical uses for PCS measurements of HNT dispersions

In the literature, the size output obtained from a PCS instrument when measuring dispersions of HNTs is usually reported as the apparent hydrodynamic radius of the suspended particles without further comment,^{111,173-176} even though these values are presumably (and in some cases explicitly^{111,176}) obtained by fitting intensity data with a model for a spherical particle.

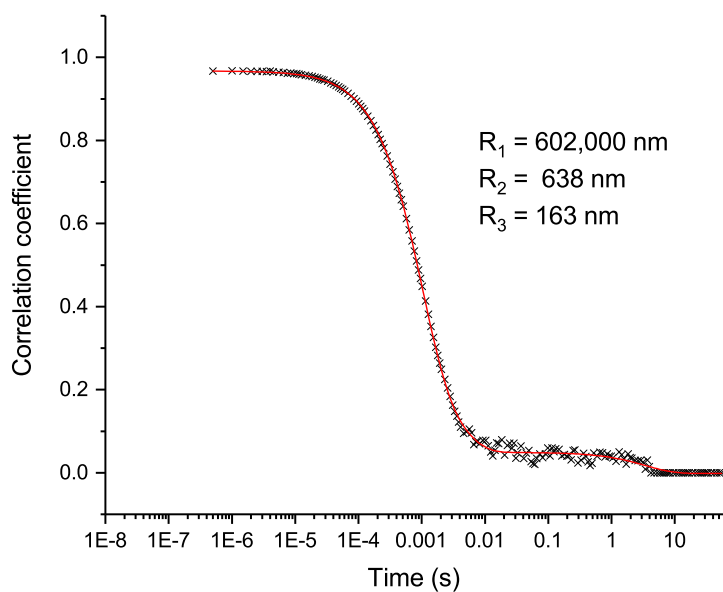
However, even though PCS cannot and has not been used to determine the dimensions of HNTs, it is useful for giving an indication of the level of HNT dispersion in suspension.¹¹¹ More specifically, if a larger size is measured for HNTs in one suspension than in another, it can be concluded that larger aggregates of particles are present in the first suspension. This is useful for studying aggregation of the particles,¹⁷⁶ and could be useful

for studying destruction of the particles after some high-energy process, to give just two possible examples.

Because of this, PCS measurements of HNTs were taken. The measurements were taken using water at pH 12, and after mixing with a high-shear homogeniser. This means that the 'size' measured should be that of individually dispersed particles. The size obtained for such a sample using the cumulant method and a scattering angle of 173° is (395 ± 1) nm, where the uncertainty is the standard deviation of three measurements. The autocorrelation data for these measurements is shown in figure 2.47a. The cumulant method fits a single exponential decay function to these data, but it can be seen that the data deviate from a simple exponential decay function at long delay times. However, as can be seen in figure 2.47b, fitting the data with the CONTIN algorithm, which can fit multiple exponential functions to the data, yields nonsensical size results (i.e. several hundred micron even though there were no visible particles in suspension). It is clear that existing methods are not sufficient to describe DLS by samples of HNTs.



(a)



(b)

Figure 2.47: The raw correlation data for HNTs in water at pH 12 (a), and the same data fitted with three multiple exponential decay functions (representing different particle populations) using the CONTIN algorithm (b). Fitting this way does achieve a close fit to the data, but yields some nonsensical size values.

2.7 Conclusions and future work

In summary, various chemical, physical and morphological properties of HNTs from I-Minerals Inc. were characterised. In general, the chemistry of the nanotubes was as expected from supplier data and the literature for HNTs in general, although ICP-MS and XRD suggested that there were more metallic and non-HNT mineral impurities than might be expected from supplier data. The morphology of the HNTs was also found to be significantly different to that indicated by the supplier data sheet.

Most significantly, it was shown that the dimensions of the HNTs are difficult to measure reliably; SAXS and DLS results suggest that it is not possible to measure the dimensions of the HNTs using scattering techniques, and it was shown that relying on manual analysis of electron micrographs is unreliable because of operator bias, as well as being time consuming.

Automation of the image analysis process was attempted to overcome these issues, and it was shown that using basic MATLAB image processing tools could provide accurate dimensions for isolated HNTs in TEM images. However, it was found to be difficult to automatically retrieve isolated tubes from the large population of non-tubular particles and agglomerated tubes. Taking inspiration from a method developed for CNTs,³ it was investigated whether the pixel intensity profile (i.e. intensity as a function of distance) across each particle in the images could be used as a criterion for automatically distinguishing isolated HNTs. However, while fitting a model derived from the Beer-Lambert law³ to this intensity data was shown to be effective for distinguishing isolated tubes from agglomerated particles, it was not always successful at distinguishing HNTs from non-tubular impurities. Future work to successfully automate image analysis would have to include developing a more sophisticated algorithm for differentiating between the different types of intensity profiles. Alternatively, a machine learning approach could be adopted, with images of each type of particle used as training data. The code would also ideally be expanded to allow it to analyse batches of images, rather than a single image at a time. In addition, it was shown that dispersing the HNTs in pH 12 water before dropping onto the TEM sample grid was the most promising route for producing TEM images containing only individually dispersed particles. Such images would be necessary to allow accurate statistical distributions of the nanotubes to be obtained by automated image analysis. It is suggested that cryo-TEM be explored as a possible route for achieving this. Regardless of the final approaches adopted (with regards to either sample preparation, or analysis algorithm), this work should be continued, as it appears that automated analysis of electron micrographs is the only way to accurately measure the dimensions of HNTs.

The results of this chapter have several implications for the manufacture of epoxy resin/HNT nanocomposites. Firstly, it is expected from section 2.4.2 that epoxy resin would only be a moderately good solvent for HNTs. From this conclusion, it can be predicted that high shear mixing techniques and/or surface functionalisation of the nanotubes would be necessary for the dispersion of individual HNTs into an epoxy resin, which is in agreement with the general trends seen in literature, as discussed in chapter 1. Additionally, it can be concluded that the degree of dispersion of HNTs in an epoxy resin nanocomposite would have to be analysed by hand in electron micrographs, rather than by automated image analysis, or by light scattering. Such manual image analysis can both take a considerable amount of time (especially if nanotube sizes are to be found), and

introduce unwanted bias into the measurements. All of these factors must be taken into account when planning the production and accurate characterisation of epoxy resin/HNT nanocomposites.

2.8 Materials and methods

2.8.1 Materials

A summary of the materials used in this chapter is given in table 2.14. Not included is deionised water, which was purified from the mains supply to a resistivity of 18.0 M Ω cm using a PureLab Option-Q water treatment unit. The solvents used for dispersability tests are also not included: these were from various suppliers, and were of at least reagent grade purity.

Table 2.14: A list of the materials used in this chapter.

Material	Supplier	Purity and/or other comments
Halloysite nanotubes	I-Minerals Inc.	ULTRA HalloPure Halloysite (2015M)
Sodium hydroxide	Fluka Analytical	>97%
Hydrochloric acid (aqueous)	Fisher Scientific	1M (stabilised)
Sodium poly(phosphate)	Acros Organic	Pure
Phosphorus pentoxide	Acros Organic	98% (extra pure)

2.8.2 Methods

Estimation of HNT sedimentation times in different solvents

For each of the solvents listed in section 2.4.2, about 50 mg of HNTs were added to about 5 mL of solvent, and the vial shaken vigorously by hand. To test the sedimentation time of the particles in each solvent, the mixtures were stirred using a magnetic follower and stirrer plate whilst being filmed using a generic digital USB microscope controlled by MATLAB code (see appendix). The first frame after stirring had been turned off is taken as time = 0 for subsequent sedimentation time estimates.

Evaluation of Hansen solubility parameters

Hansen solubility parameters for the solvents were obtained from HSPiP software.

Zeta potential measurements

Zeta potentials were measured using a Malvern Zetasizer Nano ZS. A disposable polystyrene measurement cell was used, which was flushed with a large excess of deionised water between each measurement. Samples of deionised water were made to the desired pH using either HCl or NaOH. HNTs were added to these solutions at an approx. concentration of

0.1 wt%, and these dispersions were briefly shaken once to disperse the nanotubes, and then again just before the measurement was taken. The method described by Joo *et al.*¹⁴⁹ was also attempted for samples below pH 2. Specifically, these samples were treated for several h in an ultrasonic bath, then filtered through a 0.8 μm cellulose acetate syringe filter before measurement.

ICP-MS

A few hundred mg of sample were digested using concentrated nitric acid, and analysed using an Agilent 4500 ICP-MS. Samples were digested with acid and measured by Neil Bramall in the Department of Chemistry at the University of Sheffield.

XRD

Wide-angle diffraction data for the whole 2θ range was collected using a Stoe STADI P diffractometer with a Cu $K\alpha 1$ radiation source and a Cu Imaging Plate detector. Approx. 50 mg of HNT powder was mounted sandwiched between acetate foils in a standard Stoe specimen holder. Data was acquired in 8 scans from 0° to 100° 2θ over a total acquisition time of 55 min. The data was calibrated using a Si standard (NIST 640d Si), which provides an accurate calibration for peaks at 28° 2θ and above. Peaks were indexed using Bruker EVA software with access to the International Centre for Diffraction Data (ICDD) PDF-4+ crystallography database.¹⁵²

Using a similar HNT sample to that described above, data was collected for the d_{001} region specifically using a Xenocs Xeuss 2.0 instrument (Excillum MetalJet liquid gallium source) with a vertically-offset Pilatus 1M detector, and a sample to detector distance of 544 mm. Data was collected in “high flux mode” with a collection time of 180 s. The data was calibrated using a silver behenate standard over a q -range of 0.02 - 1.5 \AA , and data reduction was done using instrument-specific Foxtrot software. The data was collected and reduced by Dr. Dan Toolan in the Department of Chemistry.

FT-IR spectroscopy

Spectra were collected on a Perkin Elmer Spectrum Two Fourier-Transform Infrared spectrometer fitted with an UATR Two sampling accessory. After a background spectrum had been taken, small amounts of powdered sample (about a mg) were placed on the crystal for analysis, with the large “shoe” fitted, and the force gauge applied to a level of about 150. Spectra were collected as an average of 10 scans between 450 and 4000 cm^{-1} . All samples were dried for at least 1 h under vacuum at 100°C before being immediately taken for measurement (about 20 min between leaving the oven and measurement).

TGA

About 15 mg of sample was measured using a Pyris TGA with a pure nitrogen atmosphere. The following heating program was used: hold for 5 min at 25 °C; heat from 25 °C to 800 °C at 10 °Cmin⁻¹; hold at 800 °C for 5 min.

TEM: standard sample preparation

Deionised water was added to HNTs to give a dispersion of approx. 1 wt%, which was shaken by hand to disperse the nanotubes. An approx. 10 μ L portion of this sample was dropped onto a carbon-coated, copper TEM grid, and the excess water was wicked away by blotting with filter paper after approx. 1 min. The samples were imaged without further preparation using an FEI Tecnai transmission electron microscope.

TEM: sample preparation for study on increasing particle separation

A solution of pH 12.5 (as measured by pH probe) was made by dissolving the appropriate amount of sodium hydroxide in deionised water and stirring overnight. A solution containing 0.066 wt% SPP was made by stirring the polymer in deionised water overnight. To about 100 mL of these solutions, and to 100 mL of pure, deionised water, were added between 0.007 and 0.009 g of HNTs. The HNTs were then dispersed by 5 min of ultrasonication with a Fisher FB-505 Ultrasonic Processor at an amplitude of 50%. A further three samples were made by diluting about 2 mL of each of these suspensions with 20 mL of deionised water, and shaking vigorously. About 10 μ L of each sample was then dropped onto a carbon-coated, copper TEM grid, before being placed in a desiccator over phosphorus pentoxide for several h to allow the water to fully dry off. The samples were imaged without further preparation using an FEI Tecnai transmission electron microscope.

Manual analysis of particles in TEM images

TEM images were analysed by hand using ImageJ. MATLAB was used to fit log-normal distribution functions to the obtained dimensions (see appendix).

Automated analysis of particles in TEM images

Images in JPEG format were filtered and fitted with ellipses using custom MATLAB code (see appendix). For fitting the BL law, screen shots were taken after zooming in on appropriate particles in the original images (note that the scale of the blown-up image is different to the original). Intensity as a function of distance was then found using MATLAB. The BL law was fitted to this data in MATLAB's curve-fitting application using the Trust-Region nonlinear least squares regression algorithm, with the starting estimates outlined in the text, and default values for the algorithm controls (e.g. minimum and maximum changes in coefficients per iteration).

SAXS

Samples were prepared by adding the required amount of HNTs to deionised water and shaking by hand to disperse the nanotubes. The samples were injected into a flow cell consisting of a glass capillary tube. Scattering patterns were collected using a Xenocs Xeuss 2.0 instrument (Excillum MetalJet liquid gallium source ($\lambda = 1.34 \text{ \AA}$) and Pilatus 1M detector), a sample to detector distance of either 6.4 m or 2.5 m, and a collection time of 600 s. Images were corrected for sample transmission and background, and radially averaged to give the intensity versus q .

Dynamic Light Scattering

A solution of about pH 12 (as measured using a pH probe) was made by addition of the appropriate amount of sodium hydroxide to deionised water. HNTs were then added to make a dispersion of about 0.1 wt%. The HNTs were dispersed into the solution using about 2 min of mixing with an IKA Ultra Turrax Homogeniser set to 25,000 rpm. This solution was then measured using a Malvern Zetasizer Nano ZS. The size measurement reported in the text is the average of those calculated by the instrument software using the cumulant method, and the quoted uncertainty is the standard deviation in the average. Fitting using the CONTIN algorithm was also attempted via SEDFIT analysis software.

Chapter 3

A Comparison of Mixing Methods for Dispersing Halloysite Nanotubes into Epoxy Resin

3.1 Introduction

As discussed in Chapter 1, epoxy resins are desirable as engineering materials because of their high specific modulus relative to traditional materials such as steel.¹⁷ However, for some high-performance applications, epoxy resins are still not robust enough to replace these denser materials. The mechanical properties of epoxy resins can be increased by the inclusion of reinforcing filler materials. However, if the filler is much denser than the epoxy, the mass of a composite with the desired mechanical properties can be prohibitively high.³⁹ The use of nanoparticles rather than micro- or macroparticles can avoid this problem. This is because nanoparticles typically have a very high surface-area-to-volume ratio, meaning that there is a much higher area for interaction between the nanoparticle and epoxy per kg of filler compared to traditional, larger particles. This means that a much lower mass of nanofiller should need to be added for the same reinforcing effect to be achieved, hence nanoparticles should be more desirable for composites than traditional fillers.³⁹

Fundamental considerations for mixing of nanoparticles into epoxy resin

While the addition of nanofillers to an epoxy resin to make a nanocomposite can lead to the improvement of the mechanical properties of the polymer, this effect relies on the nanoparticle being well dispersed into the resin, i.e. each particle needs to be individually separated from the rest.^{39,128} This maximises the amount of surface area available for interaction between the two components. If nanoparticles are not sufficiently well-dispersed in a nanocomposite, either only limited improvements in mechanical properties will be seen compared to the pure polymer, no improvement will be seen, or there may even be a reduction in performance (e.g. if agglomerates of nanofiller are large enough to act as stress concentrating flaws). Therefore, good mixing of nanoparticle (i.e. dispersion of the particles at an individual level) with the bulk is crucial for the production of nanocomposites with good mechanical properties.

However, mixing nanoparticles into liquids such as an epoxy resin monomer can be challenging. This is because the entropy of mixing for a nanoparticle with a solvent or other bulk medium is typically very low.⁴⁶ As mentioned in Chapter 2, for mixing to be spontaneous, the Gibbs free energy of mixing (ΔG_{mix}) must be negative (equation 3.1). Since the entropy of mixing (ΔS_{mix}) for nanoparticles is low, for mixing to be spontaneous, either the enthalpy of mixing (ΔH_{mix}) must be negative (i.e. there are favourable energetic interactions between the nanoparticle and the bulk), or the mixing process is endothermic and energy must be put in to disperse the particles.⁴⁶ It was concluded in Chapter 2 that epoxy resins would only be expected to be moderately good solvents for HNTs, so it is probable that extensive mixing of the two would not occur spontaneously under normal conditions. In practice, the interaction between the particle surface and the bulk can be made more energetically favourable by changing the surface chemistry of the particle, or a high-shear mixing technique can be employed to overcome inter-particle interactions and force the particles to separate. The focus of this chapter is the effect of mixing.

$$\Delta G_{\text{mix}} = \Delta H_{\text{mix}} - T\Delta S_{\text{mix}} \quad (3.1)$$

Mixing strategies for dispersing HNTs into epoxy resin

Many strategies for dispersing HNTs into epoxy resins have been reported. Often, the reported mixing techniques have been low energy, utilising only basic mechanical stirring of the HNTs in the epoxy resin,^{110,131,177-179} although it could be argued in some of these cases that the application the nanocomposite is being utilised for does not necessarily require complete dispersion of the HNTs, e.g. when improving flame retardance of a resin¹¹⁰ or improving the ability of the resin to prevent metal corrosion when applied as a protective coating.¹⁷⁷ However, many studies also report the use of two higher-shear mixing techniques, namely ultrasonication and three-roll mill processing.

Ultrasonication, i.e. treatment of the mixture with ultrasound from some variety of generator, has frequently been reported as a means of dispersing HNTs into epoxy resin.^{10,108,111,125,180,181} Treating a liquid with ultrasound causes there to be fluctuating regions of high and low pressure in the fluid.¹⁸² During low pressure cycles, bubbles form, which subsequently collapse during high-pressure cycles. The collapsing of these bubbles generates extremely high local temperatures, pressures, and shear forces, which is what allows for effective mixing of components on the nanoscale.¹⁸² Dispersing HNTs into epoxy resin with ultrasonication has been shown to lead to improvements in the mechanical properties of the final nanocomposite, including modulus, strength,^{111,125} and impact strength.¹⁰ Vahedi *et al.* compared the effectiveness of using ultrasonication to disperse HNTs into epoxy resin with mechanical mixing, and found that ultrasonication produced nanocomposites with higher impact strength and increased viscosity, suggesting that ultrasonication had led to more complete dispersion of the particles.¹⁰ In contrast, Carastan *et al.* more recently compared ultrasonication to mechanical ball-milling, and found little improvement to the flexural moduli of the nanocomposites for either technique.¹⁸³ While it is clear that ultrasonication can be sometimes be effective for making epoxy/HNT nanocomposites, the exact ultrasonic processing parameters (i.e. type of instrument, ultrasonic power, and processing time) used in the literature vary widely, and are often only vaguely reported. For example, sometimes the mixing technique is referred to simply as ultrasonication, with no reference to the type and power of the instrument used.^{111,125,180,181} Ultrasonication can also variously be carried out either on the resin/nanoparticle mixture diluted with solvent to reduce its viscosity,¹¹ or on the undiluted mixture, instead relying on the heat generated during in processing to reduce viscosity.¹⁰ Because there has been no work concerning the comparison of different ultrasonication methods, and because little work has been done to compare the technique to other methods (only low-shear mechanical mixing^{10,108} and ball-milling¹⁸³), it cannot be concluded that any one of the ultrasonication procedures described in the literature is the optimum for dispersing HNTs into epoxy resin, or indeed whether ultrasonication is the best technique for doing so.

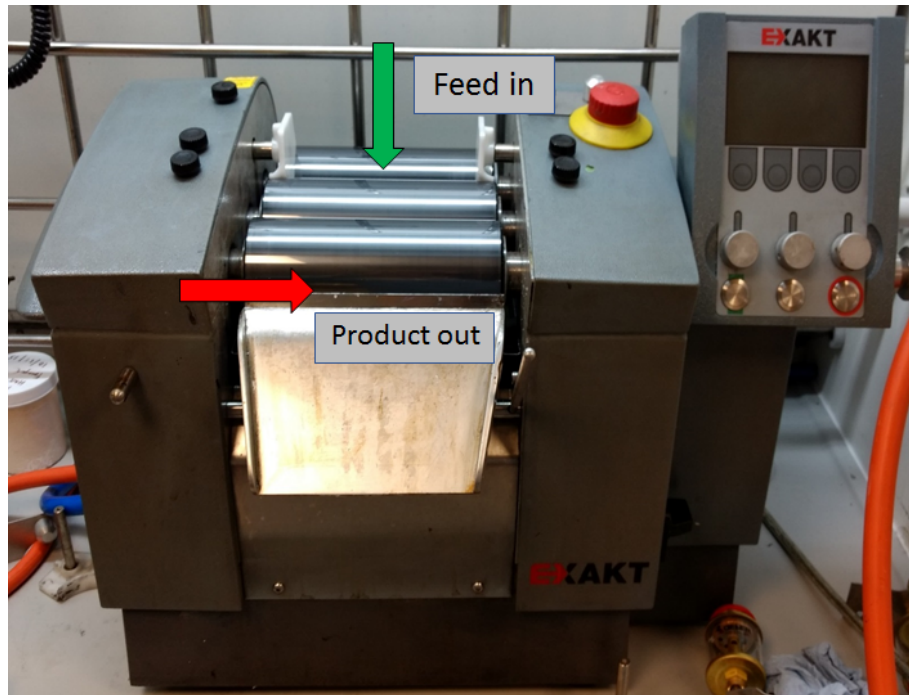
Another high-shear mixing technique which can be used to disperse nanoparticles into epoxy resin is the use of a three-roll mill (3RM). A 3RM (shown in figure 3.1) consists of three parallel rollers which rotate at different speeds and in different directions. The rear roller rotates the slowest, the middle roller three times faster, and the front roller three times faster again. The rear and front rollers rotate towards the front of the machine, with the middle roller rotating in the opposite direction. This configuration means that a viscous liquid which is fed onto the gap between the rear and middle rollers will be drawn into the machine, then pass through both the front and rear gaps and onto the front roller,

where it can be scraped off with a specially-designed knife. The rollers are driven at high torque, and the distances between them can be set to below $5\ \mu\text{m}$, which means that any material passing through the gaps experiences extremely high shear forces. This is what allows the 3RM to effectively disperse nanoparticles into viscous liquids such as epoxy resin. For example, Li *et al.* used a 3RM to effectively disperse unmodified graphene into epoxy resin, despite graphene having unfavourable energetic interactions with the epoxy.¹⁸⁴ There are two examples of a 3RM being used to disperse HNTs into epoxy resin.^{109,126} Kim *et al.* specifically looked at the flexural properties of their epoxy/HNT nanocomposites, and saw that dispersing the HNTs into the resin with a 3RM led to an improvement in the flexural strength of the final material.¹⁰⁹ However, as with ultrasonication, the reporting of the processing parameters in both these cases is vague; in fact, neither group describe any details of the mixing process beyond stating that a 3RM was used.^{109,126} This is a problem as there are several parameters that have a significant effect on dispersion quality and which can be altered when processing using a 3RM, namely processing time (i.e. how many times the sample was passed through the mill), roller speed, and inter-roller gap distances and forces.¹⁸⁴ While it is clear that the 3RM is also a good candidate for dispersing HNTs into epoxy resin, there is again a need for comparison of different processing parameters in order to establish the most effective means for doing so.

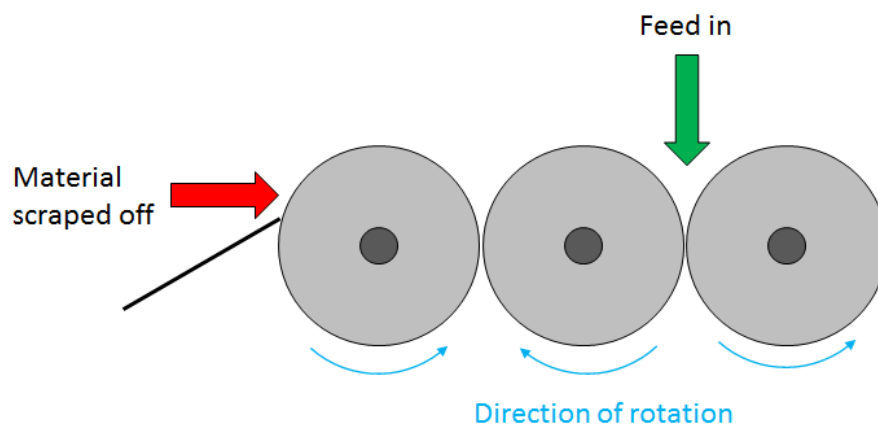
As well as achieving a good level of dispersion, it is important that a mixing technique should not damage either the filler or resin into which it is being mixed. In the case of ultrasonication of dispersions of HNTs, Rong *et al.* observed that treatment of HNTs in pure acetone at ultrasonication powers of 100 - 700 W led to significant decreases in nanotube length, with a larger extent of destruction occurring at higher ultrasonication powers and longer ultrasonication times.¹⁸⁵ Vahedi *et al.* also noted a large temperature rise in undiluted resin/HNT mixtures when ultrasonicated with no external cooling,¹⁰ so it is feasible that the resin may also be being damaged in the ultrasonication process, specifically by oxidation at high temperatures. There are no reports of damage occurring to HNTs after processing through a 3RM, but it may be that this has simply not been studied. Because the rollers in a 3RM can be set to gap distances on the order of the lengths of the longer HNTs (around $5 - 7\ \mu\text{m}$), it is feasible that breaking of the tubes may occur during processing. The ability of ultrasonication and the 3RM to produce mixtures without damaging either component must therefore also be considered alongside the degree of dispersion obtained using either method.

Aims of chapter

As was also previously highlighted in Chapter 1, when the literature for the use of HNTs in epoxy resins is taken as a whole, it is clear that there is no consistent/standard method for achieving good dispersions of the nanotubes in epoxy resins. Notably, there remains a need to compare the effectiveness of two specific high-shear mixing techniques, namely the widely-used ultrasonication technique, and the use of a 3RM. There is also a need to compare how changing processing parameters for both techniques changes the level of dispersion of HNTs into epoxy resin that can be achieved. It has also never been established whether these processing methods cause damage to HNTs when used to disperse them into epoxy resin, or to what extent any damage occurs. Therefore, it was



(a)



(b)

Figure 3.1: An example of a 3RM (a), and a diagram showing how material is fed through the rollers of the mill during processing (b).

decided that both ultrasonication and the 3RM should be trialled for making epoxy/HNT nanocomposites as a first step before carrying out any deeper work on the subject.

Initially, an additional aim of this chapter was to compare the performance of organo-modified montmorillonite clay (oMMT) as a reinforcing filler for epoxy resins to that of HNTs when nanocomposites of each were made using the same mixing strategy. As discussed in Chapter 1, this is a relevant consideration since oMMT, being already widely available, would be the main competitor to HNTs with regards to price and abundance were the use of HNTs in epoxy resins ever scaled up for commercial application. However, as will be discussed in section 3.2.4, there were significant processing challenges which prevented the manufacture of nanocomposites of oMMT in epoxy which were suitable for mechanical testing.

To aid navigation, a flowchart illustrating the structure of the chapter is given in figure 3.2.

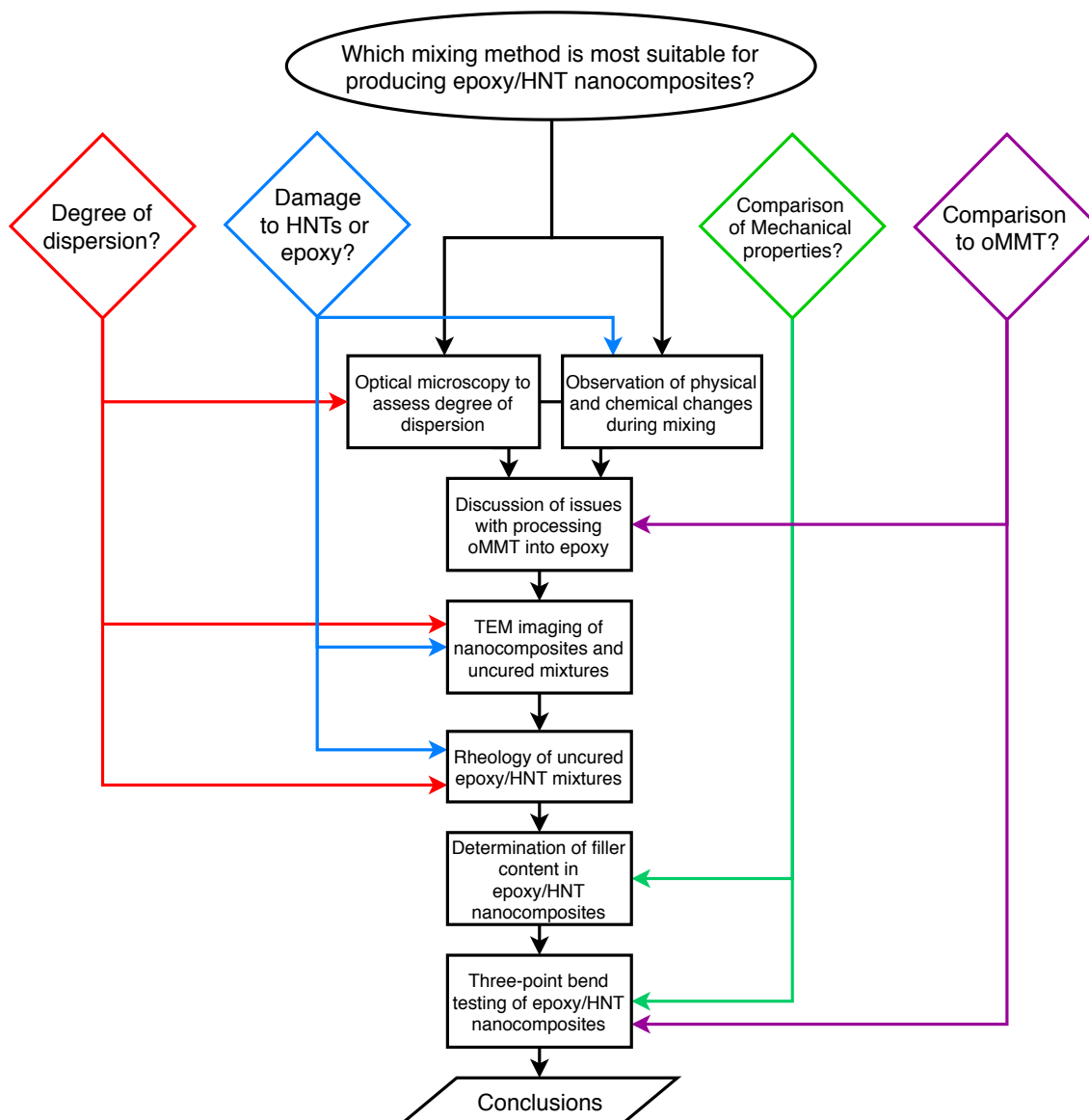


Figure 3.2: A flowchart illustrating the structure of the chapter “A Comparison of Mixing Methods for Dispersing Halloysite Nanotubes into Epoxy Resin”

3.2 Results and discussion

3.2.1 The epoxy resin system

The epoxy resin monomer chosen for use in this work was the difunctional diglycidyl ether of Bisphenol A (DGEBA), which is relatively cheap and widely used. The chemical structure of DGEBA is illustrated in figure 3.3. In terms of physical properties, DGEBA is a viscous liquid at room temperature, but becomes significantly less viscous upon heating above about 40 °C. Commercially, DGEBA is obtained by the reaction of epichlorohydrin with bisphenol A under alkali conditions, as shown in figure 3.4.¹⁸⁶ This reaction produces oligomeric as well as monomeric species, since the deprotonated phenol groups can act as nucleophiles and attack the epoxide ring.

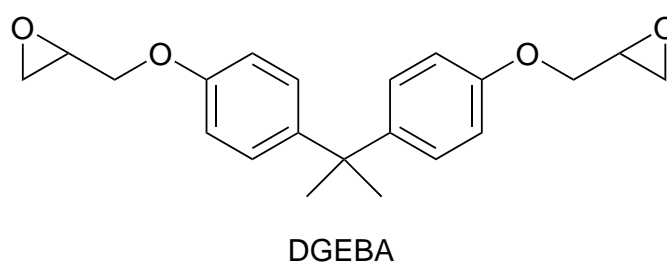


Figure 3.3: The chemical structure of DGEBA.

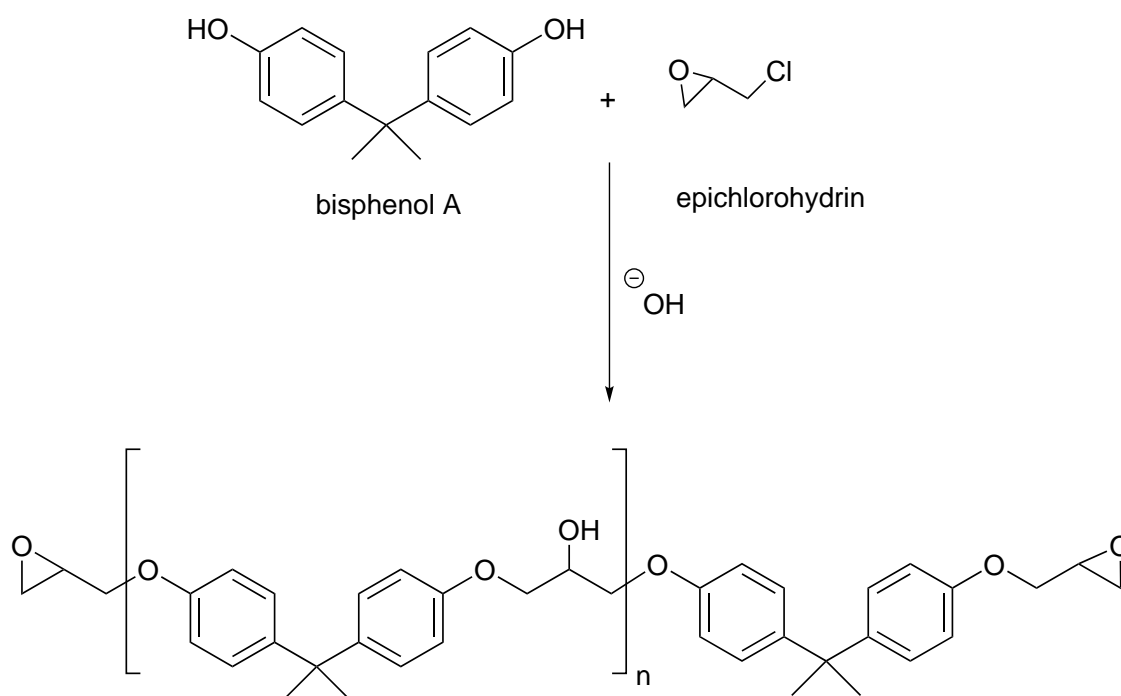
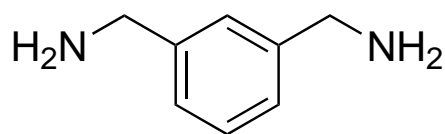


Figure 3.4: The reaction of bisphenol A with epichlorohydrin under alkali conditions produces DGEBA monomer (i.e. $n = 0$), as well as oligomeric species (i.e. $n > 0$).

As discussed in Chapter 1, epoxy resins are polymerised by the addition of a difunctional nucleophilic curing agent to the epoxy resin monomer. In this work, meta-xylylenediamine (MXDA) was chosen as the curing agent, and its chemical structure is shown in figure 3.5.

MXDA was chosen because it is a liquid which is miscible with DGEBA at room temperature, and is hence easy to incorporate into the resin, and because it represents a relatively low hazard compared to many other difunctional hardeners used to cure epoxy resins.



MXDA

Figure 3.5: The chemical structure of MXDA.

Full details of the curing process are given in the methods section, but a simple description will also be given here. The DGEBA was first mixed with MXDA to give a solution containing a slight molar excess of amine N-H groups to epoxide groups. This stoichiometric ratio had been found previously to repeatedly produce a resin with a high extent of reaction and optimum cross-link density.¹⁸⁷ This mixture was sealed in an airtight vial, and stirred repeatedly over around 1 - 2 h of pot time. After this pot time, the mixture was degassed using an ultrasonic bath for around 15 min, before being poured into the appropriate molds/vessels. The filled molds were then heated in an oven from 60 °C to around 165 °C (i.e. above the glass transition temperature of the cured resin: see section 3.2.9), where they were held for several hours to ensure that the full extent of reaction was achieved.

3.2.2 The use of ultrasonication to disperse HNTs into epoxy resin

Ultrasonication without cooling

The method described by Vahedi *et al.* was used as a first attempt to disperse HNTs into the resin.¹⁰ They used a 700 W ultrasonicator set to 50% amplitude to disperse the HNTs into resin over 1 h of processing. The ultrasonic probe used in this work was 500 W, and the amplitude was set to 70% during processing. Using equation 3.2 to convert amplitude to power gives the ultrasonication powers listed in table 3.1 (where P_s is the ultrasonication power applied to the sample, P_{\max} is the maximum power output of the ultrasonicator, and A is the amplitude). The ultrasonication power used in this work was 40% greater than that used by Vahedi *et al.*¹⁰ In their work, they noted that the temperature of the resin increased to about 100 °C during processing, so the temperature of the mixing vessel used here was monitored throughout sonication using a thermocouple attached to the vessel exterior.¹⁰

$$P_s = P_{\max} A^2 \quad (3.2)$$

Measuring the temperature of the vessel during ultrasonication showed that the temperature rose much higher than that reported by Vahedi *et al.*¹⁰ This is probably because of the higher ultrasonication power used here, although the temperature they report for the

Table 3.1: The ultrasonication powers used by Vahedi *et al.*¹⁰ versus this work.

	Ultrasonicator power/W	Amplitude/%	Ultrasonication power/W
This work	500	70	245
Vahedi <i>et al.</i> ¹⁰	700	50	175

mixture is vague, i.e. they presumably did not measure temperature continuously, so it may have risen higher than they report. As can be seen in figure 3.6, in this work, the temperature of the resin rose rapidly under continuous ultrasonication, reaching over 160 °C after about 25 min. At this temperature, the resin started to boil and even smoke, so the ultrasonication was stopped for the sake of safety. After ultrasonication, the resin/HNT mixture had turned noticeably darker than a similar concentration mixture of resin/HNTs that had not been processed in this way (figure 3.6). This suggests that some kind of oxidation of the resin had occurred at the high temperatures. Heating of the sample during continuous ultrasonication clearly puts a limit on the overall processing time that can be used (indeed, the 25 min managed here is already much lower than the 1 h reported by Vahedi *et al.*).¹⁰

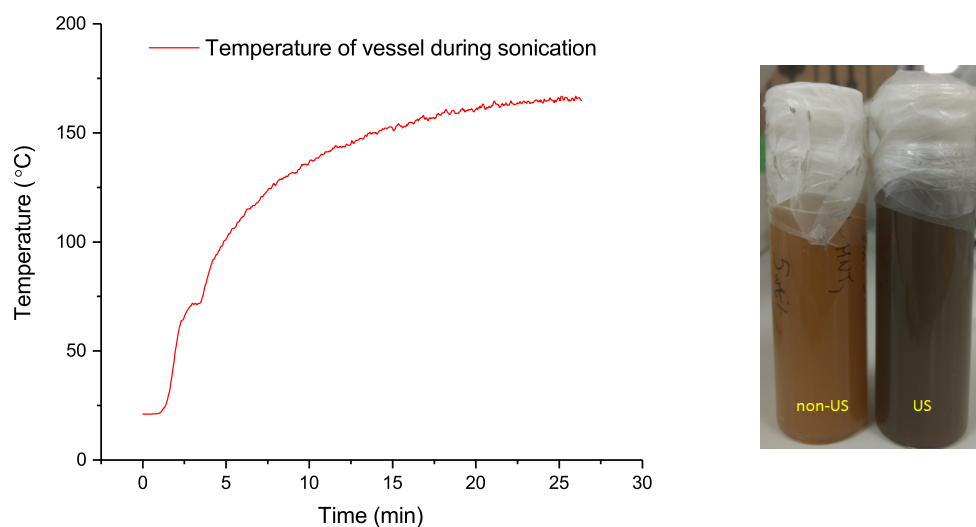


Figure 3.6: A graph showing the temperature rise of the mixing vessel during continuous ultrasonication of an epoxy/HNT mixture (left), and a comparison of resin/HNT mixtures which have and have not undergone ultrasonication (right). The mixture treated with ultrasonication (US) is much darker than the other (non-US), which suggests that oxidation of the resin has occurred.

Only a poor level of dispersion was achieved after 25 min of continuous ultrasonication. This is obvious from the large agglomerates visible in the optical microscope images taken of the samples made by continuous ultrasonication, which can be seen in figure 3.7. If the nanoparticles were dispersed as individual particles, optical microscopy would be expected to show no features since the particles are small compared to the wavelengths of visible light. Therefore, it was concluded that continuous ultrasonication processing at

245 W for 25 min was not an effective way to disperse HNTs into epoxy resin.

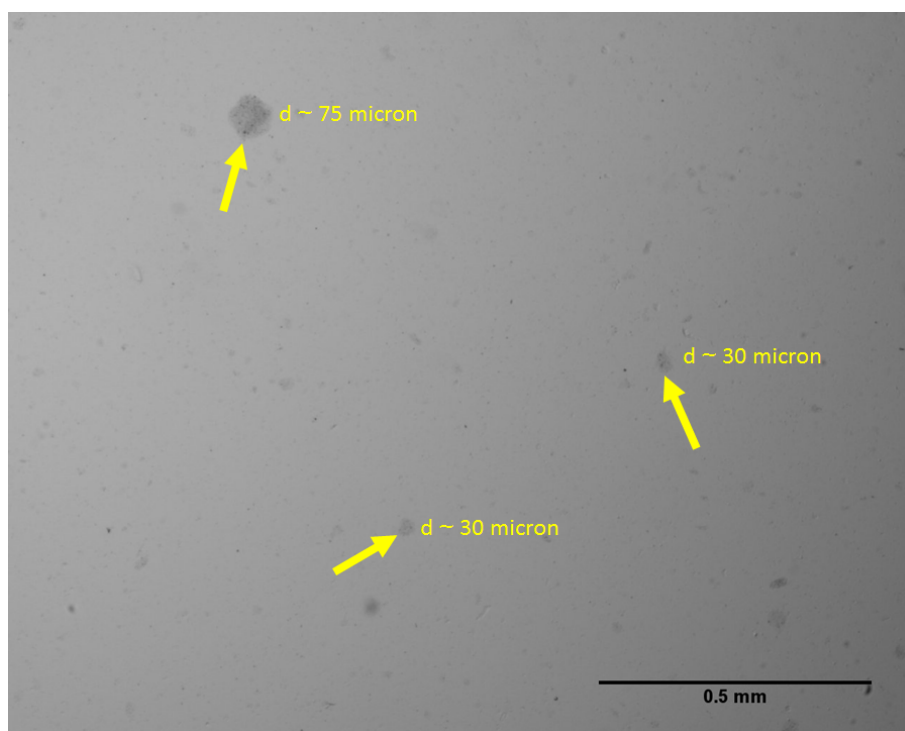


Figure 3.7: An optical microscope image of a sample of HNTs in epoxy which was treated to 25 min of continuous ultrasonication. There are still relatively large (tens of μm in diameter) agglomerates of HNTs visible, some examples of which are indicated by the yellow arrows. This shows that complete dispersion of the particles was not achieved.

However, while it is clear that this method did not fully disperse the HNTs into the resin, it was apparent that the level of dispersion did increase with increasing processing time. Figure 3.8 shows optical microscope images taken at different ultrasonication times. These seem to show, at least qualitatively, that longer ultrasonication led to increasingly small agglomerates. This suggested that ultrasonication might still be an effective method for dispersing the HNTs were it possible to extend the time for which the mixtures could be safely processed.

Ultrasonication with solvent dilution and cooling

The next method used to disperse the HNTs into the resin was ultrasonication at the same power (i.e. 245 W), but this time using dilution of the epoxy with acetone to reduce its viscosity, and external cooling of the mixture with an ice bath. As an extra measure to keep the mixture cool, ultrasonication was carried out in pulses (45 s on, 15 s off) which allowed some of the heat built up during ultrasonication cycles to dissipate. As can be seen in figure 3.9, the temperature of the vessel remained low (around 5 °C) over much of the processing time, and would presumably be able to be kept low indefinitely if the ice in the ice bath were to be replenished (or another method of continuous cooling used). Processing in this way therefore allowed the epoxy/HNT mixture to be sonicated for much longer than the previous method; mixing was stopped after 80 min, which was

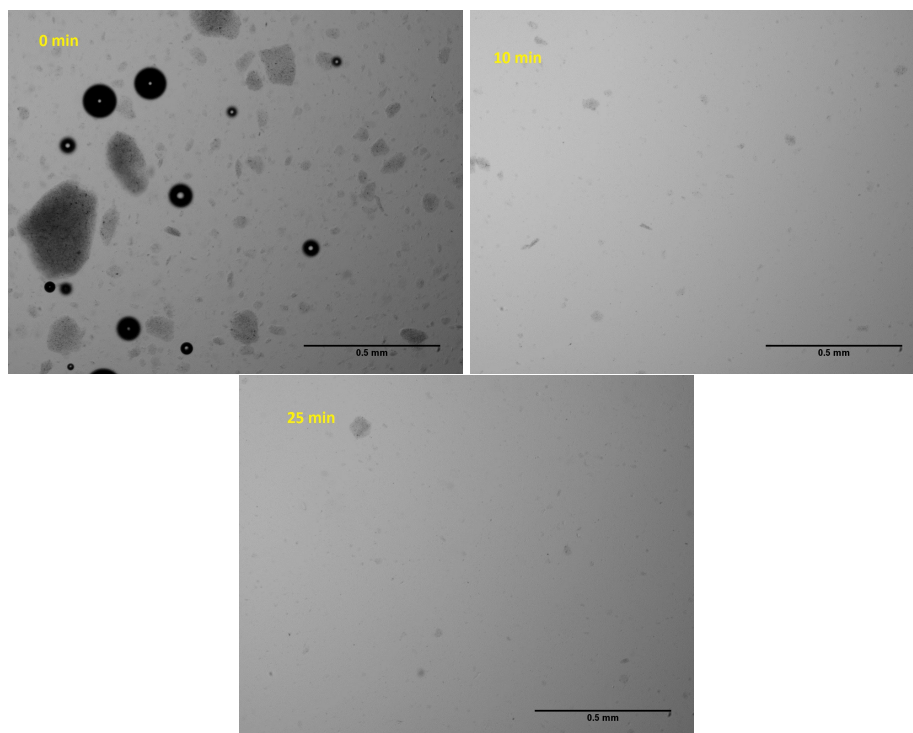


Figure 3.8: *Optical microscope images taken at different times during continuous ultrasonication of an epoxy/HNT mixture. The agglomerates decrease significantly in size and number the longer ultrasonication proceeds.*

equivalent to 60 min of the sample being treated with ultrasonication, compared to 25 min previously.

However, while ultrasonication with dilution and external cooling allowed for much longer processing times, it appears that the level of dispersion achieved reaches a maximum before extremely long processing times are reached. Specifically, DLS measurements of samples taken from the mixture at different times (figure 3.10) show that the average size of the suspended particles reaches a minimum of approximately 700 nm after around 45 min of ultrasonication (i.e. 1 h total processing time). That is not to say that this indicates that the HNTs are individually dispersed by this time, especially since neat HNTs were measured by DLS to have a size of 395 nm (see Chapter 2). Nonetheless, DLS suggests that the maximum degree of dispersion of HNTs into a diluted epoxy resin has already occurred after about 35 - 45 min of ultrasonication, at least at this ultrasonication power.

Optical microscope images also show a decrease in the size of the agglomerates over time in this processing procedure. However, as can be seen in figure 3.11, some relatively large particulates are still visible, even after 80 min of processing. This is probably due to the localised nature of the mixing by ultrasonication, i.e. mixing only occurs where a cavitation event occurs. At any given time, there may remain large agglomerates in the sample which by chance have not experienced a sufficient number of mixing events to be fully broken apart. The likelihood of an agglomerate not having interacted with a sufficient number of cavitation events decreases as time goes on, but from figure 3.11, it is at least clear that greater than 60 min of ultrasonication is required to break up absolutely all of the agglomerates in the sample.

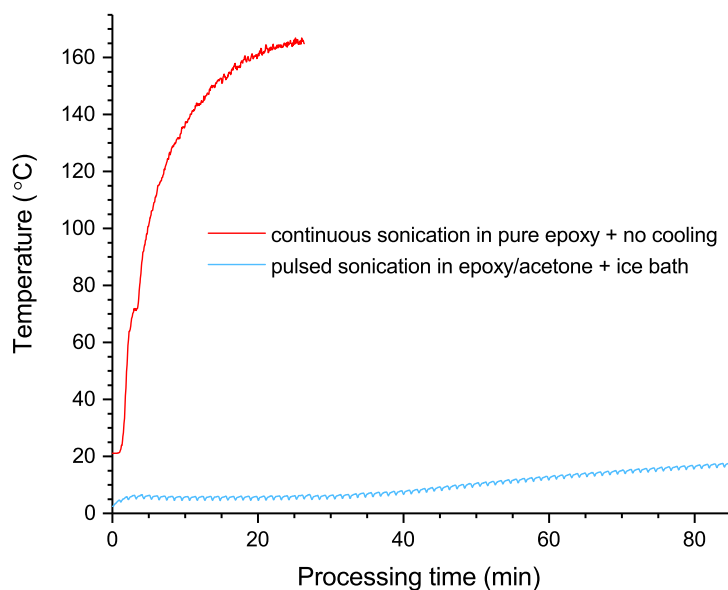


Figure 3.9: The temperature of the vessel exterior during continuous ultrasonication of an undiluted resin/HNT mixture with no cooling (red), compared to pulsed ultrasonication of a resin/HNT mixture diluted with acetone which was cooled with an ice bath (blue). With pulsed ultrasonication and external cooling, the temperature of the mixture could be kept low throughout processing.

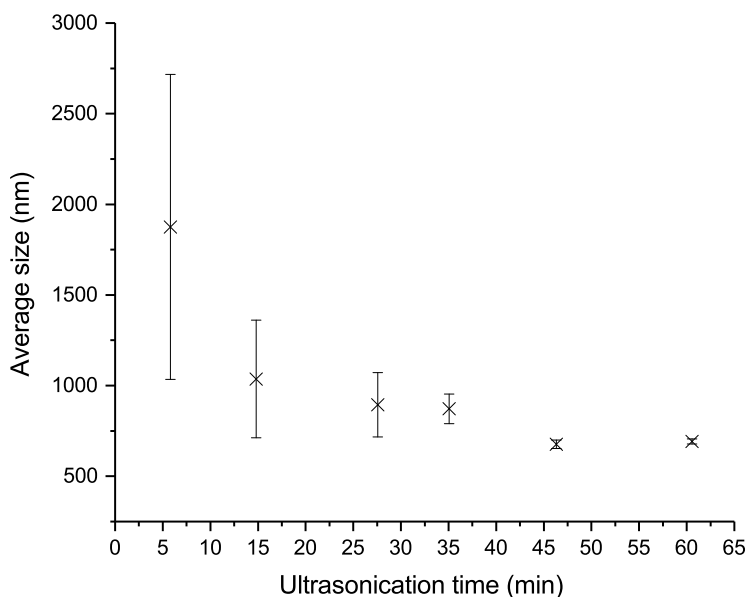


Figure 3.10: The size of HNTs during ultrasonication in epoxy diluted with acetone, as measured by DLS. The size at each time is an average of three measurements, and the error bars are the standard deviation in this average. The average size is seen to decrease as ultrasonication proceeds, until a plateau is reached after about 45 min.

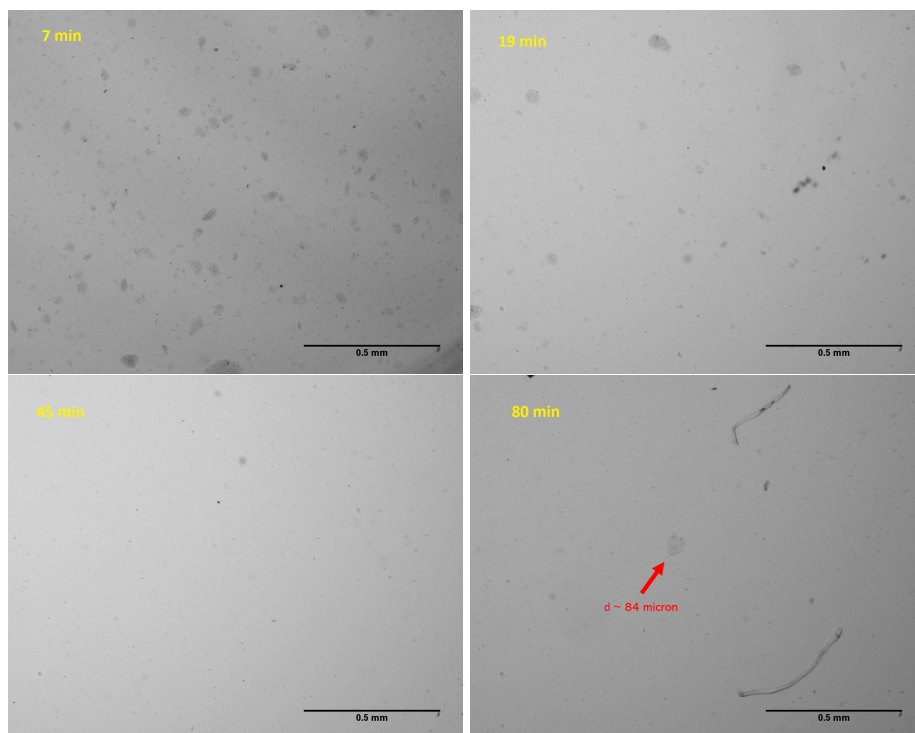


Figure 3.11: Optical microscope images taken during pulsed ultrasonication of an epoxy/HNT mixture diluted with acetone. The agglomerates decrease significantly in size and number the longer ultrasonication proceeds. However, even after 80 min, large agglomerates (an example is indicated with the red arrow) can still be found in the samples. The worm-like features in one of the images are motes of dust caught in the resin.

3.2.3 The use of a three-roll mill to disperse HNTs into epoxy resin

Choice of processing parameters for using the three-roll mill

A typical 3RM has two user-defined parameters which influence the final dispersion state of the mixture being processed, namely the inter-roller gap distances and the rotation speed of the rollers. Both of these machine parameters affect the shear forces experienced by the mixture as it goes through the rollers, as will the viscosity of the material itself.¹⁸⁴ The gaps between the rollers can be set in either gap mode or force mode, meaning that either the distance between the rollers is set by the user, or the force between the rollers is set. The minimum gap distance which can be set in gap mode is 5 μm , whereas force mode can be used to achieve gap distances of below 1 μm . This obviously means that finer dispersions can be achieved using force mode, but the use of force mode is also more risky as there is the possibility that the rollers can touch at low gap widths, which causes catastrophic damage to the machine. However, this only happens in normal operation if a portion of the rollers becomes dry during processing, meaning that force mode can only be safely used if the whole width of the rollers remains wetted with product throughout. This essentially puts a lower limit on the amount of material that can be effectively processed in force mode (from experience, this is around 100 g). In contrast, relatively small amounts of a mixture can be handled in gap mode as it is safe to use only a small portion of the rollers. This makes gap mode more desirable when materials are expensive, or only available in limited amounts.

In a typical 3RM procedure, the gap widths are initially set to be relatively large, and gradually decreased with each pass until a final minimum gap or maximum force is set. This gradually increases the fineness and homogeneity of the mixture. The mixtures are passed through the rollers at the minimum gap width several times until the desired degree of dispersion is reached. Indeed, the total number of passes through the machine is another important processing parameter. For example, Li *et al.* showed that at least eight passes through their 3RM (with the final five in force mode) were required to break stacks of graphene into individual platelets.¹⁸⁴ It is clear that all of the inter-roller gap distances/forces, the roller speeds, the mixture viscosity, and the number of passes through the machine must be considered when processing on a 3RM, and must at the very least be recorded and kept similar between batches if repeatable mixing results are to be obtained.

However, as previously mentioned, although there are examples in the literature of a 3RM being used to disperse HNTs into epoxy resin, the reporting of processing parameters in these cases is vague.^{109,126} Therefore, the processing parameters used here had to be chosen using common sense and with some technical advice from the 3RM manufacturer. More specifically, the gaps between rollers and roller speeds were simply set to values which allowed the material to be processed at a reasonable speed (a few minutes per pass through the machine), with only the front gap set to the lowest gap width/maximum force for the final passes. It was decided that gap mode would be used initially to avoid any damage to the machine, and because the minimum gap of 5 μm is close to the length of the larger HNTs, so it was unknown whether processing below this gap width would cause damage to the nanotubes.

Three-roll mill processing: gap mode

In the first trial of processing HNTs into the resin with the 3RM, the mixture was processed five times through a final gap width of $5\ \mu\text{m}$. As illustrated in figure 3.12, optical microscopy showed that many agglomerates of up to about $80\ \mu\text{m}$ remained in the sample, i.e. agglomerates much bigger than the $5\ \mu\text{m}$ gap distance.

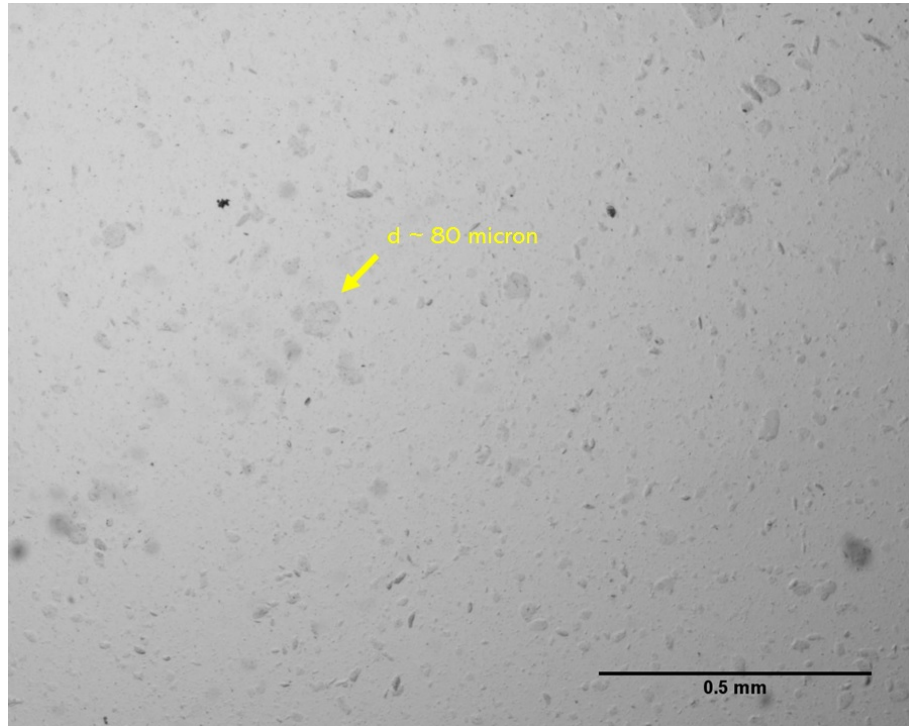


Figure 3.12: An optical microscope image taken of an approximately 5 wt% epoxy/HNT nanocomposite made by passing the epoxy/HNT mixture 5 times through the 3RM at a $5\ \mu\text{m}$ gap setting. Many large agglomerates (an example is indicated with a yellow arrow) are still visible, suggesting that this was a poor mixing technique.

This might be due to the particulates being broken up into anisotropic sheet-like particles when passing through the gap, with one dimension being $5\ \mu\text{m}$, but the other two remaining large, which is illustrated in figure 3.13. This is almost certainly an oversimplification of the dynamics of particles passing through the mill, which probably involves complex deformations of the relatively-loosely-bound agglomerates, but nonetheless it certainly seems feasible that certain large agglomerates can pass through small gap widths with little damage. In any case, it is clear that five passes through the 3RM at a final gap of $5\ \mu\text{m}$ was not sufficient to break up agglomerates and disperse the HNTs into the resin.

However, it was not known whether good dispersion could be achieved simply by passing the material through the $5\ \mu\text{m}$ gap more times. It was thought that with enough passes, each agglomerate might have passed through the gap and been broken up enough times that every dimension would be reduced to the order of $5\ \mu\text{m}$ (i.e. the order of the individual nanotubes' lengths). The process was hence repeated, but this time the mixture was passed through the final gap width 15 times. Optical microscopy (figure 3.14) once again showed that large agglomerates remained in the sample. These were smaller than those seen when only five passes were used, suggesting that increasing the number of passes through the

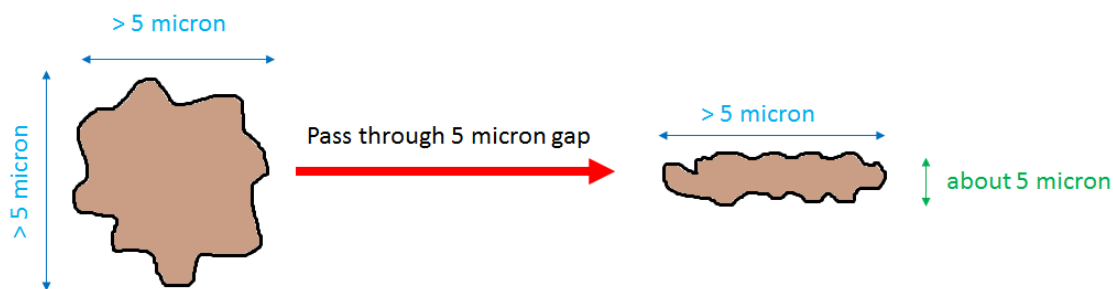


Figure 3.13: An illustration of a simple possible explanation for why agglomerates much larger than $5\ \mu\text{m}$ remain in epoxy/HNT mixtures after several passes through a $5\ \mu\text{m}$ gap width. Essentially, it is feasible that a particle can pass through the gap with a large size in one or two dimensions, so long as it has at least one dimension of $5\ \mu\text{m}$ or less.

machine was indeed effective at increasing the level of dispersion of the HNTs. However, running the material through the machine 15 times at the lowest gap width already took several hours, so it was decided that while increasing the number of passes through the 3RM at a $5\ \mu\text{m}$ gap width might eventually lead to a good dispersion of HNTs, this would almost certainly be too time and labour intensive to be practical.

Three-roll mill processing: force mode

After the use of the 3RM's gap mode to disperse the HNTs into epoxy was concluded to be ineffective, doing so using force mode was investigated. In the final mixing step, the mixture was passed 10 times through a gap set to the maximum machine force of $26\ \text{Nmm}^{-1}$. This appeared to lead to some heating of the product, but not to the extent seen during ultrasonication. More specifically, the final mixture obtained using force mode was warm to the touch, and estimated to have been around $40 - 50\ ^\circ\text{C}$. However, there is no way of telling what temperature was reached by the mixture while passing through the roller gaps; this is probably much higher because of the high shear forces being applied. Nonetheless, there was no obvious colour change to the resin as observed in section 3.2.2. The increase in temperature certainly did seem to reduce the mixture viscosity, and have an affect on the forces between the rollers. Figure 3.15 shows how the real-time inter-roller force reading decreased as the mixture heated up after repeated passes through the machine in force mode. Cooling of the rollers is possible, but it was found to cause some complications with the use of the machine. Despite heating of the mixture potentially reducing the effectiveness of mixing, optical microscopy (figure 3.16) showed very few visible agglomerates remaining in the samples made via force mode, suggesting that the process had been effective at dispersing the nanoparticles.

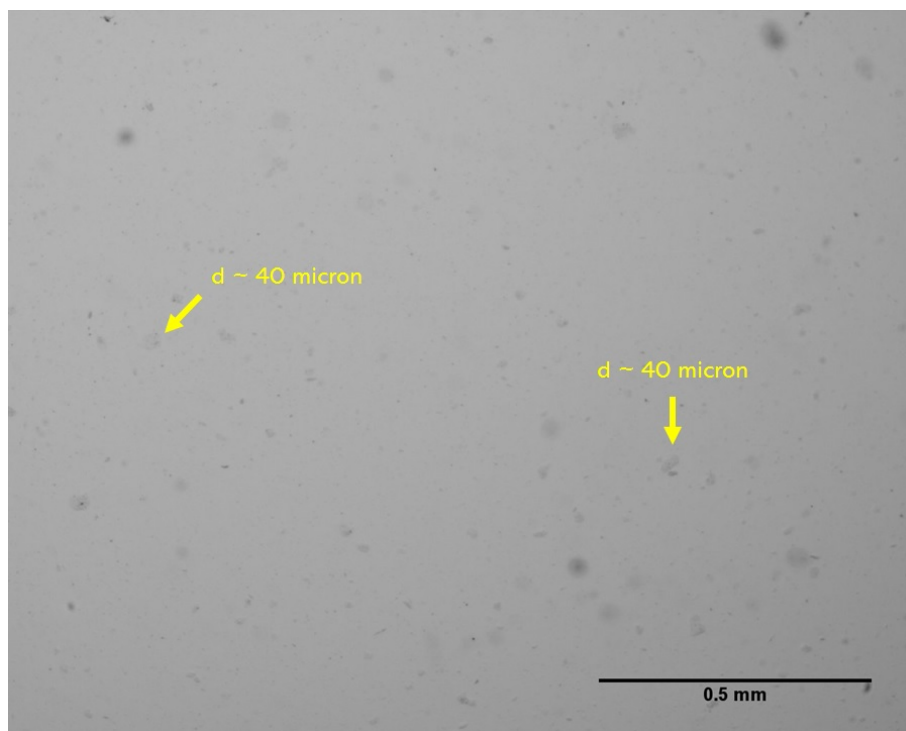


Figure 3.14: An optical microscope image taken of an approximately 2 wt% epoxy/HNT nanocomposite made by passing the epoxy/HNT mixture 15 times through the 3RM at a 5 μm gap setting. Many agglomerates are still visible (two examples are indicated with yellow arrows), suggesting that this was a poor mixing technique, but they are typically much smaller (about half the size) than the agglomerates seen after 5 passes through the mill at this gap width. This suggests that increasing the number of passes through the 3RM in gap mode can increase the level of dispersion of the particles.

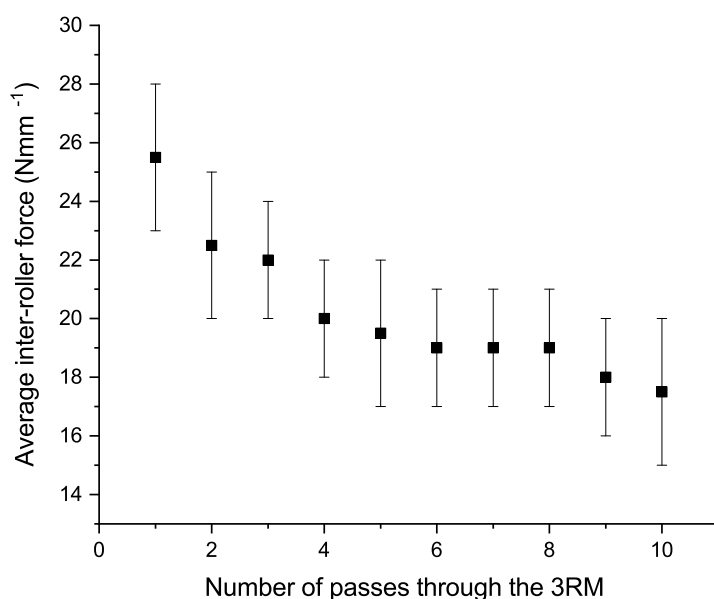


Figure 3.15: A graph showing how the mean force between the front 3RM rollers decreased as a mixture was repeatedly passed through it in force mode. Heating of the mixture reduces its viscosity, reducing the forces experienced between the rollers. The error bars are half the range of observed values.

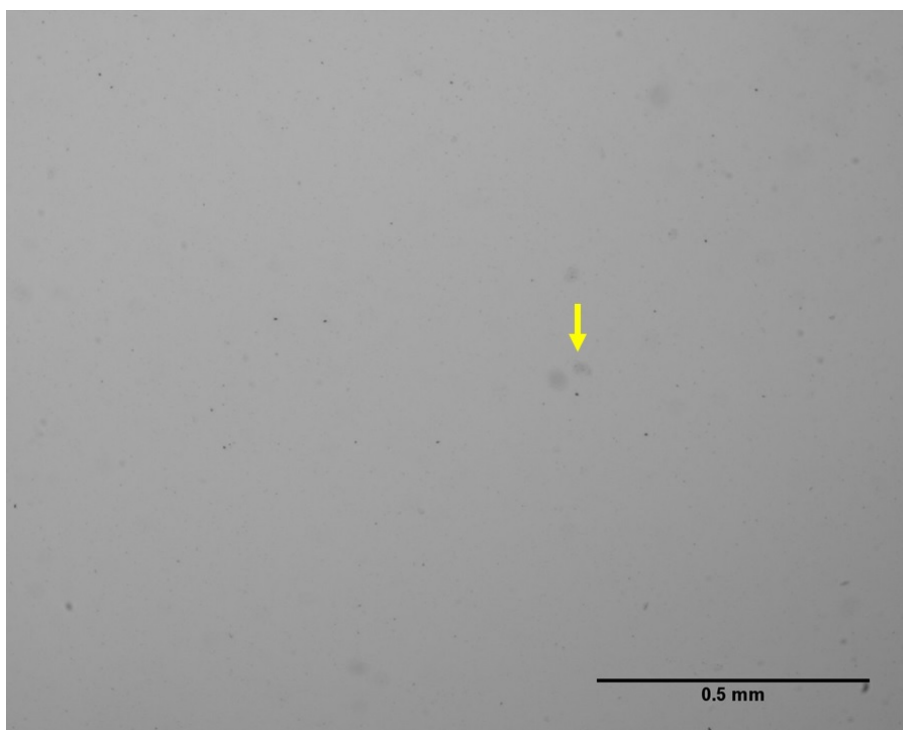


Figure 3.16: An optical microscope image taken of an approximately 2 wt% epoxy/HNT nanocomposite made by passing the epoxy/HNT mixture 10 times through the 3RM at the maximum force setting. Visible agglomerates are rare (an example is indicated with a yellow arrow), suggesting that this was a good mixing technique.

3.2.4 Issues experienced with processing organo-montmorillonite into epoxy resin

As noted in the introduction, significant processing challenges were encountered when making epoxy/oMMT nanocomposites. More specifically, mixing oMMT into epoxy resin caused a significant degree of foaming, presumably due to some combination of the alkyl ammonium species used to modify the organoclay acting as surfactants, and the hydrophobic coated particles stabilising the resulting bubbles of air. For example, figure 3.17 shows a 2 wt% mixture of oMMT in epoxy made by diluting the concentrated epoxy/oMMT paste obtained from the 3RM with pure resin, warming the vessel to 40 °C to reduce viscosity, then stirring vigorously by hand. It can be seen that the mixture is opaque because of the large number of bubbles present.

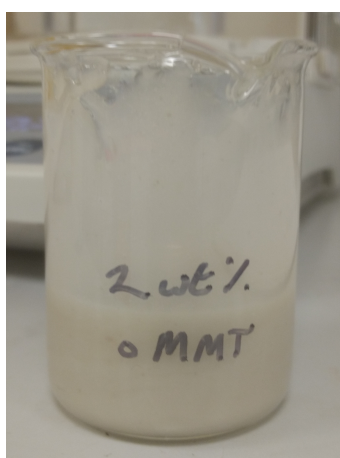


Figure 3.17: A mixture of oMMT and epoxy resin which is opaque because of the degree of foaming which occurs upon mixing.

Degassing of these mixtures was attempted, however this was found to be both labour and time intensive. Firstly, degassing was attempted simply by applying vacuum to the samples. However, this led to a substantial increase in volume of the mixture as the trapped gas expanded, meaning that the vacuum could not be left on or the mixture would spill out of the vessel. An example is shown in figure 3.18. Instead, the vacuum had to be manually cycled on and off. However, even with over two hours of vacuum cycling, and the resin being heated to reduce its viscosity, complete degassing could not be achieved using this method.

It was found that effective degassing of the uncured epoxy/oMMT mixtures could be achieved by extended treatment in an ultrasonic bath at around 40 °C. The required treatment time was on the order of hours, and increased with increasing oMMT content in the mixture. Examples of 1 and 2 wt% mixtures of epoxy/oMMT which had been degassed using an ultrasonic bath are shown in figure 3.19. However, addition of the hardener to the resin required further vigorous mixing, which served to reintroduce the bubbles. These bubbles could not be removed using the ultrasonic bath on the time scale of the pot time of the curing resins.

It was thought that these bubbles might be able to escape the resin as its viscosity decreased in the initial stages of being heated in the curing oven. However, when samples



(a) Before application of vacuum. (b) Shortly after application of vacuum.



(c) The mixture quickly begins to spill (d) Releasing the vacuum causes the expanded bubbles to collapse.

Figure 3.18: Images illustrating the rapid expansion of gas in an epoxy/oMMT mixture as vacuum is applied (in this case using a rotary evaporator).



Figure 3.19: Mixtures of 1 and 2 wt% epoxy/oMMT after around one hour of treatment in an ultrasonic bath at 40 °C. The 1 wt% sample has almost been fully degassed, although longer treatment times are needed for mixtures with a higher oMMT content than this.

of epoxy/oMMT were degassed as much as possible with the ultrasonic bath before being cured, it was found that large bubbles remained throughout the depth of the samples, which would have had a significant affect on the mechanical properties of the nanocomposites. An example is shown in figure 3.20. In contrast, all of the epoxy/HNT nanocomposites could be completely degassed with 15 min of treatment in the ultrasonic bath. Therefore, it was concluded that epoxy/oMMT nanocomposites could not be made in the same way as epoxy/HNT nanocomposites, and hence a direct comparison between the two types of filler could not be made in this work.



Figure 3.20: *A sample of epoxy/oMMT nanocomposite which had been cured after extensive degassing using an ultrasonic bath. The sample has been backlit to illustrate the large number of bubbles that remain throughout the material after curing.*

3.2.5 Sample labelling

Consistent sample labelling is used throughout the remainder of this chapter. The letters G, F, S, and AS refer to samples made using: the 3RM in Gap mode (G); the 3RM in force mode (F); ultrasonication with neither cooling, nor solvent dilution (S); and ultrasonication with dilution with acetone and external cooling (AS). In the case of the G samples, the prefixes 5 and 15 refer to the number of passes of the material through the 3RM. The suffixes 1, 2 and 5 refer to the approximate weight fraction of HNTs added to the epoxy resin before mixing (note that these weight fractions are lower than the actual fraction of filler in the final nanocomposites because of the contribution of the additional mass of the hardener). These abbreviations are also summarised in table 3.2.

Table 3.2: A summary of the abbreviations used to label samples in this chapter. The suffixes 1, 2 and 5, which are later used with these abbreviations, refer to the approximate amount of HNTs which were added to the epoxy resin before mixing (in wt%).

Abbreviation	Meaning
S	Sample made by ultrasonication in epoxy resin with neither dilution, nor cooling.
AS	Sample made by ultrasonication in epoxy resin but with both dilution with acetone, and external cooling.
5G	Sample made using five passes through a 5 μm gap with the 3RM in gap mode.
15G	Sample made using fifteen passes through a 5 μm gap with the 3RM in gap mode.
F	Sample made using ten passes through a maximum gap force with the 3RM in force mode.

3.2.6 Using TEM to study the degree of dispersion and size of halloysite nanotubes in epoxy/HNT nanocomposites

In a nanocomposite material, the optimum degree of mechanical reinforcement is achieved when the nanofiller is distributed to the level of individual particles.¹²⁸ Because of this, it is useful to have a means of studying how well dispersed the particles are in the bulk medium. Were the particles found to be poorly dispersed, it would be clear that a different mixing strategy would be required to improve the performance of the final material.

In practice, there are several possible methods for studying the dispersion of particles in a polymer, but the most appropriate method to use depends on the type of filler being studied. The most direct method is the use of microscopy at the appropriate length scale, with TEM being a widely-used example for studying nanofillers. However, sample preparation for TEM imaging of bulk polymer is not straightforward, as it requires specialised cutting tools and expertise for the preparation of very thin samples (typically <100 nm). As noted in Chapter 2, TEM is also time-consuming, subjective, and has the disadvantage of not necessarily being representative of the whole sample since only a relatively small area of the material can be studied. Bulk scattering techniques, such as SAXS, can be used to

study the aggregation state of nanofillers in polymer nanocomposites, as long as the particles have well defined shapes and are relatively mono-disperse in size, for example silica nanoparticles.^{188,189} However, as shown in Chapter 2, SAXS measurements of HNTs do not give any useful information about the size or relative positions of the particles due to their polydisperse shapes and sizes. Alternatively, WAXS can be used to study dispersions of many types of platy nanoparticles, such as graphene,¹⁸⁴ montmorillonite,¹⁹⁰ and kaolinite.⁵⁹ These particles exist as stacks of plates in their native (i.e. unmixed) states, and the interlayer spacing (i.e. d_{001}) in these stacks is an inter-particle distance. The d_{001} is typically of the right size to be measured using WAXS, and the absence of the d_{001} peak in nanocomposites containing these nanoplates can hence be used as evidence of a good degree of dispersion of the particles (although it is not conclusive evidence of this on its own).¹⁹⁰ However, the d_{001} in HNTs is an intra- rather than inter-particle distance, and hence gives no information about the degree of separation of individual particles. Since the bulk X-ray scattering techniques commonly used for other nanofillers are not applicable to HNTs, it was concluded that TEM was the most appropriate method for studying the dispersion of HNTs in epoxy/HNT nanocomposites, despite its disadvantages.

TEM imaging of nanocomposite samples

To assess the nanoscale dispersion of the HNTs in the epoxy/HNT nanocomposites, TEM images were taken of the 15G, F, S and AS samples (see table 3.2). Samples of HNTs imaged in the epoxy/HNT nanocomposites are denoted with the prefix N. These TEM images are shown in figure 3.21.

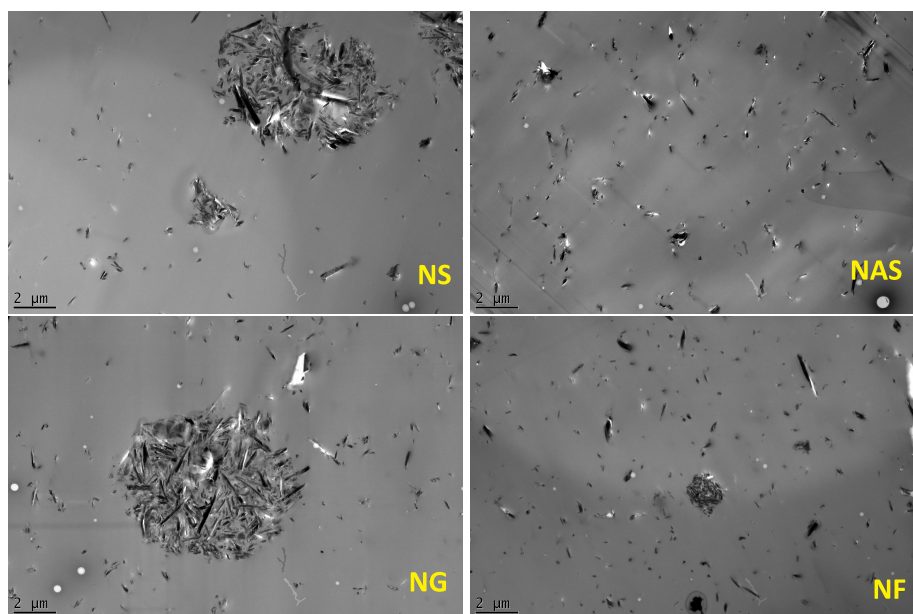


Figure 3.21: TEM images of nanocomposites of HNTs and epoxy made by different mixing methods. Large agglomerates of several μm were visible for the S and G samples, whereas most of the HNTs seemed to be individually dispersed in images of the AS and F samples.

In the area observed by TEM, both the NS and NG samples were seen to have large (i.e. many μm in diameter) agglomerates of HNTs, which was expected since many large ag-

glomerates were visible in optical microscope images of these samples. Interestingly, these samples did also contain individually dispersed HNTs, suggesting that the mixing had been successful at least to some extent. It was even possible to find areas of the badly mixed 15G sample where all of the HNTs in the frame of the TEM image were individually dispersed (figure 3.22). This is important to note, since if only this image were considered, it would be reasonable to conclude the HNTs to have been well-dispersed in this sample, which is clearly not the case. That is to say, this shows that it is important to survey a large area and take many images when conducting TEM of polymer nanocomposites.

In contrast, agglomerates in the images of NF and NAS samples were rare, and those that were observed were considerably smaller than those seen for NG and NAS. Most of the HNTs in these samples were individually dispersed. From qualitative assessment of TEM images at least, it is clear that all of the mixing techniques dispersed the HNTs as individual particles to some extent, but only in the NF and NAS samples can the HNTs be considered to have been essentially fully dispersed. On the basis of these images and those acquired by optical microscopy, using the 3RM in force mode and ultrasonating the HNTs in an epoxy/acetone solution can be concluded to be effective mixing strategies for dispersing HNTs into epoxy resins.

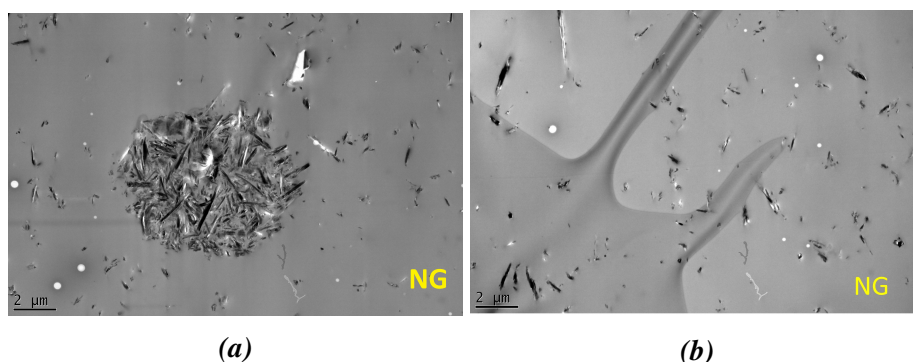


Figure 3.22: TEM images of nanocomposites of HNTs and epoxy made using the 3RM in gap mode. A large agglomerate of several μm is visible in image (a), but not image (b). This illustrates the potential for incorrect conclusions to be drawn from TEM images if only a small area/number of images is considered in isolation.

In order to determine whether any damage had occurred to the nanotubes during the mixing process, the lengths of several hundred HNTs were measured in TEM images of each sample. As would be expected from Chapter 2, the lengths in each sample appeared to follow a log-normal distribution. Table 3.3 lists the most probable (i.e. mode) lengths of the log-normal distributions fitted to the HNTs in the N samples, as well as the maximum nanotube length measured in each sample. For all of the samples, the mode tube length was considerably shorter than that which had originally been found for pure HNTs in Chapter 2 (i.e. 486 nm), and the mode length of the nanotubes were found to be much smaller for the NF and NAS samples than the NS and NG. In addition, the maximum length of HNTs measured for all of the nanocomposite samples was found to be about three times shorter than the maximum measured for the pure HNTs (i.e. 6763 nm). This might lead one to conclude that all of the mixing techniques damaged the nanotubes, specifically by breaking them into shorter lengths, as has been concluded by some authors.¹³² However, it did not make sense that two very different mixing techniques (i.e. ultrasonication and 3RM)

would cause damage to the HNTs such that they ended up very similar in length (e.g. the mode lengths of the distributions for NF and NAS were only 3 nm apart). This suggested that other factors could be at play, namely sample preparation for TEM imaging of the nanocomposites.

Table 3.3: The mode lengths of the log-normal distributions fitted to the HNTs seen in TEM images of the *N* samples, and the maximum length of tube measured for each sample.

Sample	Mode length/nm	Maximum length/nm
NS	221	2120
NAS	163	1687
NG	205	2184
NF	160	1949

To prepare the samples for TEM imaging, slices of the nanocomposites had to be prepared which were thin enough to be transparent to the electron beam. While the exact thickness of the samples was not measured, the cutting tool was set to cut slices of around 85 nm thickness. This is similar to the external diameters of many of the nanotubes, and is much smaller than the lengths of the tubes. The act of cutting these slices probably directly affects the HNT lengths measured in the images of the nanocomposites since it is probable that many nanotubes lay across a cutting face, and were subsequently chopped into two. This would lead to an increased number of short nanotubes in the final material. In addition, the 2D profile of TEM images means that any HNTs rotated to a significant degree perpendicular to the plane of the image would appear shorter. Both of these possible reasons for the apparent shortening of the HNTs in the TEM images are illustrated in figure 3.23.

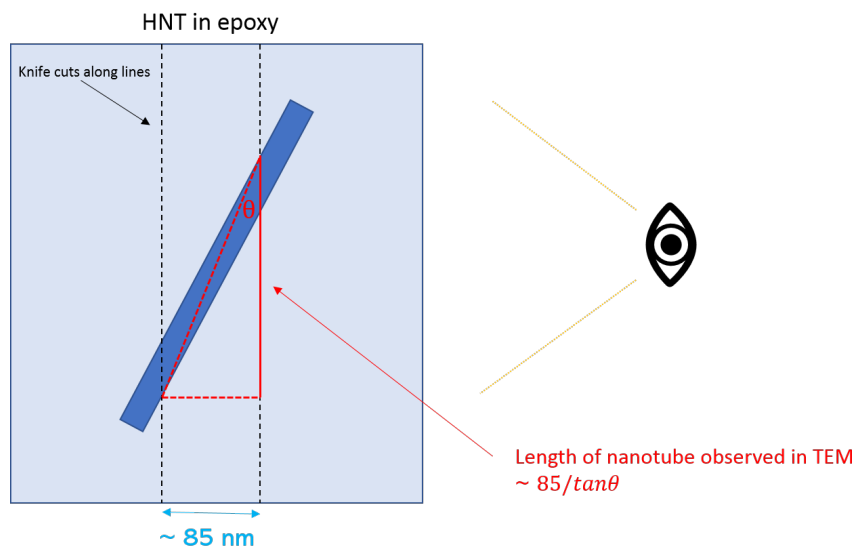


Figure 3.23: An illustration of how both cutting of the nanotubes by the microtome knife during sample preparation, and rotation of nanotubes out of the plane of the TEM image, could make HNTs in TEM images of nanocomposites appear shorter than they truly are.

In the case of rotation of nanotubes out of the plane of the image, it is even possible to quantify this effect to some degree. Assuming a slice thickness of 85 nm and that the

nanotubes are randomly oriented in space, it is possible to use equation 3.3 to get some idea of how the angle of rotation would affect the apparent length of a nanotube that would be seen in a TEM image .

$$\text{Observed length of tube} \sim \frac{85}{\tan\theta} \tag{3.3}$$

While this equation does not exactly describe the observed length of nanotube as a function of the angle of rotation, since the angle of rotation is slightly different to the angle of the triangle made by the observed length of the nanotube and the slice thickness, using it to plot apparent length as a function of angle of rotation (figure 3.24) illustrates that long nanotubes need only be rotated a small amount out of the image plane before they appear significantly shorter than they actually are. For example, at a rotation of 5°, the maximum observable nanotube length would be around 970 nm. The observation that the maximum measured lengths in the N samples are much shorter than the longest HNTs measured in Chapter 2 is explained by the fact that long tubes are rare to begin with, and that there is also only a low likelihood that they will be found in the right conformation to be observable at their true length in TEM images of the nanocomposites. It is clearly feasible that both the act of cutting the nanocomposite samples into slices and the 2D nature of TEM imaging itself could have an influence on the length of HNTs measured in TEM images. Therefore, it is impossible to conclude from TEM images taken of cured nanocomposite samples whether or not any of the mixing techniques damaged the HNTs. However, there is at least one published article where this was not taken into account, and the apparent shortening of the nanotubes seen in nanocomposite samples was attributed to damage caused by the mixing methods (ultrasonication and mechanical mixing).¹³²

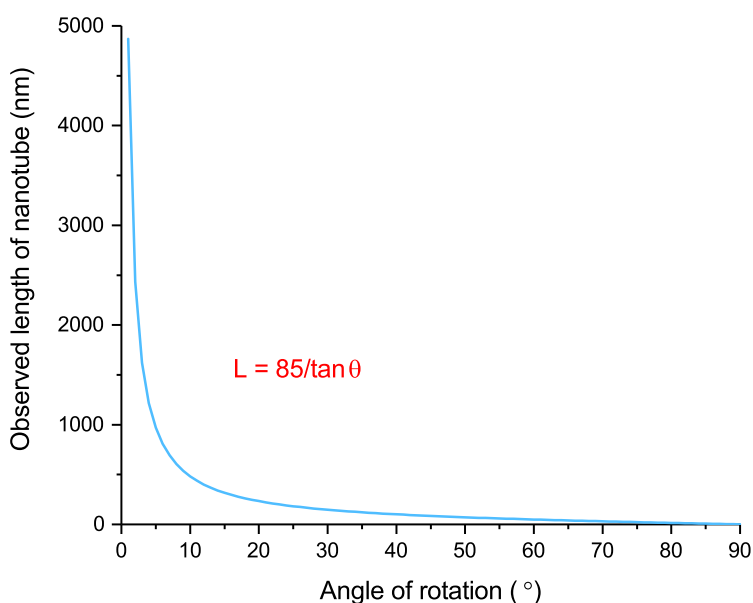


Figure 3.24: A plot of length versus angle of rotation calculated using equation 3.3. This gives an idea of how only a small rotation of a nanotube out of the plane of a TEM image is needed before it will look significantly shorter than it truly is.

TEM imaging of nanotubes washed from uncured resin mixtures

To establish whether or not the apparent reduction in both the mode and maximum observed lengths of the HNTs in nanocomposites was due to the sample preparation or the mixing process, samples of the uncured mixtures were taken for TEM imaging. In the first attempt, the resin mixtures were simply diluted with acetone to give an approximately 1 wt% dispersion of HNTs (the same concentration as that used to image pure HNTs in Chapter 2), and these solutions were dropped onto carbon-coated TEM grids. However, there was enough resin left in these solutions to form epoxy films on the grids, which were thick enough to be opaque to the electron beam. An example is shown in figure 3.25. This meant that the HNTs had to be washed out of the epoxy before they could be measured, which was done by repeated dilution with acetone, and centrifugation to retrieve the clay, which was then dried. Washing the HNTs out of the mixtures was initially avoided, as it is unknown whether centrifugation would artificially change the length distribution of the samples, i.e. it is unknown if, at a given centrifugation time, most of the nanotubes have settled out from solution, but the shortest remain suspended and might be accidentally discarded with the washing solvent. The HNTs obtained by this method no longer dispersed readily in water, but did disperse readily in acetone, suggesting either that there was some coating of the HNTs with the epoxy, or that the epoxy still had not been fully washed away. Dropping these dispersions of HNTs in acetone onto carbon-coated grids did produce samples in which the HNTs could be imaged. The samples of tubes which were washed from the uncured resin mixtures are denoted with the prefix W, and TEM images of the W samples are shown in figure 3.26.

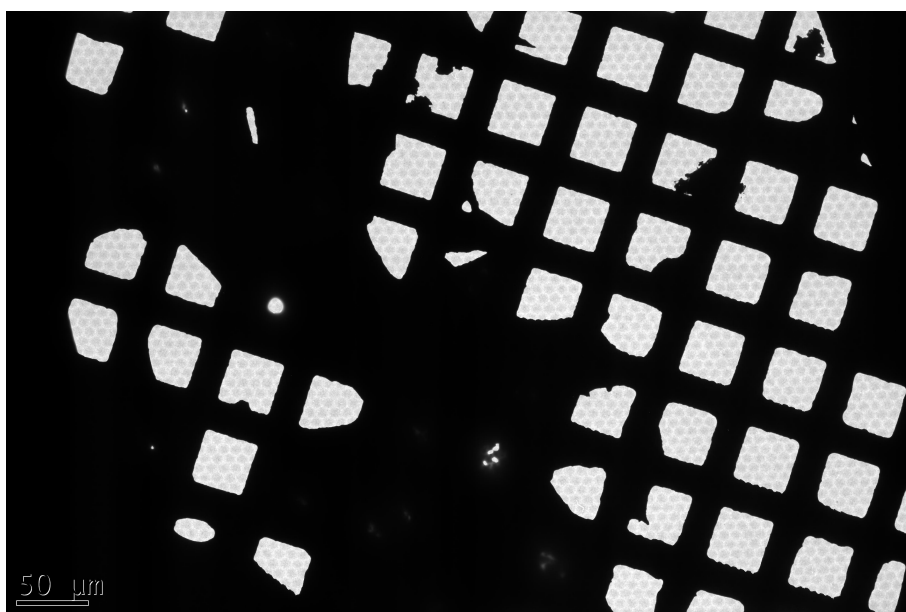


Figure 3.25: A TEM image of a sample made by dropping an acetone-diluted mixture of HNTs in epoxy onto a carbon-coated copper TEM grid. The epoxy forms a film impenetrable to the electron beam, meaning epoxy/HNT mixtures cannot be imaged in this way.

Interestingly, the nanotubes found in the WF and WS samples appeared to have a fuzzy coating, which did not appear to be present for the WAS and WG samples. The extent of this coating seemed to be greater for the WS sample than the WF sample. Examples

of coated nanotubes are shown in figure 3.27. Both of the WF and WS mixtures had heated up significantly during mixing, with the temperature of the WS sample specifically reaching over 160 °C. It might be the case that they both got hot enough that reactions between the epoxide and clay surface occurred, as well as homopolymerisation of the epoxy monomer, which would lead to a polymerised layer bound to the HNT surfaces. Homopolymerisation of epoxide monomers is a well known phenomenon, and it usually occurs in the presence of a base or Lewis acid catalyst.¹⁹¹ For example, it has been seen previously in the preparation of epoxy/oMMT nanocomposites, where the presence of the quaternary ammonium compound used to organofunctionalise the clay is thought to act as a catalyst and cause epoxide homopolymerisation between the clay plates.¹⁹² However, it is unknown whether the bare HNT surface could act as a catalyst in this reaction. In any case, further experiments would be required to prove that the resin has covalently bonded to the surface at all. One way to do so would be deliberately heating HNTs in epoxy, then thoroughly washing them before taking them for characterisation.

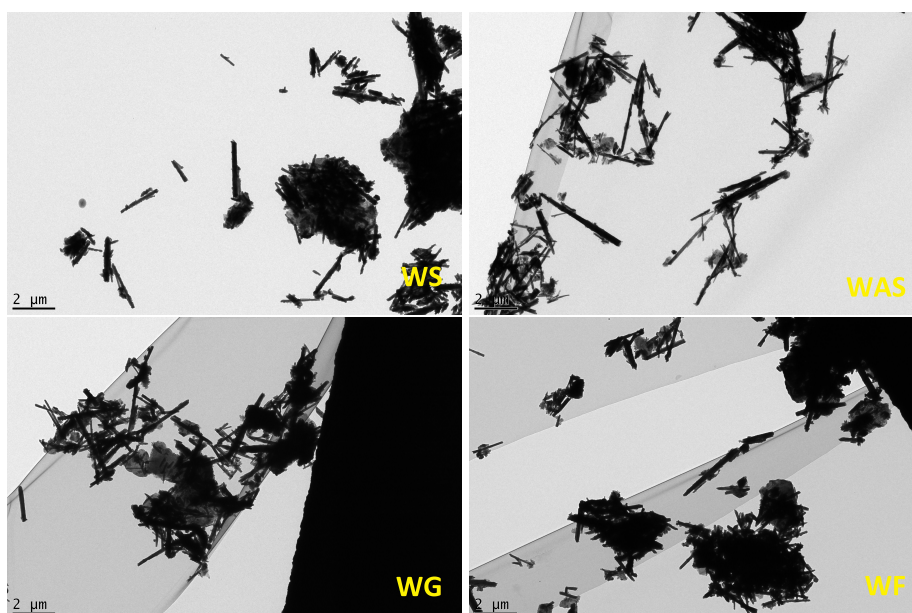


Figure 3.26: TEM images of HNTs washed from epoxy/HNT mixtures made by different mixing methods.

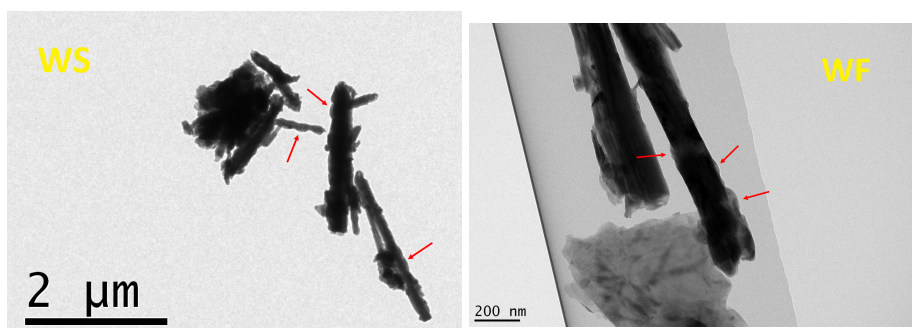


Figure 3.27: Close-up images of HNTs in the WS and WF samples which appeared to have a coating. The red arrows indicate features which are thought to be a coating of epoxy, possibly formed due to heating of the epoxy/HNT dispersion during mixing.

The results of measuring the lengths of the HNTs that had been washed from the resin are

given in table 3.4. They were found to be very similar in length to those measured in the nanocomposites, although there were many more long nanotubes in the washed samples, and the maximum length of nanotube measured for the washed samples was generally around twice that measured for the nanocomposite samples. Again, at this point, one might have concluded that all of the mixing techniques had caused a reduction in length of the nanotubes. However, one possibility remained: the original length measurement of the pure HNTs might have been inaccurate.

Table 3.4: *The mode lengths of the log-normal distributions fitted to the HNTs seen in TEM images of the N and W samples, and the maximum length of tube measured for each sample.*

Sample	Mode length/nm	Maximum length/nm
NS	221	2120
WS	312	3689
NAS	163	1687
WAS	186	4810
NG	205	2184
WG	219	4537
NF	160	1949
WF	192	3952

As discussed in Chapter 2, at this point it was found to be the case that the original measurements of the HNTs' lengths that were made were inaccurate. More specifically, returning to the TEM images of the pure HNTs, and measuring as many nanotubes as possible (560) without disregarding any, showed their mode length to be around 164 nm, much shorter than the original 486 nm that was found. Using the 95% confidence intervals for MATLAB's estimates of the log-normal parameters for each set of lengths measured, uncertainties can be added for each sample. Doing so reveals that the mode lengths of all but one sample are within error of one another (figure 3.28).

An anomalously large length was found for the WS sample. This may have been due to the fact that the HNTs in this sample appeared to have a significant polymer coating, which might have improved the stability of their dispersion in acetone, and meant that not all of the small nanotubes had sedimented from solution during centrifugation (i.e. during preparation of the W sample), which would artificially deplete the population of shorter nanotubes seen in TEM images. However, when DLS measurements of a sample of a 2S resin mixture dispersed in acetone were taken at increasing centrifugation times (figure 3.29), it was seen that all of the nanotubes appeared to have been retrieved from solution by 30 min of centrifugation (the time used to retrieve the HNTs when making the W samples). Therefore, the anomalously large size of the HNTs in the WS sample is not due to small nanotubes remaining in the acetone during preparation. Alternatively, it might be the case that the fuzzy coating may have caused the nanotubes to have been measured to be longer than they actually were, and/or may have obscured some of the smaller nanotubes (e.g. that were lying close to large ones in agglomerates) and prevented them being measured. In any case, ignoring the result for WS samples, the fact that all of the other W samples and the pure HNTs had very similar mode lengths suggests they are actually all following the same size distribution.

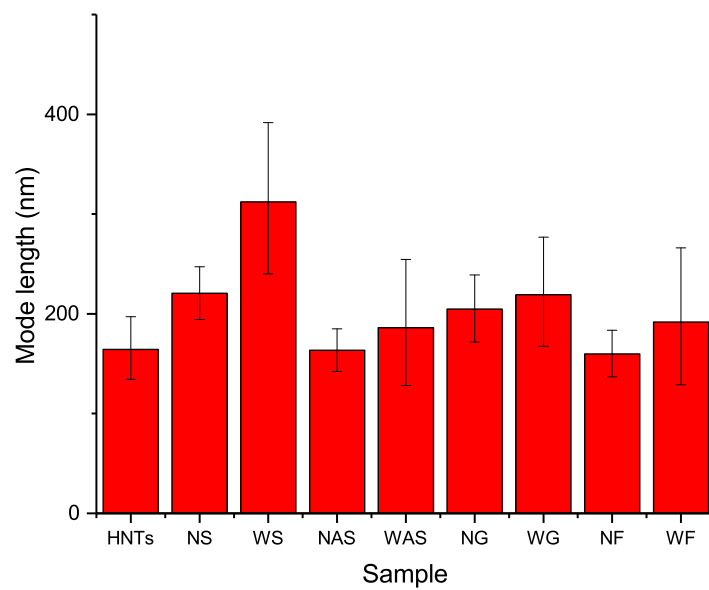


Figure 3.28: A comparison of the mode values of the log-normal probability density functions of HNT length found for pure HNTs and both N and W samples. All of the samples bar WS seem to have overlapping uncertainties, suggesting that they are probably all following the same size distribution. The uncertainties are the mode values calculated using the 95% confidence intervals of the log-normal parameters μ and σ fitted to the data using MATLAB.

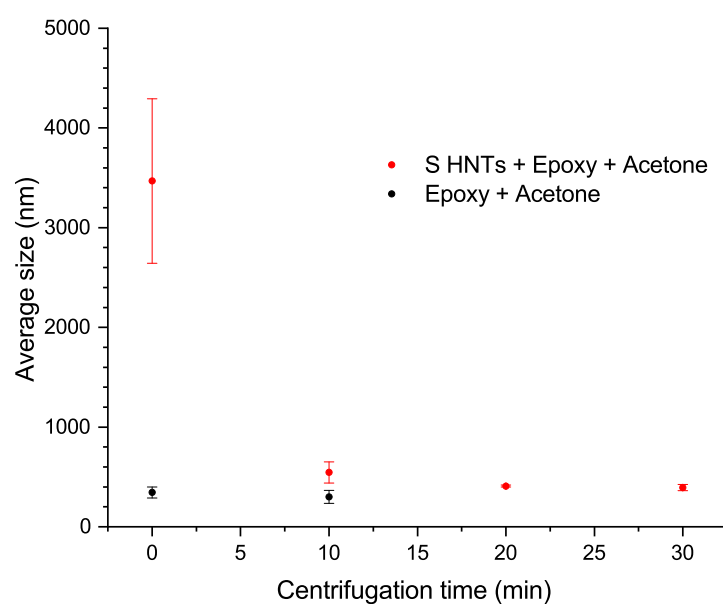


Figure 3.29: DLS measurements of S HNTs in an epoxy/acetone solution at different centrifugation times (at 3000 rpm). By 20 min of centrifugation, the measured ‘size’ of the S sample is the same as that of a pure epoxy + acetone solution, and this does not change after 30 min. Therefore, it is concluded that all of the HNTs have been retrieved from solution by 30 min of centrifugation. The error bars are the standard deviation of three size measurements.

Conclusions drawn from length measurements in TEM images

The preceding results highlight the fact that the log-normal fits of the data sets are probably not useful for comparing lengths between different samples of HNTs. More specifically, all of the fitted mode lengths are within uncertainty of one another, yet there are clearly many more long nanotubes in the W samples than in the N samples. That is to say, the fitted length distributions are so dominated by short nanotubes, that the absence of the longest tubes does not significantly change them. As such, it is probably better to return to the raw length data for each sample to compare between them, specifically to compare the fractions of long nanotubes present for each sample.

Figure 3.30 shows the percentages of nanotubes that were found to have lengths of above 1000 nm, 2000 nm, 3000 nm, 4000 nm, and 5000 nm for the pure HNTs and the W samples. It can be seen that all of the W samples have a similar percentage of longer nanotubes, and indeed the W samples all have a higher percentage of nanotubes over 2000 nm long than the pure HNTs do. Only the pure HNT sample was seen to have a nanotube longer than 5000 nm, but this amounted to one tube out of 560 (0.2%), so nanotubes above this length are probably just very rare, and not necessarily always found in the relatively small sample area measured by TEM. The comparable amount of longer nanotubes seen for all of the W samples and pure HNTs is compelling evidence that none of the mixing methods used reduced the lengths of the nanotubes, not even ultrasonication, which had previously been shown by Rong *et al.* to cut HNTs into shorter lengths,¹⁸⁵ and suggested to do so by Brantseva *et al.*¹³²

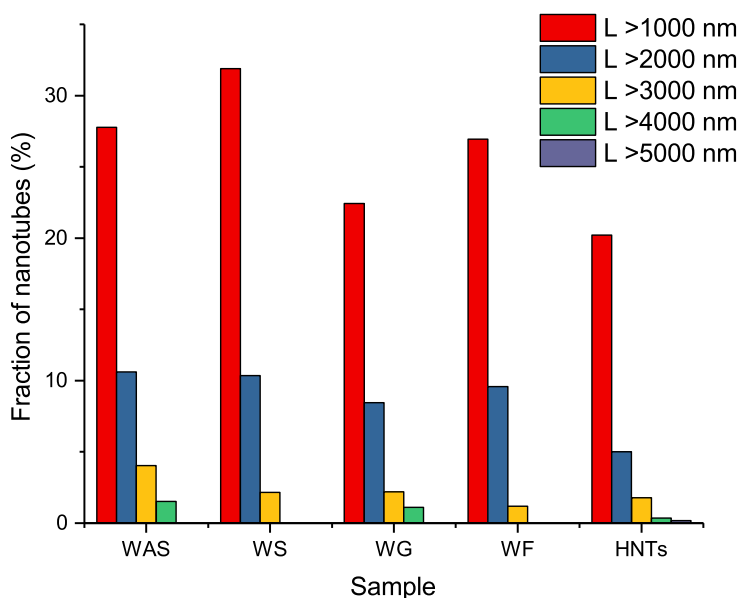


Figure 3.30: A comparison of the percentages of HNTs over certain lengths found for pure HNTs and the W samples. The W samples actually seem to have a larger proportion of longer tubes than the pure sample, which suggests that the mixing techniques used did not damage the HNTs (i.e. did not reduce their length).

3.2.7 Investigating rheometry as a means for determining the degree of dispersion of halloysite nanotubes

The viscosity (η) of a liquid can be described simply as its tendency to resist flowing when an external force is applied.¹⁹³ It is described mathematically as the ratio between the shear stress (σ), i.e. the pressure being applied to the fluid, and the shear rate (γ), i.e. the rate of change of velocity at which layers in the fluid are being made to flow over one another (equation 3.4). In Newtonian fluids (e.g. most solvents), the viscosity does not change with changing shear rate. In non-Newtonian fluids, viscosity does change with changing shear rate. If the viscosity increases as shear rate increases, then the fluid is said to be shear thickening, and if viscosity decreases as shear rate increases, it is said to be shear thinning.¹⁹³

$$\eta = \frac{\sigma}{\gamma} \quad (3.4)$$

Adding a second, dispersed phase, e.g. a solid particle, to a fluid will often increase its viscosity.¹⁹³ This is because collisions between the dispersed particles increase friction in the fluid and enhance its resistance to flow. The viscosity increases as filler concentration increases, because inter-particle collisions become more frequent, and the type of collisions can change from single to many body. For example, at high enough filler concentrations, particles can form relatively large, networked structures in the fluid. Particle dispersions often also show non-Newtonian behaviour.¹⁹³ For example, shear thinning can occur when anisotropic particles preferentially align in the direction of flow, thereby lowering their collision cross-sections in that direction, and shear-thickening can occur when the applied shear force causes the particles to come together to form networked structures more resistant to flow. Nanoparticles dispersed in pre-polymer blends (e.g. uncured epoxy resin) and polymer melts are essentially a dispersed phase in a bulk phase, and study of the rheological properties of these materials can hence give an indication of the structure of the dispersed particles. For example, it has been shown that a marked increase in shear thinning behaviour is seen for nanocomposites containing oMMT when complete exfoliation of the plates is achieved.¹⁹⁴

Investigations regarding the rheology of dispersions of HNTs in epoxy resin have typically been justified for two reasons: firstly, the viscosity of an epoxy/HNT mixture could be an important factor when considering possible applications of the nanocomposites (e.g. it might need to be low enough to allow for injection in a resin transfer molding process),¹⁰ and secondly, it might be a good indicator of the degree of dispersion of epoxy/HNT mixtures made by different mixing techniques.^{10, 132, 183} Vahedi *et al.* specifically used an increase in viscosity seen for an epoxy/HNT sample made by ultrasonication versus one made by mechanical mixing as evidence for better mixing in the ultrasonicated sample.¹⁰ Rheometry was used here for a similar reason, i.e. to ascertain if there was a viscosity criterion which could be used to distinguish between poorly mixed and well mixed samples without having to go to the extent of looking at the samples using TEM (which is both expensive and time-consuming). Were viscosity found to be significantly dependent on the degree of dispersion of the HNTs, it was hoped that a simple bench-top experiment could then be designed to ascertain whether a particular sample matched the viscosity criterion for being well mixed. This would allow real-time evaluation of the degree of

dispersion of HNTs in portions of a sample taken at different stages during mixing (e.g. at increasing ultrasonication time, or increasing number of passes through the 3RM), and hence present a quick way of establishing the minimum degree of processing needed to fully disperse the HNTs.

Along with measuring the viscosities of the uncured epoxy/HNT samples, their filler contents had to be known, since the viscosity of a particle/fluid mixture is dependent on the particle concentration.¹⁹³ These samples were prepared separately to the ones used for mechanical testing, so their filler contents could not simply be extrapolated from those measured in section 3.2.8. Despite the dependence of mixture viscosity on filler fraction, this was not measured in any of the three cited examples of measurements of the viscosities of epoxy/HNT mixtures.^{10,132,183} Indeed, correspondence with one set of authors revealed that the value of 3 wt% that they list for the mixtures they measured was actually nominal, and based on the approximate amount of filler assumed to be in the cured nanocomposites (i.e. HNTs + epoxy + hardener), rather than the actual amount in the mixtures, which must be much lower.^{183,195} In order to avoid confusion, and to confirm that any difference in rheological properties seen between different samples is not simply due to a difference in filler content, it is important to have a means of measuring this for the uncured epoxy/HNT mixtures.

The most straightforward way of determining the filler content in uncured epoxy/HNT mixtures is to wash the resin out with an appropriate solvent (e.g. acetone), and dry and weigh the remaining solid. Soxhlet extraction seems ideal for this, as it allows for many washes of the sample with solvent to be carried out easily, meaning that one could be confident all the resin had been removed. In addition, there would be little chance of any HNTs being inadvertently lost during the washing process (which would lead to an underestimation of filler content); if the washing solution was clear at the end of extraction, it would be safe to assume that none or only minimal amounts of HNTs had been lost from the thimble. However, it was found that mass measurements of the cellulose thimbles used for extraction were unreliable. Figure 3.31 shows that the mass uptake of a cellulose thimble that had been weighed, soaked in acetone, dried in a vacuum oven, then weighed again once dry. The mass of the thimble after drying took a long time to become stable, and it was never seen to reach its original mass. This would introduce significant and unpredictable error into the measurement of HNT content, since while the absolute uncertainty in the mass of the thimble caused by drying was only small (a few tens of mg), the masses of HNTs being measured were also small (on the order of a hundred mg). Instead, the filler content was determined by repeated washing and centrifugation of the samples. Instrumental uncertainties for this method are low (relying on three mass measurements made using a precise balance), however there is always potential for unintentional loss of clay from the sample, e.g. through spillages. Nonetheless, it was determined to be the only viable way to find filler content values for the uncured mixtures, which are listed in table 3.5.

The results of measuring sample viscosity as a function of shear rate for pure epoxy and the epoxy/HNT samples made by different mixing methods are shown in figure 3.32. Measurements of viscosity were taken during an initial ramp up from a shear rate of 0 s^{-1} to 1000 s^{-1} , and then again as the shear rate was decreased from 1000 s^{-1} to 0 s^{-1} . All of the nanocomposite mixtures had viscosity greater than the pure resin, and, ignoring the anomalous AS sample for the time being, they seemed to show similar rheological

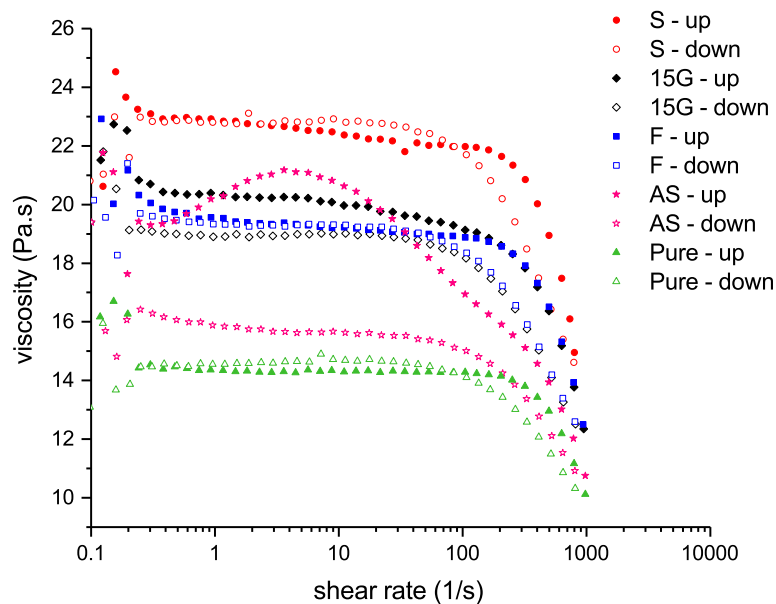


Figure 3.32: Viscosity plotted against shear rate for pure epoxy and the epoxy/HNT samples made by different mixing methods. Up and down refer to measurements made during an initial increase of shear rate from 0 s^{-1} (up), and subsequent measurements made as the shear rate was decreased from 1000 s^{-1} (down).

reported by Vahedi *et al.* may well have actually been due to a chemical change in the epoxy resin, rather than an increase in the degree of dispersion of filler, which is what they attribute it to.¹⁰ Similarly, Brantseva *et al.* noted an increase in viscosity for samples made by ultrasonication, which they attributed to breakage of the nanotubes leading to a greater number concentration of particles in the mixture (and a subsequent increase in viscosity).¹³² However, it was shown in section 3.2.6 that ultrasonication probably does not break the nanotubes, so it is possible that the increase in viscosity they saw was also due to a change in the composition of the resin. It is therefore clear that this is a factor that needs to be taken into account when studying the rheology of epoxy resin nanocomposite mixtures made by ultrasonication.

The AS sample showed completely different rheological behaviour to the others. Specifically, shear thickening occurred on the ramp up from zero, followed by rapid thinning. The reverse behaviour is subsequently not seen during the ramp down, and is not seen when the sample is kept in the instrument and subjected to a repeat of the shear sweep. This suggests that there is some kind of microstructure in the AS sample which initially resists shear deformation, then is broken up as shear rate increases, and cannot recover its original structure on the timescale of the experiment. The filler content of the AS sample (4.9 wt%) was found to be similar to (albeit slightly lower than) the other samples (5.3 - 6.7 wt%), and the sample showed a similar degree of dispersion of HNTs as the F sample. Therefore, this shear thickening behaviour is probably not due to the AS sample containing a uniquely percolated network of nanotubes compared to the other mixtures. It is suggested that it is instead due to the presence of traces of acetone in the sample, although exactly how that would lead to a shear-thickening network is unclear. However,

the fact that the viscosity of this sample after thickening and subsequent thinning is much lower than the other nanocomposite mixtures is consistent with the presence of acetone, which is known to reduce the viscosity of epoxy resins.¹⁹⁷

It is acknowledged that this amounts to quite a superficial analysis of the rheological properties of these samples. Indeed, in hindsight, oscillatory rheometry rather than the continuous shear sweep used here would have been more appropriate, as it would have yielded more information about the alignment of the nanotubes, and may have allowed for more quantitative analysis of the degree of dispersion of the mixtures.¹⁹⁴ However, even from brief inspection, it is clear that rheometry is not a good way to compare the degree of dispersion of HNTs in samples using the 3RM and ultrasonication. Specifically, the samples made by ultrasonication can probably both be assumed to have a different fluid phase than simply pure resin, due to the probable presence of acetone and higher molecular weight species for AS and S, respectively. That is to say, it would be difficult to justify changes in rheological properties as being due to a difference in the level of dispersion of filler rather than a difference in the composition of the resin.

3.2.8 Determining HNT content in epoxy/HNT nanocomposites

It is well established that the mechanical properties of a nanocomposite are a function of the amount of filler added to the material.¹⁹⁸ Unsurprisingly, this has also shown to be true for nanocomposites of HNTs in epoxy: for example, Sun *et al.* observed a 4% increase in the Young's modulus and a 5% increase in the tensile strength of epoxy/HNT nanocomposites when they increased the HNT loading from 2.5 to 5 wt%,¹¹ and Kim *et al.* saw a steady increase in the flexural strength of their epoxy/HNT nanocomposites up to a 15 wt% loading (after which, the strength dropped off sharply).¹⁰⁹ Since the mechanical properties of epoxy/HNT nanocomposites are so dependent on the filler content in the material, it is important to have a means of measuring this.

Despite the importance of filler concentration in relation to nanocomposite mechanical properties, its measurement is often not discussed in literature. Indeed, for the specific subject of epoxy/HNT nanocomposites, published articles do not mention the measurement of filler content; the values of filler content reported are presumably calculated from the amount that was added to the epoxy before mixing.^{10, 11, 125, 126, 178, 179} This might seem reasonable assuming careful experimentation on behalf of the authors, however it was found in this work that it was difficult to ensure that all of the clay added to the resin ended up as part of the final material. For the example of the S samples specifically, there are clearly many large agglomerates at the bottom of the mixing vessel after sonication and decanting of the mixture (illustrated in figure 3.33). This is presumably due to the fact that these agglomerates were large enough to sink and be deposited before having a chance to be dispersed by the sonication. Similar effects were seen for the AS sample, and, albeit to a lesser extent, the samples made using the 3RM (in the latter case, the issue arises when transferring the mixture from its original vessel to the mill). In light of this, the filler content of the mixture certainly should not be assumed to be the amount added to the resin. What was uncertain was how far off estimates of filler content based on the initial amounts added were to the actual values. Because it was unknown how much the filler contents of the final nanocomposites differed from the filler contents of the initial mixtures, several methods of determining this were investigated.



Figure 3.33: A photo of the bottom of the mixing vessel for an S sample after sonication and decanting of most of the mixture. There are clearly many large agglomerates remaining in the vessel (highlighted with the red arrow), so the filler content in the decanted mixture must be lower than that which was originally added before mixing.

Filler content determination using TGA

As already mentioned, literature regarding the determination of filler contents in nanocomposites is thin on the ground, especially with regards to HNT nanocomposites. Nonetheless, there are reports of filler content for related clay nanocomposites being determined by burning the polymer off in a furnace and using the remaining mass as an indicator of filler content.¹⁹⁹ Therefore, as a first experiment for determining the filler content in the epoxy/HNT nanocomposites, TGA was used. Filler content analysis using TGA has the advantage of using a very precise mass balance. However, there has previously been some suggestion that the very small sample size analysed in TGA (on the order of mg to tens of mg) means that samples taken from different parts of a material might have different filler content, and not represent the material as a whole.²⁰⁰ For all of the TGA analyses, the filler content of the nanocomposite was calculated using equation 3.5 (the variables are explained in table 3.6). Essentially, the difference between the mass of the nanocomposite and the mass of a pure epoxy heated to the same temperature is assumed to be the mass of filler remaining in the nanocomposite, which is then adjusted to take into account the mass that pure HNTs will have lost by that temperature. It should be noted that this assumes that the thermal degradation of the HNTs and epoxy are independent processes, which might not be the case.

$$\text{Filler content/wt\%} = \frac{a - b}{0.01c} \quad (3.5)$$

Table 3.6: Explanation of the variables used in equation 3.5

Variable	Assignment
a	The mass, in wt%, of nanocomposite remaining at the end of the TGA run.
b	The mass, in wt%, of pure epoxy remaining at the end of the TGA run.
c	The mass, in in wt%, of pure HNTs remaining at the end of the TGA run.

TGA was attempted on different sets of samples in three different atmospheres: pure nitrogen, a mixture of nitrogen and air, and air. The filler contents found for each sample analysed by TGA are given in table 3.7. In the first attempt, analysis of the 5G samples was carried out under nitrogen atmosphere. However, this was found to give a high char yield of around 18 wt% for the pure epoxy. This in turn led to a nonsensical, negative filler content being calculated for 5G1, so TGA in nitrogen atmosphere was clearly unsuitable for determining filler content. The analysis was then attempted using the 15G samples and a mix of air and nitrogen, which led to a lower char yield for the pure epoxy (about 1.3 wt%) than in pure nitrogen (about 18 wt%). However, subsequent calculation of filler content again gave a negative result (this time for the 15G1 sample). Finally, TGA was carried out on S1 and S5 in an air atmosphere. This time, the pure epoxy had burned away completely after it had been held at 800 °C for 15 min. The TGA traces for pure epoxy in each atmosphere are shown in figure 3.34. Calculating the filler content of the nanocomposites heated in air did not give any negative results, but did give significantly

lower filler contents than were expected considering the amount of HNTs that had been added to the epoxy. The analysis under air was repeated three times each on different samples of S1 and S5, so average values could be calculated. For the S1 sample a standard deviation of 20% was calculated, but there was only a 2% deviation for the S5 sample. This suggested at least that TGA in air was a repeatable method of determining the HNT filler content, but it remained to be seen whether any of the filler contents determined by TGA were accurate.

Table 3.7: *The filler contents of various epoxy/HNT samples as found by TGA in different atmospheres. Only TGA in air does not give nonsensical, negative values.*

Sample	Filler content (TGA)/wt%	Atmosphere
5G1	-0.04	Nitrogen
5G2	1.01	Nitrogen
5G5	3.90	Nitrogen
15G1	-0.003	Nitrogen/air mix
15G2	0.30	Nitrogen/air mix
15G5	4.37	Nitrogen/air mix
S1	0.6 ± 0.1	Air
S5	3.00 ± 0.07	Air

It is also worth noting at this point that TGA analysis of the epoxy nanocomposites is potentially hazardous: after each measurement, a strong smell of burning plastic pervaded the lab, and while the exact composition of these fumes is unknown, they may well have included toxic compounds such as acrolein, allyl alcohol, and various volatile aromatics,²⁰¹ exposure to which it is important to avoid. The gases evolved from samples during TGA are usually extracted from the heating chamber, but often not extracted from the vicinity of the chamber after the measurement has finished and the chamber has opened. To safely heat cured epoxy resins, the sample must therefore either be kept in the sample chamber until all gases have been extracted, or external extraction must be applied in the vicinity of the instrument. In the former case, this can add a lot of time to the TGA measurement. For example, in the case of the samples heated in a nitrogen/air mixture, it took tens of minutes after heating to the final temperature for all of the gases to be evolved, and even then a smell still remained when the furnace chamber was opened. Applying external extraction is therefore the most appropriate way to ensure safety during these measurements, but it should be noted that this is not always available or practical. Nonetheless, it is advised that TGA of cured epoxy resins up to high temperatures should not be carried out unless appropriate extraction can be guaranteed.

Filler content determination using density

Another feasible way of calculating the filler content of a composite is via measuring its density. Compared to TGA, this has the advantage of being non-destructive and uses a larger sample amount which should be more representative of the composite as a whole. The density of a composite sample (ρ_s) can be expressed in terms of the density of the bulk material (ρ_b), and the density and volume fraction of the filler material (ρ_f and ϕ_f respectively), as shown in equation 3.6. This can be rearranged to give the volume fraction

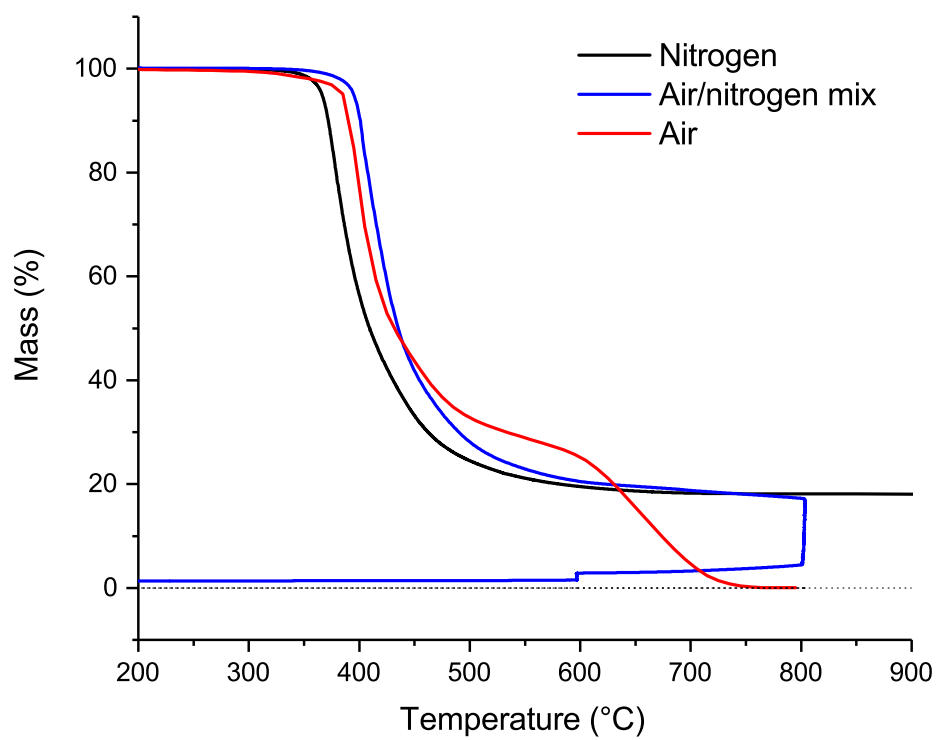


Figure 3.34: TGA of pure cured epoxy under different atmospheres. Only heating under air leads to complete combustion and no mass remaining at the end of the run. The dotted line is at $y = 0$ wt%.

of filler in terms of the density of the composite, and the density of the two separate materials (equation 3.7). From this, the mass percentage of filler in the nanocomposite can be described using equation 3.8.

$$\rho_s = \phi_f \rho_f + (1 - \phi_f) \rho_b \quad (3.6)$$

$$\phi_f = \frac{\rho_s - \rho_b}{\rho_f - \rho_b} \quad (3.7)$$

$$\text{Filler content/wt}\% = \frac{100\phi_f \rho_f}{\rho_s} \quad (3.8)$$

It is worth noting that the uncertainty in filler content determination made via density measurements is governed by the uncertainty in the densities and ϕ_f . The uncertainty in ϕ_f is in turn governed by the relative uncertainties in the values $\rho_s - \rho_b$ and $\rho_f - \rho_b$. These relative uncertainties increase with a decreasing difference between the densities of filler and bulk. For example, the relative uncertainty in $\rho_f - \rho_b$ is given in equation 3.9. This means that the determination of filler content in a polymer nanocomposite by measuring its density would be expected to be more precise for denser fillers, and hence is probably more appropriate for inorganic (and relatively dense) fillers than it would be for organic fillers, which would have a density more similar to the polymer.

$$\frac{\delta(\rho_f - \rho_b)}{\rho_f - \rho_b} = \frac{\sqrt{\delta\rho_f^2 + \delta\rho_b^2}}{\rho_f - \rho_b} \quad (3.9)$$

To provide densities with which to calculate filler contents, Helium (He) pycnometry was used. He pycnometry is a technique which can be used to measure the volume of solids in samples for which it is otherwise difficult to do so, for example porous materials and powders, which do not fill the entire volume of a container.²⁰² Helium atoms are so small that they are able to pervade even the narrowest pores in a sample, and they do not typically adsorb strongly to surfaces.²⁰² This means that in a sealed cell of known volume containing only helium and a solid sample, the volume in the cell not occupied by helium must be the true volume of the sample. In practice, the pressure in the cell is measured to give the volume of helium within it (obtained using Boyle's law). By comparison of the volume of the empty cell to the cell containing sample, the volume of sample can be found. Providing that the mass of sample is known, the density of sample can subsequently be calculated. Precise measurements of density can be found using He pycnometry. The densities of HNTs and pure, cured epoxy found by He pycnometry are given in table 3.8.

Subsequently, the densities of the samples S1, S5, 15G1, 15G2, 15G5, 5G1 and 5G2 were also measured using He pycnometry, and the filler content in these samples calculated using equation 3.8. These values are listed in table 3.9. For the S samples, the calculated filler contents agreed well with those found by TGA in air; indeed, as shown in figure 3.35, the value for S5 found by He pycnometry was within the standard deviation

Table 3.8: *The densities of HNTs and cured epoxy (with no filler).*

Material	Density/gcm⁻³
HNTs	2.5479 ± 0.0022
Cured epoxy	1.1884 ± 0.0002

of the values found by TGA. This suggests that the filler content found by both He pycnometry and TGA in air is accurate, and that the actual filler content of these samples was much lower than that which was expected from the amount of HNTs added to the epoxy. Equation 3.5 assumes that the thermal degradation of the epoxy and HNTs are independent, so it is probable that incorrect values of filler content are found when incomplete combustion occurs (i.e. under nitrogen and a nitrogen/air mix) because the presence of HNTs influences the charring process.

Table 3.9: *Values of filler content found via He pycnometry.*

Sample	Density/gcm⁻³	Filler content/wt%
S1	1.1912 ± 0.0002	0.44 ± 0.04
S5	1.2074 ± 0.0003	2.95 ± 0.06
15G1	1.1912 ± 0.0006	0.4 ± 0.1
15G2	1.1969 ± 0.0004	1.33 ± 0.07
15G5	1.2115 ± 0.0005	3.57 ± 0.08
5G1	1.1944 ± 0.0005	0.94 ± 0.08
5G2	1.1996 ± 0.0001	1.75 ± 0.04

Because measuring the density of the nanocomposite samples had been shown to be a reasonable method of finding the HNT filler content in the samples, the same was attempted using bulk volume measurements. More specifically, the density of the 15G samples was found by measuring the dimensions and masses of the tokens being used for mechanical testing. Bulk measurements are much quicker and simpler than He pycnometry, and measure a substantially larger amount of sample. However, this method gave different densities for each sample compared to He pycnometry. For example, the density of the pure epoxy was found to be 1.1884 gcm⁻³ by He pycnometry, but 1.1542 gcm⁻³ by bulk measurements (a difference of 3%). This in turn led to significantly different filler content being measured for the nanocomposite samples, with bigger disparities for the 15G1 and 15G2 samples than the 15G5 sample, for which the filler content measurement for the bulk sample is not too different than He pycnometry (the bulk filler content is about 96% of that measured by He pycnometry). A comparison between these measurements is shown in figure 3.36.

As filler contents found by He pycnometry were similar to those found by TGA, it was concluded that the bulk density measurements were the inaccurate data. This is probably because measuring the dimensions of the sample (i.e. length, height and width) with a micrometer does not take into account surface roughness, and because only three measurements were taken of each dimension, so the exact measured shape of the samples was probably inaccurate. The fact that the filler content value obtained via bulk measurements was more accurate for the 15G5 sample could just be because these samples were

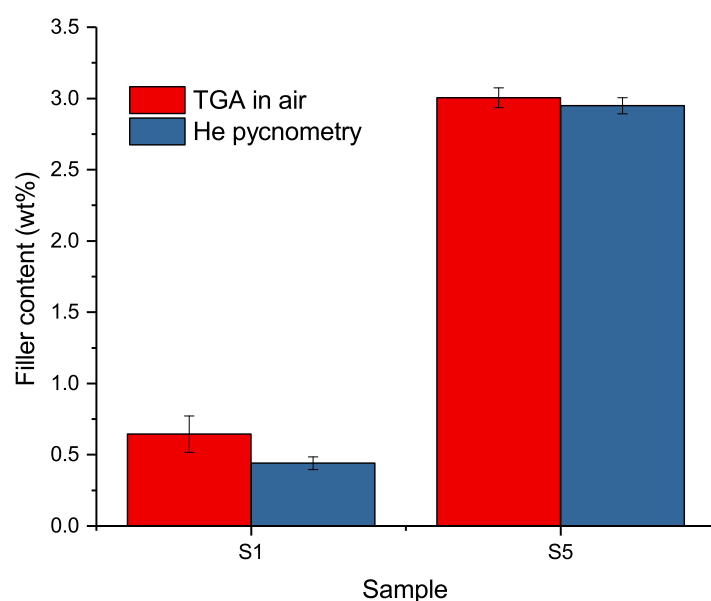


Figure 3.35: A comparison of the filler content measured for the S1 and S5 samples using TGA in air and He pycnometry. The values measured by both techniques are similar, suggesting that both are accurate. The uncertainties in the TGA measurements are a standard deviation of three measurements, while the instrumental uncertainties are given for He pycnometry.

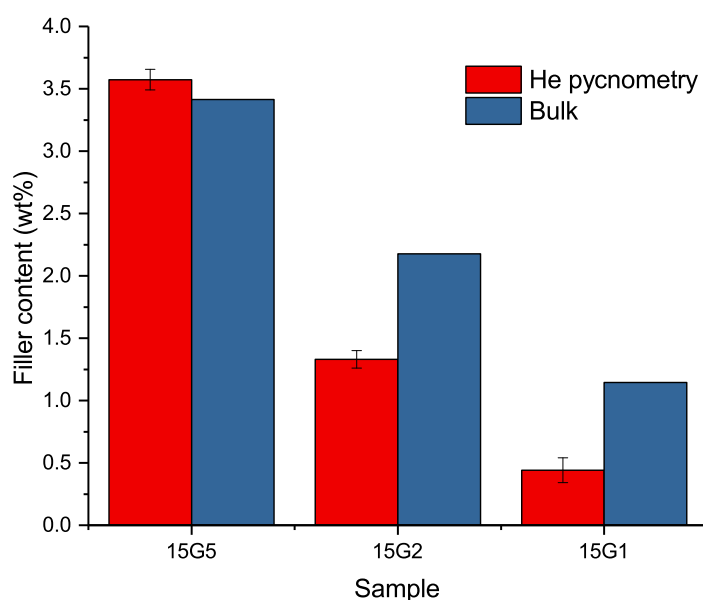


Figure 3.36: A comparison of the filler content measured for the 15G samples using densities found via He pycnometry and bulk measurements. The bulk measurement gives filler content close to that found via pycnometry for the 15G5 sample, but the bulk measurements give very different filler contents to the pycnometry values for 15G2 and 15G1. The error bars associated with He pycnometry values are instrumental uncertainties.

coincidentally more uniformly shaped. Because measuring filler content via bulk measurements of sample density generally gave values very different to those obtained by He pycnometry, it was deemed an inappropriate method, at least for these samples.

Filler content determination by burn-off in a furnace

While TGA in air and He pycnometry both seemed to be accurate methods for determining filler content in the epoxy/HNT nanocomposites, they share the same disadvantages; both techniques are relatively time and labour intensive, and both measure a relatively small sample amount. In addition, instrument time on the TGA can be expensive. Because of these disadvantages, determination of filler content was also attempted using a furnace heated to 800 °C to burn off the resin. This is essentially the same process as TGA in air, but using a less precise mass balance. However, a much larger portion of each sample can be heated in a furnace, so the results are more representative of the sample as a whole, and many samples can be heated at once (>10). In addition, there are furnaces available at the University of Sheffield which are continuously extracted, so the hazardous fumes from the burning resin are not an issue. Therefore, the use of a furnace should be the ideal way to measure the HNT filler content of a large number of epoxy samples quickly, and to a reasonable degree of accuracy.

However, there are several significant sources of uncertainty when determining the filler content of nanocomposite samples using a furnace. Firstly, the precision of the balance must be taken account, and this error must be propagated for the several mass measurements taken during the process. This is especially important when small samples are being burned, and/or when less precise balances are used. In both of these cases, the relative error in the mass measurements may be quite high. Secondly, and more significantly, the crucibles used for burning off resin in the furnace were made of mullite (a clay mineral), which also loses a small amount of mass during heating (presumably due to moisture loss). In some cases, the amount of mass lost by the crucible can be similar to the mass of filler remaining at the end of heating. Both the precision of the balance used and the mass lost by the crucible must be taken into account when calculating the uncertainty in filler content.

To account for the mass lost by the mullite crucibles during heating to 800 °C, the masses of 12 empty crucibles of different sizes were measured before heating and after they had cooled down the following day. The mass loss of the empty crucibles appeared not to correlate to their size, so it was therefore felt that an average of the mass fraction lost by all the crucibles could be used to correct data for nanocomposite samples. The standard deviation of this average mass loss would then be treated as the uncertainty in the mass lost by the crucibles. The average mass loss of the empty crucibles was found to be (0.008 ± 0.003) wt%, and these values are used in all subsequent filler content calculations.

Equation 3.10 was used to calculate the filler content of the nanocomposite samples, and the variables are explained in table 3.10. The equation assumes that all of the mass left in the crucible after heating is the filler. All of the variables in equation 3.10 have an associated uncertainty, and these must all be propagated to find the final uncertainty in the filler content of the samples. The equations used to propagate the error in filler content

are included in the appendix.

$$\text{Filler mass fraction} = \frac{m_f - m_c + m_x}{lm_s} \quad (3.10)$$

Table 3.10: Explanation of the variables used in equation 3.10

Variable	Assignment
m_f	The mass of the crucible + sample after heating.
m_c	The mass of the empty crucible.
m_x	The mass lost by the crucible lost during heating ($m_x = 0.00008m_c$)
m_s	The mass of the sample before heating.
l	The mass fraction of filler remaining after heating (for HNTs, this is 0.8580 ± 0.0006)

The uncertainty in the calculated filler content can be mitigated by either using a more precise balance, or using a larger sample amount. In both cases, this reduces the relative error of the mass measurements made. However, the limit of precision for most laboratory balances is 0.0001 g, and indeed the balance used here was only felt to be precise to 0.001 g, despite nominally having a precision of 0.0001 g, because the fourth decimal place was fluctuating by more than 0.0001 g (but less than 0.001 g). The simplest way, therefore, to reduce uncertainty in filler content is by using a larger sample amount.

However, by the time it was decided to try using the furnace to measure filler content, there were only small amounts remaining of some samples, as the rest had already been used, e.g. for TGA measurements. For some samples, there was very little material to attempt heating in the furnace. In addition, the only balance available for the first attempt at the process was precise to 0.01 g rather than 0.001 g, which further compounded the large uncertainties in some measurements. Nonetheless, the values of filler content found using the furnace are listed in table 3.11 for all samples. Asterisks indicate those samples with particularly large uncertainties in filler content caused by using an imprecise balance and/or limited availability of sample for measurement.

The filler contents measured by heating samples 15G5, 5G1 and 5G2 in the furnace had relatively low uncertainty, and these samples had also been measured using pycnometry. There was good agreement between the values found using the furnace and pycnometry for all three of these samples, as illustrated in figure 3.37. Therefore, the values of filler content found using the furnace were concluded to be accurate.

Determination of HNT filler content in epoxy: summary

In summary, all three of TGA in air, He pycnometry, and burn-off in a furnace were deemed to be suitable techniques for accurate measurements of HNT filler content in epoxy/HNT nanocomposites. This is because filler contents found via TGA in air were close to those found by He pycnometry for the same samples, and values found by He pycnometry were in turn close to those found by burn-off in a furnace for the same samples.

Table 3.11: The filler content of various epoxy/HNT samples as found by heating in a furnace. Asterisks indicate samples with particularly large uncertainties in filler content (arising from a low sample mass and/or an imprecise balance being used).

Sample	Filler content/wt%	Relative uncertainty/%
5G1	0.9 ± 0.1	11
5G2	1.54 ± 0.06	4
5G5	3.94 ± 0.08	2
15G1*	1.0 ± 1.2	120
15G2*	1.6 ± 1.4	90
15G5*	4.0 ± 1.0	26
F1	1.2 ± 0.2	16
F2*	1.6 ± 0.9	55
F5	4.0 ± 0.2	5
S1*	0.2 ± 1.4	628
S2	1.7 ± 0.1	7
S5*	4.3 ± 2.8	64
AS1	0.8 ± 0.1	14
AS2	1.4 ± 0.1	10
AS5	4.0 ± 0.1	4

Unfortunately, the availability of samples meant that all three techniques could not be used for all samples. As such, the filler content for each sample is taken from the method which was found to give the lowest uncertainty for that particular sample. These values are given in table 3.12.

Also in table 3.12, the measured values of filler content for each sample are compared to those that were calculated from the initial amount of HNTs added to the epoxy before mixing (excluding the 5G2 sample, for which the recorded value of the initial amount of HNTs added could not be found). The same values are plotted in figure 3.38 for a visual comparison. It can be seen that the measured values of filler content are significantly lower for many of the samples. This is most notable for the S and AS samples, which makes sense considering the sedimentation of agglomerates which was seen during mixing. The disparity between the measured and calculated filler contents for these samples is important, considering how common ultrasonication is in the literature, and how rare filler content measurements are. Specifically, this may bring into question comparisons between the properties of samples which have been given nominal filler contents, especially if differences in properties are seen to be small. Interestingly, the measured values of filler content for the 5G and F samples are mostly close to the calculated values. This is not only further evidence for the accuracy of burn-off in the furnace as a technique, but also suggests that it is possible to mix almost all of the added HNTs into the resin using the 3RM. The measured filler contents were slightly higher than expected for 5G1 and F1. However, the expected value is just about within the experimental uncertainty for 5G1, and may well be within a second standard deviation for the F1 sample, i.e. both of these discrepancies may just be statistical coincidences. Taken as a whole, these results indicate that the filler content of an epoxy/HNT nanocomposite, and probably any type of nanocomposite, should not be assumed to be the same as can be calculated from the

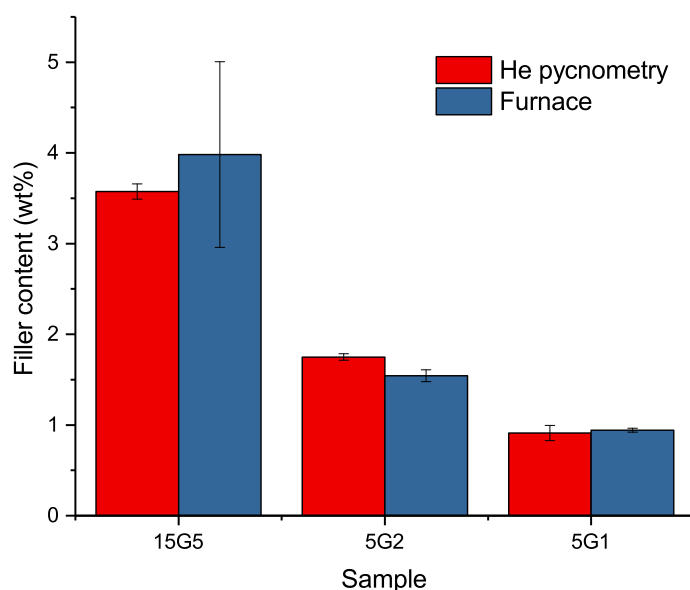


Figure 3.37: A comparison of filler contents found for three samples via He pycnometry and burn-off in a furnace. The two measurements seem to be in good agreement with one another.

Table 3.12: The filler content of various epoxy/HNT samples found by either TGA in air, He pycnometry, or burn-off in a furnace. These are compared to the expected filler contents calculated from the amount added to the resin before mixing.

Sample	Method	Filler content (actual)/wt%	Filler content (expected)/wt%
5G1	Furnace	0.9 ± 0.1	0.8
5G2	Furnace	1.54 ± 0.06	n/a
5G5	Furnace	3.94 ± 0.08	4.15
15G1	He pycnometry	0.4 ± 0.1	0.9
15G2	He pycnometry	1.33 ± 0.07	1.60
15G5	He pycnometry	3.57 ± 0.08	4.00
F1	Furnace	1.2 ± 0.2	0.9
F2	Furnace	1.6 ± 0.9	1.7
F5	Furnace	4.0 ± 0.2	4.1
S1	TGA in air	0.6 ± 0.1	0.8
S2	Furnace	1.7 ± 0.1	2.1
S5	TGA in air	3.00 ± 0.07	4.30
AS1	Furnace	0.8 ± 0.1	0.9
AS2	Furnace	1.4 ± 0.1	1.8
AS5	Furnace	4.0 ± 0.1	4.9

amount of filler added, especially if ultrasonication is used as the mixing technique.

On a practical note, because burning the resin off in the furnace allowed analysis of such

large sample amounts and so many samples at once while still giving reasonably accurate measurements, it was concluded that this was the best method for determining the filler content in the epoxy/HNT nanocomposites.

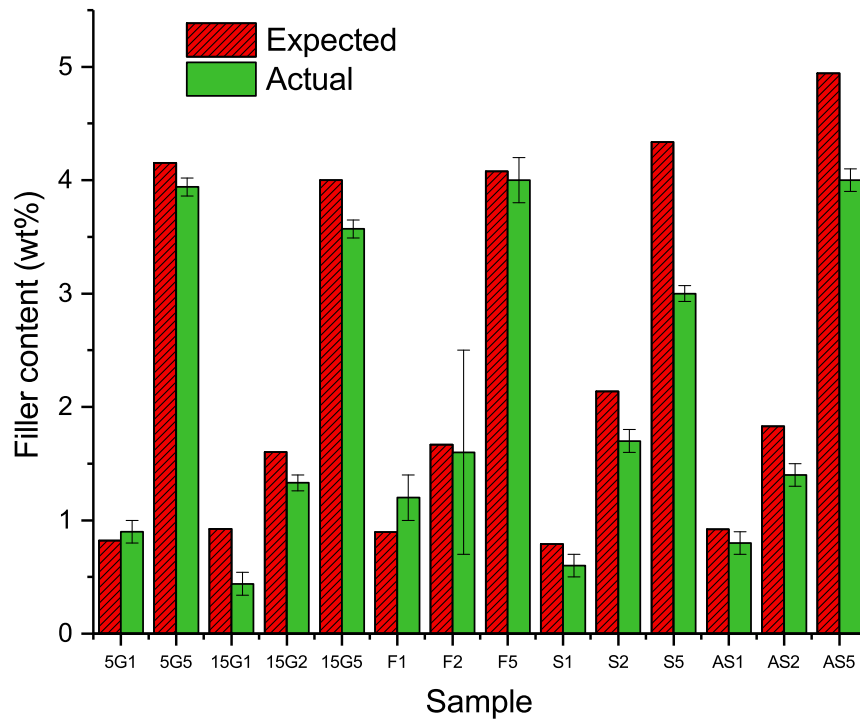


Figure 3.38: A comparison of actual filler contents found for the nanocomposite samples versus the expected filler contents calculated from the amount added to the resin before mixing.

3.2.9 The glass transition temperatures of epoxy/HNT nanocomposites

The glass transition temperature (T_g) of a polymer is the temperature above which it acts like a rubber, and below which, it is a relatively stiff, polymer glass.²⁰³ There are a number of factors which affect the T_g of a polymer, and several theories about its exact origin. It is often justified in simple terms as being related to the amount of free volume in and the inherent flexibility of the polymer network, i.e. the amount of free space in the network, and the ability of the polymer to explore that space. Because the amount of free volume in a material increases as it heats up and expands, the T_g is then considered to be the temperature above which there is enough room in the network for large-scale motions (e.g. translation, rotation, etc.) of polymer segments to take place.²⁰³

For cured epoxy resins, the glass transition temperature has been shown to be an indicator of the degree of cure of the material.¹⁸⁷ Specifically, a higher glass transition temperature usually indicates a greater cross-link density in the cured epoxy (and vice versa), which in turn corresponds to greater strength and stiffness of the material. As such, two different samples of cured epoxy resin of the same composition would be expected to have similar mechanical properties if they were to have a similar T_g .¹⁸⁷

In some cases, the presence of nanoparticles in a polymer nanocomposite can lead to changes in the T_g of the polymer.^{188,204} This is thought to be because polymer chain dynamics near a polymer/particle interface are different than in the bulk polymer.^{188,204} For example, attractive interactions between polymer and filler may lead to anchoring of polymer chains to the surface, causing local increases in chain entanglements and segmental packing.¹⁸⁸ Because of the large surface-area-to-volume ratio of nanoparticles, there should be a correspondingly large polymer/particle interfacial area in a nanocomposite containing individually dispersed nanoparticles. It is thought that there may be a large enough volume of the interfacial region in such polymer nanocomposites that the changes in polymer chain dynamics in the microscopic interfacial region can manifest as changes in the macroscopic properties of the polymer, notably its T_g , and possibly even its mechanical properties.

The T_g s of all of the epoxy/HNT nanocomposite samples made using different mixing methods were measured. This was done for two reasons: firstly, to assess whether the addition of HNTs had any effect on the T_g of the resin, and, if it did, to see whether this correlated to the filler content or degree of dispersion of the particles; secondly, if no change in T_g was observed, it could be used to confirm that all the resins had been cured to a similar extent. In both of these cases, the T_g would be useful for justifying any changes in mechanical properties seen between samples.

Dynamic Mechanical Analysis (DMA) was chosen as the method for measuring T_g . In DMA, a sample is heated and subjected to deformation at a constant displacement and frequency, while the load required to deform it is measured. At the T_g , the sample transitions from glassy to rubbery, and its modulus drops sharply. The T_g was taken as the centre of a gaussian curve fitted to the peak in a plot of $\tan\delta$ versus temperature, where δ is the angle between the complex modulus and the storage modulus of the sample, and $\tan\delta$ is the ratio between loss and storage moduli (i.e. inelastic and elastic moduli). DMA was chosen for determining T_g instead of the other commonly used technique, DSC, as

fitting the $\tan\delta$ curve in DMA to obtain the T_g is less subjective than fitting the curves obtained by DSC.

The T_g s found by DMA for all of the pure epoxy and epoxy/HNT nanocomposite samples are listed in table 3.13. The T_g s of all of the pure epoxy samples made were found to be between 129-130 °C. The T_g s of all of the nanocomposite samples were similar, although there was several degrees variation either side: the minimum T_g seen was 125 °C, and the maximum was 132 °C. However, this variation showed no correlation with either degree of dispersion or HNT content. Therefore, it is concluded that the presence of HNTs in epoxy resin had no effect on the final T_g of the material, at least not at concentrations below about 4 wt%. The similarity in T_g for all samples suggests that they were all cured to the same extent, i.e. all of the epoxy networks were similar. This is important, as it means that any changes in the mechanical properties seen between samples are probably due to the presence of the HNTs, and not due to any differences in the network structures of the epoxies.

Table 3.13: The T_g s of pure cured epoxy and all of the epoxy/HNT nanocomposites made by different mixing methods, as found using DMA.

Sample type	HNT content/wt%	$T_g/^\circ\text{C}$
Pure cured epoxy	0	129 - 130
S	0.44 ±0.01	125
S	1.7 ±0.1	131
S	2.95 ±0.07	126
AS	0.8 ±0.1	129
AS	1.4 ±0.1	129
AS	4.0 ±0.1	126
5G	0.9 ±0.1	127
5G	1.54 ±0.06	128
5G	3.94 ±0.08	132
15G	0.4 ±0.1	130
15G	1.33 ±0.03	130
15G	3.57 ±0.08	127
F	1.2 ±0.2	130
F	1.6 ±0.9	125
F	4.0 ±0.2	129

3.2.10 The effect of mixing method on the mechanical properties of the obtained composites

Perhaps the most important criterion for evaluating the effectiveness of a method for mixing nanoparticles into epoxy resin is the mechanical performance of the obtained nanocomposites. One of the most common ways to assess a material's mechanical performance is by subjecting it to deformation (i.e. deflection) at a constant rate, and measuring the resulting load experienced by the material. While there are several different ways to do this, flexural testing using a three-point bend set-up was chosen in this work. This

is mostly because of the ease of preparing samples for three-point bend testing; only a simple rectangle was required, and samples could be made small enough for them to be easily polished to the correct thickness. Three-point bend tests involve applying a downwards load to the midpoint of a (usually) cuboid-shaped sample supported by two parallel beams. The test can be used to measure the flexural modulus (i.e. stiffness) of the material, and its flexural strength (i.e. the load at which it yields or breaks).

Samples were made and tested to the specifications given in the British Standard ISO 178:2010.²⁰⁵ As per the standard, the flexural stress experienced by the sample was calculated using equation 3.11, where σ_f is flexural stress, F is the applied load, b is the test specimen width, h is the test specimen thickness, and L is the span between the two support beams. The flexural strain was calculated using equation 3.12, where ε_f is flexural strain, and s is deflection. Flexural modulus was then found by taking the gradient of flexural stress plotted against flexural strain (i.e. equation 3.13) in the low strain region. The flexural strength of a sample is taken as the maximum value of flexural stress experienced before it broke or yielded.

$$\sigma_f = \frac{3FL}{2bh^2} \quad (3.11)$$

$$\varepsilon_f = \frac{6sh}{L^2} \quad (3.12)$$

$$\text{Flexural modulus} = \frac{\sigma_f}{\varepsilon_f} \quad (3.13)$$

A note about issues with tensometer

Three-point bend tests were carried out using a small tensometer which was relatively old and infrequently maintained. It was chosen because it had a load cell with a relatively low load rating, and hence high enough precision to test small samples, and because access to it was both free and readily available. However, it became clear about halfway through the experiments that there was a problem with the set-up: the fixing used to attach the supporting beam to the tensometer base was changed, resulting in a change in modulus values of about 10%, even after adjusting for machine compliance. It is unclear why this happened, since checking the accuracy of the load cell showed no issues. However, normalising modulus values for samples measured before and after the change in the fixing relative to the modulus of a sample of pure epoxy measured in the appropriate configuration (i.e. before or after) seemed to give reasonable values for comparison regardless of the configuration in which the measurement was taken. Therefore, it was concluded that while absolute values of modulus for the samples could not be compared, it was reasonable to compare their relative moduli. All absolute and relative values of flexural modulus are given in table 3.14 to allow the reader to assess for themselves whether this is an accurate conclusion.

Table 3.14: The results of flexural testing of the nanocomposite samples. Because of problems with the tensometer, samples were essentially measured in two different set-ups (original and changed), and the flexural moduli are normalised using that of a pure epoxy measured in each set-up. The error in flexural modulus is the standard error of several measurements, and the error in relative flexural modulus is that error for each nanocomposite propagated with the standard error in the epoxy measurement.

Sample	Set-up	Absolute Flexural Modulus/MPa	Relative Flexural Modulus/%
Pure epoxy	Original	2550 ± 30	100 ± 1
Pure epoxy	Changed	2690 ± 40	100 ± 2
5G1	Original	2600 ± 40	102 ± 2
5G2	Original	2590 ± 50	101 ± 2
5G5	Original	2700 ± 100	107 ± 5
15G1	Original	2490 ± 20	98 ± 1
15G2	Original	2610 ± 40	102 ± 2
15G5	Original	2630 ± 20	103 ± 1
F1	Changed	2600 ± 30	97 ± 2
F2	Changed	2730 ± 40	102 ± 2
F5	Changed	3020 ± 30	112 ± 2
S1	Changed	2770 ± 20	103 ± 2
S2	Changed	2790 ± 40	103 ± 2
S5	Changed	2910 ± 10	108 ± 2
AS1	Original	2490 ± 10	97 ± 1
AS2	Original	2460 ± 30	97 ± 2
AS5	Original	2550 ± 50	100 ± 2

A comparison of the flexural moduli of epoxy/HNT nanocomposites obtained by different mixing methods

The relative moduli of the samples of epoxy/HNT nanocomposites made by different mixing methods are shown as a function of filler content in figure 3.39. Most of the samples showed a small increase in flexural modulus of a few percent relative to the pure epoxy, and only the S5 and F5 samples showed a larger increases of about 8% and 12% respectively. There was a larger amount of filler in the F5 sample than the S5, but it is unknown whether this accounts for all of the difference in modulus seen between the two samples. In contrast, the 15G1, F2, and AS1 and AS2 samples had lower moduli than the pure epoxy, and there was no improvement seen for the AS5 sample. The 5G5 sample has a larger uncertainty which extends into this range, but no conclusion is drawn from it; this was one of the first samples made, so the samples used for mechanical testing may well have not been ideal (e.g. they may have been misshapen). The overall conclusions are that mixing using the 3RM force mode led to the greatest improvement in flexural modulus, with ultrasonication in undiluted resin leading to some improvement in flexural modulus, mixing with the 3RM in gap mode leading to a small improvement, and mixing using ultrasonication in diluted resin leading to no improvement.

The largest improvement being seen for the F samples is not surprising, as HNTs in these

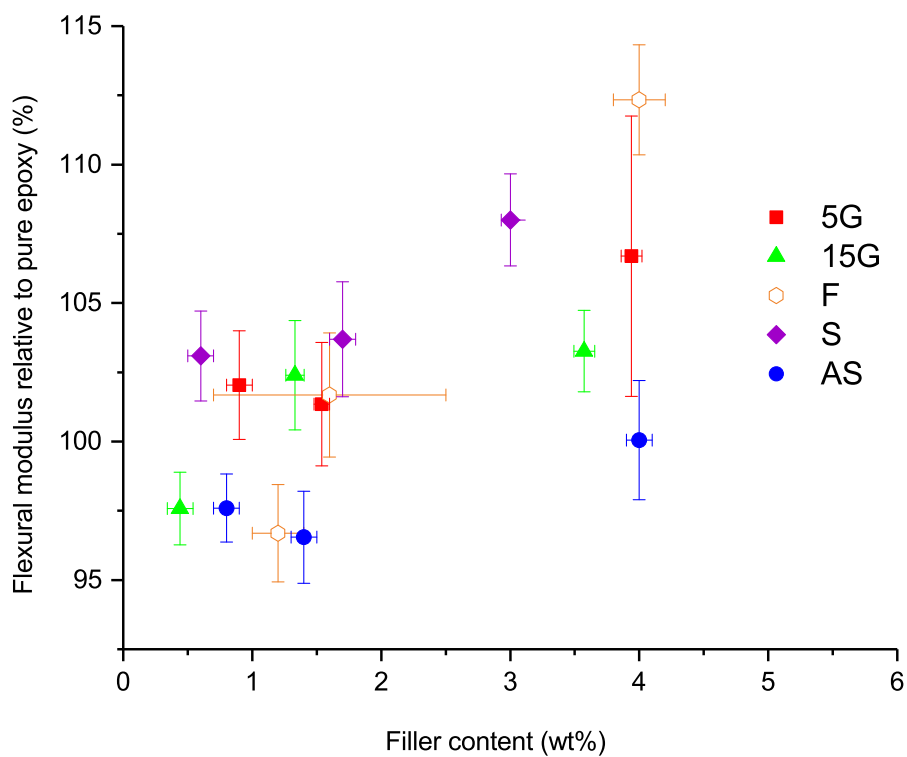


Figure 3.39: The flexural moduli relative to that of pure epoxy for samples of different filler content made by different mixing methods. The uncertainty in filler content is that found in section 3.2.8, and the uncertainty in relative flexural modulus is propagated from the standard error of several nanocomposite and pure epoxy samples.

samples were well dispersed, as shown by both TEM and optical microscopy. It was surprising that the S samples showed such an improvement in modulus, as HNTs in these samples had appeared quite badly dispersed in optical microscope images. However, TEM showed that the agglomerates of HNTs in badly mixed samples existed alongside many individually dispersed particles. It is therefore likely that enough of the particles were individually dispersed in the S samples for mechanical reinforcement to occur, albeit to a lesser extent than when all the particles were individually dispersed as in the F5 sample. This highlights the importance of complete particle dispersion for achieving the optimum improvement to mechanical properties.

Perhaps most surprising is the fact that the AS samples were all worse or no better than the pure epoxy, despite having appeared to contain well dispersed particles in both optical microscope and TEM images. This is probably unrelated to the dispersion state of the particles, but rather due to the presence of traces of acetone remaining in the sample, despite the extensive effort made to remove it.¹⁹⁷ This is supported by the presence of a low temperature peak in the DMA trace for the AS5 sample (figure 3.40), which indicates plasticisation of the material by the remaining solvent, and is also consistent with the anomalous rheological behaviour seen for the AS sample in section 3.2.7. It would probably be possible to remove all of the acetone from the sample with even more extensive effort, however the need to do so should be noted as a major disadvantage of the AS mixing method.

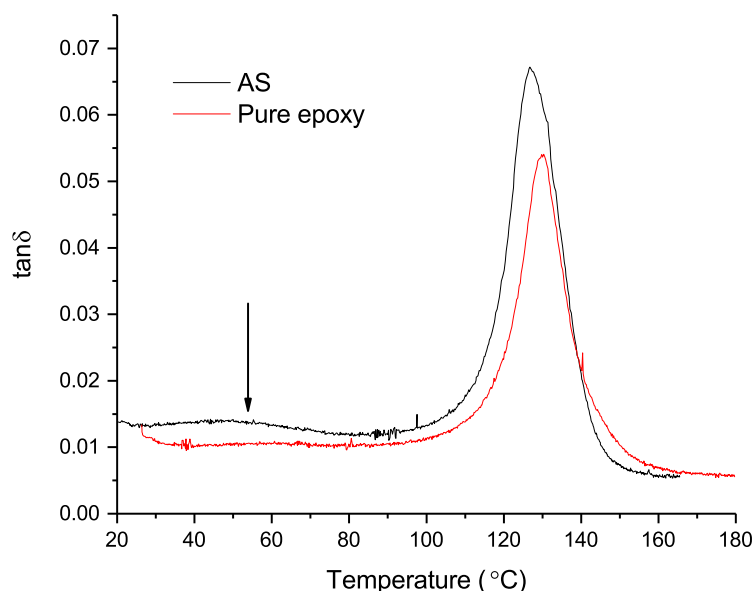


Figure 3.40: The DMA trace for the AS5 sample. A low temperature peak is observed, which is not seen for the other samples (e.g. the pure epoxy sample also shown here). This suggests that the sample is being plasticised to some degree by solvent remaining from the mixing step.

A comparison of the flexural strengths of epoxy/HNT nanocomposites obtained by different mixing methods

Figure 3.41 shows the flexural strength of each sample. While most of the samples seem to have a slightly higher strength than the pure epoxy (by a few percent), there is no apparent trend correlating flexural strength with either the degree of dispersion or the filler fraction of the HNTs. These observations are perhaps unsurprising considering that the surface of the HNTs was unmodified with coupling agents. That is to say, it appears that, since there was no covalent bridge between the surface of the HNTs and the epoxy network, stresses could not be effectively transferred between the two phases at high loads.

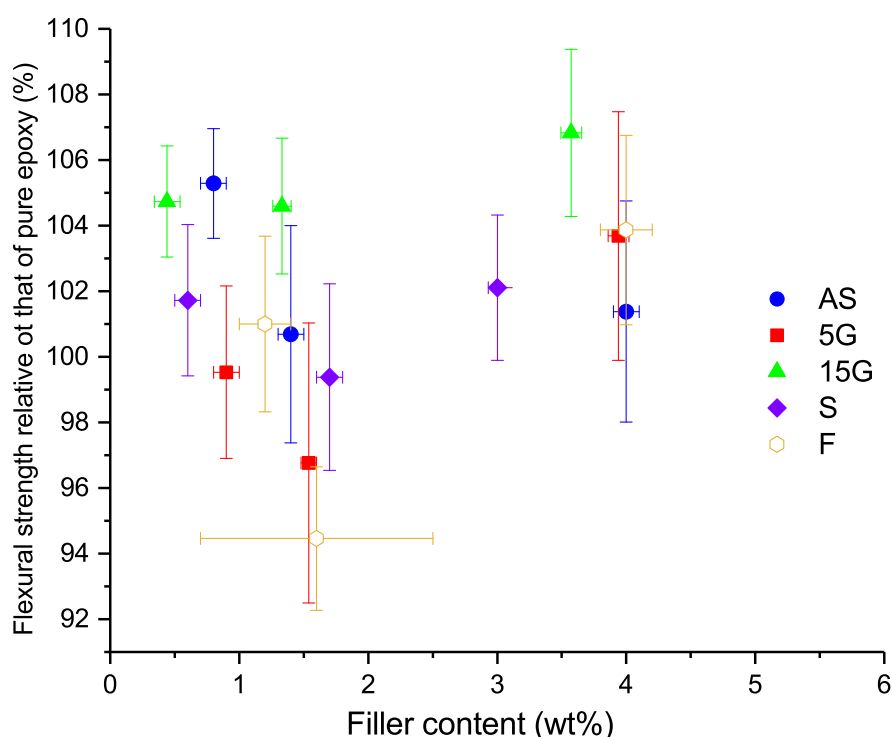


Figure 3.41: The flexural strength relative to that of pure epoxy for samples of different filler content made by different mixing methods. The uncertainty in filler content is that found in section 3.2.8, and the uncertainty in relative flexural strength is propagated from the standard error of several nanocomposite and pure epoxy samples.

It might have been expected that HNTs in the S samples, which appeared to have a substantial coating of epoxy homopolymer, would be able to react into the bulk epoxy network. However, the chemical structure of this coating remains unknown, so it is difficult to speculate about its reactivity. Nonetheless, it would appear from these results that the coating formed on the surface of the HNTs does not have a sufficient surface concentration of epoxide or nucleophilic groups to be able to effectively couple the HNT surface to the curing epoxy network, which would have improved the strength of the resulting nanocomposite.

Comparison of HNT to oMMT in epoxy nanocomposites

As discussed in section 3.2.4, epoxy/oMMT nanocomposites could not be made for direct comparison with epoxy/HNT nanocomposites. Therefore, the only comparison that can be made is with examples of epoxy/oMMT nanocomposites from literature. Two pieces of work by Yasmin *et al.* are good points of reference for this.^{5,51} In both cases, they processed oMMT into a DGEBA-based epoxy using high shear techniques (a 3RM⁵¹ and a high-shear mixer⁵), and proved that the plates were well exfoliated by using XRD and TEM. They found that a 5 wt% loading of oMMT led to an increase in Young's modulus of around 50%. An example plot of modulus versus clay loading is shown in figure 3.42.⁵ Similarly, Wang *et al.* saw a 40% improvement in the Young's modulus of their epoxy/oMMT nanocomposites at 5 wt% clay.¹²⁴ These increases are much higher than the maximum increase in flexural modulus of 12% seen in this work for an epoxy/HNT nanocomposite at a filler loading of about 4 wt%. Comparing the performance of two nanofillers based on their mass fraction can be misleading, as reinforcement depends on the volume fraction of filler used, and the volume fraction of filler in two nanocomposites with the same mass fraction of filler will be different if the fillers have different densities. However, commercially available oMMT typically contains a large amount of organic material (over 30 wt%), which means that the reinforcement of epoxy seen for oMMT in the literature probably actually occurred at a lower volume fraction of inorganic material than in the epoxy/HNT nanocomposites made here. Based on the fact that improvements in modulus were much greater for epoxy/oMMT nanocomposites reported in literature than for the epoxy/HNTs made here, the obvious conclusion is that oMMT is a much better reinforcing agent for epoxy resins than HNTs. This may be due to MMT nanoplates having a relatively higher modulus compared to HNTs (180 GPa⁴⁸ versus 140 GPa,¹ respectively), but it is also due to the fact that plate-like geometries are expected to offer more efficient reinforcement in a composite than tubular particles when the particles are randomly oriented in space.¹²⁸

However, while oMMT is clearly more effective at improving the stiffness of epoxy resins, it can be detrimental to their strength. When reporting the preparation of epoxy/oMMT nanocomposites, Yasmin *et al.* noted similar processing issues as reported in this work, i.e. foaming of the nanocomposite mixtures, which was difficult to alleviate. In turn, they found that the strength of the nanocomposites decreased by almost 50% upon the addition of 1 wt% of clay or more (figure 3.43). They attribute this to the nanocomposites failing due to the presence of microbubbles in the material acting as stress-concentrating flaws.^{5,51} This is supported by the fact that the strength of all of their nanocomposites was decreased by about the same amount, regardless of filler content, which suggests that the failure was not due to the oMMT particles themselves.⁵¹ This drop in strength upon the addition of oMMT to epoxy has been seen by some other authors,¹²⁴ but not all.^{206,207} Nonetheless, taking into account literature, as well as the difficulty of producing epoxy/oMMT nanocomposites in this work relative to the production of epoxy/HNT nanocomposites, it can be concluded that while HNTs are clearly not as efficient at improving the stiffness of epoxy resins as oMMT, they are much more easily incorporated without detriment to the strength of the final material.

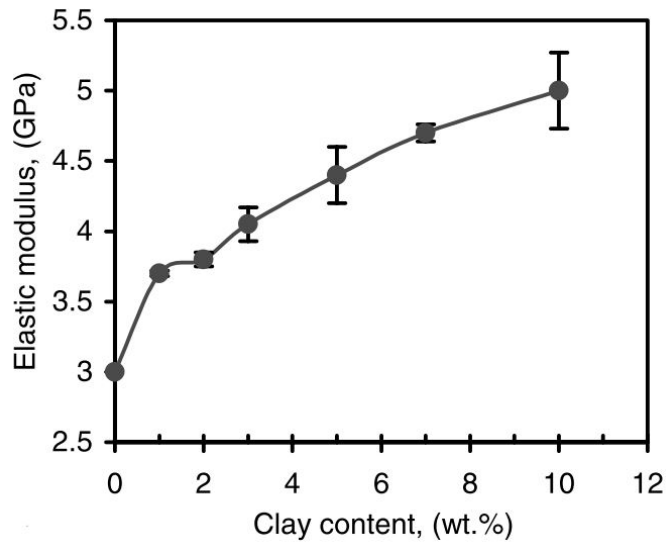


Figure 3.42: A plot of modulus versus oMMT content for a series of epoxy/oMMT nanocomposites, adapted with permission from work by Yasmin et al.⁵ The improvements in modulus are much greater than those seen for the epoxy/HNT nanocomposites made here.

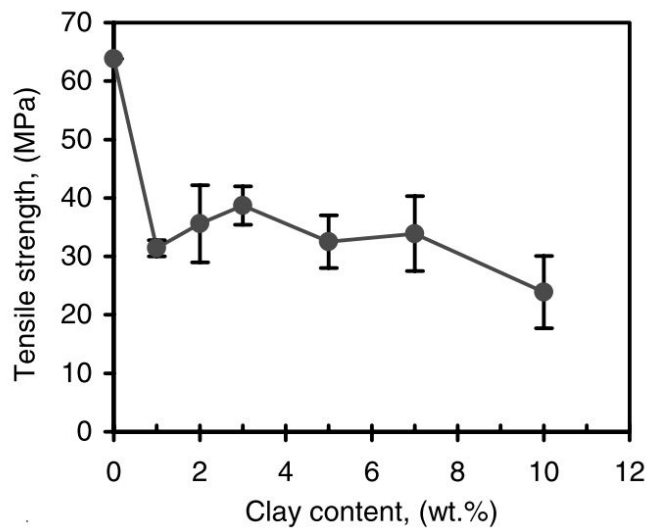


Figure 3.43: A plot of tensile strength versus clay content for a series of epoxy/oMMT nanocomposites, adapted with permission from work by Yasmin et al.⁵ The strength is seen to drop significantly upon the addition of oMMT, which they attribute to the formation of difficult-to-remove bubbles during processing.⁵

3.3 Conclusions and future work

The most practical conclusion from this piece of work is that the use of a 3RM in force mode is the best way to mix HNTs into epoxy resin to produce an epoxy/HNT nanocomposite. This is because this was the only method that produced a material that both contained mostly individually dispersed HNTs (shown by optical microscopy and TEM), and showed a significantly improved flexural modulus. The improvement in flexural modulus was much lower than that seen for epoxy/oMMT nanocomposites made in the same manner in the literature,⁵¹ but where the addition of oMMT was seen in the literature to reduce the strength of the epoxy,⁵¹ it was found here that the addition of HNTs does not cause a change in strength. The decrease in strength seen for the epoxy/oMMT nanocomposites was attributed to bubbles formed during processing of the oMMT into the epoxy, which were difficult to remove.^{5,51} A similar problem was encountered in this work, with foaming of the mixture making it impossible to manufacture suitable nanocomposite samples for mechanical testing. It is therefore concluded that the main advantage of using HNTs rather than oMMT as a reinforcing filler in epoxy resins is the fact that HNTs can improve the modulus of the material without affecting its strength. Future work would include testing the strength of nanocomposites containing coupling-agent-coated HNTs, in which the strength of the material may be increased because of more effective load transfer between the epoxy and the HNTs.

It was also shown through analysis of TEM images that none of the mixing methods appeared to damage (i.e. reduce the length) of the HNTs. This specifically contradicts earlier work suggesting that ultrasonication does cause a decrease in length of HNTs,¹⁸⁵ and is a useful conclusion in that it suggests that these nanotubes can withstand quite violent processing techniques, which might be relevant to their use in some applications. The large potential for inaccuracy surrounding the measurement of HNT lengths by TEM generally, and in nanocomposites specifically, was also highlighted. It is important to be aware of this, especially considering that it has already led to confusion in at least one published article.¹³²

Another important observation was that ultrasonication might change the fundamental chemistry of the epoxy resin. More specifically, the high temperatures reached during ultrasonication in an epoxy with no dilution or cooling certainly seemed to oxidise the sample, and may have been high enough to cause homopolymerisation of the epoxy. The HNTs washed from the ultrasonicated resin also seemed to have a significant degree of coating, which may have formed when the high temperatures led to reaction of the epoxy with the HNT surface, and/or homopolymerisation of the epoxy around the nanotubes. In addition, the viscosity of the ultrasonicated epoxy/HNT mixture was found to be much higher than expected considering its filler content and the degree of dispersion of the particles within, which is consistent with an increased concentration of higher molecular weight molecules. One should hence bear in mind the possibility for changes in the composition of epoxy resins when treated with ultrasonication without cooling.

Finally, it was shown that the HNT content in epoxy/HNT nanocomposites could be determined by all of He pycnometry, TGA in air, and burn-off in a furnace. Burn-off in particular is suggested to be a good technique for filler content determination, since it allows for accurate measurement of a large amount of sample and many samples at once (providing a precise enough balance is used and enough sample is available for measurement). It

was shown that the filler content of the final nanocomposites was often significantly lower than that which would be expected from the initial amount of HNTs added, especially for the samples prepared using ultrasonication. Perhaps the most important general conclusion from the chapter is hence that the filler content of a nanocomposite sample should always be measured, especially considering how many published articles do not do so, and how frequently ultrasonication is used to prepare nanocomposites.

3.4 Materials and methods

3.4.1 Materials

A summary of the materials used in this chapter is given in table 3.15. Not included is deionised water, which was purified from the mains supply to a resistivity of 18.0 M Ω cm using a PureLab Option-Q water treatment unit.

Table 3.15: A list of the materials used in this chapter.

Material	Supplier	Purity and/or other comments
Halloysite nanotubes	I-Minerals Inc.	ULTRA HalloPure Halloysite (2015M)
Epikote 828 (DGEBA epoxy resin)	Delta Resins Ltd.	Number average molecular weight < 700
meta-Xylylenediamine (MXDA)	Acros Organics	99%, N ₂ (g) flushed
Acetone	Merck	≥99.8%
Nanomer I.44P (oMMT)	Sigma-Aldrich	35-45 wt% dimethyl dialkyl (C14-C18) amine

3.4.2 Synthetic methods

Ultrasonication of epoxy/HNTs without cooling or solvent dilution (S)

About 60 g of a mixture containing DGEBA epoxy resin and about 5 wt% HNTs was mixed with an overhead stirrer, then ultrasonicated continuously using a Fisher Scientific FB-505 500 W Sonic Dismembrator at 70% amplitude for 25 min. The temperature of the vessel was measured throughout sonication using a data logger connected to a thermocouple attached to the exterior of the beaker using high-temperature sticky tape.

Ultrasonication of epoxy/HNTs with both cooling and solvent dilution (AS)

In a sealed flask, about 60 g of epoxy was dissolved in around 90 g of acetone using magnetic stirring. HNTs were added to give a HNT/epoxy mass ratio of about 0.05 (i.e. to give

a final HNT content in the pure epoxy of about 5 wt%). After a short period of stirring, the mixture was transferred to a 500 mL beaker and sonicated using a Fisher Scientific FB-505 500 W Sonic Dismembrator at 70% amplitude, with pulsed sonication (45 s on, 15 s off), and a total processing time of 80 min (i.e. 60 min of ultrasonics on). The mixture was kept cool during sonication by keeping the vessel in a large (>2 L) volume of ice water, which was magnetically stirred to ensure optimum cooling of the vessel. The temperature of the vessel throughout sonication was measured using a thermocouple attached to the exterior of the beaker with high-temperature sticky tape. Acetone was removed from the sample by several hours of rotary evaporation under vacuum with water-bath heating at 40 °C, until the change in the mass of the flask when weighed at 15 min intervals was less than the precision of the balance (± 0.01 g).

Processing of epoxy/HNTs with the 3RM: gap mode (5G and 15G)

HNTs were carefully mixed into epoxy with an overhead stirrer to give a mixture of about 30 wt%. This mixture was then processed by passing it 15 times through an Exakt 80e three-roll mill with the parameters listed in table 3.16.

Table 3.16: The 3RM parameters used to process the epoxy/HNT mixtures in gap mode.

Pass through the machine	Rear gap width/ μm	Front gap width/ μm	Roller speed/rpm
1	120	40	80
2	90	30	80
3	60	15	100
4 - 19	15	5	100

Processing of epoxy/HNTs with the 3RM: force mode (F)

HNTs were carefully mixed into epoxy with an overhead stirrer to give a mixture of about 30 wt%. This mixture was then processed by passing it 10 times through an Exakt 80e three-roll mill with the parameters listed in table 3.17.

Table 3.17: The 3RM parameters used to process the epoxy/HNT mixtures in force mode.

Pass through the machine	Rear gap width/ μm	Front gap width/ μm	Front gap force/ Nmm^{-1}	Roller speed/rpm
1	120	40	n/a	80
2	90	30	n/a	80
3	60	15	n/a	100
4	15	5	n/a	100
5 - 15	15	<1	26	120

Curing epoxy/HNT nanocomposites

In all cases, a nanocomposite mixture of about the right HNT content was made by diluting with pure resin the original samples made by each mixing method. Once diluted to the right composition, each sample was heated to 40 °C then vigorously mixed by hand until it appeared homogeneous. After cooling to room temperature, the diamine-functional curing agent, MXDA, was added to give a molar ratio of N-H/epoxide groups of between 1.01 and 1.05. These mixtures were sealed in vials with parafilm to limit carbamation of the MXDA, then stirred repeatedly over a pot time of about 1.5 h, before being poured into poly(tetrafluoroethylene) (PTFE) molds. Curing was carried out by heating the samples in an oven from 60 °C to 165 °C at a heating ramp rate of 1 °Cmin⁻¹, then holding the oven temperature at 165 °C for a further 3 h. After curing, the molds were removed from the oven, and the samples were removed from the molds, then stored in a desiccator over phosphorus pentoxide.

Preparation of samples for mechanical testing

Cured samples were polished to a thickness of about 1 mm using a MetPrep grinder/polisher and P240 grit wet and dry paper, being careful to ensure that the samples remained cuboid-shaped with parallel faces. After polishing, samples were dried with paper towel, then kept in a desiccator over phosphorus pentoxide for at least a day before mechanical testing.

3.4.3 Characterisation

Measuring vessel temperatures with a thermocouple

To measure the temperature of vessels during ultrasonication of epoxy/HNT mixtures, one Class 1 K-type thermocouple (precision = ± 2 °C) was attached to the exterior of the vessel wall using high temperature sticky tape. Temperature data was recorded at a sample rate of 1 s⁻¹ using a Pico Logger.

Optical microscopy

Samples for optical microscopy were made by curing a drop of the epoxy/curing-agent mixture described in section 3.4.2 between two glass coverslips. Images were taken in a transmission configuration using a Olympus BX50 microscope with a 4X magnification lens and a Pixelink digital camera. The scale of the images was calibrated by comparison with an image of a graticule with known dimensions at 4X magnification.

DLS measurement of the AS sample

To measure the size of the AS sample during sonication, an approx. 0.5 - 1 mL portion of the HNT/epoxy/acetone mixture was taken at each time interval, then diluted by shaking with about 10 mL of pure acetone. These samples were immediately placed into a quartz cuvette and analysed using a Malvern Zetasizer Nano S.

DMA

The T_g s of the cured nanocomposites were measured by Dynamic Mechanical Analysis (DMA) using a PerkinElmer DMA 8000. Samples were made for measurement with DMA by curing portions of the mixtures described in section 3.4.2 in aluminium materials pockets (Perkin-Elmer). The samples were tested using a single-cantilever bending set-up, with a frequency of 1 Hz. The sample temperature was ramped from room temperature up to 180 °C at a rate of 2 °Cmin⁻¹. The T_g was taken as the centre of a Gaussian curve fitted to the peak in a plot $\tan\delta$ versus temperature.

Flexural testing

Samples with dimensions of approx. (25 x 25 x 1) mm were tested with a three-point bend set-up using a span width of 20 mm, support beam and loading crosshead radii of 1 mm and 5 mm respectively, and a test speed of 1 (mm)min⁻¹. These sample dimensions and experimental set-up are similar to those described in British Standard ISO 178:2013.²⁰⁵ The tensometer was a Lloyd Texture Analyser fitted with a 500 N load cell. After adjusting for machine compliance by comparison to the load/displacement response of a thick, metal bar, the flexural moduli were obtained by fitting the stress/strain curves with a straight line in the region between 0.015 and 0.035 strain, and flexural strengths were obtained as the maximum stress endured by the sample before breaking or yielding.

Rheometry of uncured mixtures

Rheometry data was collected using a TA Instruments AR-G2 rheometer with a cone and plate configuration. The cone had a base diameter of 40 mm, an angle of 2°, and a truncation of 56 μ m. The viscosity of the mixtures was measured at increasing shear rates from 0.1 to 1000 s⁻¹. The temperature of the plate was maintained at 25 °C throughout the acquisition of data.

TEM of cured epoxy/HNT nanocomposites (N)

Samples of epoxy/HNTs containing approx. 5 wt% filler were cured as per section 3.4.2 in PTFE molds. After curing, samples were cut by hand with a junior hacksaw, then polished to give samples with an approximately quadrilateral cross-section of about (5 x 5) mm. These samples were prepared for TEM imaging by cutting off approx. 85 nm

thick slices using a Reichert-Jung Ultracut E ultramicrotome. They were then imaged using an FEI Tecnai transmission electron microscope. Cutting of the samples with the ultramicrotome was performed by Christopher J. Hill in the department of Biomedical Science at the University of Sheffield.

TEM of uncured epoxy/HNT nanocomposites (W)

As noted in the section 3.2.6, samples of uncured epoxy/HNT were first imaged without washing away the resin. These samples were made by diluting the mixtures described in section 3.4.2 with acetone to make dispersions containing approx. 1 wt% HNTs. Approx. 10 μL portions of these dispersions were then dropped onto carbon-coated TEM grids, and the excess liquid wicked away after approx. 1 min. They were then imaged using an FEI Tecnai transmission electron microscope.

To prepare samples of HNTs washed from epoxy/HNT mixtures, approx. 5 g portions of each sample were dissolved in about 40 mL of acetone. Once fully dissolved, these samples were centrifuged at 3000 rpm for 30 min to retrieve the solid. The solution was discarded, taking care not to disturb the settled solid. Fresh acetone (approx. 40 mL) was then added, and the mixture shaken to re-suspend the HNTs, before re-centrifugation. This cycle was repeated five times. Portions of the final solid were then suspended in acetone to give a dispersion of about 1 wt% HNTs. Approx. 10 μL portions of these dispersions were then dropped onto carbon-coated TEM grids, and the excess liquid wicked away after approx. 1 min. They were then imaged using an FEI Tecnai transmission electron microscope.

TGA in nitrogen atmosphere

Small droplets of sample (about 20 - 50 mg) were cured on the surface of a clean block of PTFE. These samples were then measured on a Perkin-Elmer Pyris1 TGA with a pure nitrogen atmosphere. Filler content was then calculated as described in section 3.2.8. The following heating schedule was used: hold for 5 min at 25 °C; heat from 25 °C to 800 °C at 10 °Cmin⁻¹; hold at 800 °C for 5 min.

TGA in nitrogen/air atmosphere

Small droplets of sample (about 20 - 50 mg) were cured on the surface of a clean block of PTFE. These samples were then measured on a Perkin-Elmer Pyris1 TGA with a mixed nitrogen/air atmosphere (2:1 nitrogen:air). Filler content was then calculated as described in section 3.2.8. Samples were heated as follows: heat from 25 °C to 800 °C at a rate of 40 °Cmin⁻¹; hold for 15 min at 800 °C; cool from 800 °C to 600 °C at a rate of 40 °Cmin⁻¹; hold at 600 °C for 20 min; cool from 600 °C to 25 °C at 40 °Cmin⁻¹; hold for 10 min at 25 °C.

TGA in an air atmosphere

Small droplets of sample (about 20 - 50 mg) were cured on the surface of a clean block of PTFE. Three of each of these samples were then measured using a TA Instruments Q500 with a compressed air atmosphere. An extraction hose was available for this instrument, which was placed directly next to the sample chamber to remove any gases evolved once the chamber had opened. Samples were heated from 30 °C to 800 °C at a heating rate of 20 °Cmin⁻¹, then held at 800 °C for 15 min.

He pycnometry

Densities were measured using a micromeritics AccuPyc 1330 pycnometer with a 1 cm³ sample cell. The density of HNTs was measured by weighing the powder into the cell. The densities of pure epoxy and epoxy/HNT nanocomposites were measured by filling the sample cell as much as possible with fragments of the nanocomposite samples which had been used for mechanical testing. In general, sample masses were on the order of a few hundred mg.

Burn-off in a furnace

Fragments of the nanocomposite samples used for the mechanical testing described in section 3.4.3 were placed in mullite crucibles of masses between 22 - 77 g, and the crucibles were weighed. The crucibles were then heated to 800 °C in a Lenton AWF115/25 furnace at a heating rate of 5 °Cmin⁻¹, after which the furnace was left to cool overnight. The crucibles were then weighed again, being careful not to disturb the remaining solid. Filler content was calculated as outlined in section 3.2.8.

Chapter 4

Functionalisation of Halloysite Nanotubes with Alkoxysilane and Activation with Piranha Solution

4.1 Introduction

4.1.1 Justification for alkoxy silane coating

As noted in Chapter 1, the ability to control the surface properties of a filler is useful for achieving optimum mechanical properties in reinforced polymer composite materials. More specifically, the surface of the filler is frequently chemically altered in order to enhance wetting by the bulk phase, and often also to provide a means for the formation of a bridge of covalently-bonded molecules between the filler surface and the polymer. In composites using macro- or microfillers, the enhanced wetting helps mitigate the formation of voids in the composite where the bulk has either not been able to penetrate between separate filler units, or has dewetted from the filler surface. In nanocomposites, the enhanced wetting can make it much easier to effectively disperse the nanoparticles, which is justified by the Gibbs free energy equation discussed in Chapters 2 and 3. Formation of a covalent bridge between the filler surface and bulk should enhance stress transfer between the phases, which leads to large gains in material strength in particular.²⁰⁸ Commercially produced reinforcing filler materials, e.g. glass, are usually treated with a “sizing” formulation to promote adhesion in the final composite.^{27,29} A common component of such sizings is some variety of alkoxy silane, which provides the covalent bridge between bulk and filler.²⁹

The reaction of a surface with an alkoxy silane is a commonly-used, simple way to achieve a surface coating. More specifically, alkoxy silanes can form covalent bonds with hydroxyl groups (which are present on many types of surfaces), leading to relatively robust surface layers. An alkoxy silane consists of a central, tetra-valent silicon atom, which is bonded to up to three alkoxy groups, with the remaining functional group/groups being some organic moiety, as shown in figure 4.1. It is this organic moiety which allows for chemical interaction between the coated-surface and the bulk medium, and a wide variety of organic functional groups can be included as part of an alkoxy silane molecule (some examples are included in figure 4.1). Because of this, alkoxy silanes are useful for changing the physical and chemical properties of the surfaces of reinforcing fillers used in polymer composites.

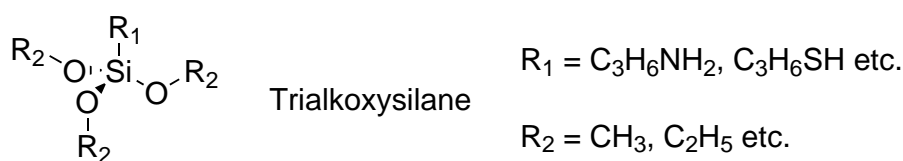


Figure 4.1: The structure of a generic trialkoxy silane.

4.1.2 Introduction to alkoxy silane chemistry

The formation of an alkoxy silane coating on a surface is a complex chemical process. It consists of several reaction steps, each of which exists in an equilibrium affected by a number of factors. The example of the reaction of a trialkoxy silane, the most typical type of organosilane used for coating reactions,²⁰⁹ is shown in figure 4.2.

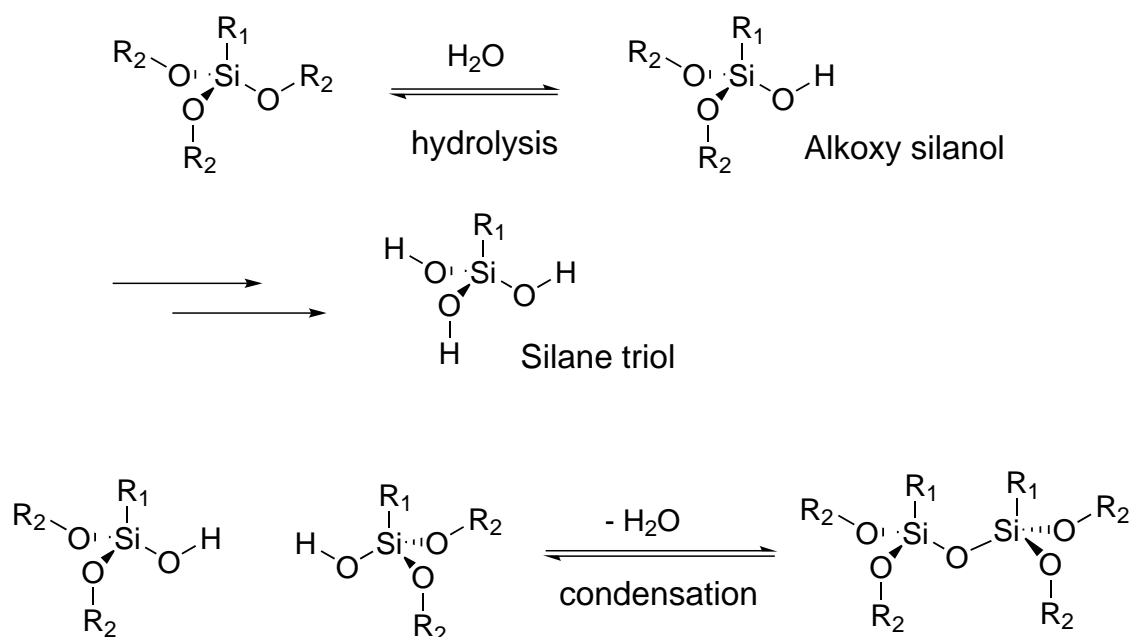


Figure 4.2: A reaction scheme showing the hydrolysis of a trialkoxysilane followed by subsequent condensation, in this case with another a silanol, but which can also take place with hydroxyl groups on a surface to form a coating.

The trialkoxysilane first undergoes hydrolysis to form an alkoxy silanol, and eventually a silane triol if repeated substitutions occur.²⁰⁹ These species are reactive, and undergo rapid condensation reactions, either with surface hydroxyl groups, or with other silanols. Depending on reaction conditions, the latter reaction can lead to dimers and eventually oligomers, although these can then be broken down again by subsequent hydrolysis or alcoholysis in a process referred to as depolymerisation.²⁰⁹

The roles of reactant concentrations and pH

It is obvious from Le Chatelier's principle that the concentrations of silane and water will influence the position of the equilibrium for each step of the reaction shown in figure 4.2. Specifically, an increased concentration of water will favour hydrolysis (which removes water) and disfavour condensation (which produces water). Similarly, an increase in the concentration of silane in a coating reaction favours the formation of polymeric species over the surface-grafting of monomeric silanols. It is therefore important to take the concentration of both water and alkoxy silane into account when designing these coating processes.

The rates of the hydrolysis and condensation steps also depend strongly on pH, because hydronium and hydroxide ions will both catalyse the reaction via different transition states (figure 4.3). The rates of hydrolysis and condensation reactions show minima at about pH 7 and about pH 2.5, respectively.²¹⁰

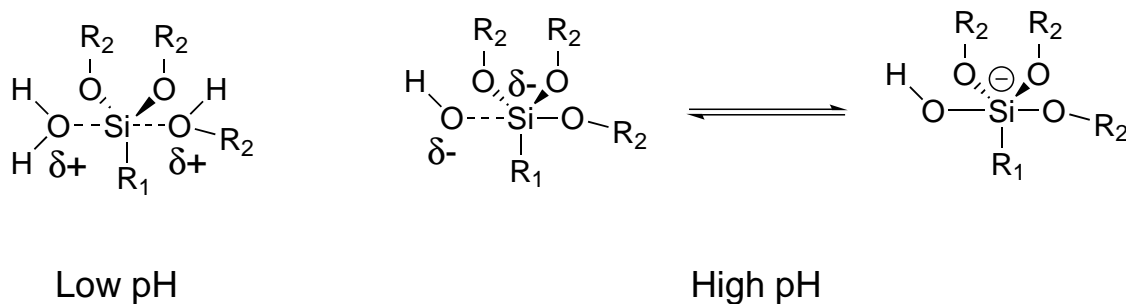


Figure 4.3: The different transition states which occur during the hydrolysis of alkoxy-silanes under acidic (left) and basic (right) conditions.

The role of the alkoxy substituent

It is the size of the substituents on the alkoxy group rather than their chemical nature that has more influence on the reaction. More specifically, the rate of hydrolysis decreases with increasing size of the alkyl substituent because of an increased degree of steric hindrance. As would be expected, substituents containing long, branched alkyl chains will slow the rate of hydrolysis the most.²⁰⁹

While size is the most important factor, the electronegativity of the substituents does also have some influence on the rate of hydrolysis in base or acid catalysed reactions. Electron withdrawing substituents (e.g. -OH) will stabilise the transition state at high pH, and inductively electron donating substituents (e.g. alkanes) will stabilise the positively charged transition state which occurs at low pH, thereby lowering the activation energy of the hydrolysis step.²⁰⁹

The structure of an alkoxy-silane coating

The reaction conditions are important in determining the final structure of the silicate. Using solutions with intermediate pH and/or low concentrations of water, thereby favouring condensation over hydrolysis, produces “weakly-branched” structures which arise from diffusion-limited particle growth,²⁰⁹ i.e. each new unit added to the polymer remains at the site it first reached and at which it reacted. In contrast, performing the reaction at high pH in aqueous conditions, i.e. favouring hydrolysis over condensation, leads to highly-branched, essentially smooth, spherical particles.²⁰⁹ These arise from reaction-limited particle growth.²⁰⁹ That is to say, the increased rate of hydrolysis and de-polymerisation allows the polymer to be repeatedly broken down and reorganised (i.e. by subsequent condensation reactions) until it reaches its most thermodynamically favourable structure. Both types of particle are illustrated in figure 4.4.

A monolayer coating refers to when the surface is coated with a layer which is effectively only one molecule thick, which would correspond to an alkoxy-silane molecule reacting with the surface without undergoing any reactions with other alkoxy-silane molecules. To achieve this, polymerisation of the silanols needs to be avoided, i.e. condensation reactions should ideally only occur between silanols and surface hydroxyl groups. This is most favoured under dry conditions in an aprotic solvent, with a low concentration of

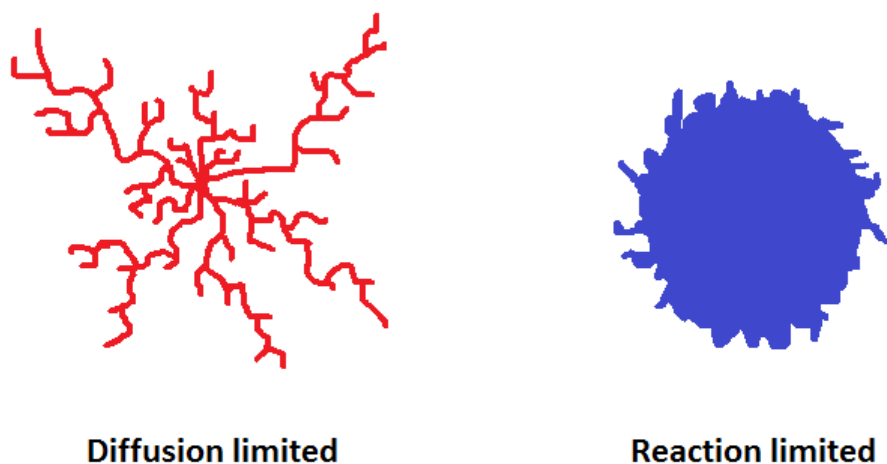


Figure 4.4: Simple 2D representations of the types of structures obtained from diffusion limited (left) and reaction limited (right) growth. In the context of silane coatings, diffusion and reaction limited structures are obtained when hydrolysis is disfavoured and favoured respectively.

alkoxysilane. If an alkoxysilane does polymerise from the surface with other molecules in solution, or oligomeric alkoxysilanes form in solution before condensation onto the surface, a coating will form which is several molecules or more thick. This is known as a multilayer coating. In the context of surface functionalisation, the goal is often to achieve a monolayer of coating on the surface.⁷

The special case of amine-functional alkoxysilanes

The use of (3-aminopropyl)trialkoxysilanes and related amine-functional silanes are a special case.²¹¹ This is because of several factors: the amine group can participate in the reaction as a catalyst, which complicates the kinetics; protonation of the amine to form an ammonium ion gives the resulting silicates a net positive charge, which can also coordinate to any anions present (e.g. Si-O^-); and hydrogen bonding of the amines with each other and with any oxygen bearing species leads to a much more complicated structure within the silicate. Some examples of these interactions are shown in figure 4.5.²¹¹

The positive charge on any silicates formed by condensation of aminoalkoxysilanes can be especially problematic when attempting to coat silica surfaces. This is because silica surfaces have a negative charge above about pH 2, meaning that polymeric silicates formed in solution may adhere to the surface via electrostatic/dipole and hydrogen bonding interactions rather than covalent bonds.²¹² This relatively loosely-bound layer would lead to a weaker interphase between surface and bulk were it part of a reinforcing filler in a polymer composite.²¹³

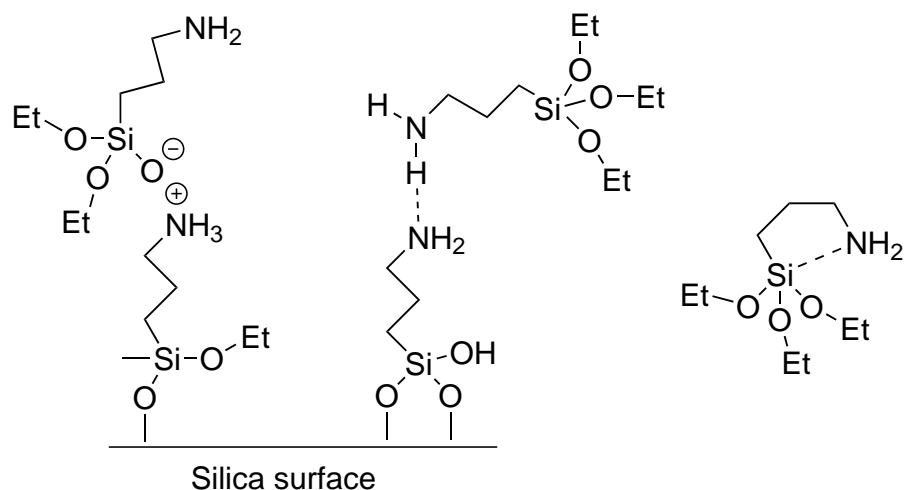


Figure 4.5: Some examples of the complex structures that amine-functional alkoxy-silanes (in this case APTES) can form on silica surfaces via various means of inter- and intramolecular bonding.

4.1.3 Alkoxy-silane coating in practice

Many examples of different silane coating procedures can be found in the literature. The use of toluene is common,^{7, 156, 211, 214–216} as it is a hydrophobic, aprotic solvent, and presumably also because it is so readily available. Toluene should naturally have low water content, but nonetheless it is sometimes also rigorously dried before being used as a solvent for silane coating.^{7, 211, 216} The use of ethanol is also common,^{103, 163, 217, 218} which is a protic and hygroscopic solvent. Some groups even report adding water to the silane coating reaction.^{217, 218} In these cases, a monolayer coating of silane is presumably not deemed an important requirement. There are also examples of coating reactions being carried out in other solvents, such as acetone,²¹⁹ as well as some simply in pure alkoxy-silane.²²⁰ It is also possible to avoid using solution reactions at all, as coatings can be achieved by exposing the surface to silane vapour.²¹¹ So, while the fundamental chemistry behind silane coating is complex, it is clear that they are reactions which are easy to carry out under a range of conditions. However, whether all of these conditions lead to optimum surface coating amounts and structures is a different matter. Indeed, the structure of the obtained silane coating is often not assessed.

Zhu *et al.* are one of the few groups to have compared the effectiveness of different silane coating techniques.²¹¹ Specifically, they were interested in comparing a reaction in toluene to a vapour-phase reaction for preparing (3-aminopropyl)triethoxysilane (APTES) functional silicon surfaces. It was found that coating in toluene produced multilayers, and, importantly, they found significant deviation between the amount of silane which was grafted to the surface when this procedure was repeated. This persisted despite rigorous purification and drying of solvents and reaction vessels. They suggest that variations in batches of APTES and even ambient humidity can have an affect on the repeatability of preparing coatings in this way. In contrast, coating the silicon by exposing it to APTES vapour produced repeatable, stable monolayers of silane.²¹¹ It is clear from this work that silane coating reactions should ideally be done using silane vapour rather than in

solution, as this method was concluded to be the only way to produce repeatable silane monolayers.²¹¹

However, while vapour-phase reactions are clearly the best route for producing silane monolayers on surfaces,²¹¹ it is not clear how practical or necessary this is when coating HNTs with silane. For instance, the exterior surface of HNTs is supposed to only have a relatively low density of hydroxyl groups,⁷ so monolayer coverage might be so minimal that there would not be a great change in the wettability of the surface, and only few sites for reaction into the network. In this case, a multilayer coverage might even be preferable in terms of improving the surface compatibility with the bulk. In addition, in terms of experimental practicality, a vapour phase reaction would be difficult to carry out on HNTs. A vapour phase coating requires a bespoke reaction vessel in which the surface to be coated can be suspended above the liquid silane.²¹¹ For HNTs, it would be difficult to construct a vessel that allows the powder to be both suspended above the liquid and have all of its surface area exposed to the vapour. This would be especially problematic if large quantities of HNTs needed to be coated, e.g. for large-scale use in polymer nanocomposites. That is to say, despite their proven disadvantages relative to vapour-phase reactions, solution-phase coating reactions seem like the most appropriate for functionalising HNT surfaces with alkoxysilanes.

4.1.4 Piranha solution pretreatments

Piranha solution is the name of a reactive mixture made by adding aqueous hydrogen peroxide to concentrated sulfuric acid (typically in the ratio 1:3 vol/vol peroxide to acid). This solution heats up rapidly upon mixing, due to the exothermic hydration of the concentrated sulfuric acid,⁶ and it subsequently undergoes rapid, sometimes explosive,^{221,222} reactions with organic compounds. Piranha solution can hence be quite hazardous, but it is especially effective at cleaning organic residues off a variety of substrates, and is therefore widely used in applications where clean surfaces are important (e.g. in microelectronics), despite the associated risk.

The active component of piranha solution is peroxymonosulfuric acid, which is also often referred to as Caro's acid.⁶ The formation and structure of Caro's acid is illustrated in figure 4.6. Caro's acid is a powerful oxidising agent, capable of oxidising many metallic²²³ and organic²²⁴ species, which is why it is so effective at removing organic compounds from substrates. The extremely low pH of piranha solutions is also thought to play a role in its interactions with organic compounds, i.e. by catalysing hydrolysis reactions and causing extensive dehydration. However, it should be noted that much of the information available regarding the mechanism of action of piranha solution appears to be well-informed speculation, and it is difficult to trace the origins of these theories to peer-reviewed literature; for most researchers, it appears to be enough to know that piranha solution works well for cleaning substrates, and how it does so is less important. Nonetheless, the consensus seems to be that piranha solution works to solvate organic compounds via both oxidation due to the formation of Caro's acid, and hydrolysis/dehydration in the extremely concentrated sulfuric acid.

Silica glass surfaces are among those that are often cleaned with piranha solution before use,²²⁵ and there has been some suggestion that the piranha treatment not only cleans the

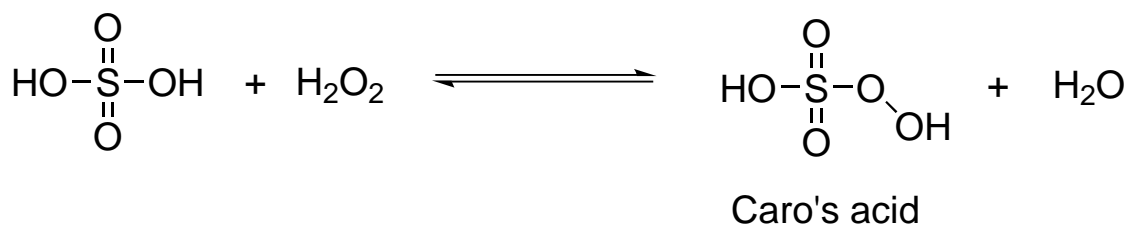


Figure 4.6: Upon mixing, sulfuric acid and hydrogen peroxide react to form Caro's acid, a powerful oxidising agent.⁶

silica surface, but also reacts with it. For example, piranha solution has been suggested to etch silica surfaces,^{226,227} and make them inherently more hydrophilic by increasing the concentration of silanol (i.e. Si-OH) groups on the surface.²²⁶ However, considering the chemistry of both components, it is difficult to see how this could be the case. Seu *et al.* suggest that it is because piranha solution “is a strong oxidizer and will hydroxylate the surface by increasing silanol groups and Si-O⁻ species on the glass support”,²²⁶ but it does not make sense for silica (i.e. SiO₂) to be able to be oxidised further; the oxidation numbers of neither Si nor O change upon transformation from Si-O-Si to Si-OH. Acid-catalysed hydrolysis and subsequent dissolution of silica would be a more reasonable explanation, and a hypothetical mechanism for this is given in figure 4.7. However, the equilibrium solubility of amorphous silica in water at low pH is relatively low,^{228,229} and it takes days for this equilibrium to be reached at room temperature,²²⁸ compared to the tens of minutes over which piranha solution is typically applied. Nonetheless, Seu *et al.* showed using AFM that the nano-scale roughness of glass slides increased as they were subjected to an increasing treatment time with piranha solution.²²⁶ Therefore, while the mechanism of the interaction between silica surfaces and piranha solution is not clear, it does not seem unreasonable to conclude that it can have some effect on silica beyond simply removing organic residues from it.

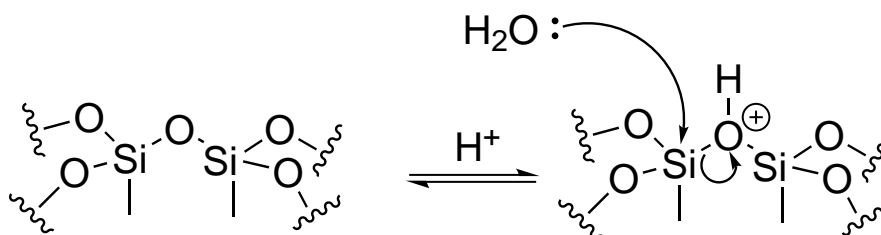


Figure 4.7: A hypothetical mechanism for the acid-catalysed hydrolysis of silica.

Similar to silica glass, the external surface of HNTs is composed mainly of Si-O-Si bonds, with Si-OH groups only accessible at surface edges and defects.⁵⁵ This is thought to limit the area of the HNT surface that is accessible for functionalisation with alkoxy silanes.⁷ Being able to increase the surface concentration of silanol groups on HNTs before subsequent silane coating would allow the inclusion of the useful, silane-borne functional group over a greater area, potentially leading to improved performance of the coated HNTs. For example, inclusion of a greater number of amine groups might lead to a greater area of the HNTs being able to react into an epoxy network, thereby improving interfacial adhesion in the subsequent nanocomposite. Therefore, were piranha solution able to increase the concentration of silanol groups on a silica surface, it would be interesting for application

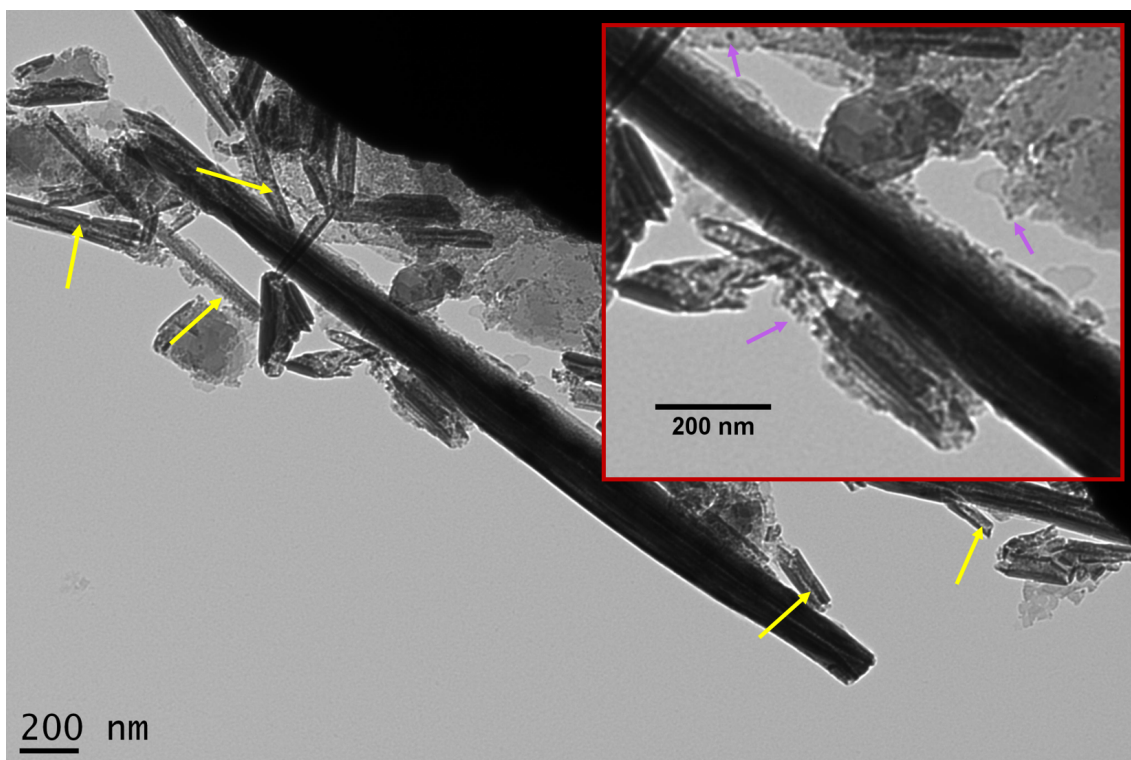
to HNTs intended for use as fillers in epoxy resin nanocomposites.

Halloysite is composed of alumina as well as silica. In contrast to silica, alumina is highly soluble at low pH.²²⁹ The interior surface of HNTs (i.e. the wall of the nanotube lumen) consists of exposed alumina, and several studies have shown that treatment of HNTs with aqueous acid can damage these interior surfaces, specifically by acid-catalysed hydrolysis.^{155,229,230} In physical terms, this leads to enlargement of the HNTs' lumina from the inside out, which is accompanied by the formation of silica nanoparticles (Si-NPs) of about 10 - 20 nm in diameter. Eventually, only a nanotubular, silica skeleton is left. An example of nanotubes damaged by acid-etching is shown in figure 4.8. Abdullayev *et al.* studied the kinetics of sulfuric acid etching of HNTs.¹⁵⁵ They found the process (i.e. dissolution of alumina) to be first order with respect to the acid at 50 °C, and zeroth order above 80 °C. With respect to HNT concentration, the process was found to be pseudo-zeroth order below 70 °C, and approximately two-thirds order above this temperature. The zero order kinetic regimes are explained as being due to diffusion of acid into, and etching products out of, the narrow nanotube opening. That is to say, in these regimes, the process can only happen as fast as diffusion in and out of the tube can occur.¹⁵⁵ At ambient and intermediate temperatures, it took days for significant dissolution of the alumina to occur, but it took place in a matter of hours above 70 °C: at a treatment temperature of 90 °C, 100% of the alumina was removed in under 10 h.¹⁵⁵ Because of this, when applying a piranha solution pretreatment, it is important to take into account the potential for damage to HNTs due to acid-etching of their interior alumina surfaces.

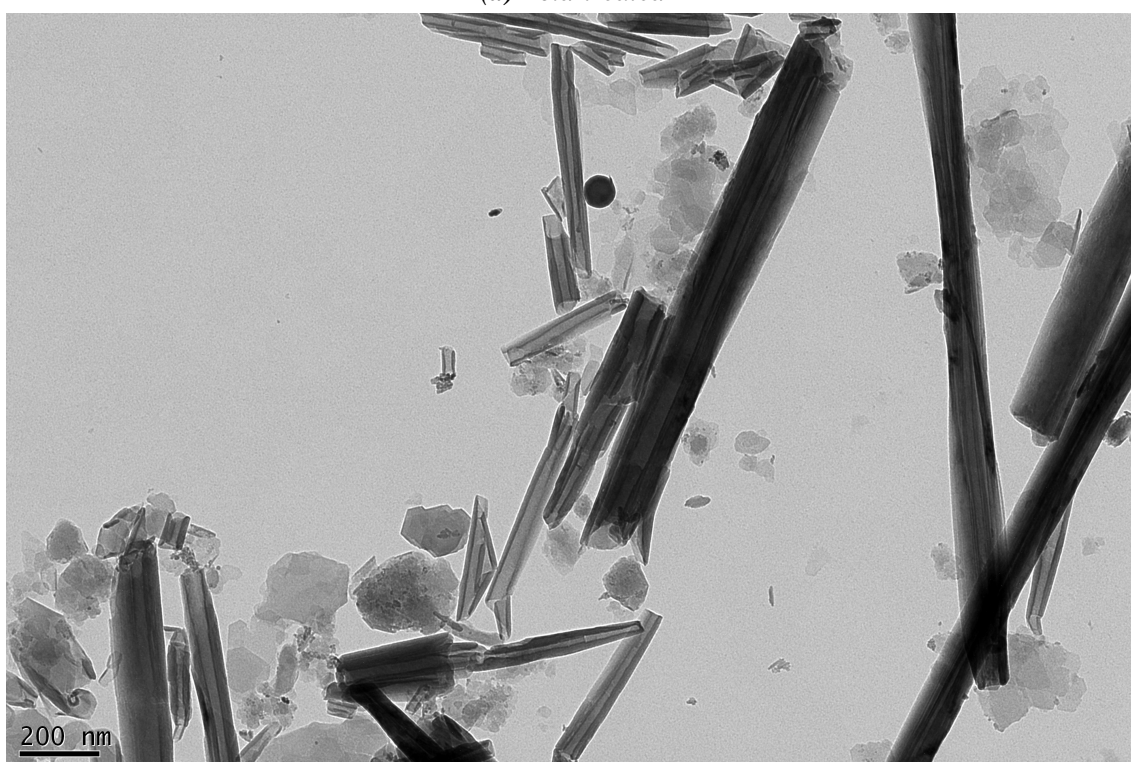
In 2015, Sun *et al.* studied the affect of treating HNTs with piranha solution, and compared the outcomes of APTES coating reactions using either untreated or piranha solution treated HNTs.⁷ They inferred hydroxylation of (i.e. formation of new Si-OH groups on) the piranha treated HNT surface from the appearance of new peaks in IR spectroscopy and X-ray photoelectron spectroscopy (XPS) data. Data from XRD and TEM appeared to indicate that the structure of the nanotubes was largely retained after piranha solution treatment, despite the highly acidic environment. Specifically, while the porosity of the nanotubes was seen to increase slightly, there was no observable damage in TEM images. Most notably, they found that the grafted amount of APTES increased from 1.55 wt% on untreated HNTs to 2.78 wt% on piranha solution treated HNTs, an increase of 80%. From their work, it seems clear that piranha solution treatment of HNTs is a good way to increase the extent to which the nanotubes can be coated with alkoxysilane.⁷ However, they only studied the outcomes of the coating reactions, and did not investigate whether the increased degree of coating led to any improvements when the HNTs were used in a specific application, for example, as reinforcing fillers in a nanocomposite.

4.1.5 Aims of chapter

The aim of this chapter was to study the coating of HNTs with alkoxysilane, with particular attention to the repeatability and scale-up of this process. An additional goal was to replicate the “activating” effect of piranha solution treatment described by Sun *et al.* to increase the degree of coating of the HNT surface.⁷ This was done with a mind to use and compare the various coated samples as fillers in an epoxy resin nanocomposite, but unfortunately the three-roll mill broke towards the end of the project, before this work



(a) Acid-treated



(b) Pristine

Figure 4.8: An example of HNTs which have been damaged during treatment with aqueous acid (a), compared to pristine, untreated HNTs (b). The damage manifests itself as enlargement and roughening of the nanotube interior as the alumina surface is removed (some examples in (a) are indicated with yellow arrows), which is accompanied by the formation of Si-NPs (some examples are indicated with purple arrows in the inset image in (a), which shows a zoomed-in view of part of the same TEM image).

could be carried out. To aid navigation, a flowchart illustrating the structure of the chapter is given in figure 4.9.

4.2 Results and discussion

4.2.1 Initial investigation of silane coating of HNTs

Early in the project, the intention was to use HNTs as fillers in poly(acrylate) polymers. Because of this, silane coating reactions on HNTs were first attempted using 3-(trimethoxysilyl)propyl methacrylate (TMPM), the structure of which is shown in figure 4.10. A reaction similar to that described by Sun *et al.* was used.⁷ Specifically, the HNTs and silane were heated for 24 h in refluxing toluene. The TMPM concentration was above 2 wt%, as Sun *et al.* had found the grafted amount of silane to level off after this concentration.⁷ However, the method used here differs from that of Sun *et al.* in that dry toluene was not used, and the dispersions of HNTs in toluene were not treated with 30 min of ultrasonication before heating (they do not specify the instrument type or power). In the case of ultrasonication, this was neglected because HNTs do not disperse very readily into toluene (see Chapter 2), so it was unknown how much effect low power ultrasonication from an ultrasonic bath (the only ultrasonic instrument available at the time) would have in terms of dispersing the HNTs such that a significantly larger surface area was exposed for reaction. That is to say, it was uncertain what advantage ultrasonication would provide, especially considering that facilitating ultrasonication significantly complicates the process. Dry toluene was not used since the solubility of water in toluene is low under ambient conditions, and presumably very low in boiling toluene. Drying large amounts of toluene for this procedure was hence seen as an unnecessary complication, especially considering that doing so would become increasingly impractical as the process was scaled up. A simple measure to prevent too much exposure of the system to water was the fitting of a drying tube to the reflux condenser. In addition, TMPM was only added once the mixture of HNTs and toluene had reached reflux. Because the boiling point of toluene (110 °C) is above that of water, it was expected that this would be sufficient to remove water to the extent that the rate of hydrolysis of the silane was not so high as to limit the grafting of silane to the HNT surface. The above method for coating the HNTs is denoted procedure 1 (P1).

Several methods were used to indicate the success of the coating reaction. Firstly, TGA analysis showed significantly more mass loss for the coated HNTs than for the untreated nanotubes, as shown in figure 4.11. Subsequent IR spectroscopy (figure 4.12) showed the presence of absorption peaks corresponding to sp^3 hybridised C-H bonds, as well as the carbonyl (C=O) bond, and ester C-O bond. More absorption peaks would be expected for the TMPM molecule, but because it is only present in low concentrations, only the most strongly absorbing peaks can be observed. Most notably, the sp^2 C=C could not be observed, which is significant as this is the bond that would allow reaction of the surface coating into the bulk network if the HNTs were then used to make poly(acrylate) nanocomposites by free-radical polymerisation. Additionally, the water contact angle of the coated HNTs was much greater than that of the pure nanotubes, as can be seen in figure 4.13, which indicates that a (relatively) hydrophobic coating has been achieved

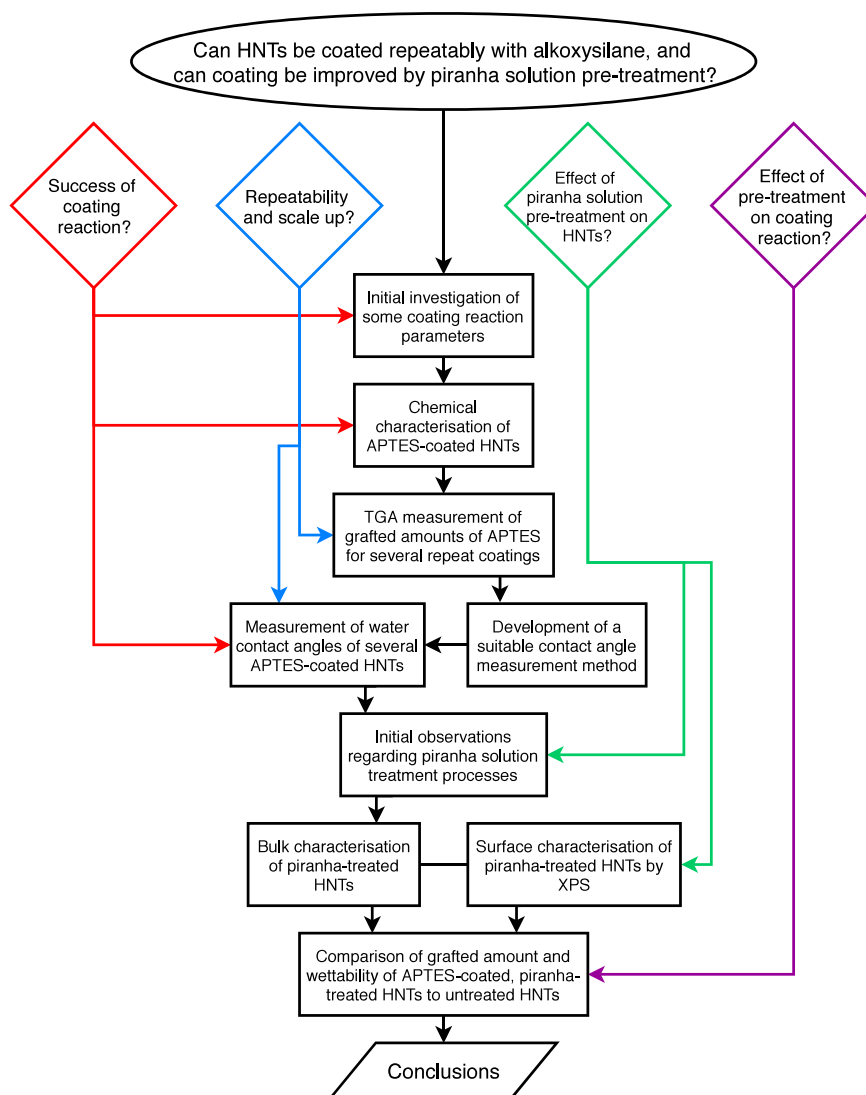


Figure 4.9: A flowchart illustrating the structure of the chapter “Functionalisation of Halloysite Nanotubes with Alkoxysilane and Activation with Piranha Solution”

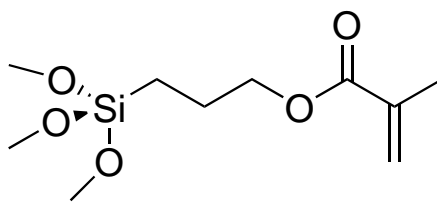


Figure 4.10: The structure of 3-(trimethoxysilyl)propyl methacrylate (TMPPM).

on the HNTs (contact angle measurements will be discussed in more detail later in the chapter). TEM images of the coated nanotubes appear to show to a new layer of coating on some of the surfaces of the nanotubes (figure 4.14). As would be expected from the non-uniform coverage of the HNT surface with hydroxyl groups, this surface layer appears to be patchy rather than homogeneous. It also extends many nanometres from the surface, indicating that a polymerised, multilayer network has been formed. However, it cannot be concluded that this is solely due to the formation of a silicate, as it is unknown whether the TMPPM polymerised via a free-radical pathway in the relatively high temperature reaction. Taken together, the above characterisation methods showed that the modified version of the reaction described by Sun *et al.*⁷ was able to be used to coat HNTs in TMPPM with a heterogeneous multilayer coating that significantly increased the hydrophobicity of the nanotubes. However, it is unknown whether the reactive alkene bonds survived the coating process.

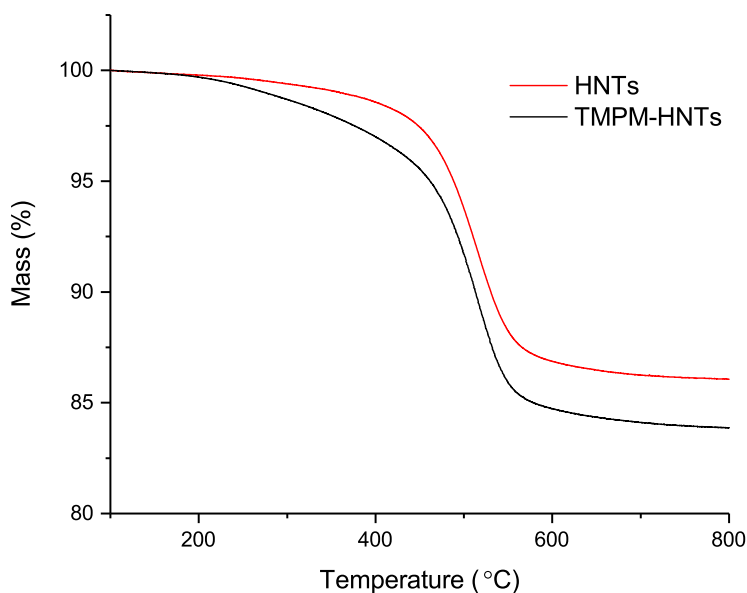


Figure 4.11: A greater mass loss is seen for TMPPM-coated HNTs than for untreated HNTs, and this mass loss occurs at a lower onset temperature. This suggests that an organic coating is present, i.e. that the reaction was successful.

A comparison of different washing methods for purifying the coated HNTs was also made. Washing is supposed to remove any unreacted silane and silicates from the final sample, and should be sufficiently thorough to ensure that any material that appears to be ‘grafted’

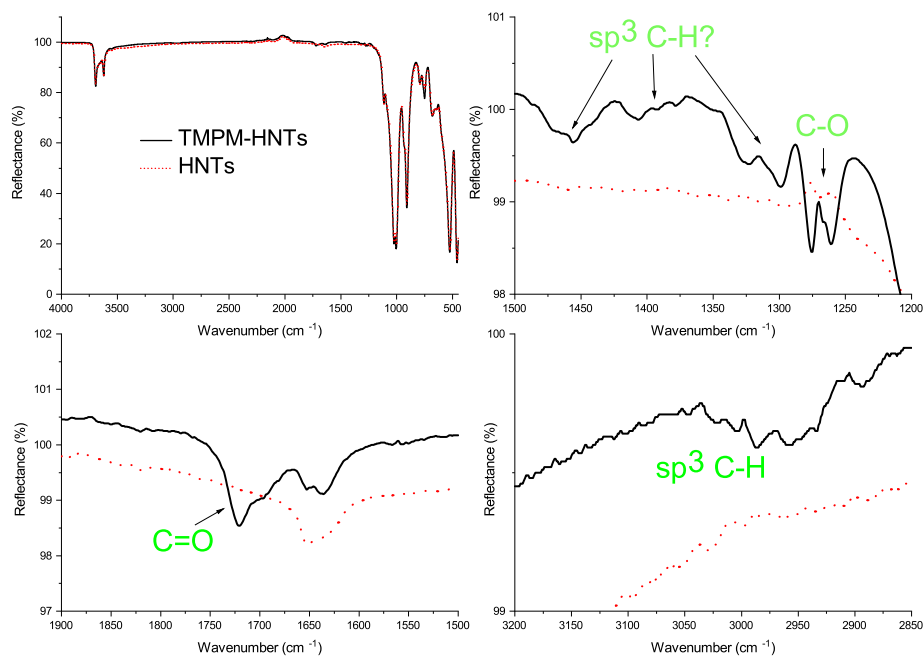


Figure 4.12: The IR spectra of HNTs and TPM-HNTs. After silane coating, new absorption peaks can be seen, which are associated with various organic functional groups on the coating molecule. However, no absorption peaks associated with the C=C bond can be identified.

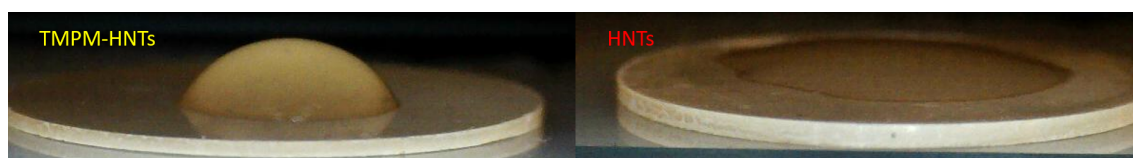


Figure 4.13: A side-by-side comparison of a water droplet on TPM coated HNTs and unmodified HNTs. The coated HNTs appear to have a relatively high water contact angle, while the untreated HNTs have a much lower contact angle, that quickly recedes to 0 as the water is absorbed by the HNT pellet.

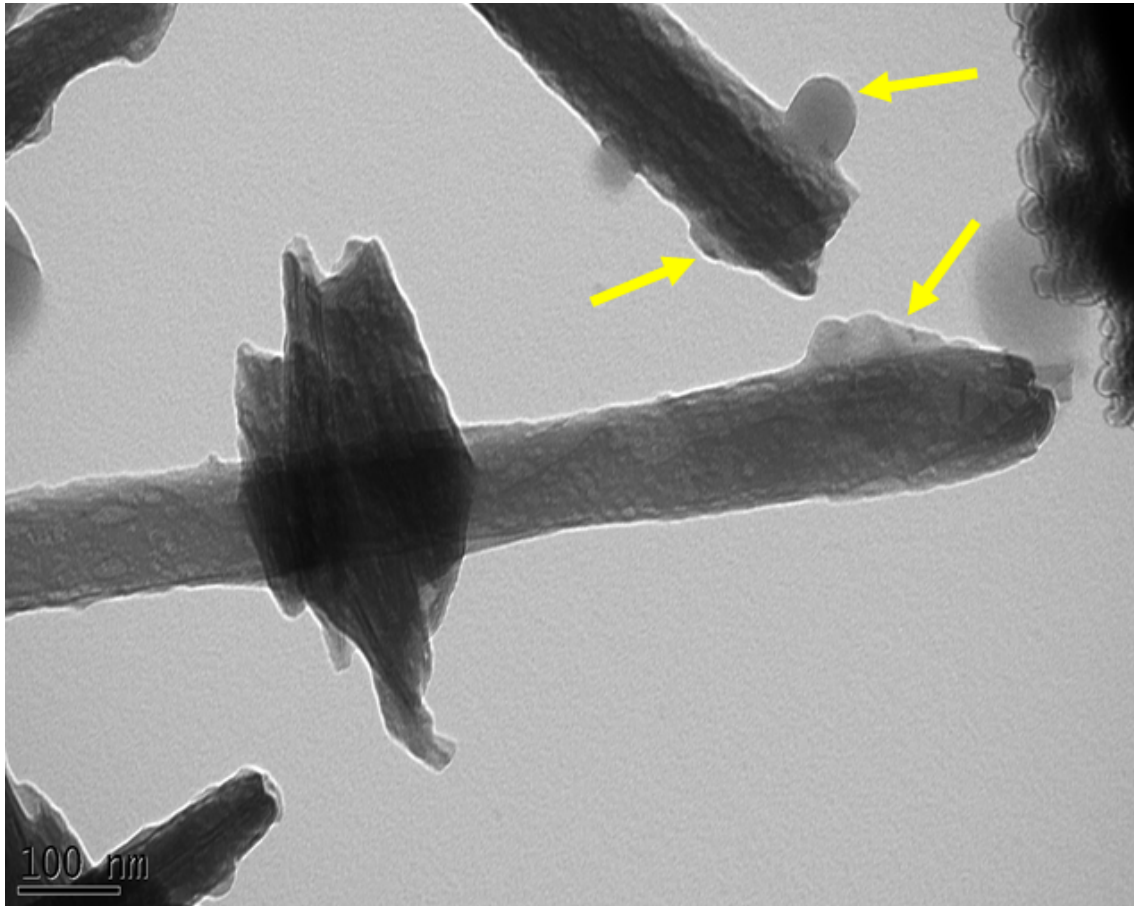


Figure 4.14: A TEM image of TPM coated HNTs. The yellow arrows indicate features which are thought to be the silane coating, as they are not seen in TEM images of pure HNTs. In places, these features extend many nanometres away from the HNT surface, indicating a multilayer coating of silane.

is actually covalently bonded to the surface rather than weakly bonded and free to leave.²³¹ This is especially important when coating reinforcing fillers, since a weakly bound layer of silane in the interphase will be detrimental to mechanical properties.²¹³ Washing HNTs by filtration was found to be time consuming, especially if large amounts of solvents need to be used, because the clay is able to clog the filtration medium. Instead, the coated clay was washed by removing it from solution with a centrifuge, dispersing the solid in fresh toluene, then repeating the process. This was compared to using a soxhlet extraction. In a soxhlet extraction, a sample is added to a cellulose thimble in a specially designed extractor, in which it is repeatedly rinsed with solvent which is being boiled in a flask below the thimble. The solvent condenses in the chamber containing the sample, and is drained once a certain fluid level is reached within the chamber, thereby being recycled. Soxhlet extraction has several advantages over hand-washing: it is less intensive for the operator, as the washing is essentially automated and continuous once reflux has begun, and many more wash cycles can be carried out for little additional effort; less solvent has to be used, as it is repeatedly recycled and purified by distillation; and it exposes the operator to less solvent, hence reducing hazard. The main disadvantages to soxhlet extraction are that it is slower than hand-washing if only a few rinses are needed, and the reflux can be energy intensive as it requires constant heating.

To compare hand-washing to soxhlet extraction, a sample was coated with TMPM, then half was taken to be washed by either method. Using hand-washing, the sample was able to be rinsed with several hundred mL of toluene over an hour or two of dedicated work. With soxhlet extraction, about half an hour of set-up was required. It took around an hour for the extractor to fill and drain, but the extraction was left running for 48 h, meaning that 48 washes of around 100 mL of solvent could be achieved for little extra effort. TGA (figure 4.15) showed 0.34 wt% lower mass loss for the soxhlet extracted sample than the hand washed sample, indicating that soxhlet extraction was indeed more effective at removing non-grafted products from the clay. Because of this, and the fact that it was easier and safer, soxhlet extraction of the coated HNTs with toluene was chosen as the washing method going forward.

Reactions were also carried out in ethanol for comparison to toluene. This was because the most common solvent seen for silane coatings in the literature other than toluene appears to be ethanol, and because HNTs disperse much more readily in ethanol than in toluene. It was thought that this increased compatibility might lead to a greater extent of the HNT surfaces being available for coating than in toluene (i.e. fewer surfaces would be blocked by the nanotubes agglomerating together). For a first comparison, a completely different reaction procedure was used (denoted P2), which is a modified version of that described by Guo *et al.*¹⁰³ A similar concentration of HNTs and TMPM was used as in their work, but they also acidified the mixture with acetic acid, which was not done here, and they ran the reflux for 1 h, whereas the reaction here was for 24 h. While IR spectroscopy showed that the same functional groups were present in the modified clay, TGA analysis on the product of P2 suggested it had significantly less TMPM coating than that of P1; the mass of the P2 sample at 800 °C was 1.18 wt% higher than that of the P1 sample. However, in P1, the sample was extracted exclusively with toluene, whereas P2 was extracted with ethanol. To check whether washing with different solvents had made the difference, the P1 product was subjected to further extraction with ethanol. However, this led to only a 0.2 wt% decrease in mass at 800 °C, much lower than that difference between P1 and P2. The difference in grafted amount between P1 and P2 is more likely

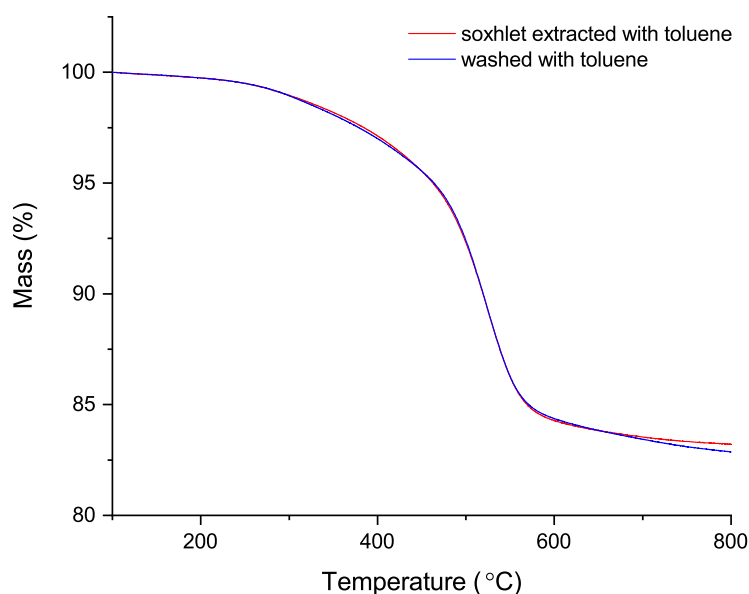


Figure 4.15: TGA of the same TPM-HNT sample, half of which was washed using soxhlet extraction, the other half by hand (as described in the text). The higher mass remaining for the soxhlet extracted sample indicates that this was the better method for washing non-grafted species away from the HNTs.

due to the much higher concentration of TPM used in P2, leading to a much higher degree of polymerisation of the silane, which subsequently did not graft to the surface of the HNTs.

The reaction was then repeated, but this time using a much lower concentration of TPM, i.e. essentially the same procedure as P1, but with ethanol instead of toluene. In this new procedure (denoted P3), TGA showed that the mass remaining in the sample at 800 °C was only 0.31 wt% higher than the sample obtained by P1. However, the water contact angle of the sample obtained via P3 was significantly lower than that from P1 (figure 4.17). Possible reasons for the difference could be the increased reaction temperature which is reached by boiling toluene versus ethanol (bp = 110 °C versus 78 °C), or the fact that both water (which is more difficult to remove from ethanol than toluene) and even the ethanol itself could hydrolyse/alcoholise and remove surface-grafted silane in P2 and P3, leading to a different surface silane structure than in P1. Regardless of the exact reason, it was concluded that using toluene as a solvent for the coating was better than using ethanol, as it produced a more hydrophobic sample with a higher grafted amount of silane.

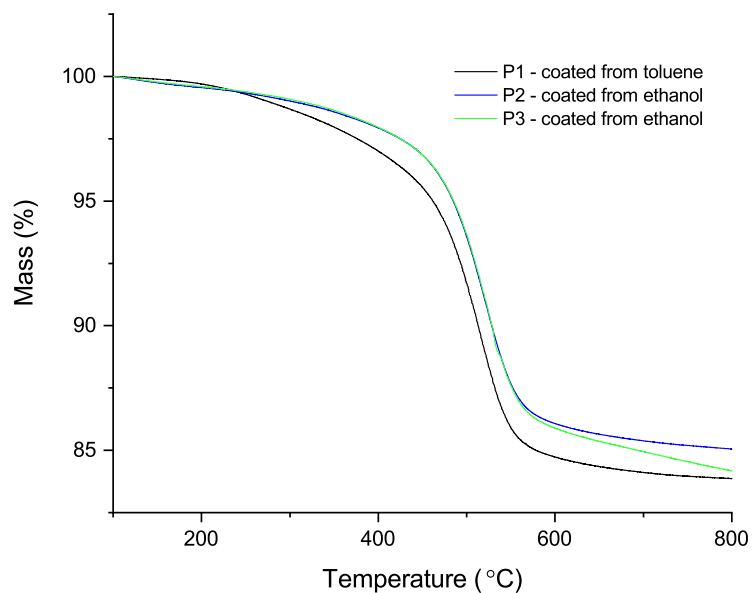


Figure 4.16: TGA for TPM-HNTs coated using toluene and ethanol. Coating in ethanol with a high TPM concentration (P2) led to a much lower grafted amount than using toluene. Coating in ethanol with the same TPM concentration as was used in P1, i.e. P3, led to different thermal degradation behaviour, and a somewhat lower grafted amount.

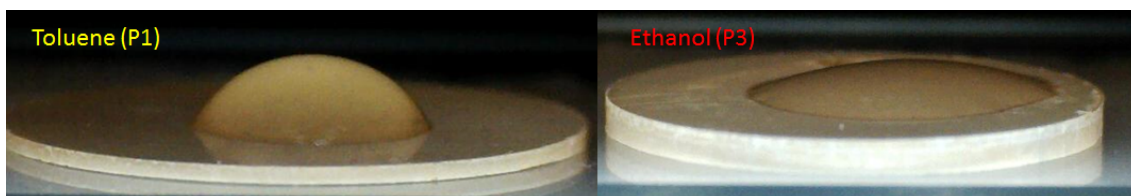


Figure 4.17: A side-by-side comparison of the water contact angles of TPM coated HNT samples made by reaction in toluene or ethanol (i.e. by using P1 or P3, respectively).

4.2.2 Coating HNTs with APTES

In order to coat the surface of the HNTs with amine groups, and thereby allow for reaction into an epoxy resin network, the nanotubes were coated using (3-aminopropyl)triethoxysilane (APTES). The structure of APTES is shown in figure 4.18.

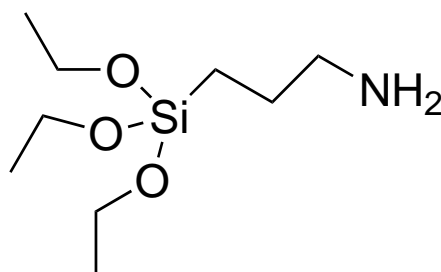


Figure 4.18: The structure of (3-aminopropyl)triethoxysilane (APTES).

As with the TMPM-HNTs, the success of the APTES coating reaction was determined using several techniques. TGA (figure 4.19) showed there to be material grafted to the APTES treated HNTs (NH₂-HNTs) as they had a higher mass loss upon heating than the pure HNTs. As shown in figure 4.20, the sp³ C-H absorptions were again seen in the IR absorption spectrum of the NH₂-HNTs, although the absorption peak for the amine, which would have been expected at around 3500 cm⁻¹, was not observed. This is probably due to the low concentration of amine groups on the surface of the HNTs. The presence of the amine group was instead confirmed with XPS (which will be discussed in more detail in section 4.2.3): a peak corresponding to the N 1s orbital was found for NH₂-HNTs, but not untreated HNTs (figure 4.21). While XPS cannot be used to infer the identity of the exact nitrogen functional group, the element can only have come from the amine group on APTES. On the basis of TGA, IR spectroscopy, and XPS, it can be concluded that the HNTs were successfully functionalised with APTES to introduce amine groups to the nanotube surface.

TEM images of a sample of the NH₂-HNTs were taken, and examples are shown in figure 4.22. As with the TMPM-HNTs, it was possible to find areas where there appeared to be a multi-layered coating extending many nanometres away from the nanotube surface. However, these features were rare, and not seen for most nanotubes. That is not to say that most of the nanotubes had no coating, since it is possible that the coating was too thin to be observed by TEM. The most that can be concluded from TEM images is that the reaction probably produced an inhomogeneous surface coating on the order of nanometres in thickness.

For one portion of NH₂-HNTs, an additional 24 h of soxhlet extraction was carried out, this time with ethanol as the washing solvent. This is partly because Sun *et al.* had carried out additional washing of their product with methanol after washing with toluene,⁷ but also because APTES is known to be able to undergo hydrogen bonding and other non-covalent interactions with silica surfaces.²¹¹ The second wash was therefore carried out to determine whether there were any non-covalently bound APTES species remaining on the HNTs surface; these may have remained bound to the surface in toluene, but should come off in ethanol, which is much more polar and can undergo hydrogen bonding itself (and indeed will probably have contained a significant amount of water since it was stored

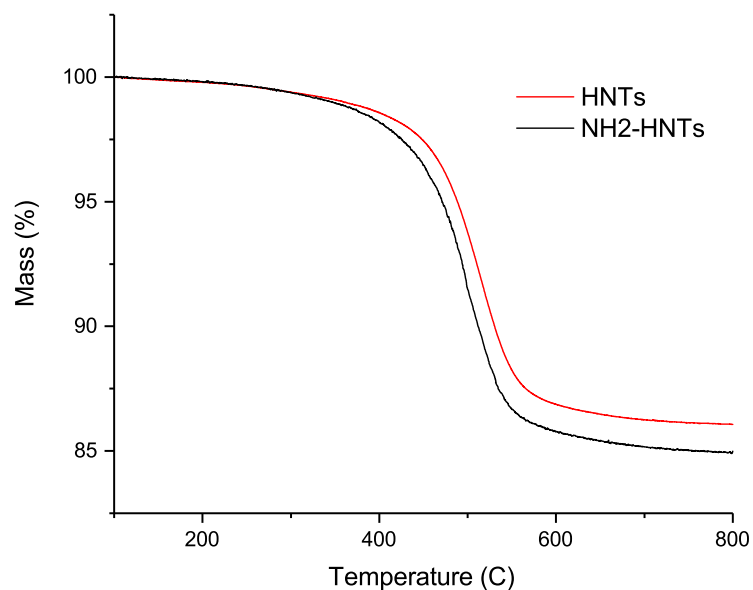


Figure 4.19: A greater mass loss is seen for NH₂-HNTs than for untreated HNTs, which suggests that the APTES coating reaction was successful.

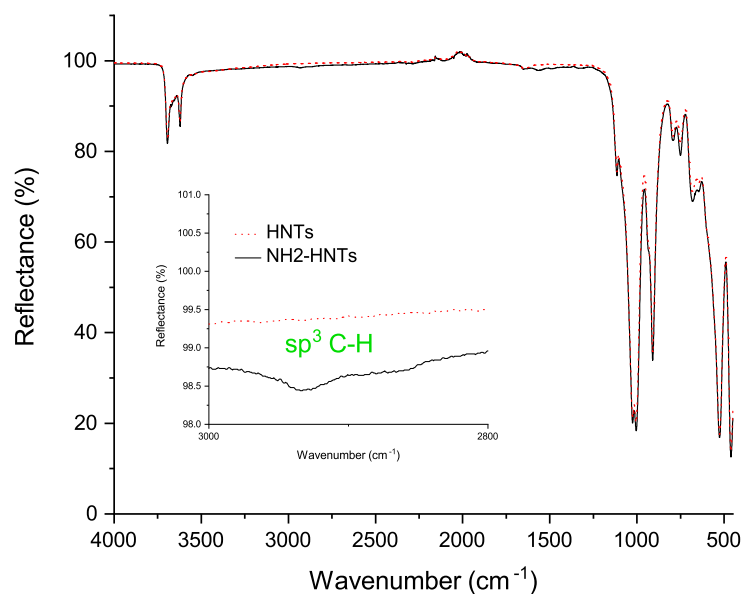


Figure 4.20: The IR spectrum of a sample of NH₂-HNTs compared to that of unmodified HNTs. The presence of a C-H stretching absorption suggests that APTES grafting has been successful, but the signature vibrations of the amine group cannot be seen, presumably due to their low concentration and relatively low absorption coefficient.

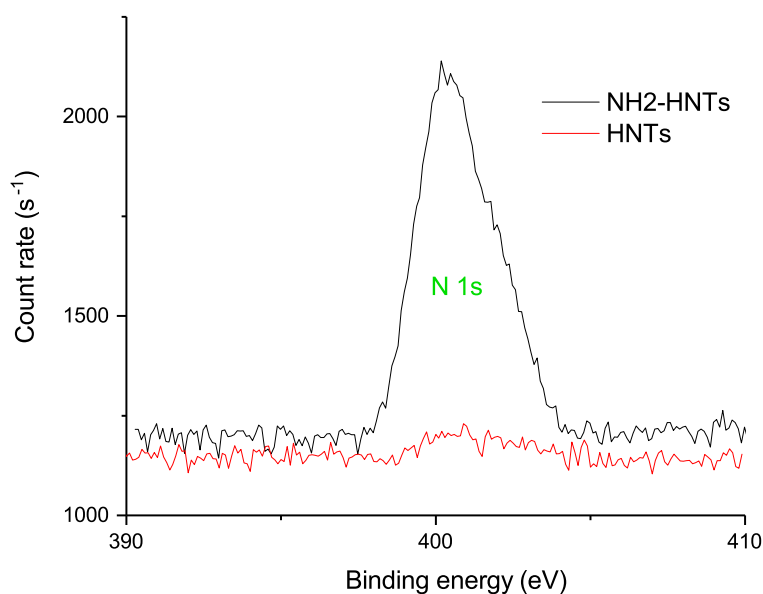


Figure 4.21: There is a peak for the N 1s electron orbital in XPS of NH₂-HNTs, but not in the spectra of HNTs. This can be taken as proof that APTES has been grafted onto the surface of the HNTs.

under ambient conditions). The sample washed with ethanol in addition to toluene showed the same amount of mass remaining at 800 °C as that which was washed with toluene only (figure 4.23), suggesting that further washing of the NH₂-HNTs after soxhlet extraction with toluene is unnecessary. This also suggests that grafted amounts obtained by TGA are repeatable for the same sample.

Once it had been shown to be successful, this APTES coating procedure was repeated several times. This is because Zhu *et al.* had noted that they found the results of APTES coating of silica surfaces in toluene to show significant variability between samples, regardless of the rigour with which it was carried out, which they attribute to variations in ambient humidity.²¹¹ As such, it was important to get an idea of the variability of the APTES coating reaction, especially as conditions used in this work were far less rigorous than those described by Zhu *et al.*²¹¹ Repeating the coating reaction several times did seem to lead to variation in the grafted amount of silane on the HNTs, which ranged from 1.07 wt% to 1.79 wt%. For comparison, Sun *et al.* found a grafted amount of APTES of 1.55 wt% when they carried out their procedure on untreated HNTs,⁷ which is well within the range of the grafted amounts found here.

As shown in figure 4.24, there were some differences in the amounts of reagents used in the process, but grafted amount correlated neither with the absolute concentrations, nor the relative concentrations of APTES or HNTs. It is expected that variations in the exact batch of APTES (i.e. the presence of oligomers and other impurities) used may affect the results of surface coating. However, all of these reactions were carried out using APTES from the same bottle, and there was also no correlation between the date of the coating reaction and the grafted amount, which suggests that aging of the batch of APTES (i.e. polymerisation caused by adventitious water) was not the cause of the

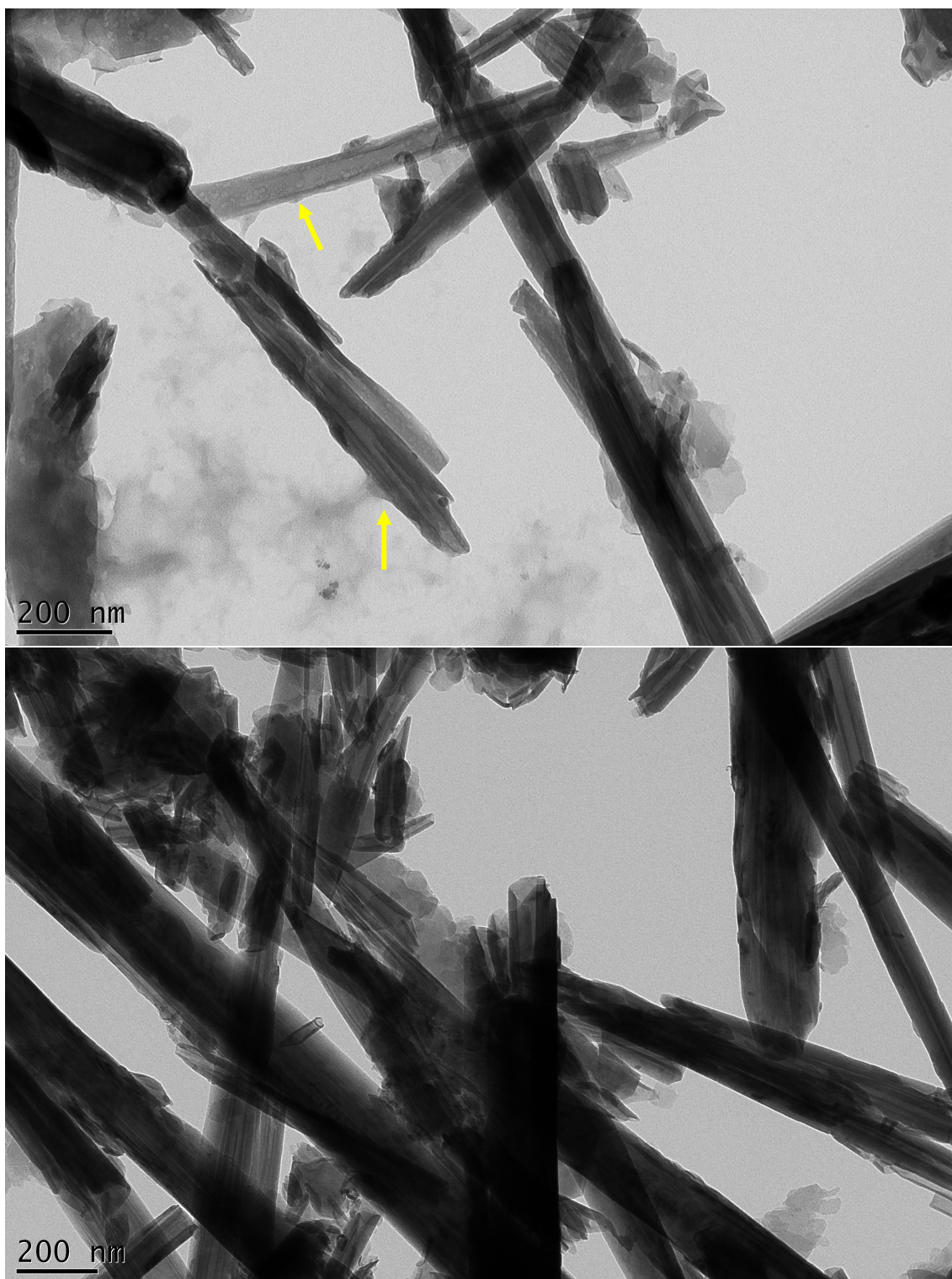


Figure 4.22: TEM images of a sample of NH₂-HNTs. In some areas, there appears to be a multilayer coating of APTES on the nanotubes (indicated with yellow arrows), but these features are rare.

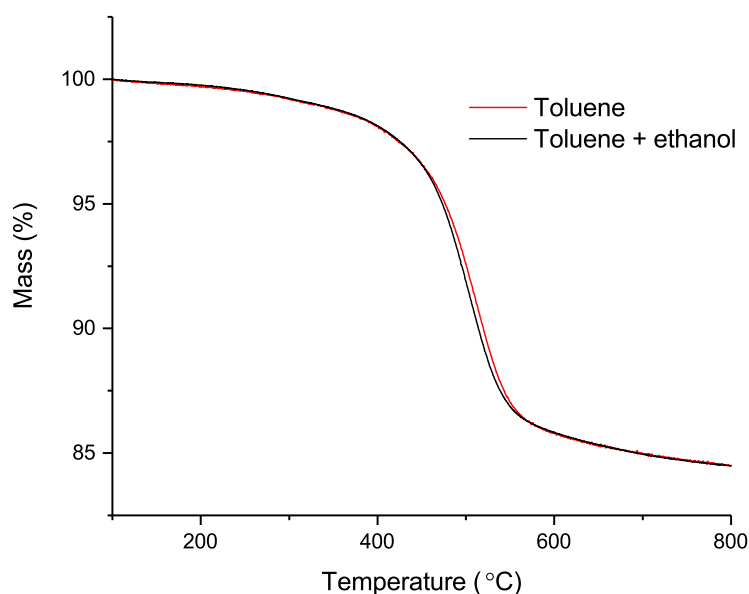


Figure 4.23: The mass remaining at 800 °C for NH₂-HNTs extracted with toluene and NH₂-HNTs extracted with toluene followed by ethanol is virtually identical. This suggests that the toluene wash removes all non-grafted silane species, and further washing with a more polar solvent is unnecessary.

variation. Therefore, the variation seen in the amount of APTES grafted to the HNTs' surfaces can only be assumed to arise from variations in ambient humidity, as previously suggested by Zhu *et al.*²¹¹

Figure 4.25 shows the relative humidity in our lab measured over three months (March to May) using a humidity probe. The relative humidity was seen to vary between 20% and 62% over the course of the three months, and could vary to a significant degree over the course of just a few days. The probe in our lab was in the vicinity of the reaction fumehood, not in the fumehood itself, and the measurement dates do not overlap with the dates on which the coatings were carried out. Nonetheless, the data illustrates that there is significant variation in the ambient humidity of our lab. In addition, this variation is certainly to the extent that it could affect the outcome of alkoxy silane coating reactions; for example, Zhu *et al.* measured an N-(2-aminoethyl)-3-aminopropyltriethoxysilane coating thickness of (92 ± 11) Å when the reaction was carried out at 39% humidity, compared to a thickness of (355 ± 100) Å when the reaction was carried out at 59% humidity.²¹¹ That is to say, increased humidity leads to a thicker, more variable silane coating. It is therefore reasonable to conclude that variations in ambient humidity played a part in the variable grafted amounts of APTES on HNTs seen in this work.

Within these results are two APTES coatings carried out on 40 g of HNTs in 240 mL of toluene, compared to the others at 10 g in 120 mL, and Sun *et al.*,⁷ who used 2 g of HNTs in 100 g of toluene (about 120 mL). However, the ratio [APTES]/[HNTs] was kept similar for all samples, and doing so seems to allow for similar coating results to be achieved, regardless of the change in the absolute concentrations of all species. This is important, as the ability to scale the process up to 40 g and above without significantly

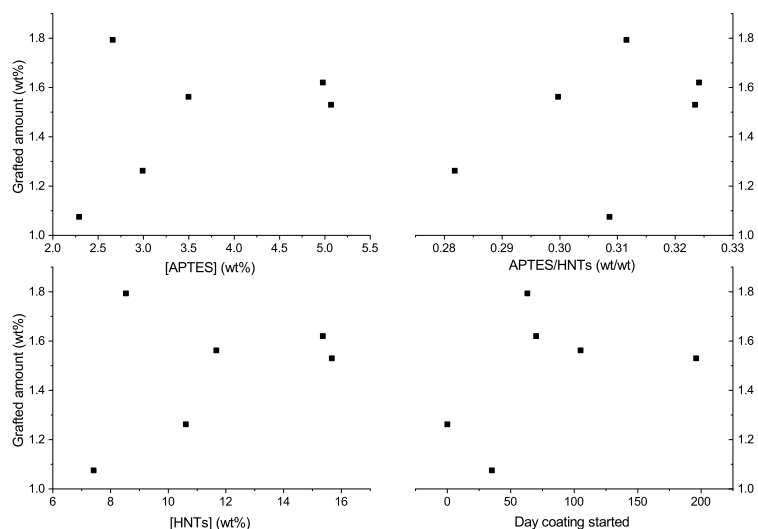


Figure 4.24: The amount of grafted APTES found on HNTs by TGA plotted against several variables. There does not seem to be any correlation between the grafted amount of APTES, and any of the variables listed here.

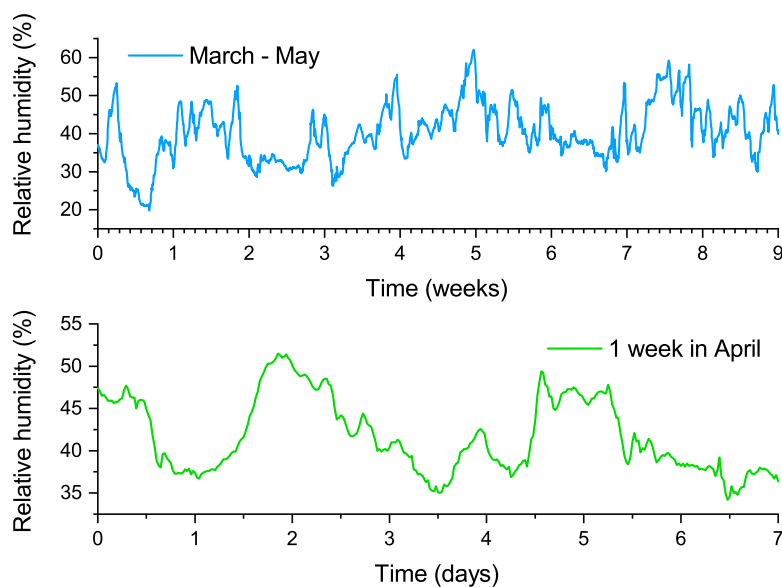


Figure 4.25: The relative humidity in our lab measured between March and May, and over one week in April (note that these dates do not overlap with the APTES coatings reported here). It can be seen that ambient humidity varies significantly (within a range of 42%), even over the course of a few days.

different results means that the coated HNTs would be able to be produced in amounts usable for making nanocomposite parts, e.g. using the three-roll mill (which requires about 30 g of HNTs for mixing in force mode, as noted in Chapter 3).

It is clear that the coating of HNTs with APTES in toluene produces variable grafted amounts of coating. However, it remained to be seen whether this variation produced any meaningful differences in the micro- and macroscopic properties of the obtained HNTs. As a way to study this, it was decided that the water contact angle of each sample be measured.

Measurement of water contact angles of APTES coated HNTs

In a three phase system consisting of a solid interface (A) and two fluid phases (B and C), one of the fluid phases can adhere to the solid surface as a discrete droplet provided that the strength of the energetic interaction between the surface and the fluids is intermediate between the strength of interaction between the two fluids.²³² Such a droplet is illustrated in figure 4.26. If the energetic interaction between either of the fluids (B or C) and the surface (A) is too great or small, then there will either be complete wetting of the surface (i.e. the formation of a film), or no wetting at all, depending on the relative amounts of B and C.²³²

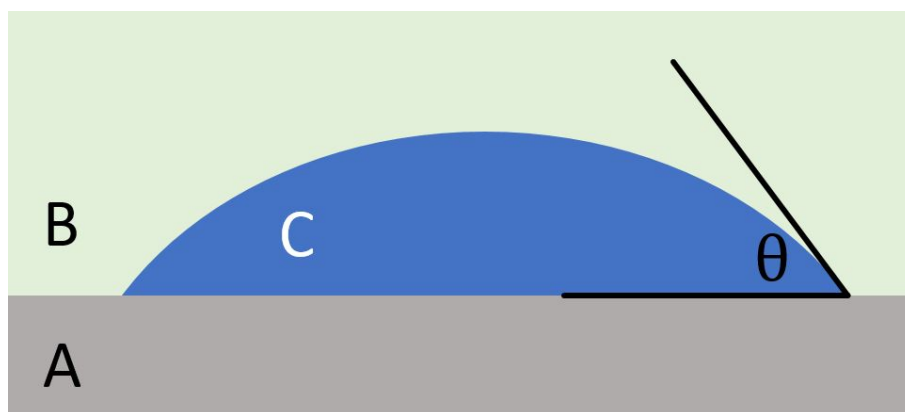


Figure 4.26: In a system consisting of two fluid phases (B and C), and a solid surface, a droplet can form on the surface provided that the energetic interaction between the surface and the fluid phases is intermediate between the interactions between the two fluid phases. The angle, θ , between the surface and the edge of the adhered droplet is known as the contact angle.

When a droplet forms at the interface, and the interfacial energy of the system is minimised, the interactions can be described using the Young equation (equation 4.1). Here, γ_{AB} is the interfacial energy between A and B etc., and θ is known as the contact angle. Equation 4.1 can be rearranged to give equation 4.2. The more favourable the energetic interaction between the droplet and the surface (relative to the interaction between the fluids), the lower the contact angle will be, and vice versa.

$$\gamma_{AC} + \gamma_{BC}\cos\theta = \gamma_{AB} \quad (4.1)$$

$$\cos\theta = \frac{\gamma_{AB} - \gamma_{AC}}{\gamma_{BC}} \quad (4.2)$$

This model is an oversimplification, as it assumes that the surface involved is physically and chemically homogeneous. Real world surfaces may be chemically heterogeneous, for example a surface might have a patchy coating of alkoxy silane, and almost all surfaces are likely to be rough at small length scales.²³³ Both of these factors can affect measured contact angles. Nonetheless, measurement of the contact angle of a droplet on a surface is a widely used method for studying the surface's chemical properties, e.g. to ascertain the success of a process which was intended to coat the surface. Water is typically the liquid of choice, presumably due to its low price, low hazard, and relatively low vapour pressure (compared to other common laboratory solvents), which means evaporation from the droplet should not affect the macroscopic properties of the droplet on the time-scale of the measurement. A high contact angle for a droplet of water on a surface indicates that the surface is hydrophobic, and a low contact angle indicates that it is hydrophilic.

A typical instrument for measuring the contact angle of a water droplet on a surface consists of: a flat, adjustable stage on which to place the sample surface; a syringe or pipette to repeatably deliver a precise amount of liquid onto the surface; a camera, or an optical viewing scope with a goniometer, which can be used to image the droplet at high magnification; and a diffuse backlight which increases contrast in the images, allowing for more accurate determination of the corners of the droplet. In the Department of Chemistry at the University of Sheffield, there is an analogue instrument for measuring water contact angles (i.e. using an optical viewfinder and goniometer). An example image of a droplet seen through the viewfinder is given in figure 4.27. This instrument was used to obtain initial measurements for the untreated and APTES coated HNTs.

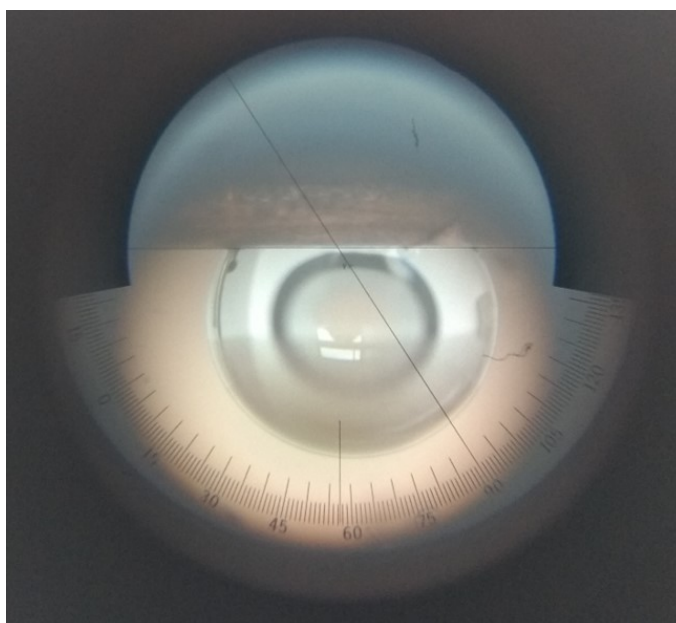


Figure 4.27: An example of a contact angle being measured using the analogue goniometer (not a sample from this work). The sample height, the viewfinder focus, and the goniometer must all be adjusted manually in order to take a measurement.

However, the analogue instrument was found to be unsuitable for measuring the contact

angles of both HNTs and NH₂-HNTs. For the measurements, each sample was pressed into a smooth, flat pellet with a metal die. These pellets were found to be porous, with a droplet of water quickly being absorbed after being placed on the surface. For the HNTs, complete absorption of the water droplet took place on the order of tens of seconds, whereas it generally took place over a few minutes for the NH₂-HNTs. In both cases, this time scale was short compared to the amount of time it took to manually adjust the viewfinder and take a measurement of the contact angle using the goniometer. Because of this, a new measurement set-up had to be made, i.e. one capable of taking contact angle measurements shortly after the droplet has been delivered to the surface.

The set-up which was made for measuring the contact angles of the HNT samples is shown in figure 4.28. Rather than an optical viewfinder, the droplet is imaged using a digital microscope, which can interface with a computer via a USB connection. Using MATLAB, it is possible to film the droplet with the microscope, and the frame rate can be altered by the user. A custom holder was made for the microscope using a 3D printer, and this was stuck to the surface of an adjustable stand. This was necessary to ensure repeatable alignment of the microscope between measurements. A small LED panel connected to a simple circuit (a battery plus an appropriate resistor) was used to provide back-lighting. A droplet of water is delivered to the sample using a micro pipette, which has been clamped in place above the surface. There are a few drawbacks to this set-up, most notably: droplets cannot be placed close enough to the microscope lens for very high magnification images to be taken, and the action of delivering the droplet to the surface is not always the same, since it requires manual grasping and plunging of the pipette. Nonetheless, the set-up can be used to obtain suitable images for the measurement of contact angles. An example is shown in figure 4.29.

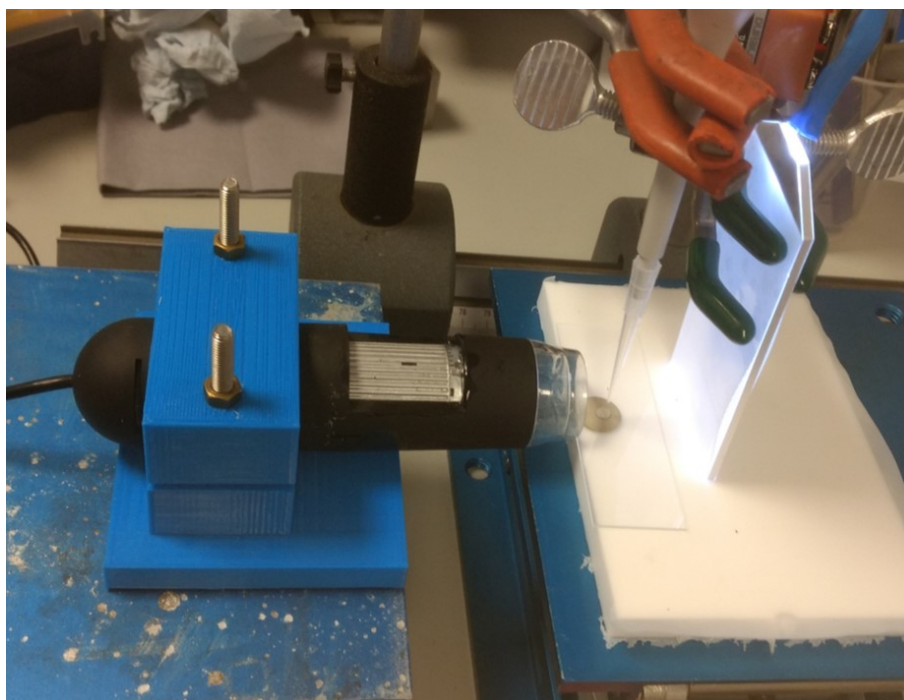


Figure 4.28: The set-up that was constructed to allow measurement of the water contact angle of HNT samples immediately after delivery of the water droplet.

Once images of the droplets are obtained, their contact angles can be evaluated using

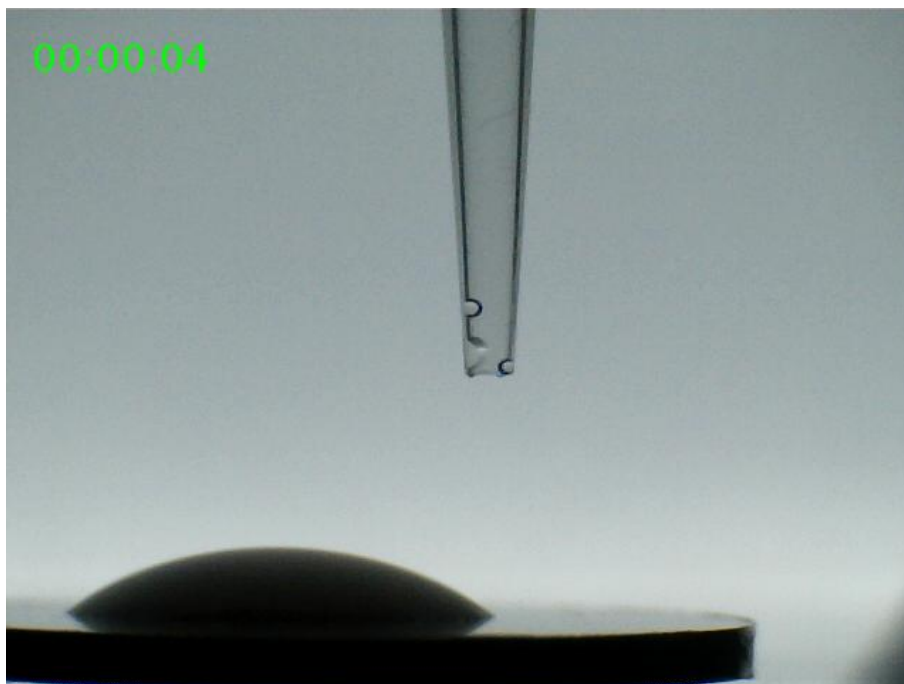


Figure 4.29: An example image of a droplet taken using the digital microscope set-up shown in figure 4.28.

image analysis software like ImageJ. This can be done simply by drawing appropriate freehand (FH) lines on the image, and measuring the angle between them. However, as illustrated in figure 4.30, the resolution of the images on the scale required to measure contact angles is limited, which makes it difficult to decide where the lines should be drawn. An alternative method is to use a “snake-based” approach, as developed by Stalder *et al.*,²³⁴ whose software is available for free as an additional feature to use in ImageJ. The software is known as DropSnake (DS). Essentially, DS allows the user to place points along the outline of the droplet. The software then uses this information, along with theoretical models that describe droplet shape, to calculate the contact angles of a droplet that would correspond to the shape in the image.²³⁴ An example of a droplet analysed using DS is shown in figure 4.31. The relatively low resolution of the images still causes problems when judging where to place the points, but the situation is far better than in the FH measurement, since the DS method takes into account the whole droplet and its reflection, so it becomes easier to determine when a measurement does not properly fit the image. It was possible to obtain apparently reasonable contact angles for the HNT samples using the new set-up and ImageJ/DS software.

In order to assess the accuracy of contact angles measured by the digital microscope, a sample was made which could both be measured on the analogue goniometer, and had already been measured in literature. This sample was the commercially available organoclay, I.44P, i.e. montmorillonite clay modified with a quaternary alkylammonium surfactant to make it hydrophobic. A pressed pellet of this clay does not absorb a droplet of water, so it can be measured on the analogue instrument available at the University of Sheffield. Measurements made using the analogue equipment were compared to those made from the digital images analysed either FH in ImageJ, or using DS software, and these are in turn compared to a literature value²³⁵ for the water contact angle of I.44P organoclay in figure 4.32. The uncertainties in contact angle are the standard deviation

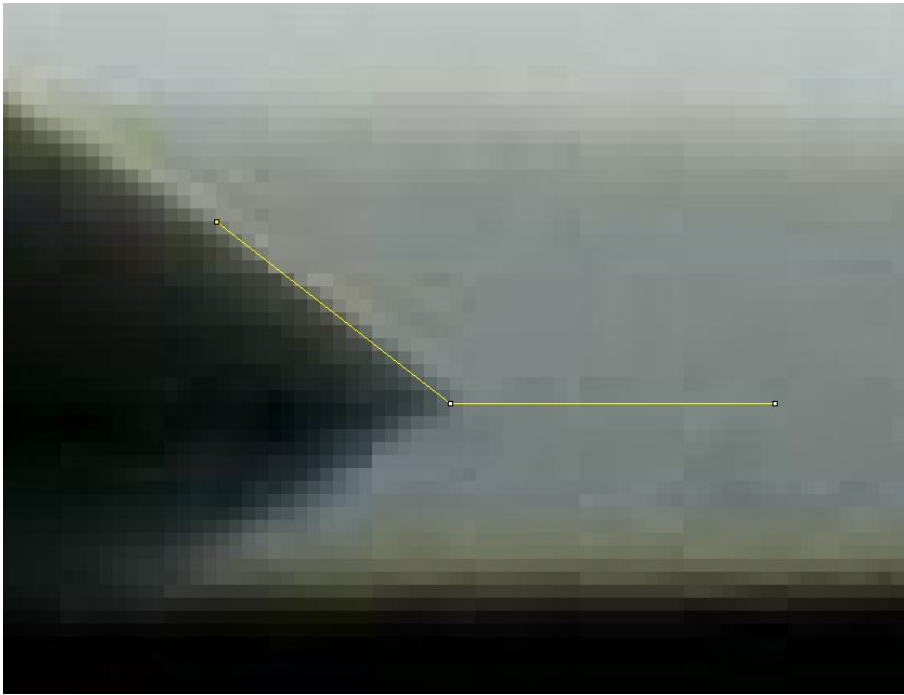


Figure 4.30: The contact angle of a water droplet on a surface can be measured by drawing freehand lines in ImageJ and evaluating the angle between them (the contact angle is 180° - this angle). However, the relatively poor resolution at small scales means that there is some uncertainty over exactly where the edge of the droplet is.

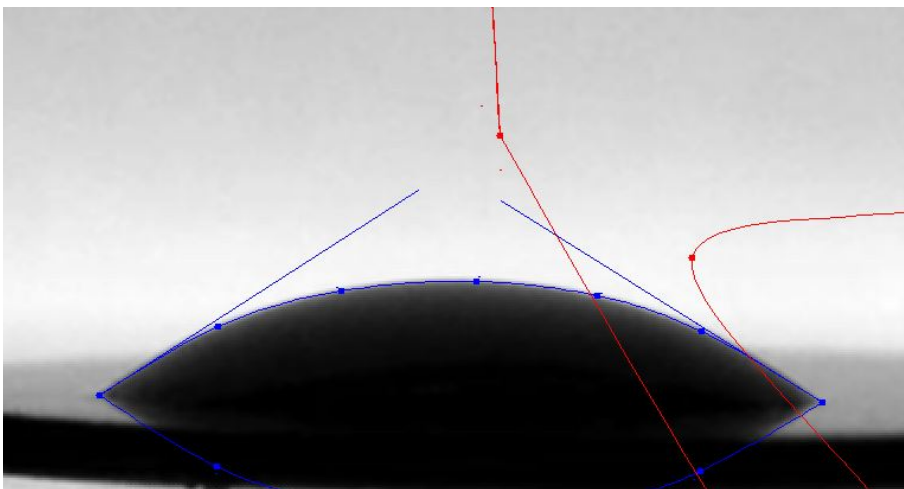


Figure 4.31: An example use of the DropSnake plug-in for ImageJ to evaluate contact angles. The software uses the droplet shape as defined by the user (the blue points) to calculate the contact angle. The red line/dots are part of a fitting feature which was not used, but could not be turned off, and should be ignored.

of several different measurements made on different samples, or different positions on the same sample. Standard deviation is preferred to standard error, since it is assumed that surface topography affects these measurements, and that the surfaces are randomly patterned, i.e. the measured contact angle would be expected to be part of a normally distributed population of contact angles dependent on the exact surface structure. Neither the analogue measurement, nor the measurement made by the FH analysis of the digital images are close to the literature value, but the measurement made using DS is in good agreement with it, with the literature value almost lying within the uncertainty of the DS measurement.²³⁵ Indeed, the literature value is reported without its associated uncertainty, and it seems reasonable to suggest that the uncertainty in the DS value probably overlaps with the unreported uncertainty in the literature value. The literature value for I.44P clay is assumed to be accurate, as it is close to other measurements made for similar materials (i.e. other surfactant-modified montmorillonites that are similar but not identical to I.44P).²³⁶ The analogue measurement of the water contact angle in particular is quite far off the literature value; it is thought that this might be due to misalignment of the viewing scope meaning that the whole of the droplet is not in view, and the contact angle measurements are therefore taken away from the true corners of the droplet. Therefore, it was concluded that the new set-up using the digital microscope was not only an accurate method for measuring the water contact angle of these samples, but it was also the most reliable method available in this case.

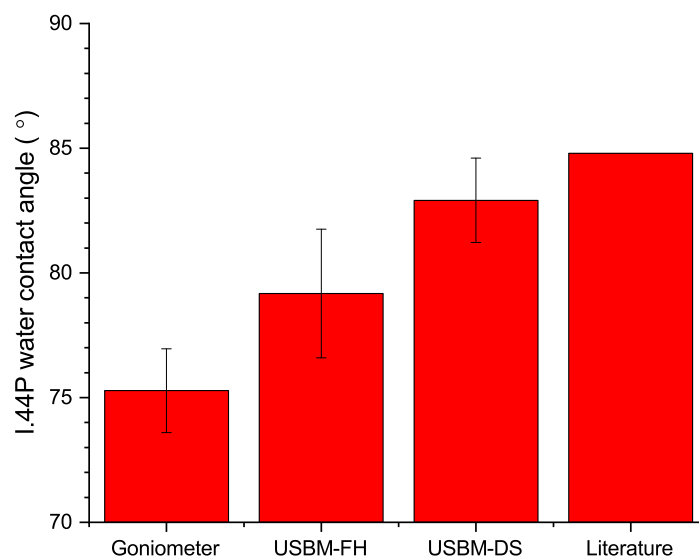


Figure 4.32: A comparison of the mean water contact angle for a sample of I.44P organoclay found in the literature to those measured using the analogue goniometer; the digital USB microscope and freehand line drawing (USBM-FH), and the microscope and Drop-Snake software (USBM-DS). The contact angle found using the USBM-DS method was closest to the literature value.

The digital microscope set-up was then used to take water contact angle measurements of samples of pure HNTs. Six measurements were taken using three separately pressed discs (i.e. a measurement on either side of three droplets); absorbing a droplet of water

was seen to cause the discs to undergo stresses which eventually led to their fracture, so each disc could only be used once. This is illustrated in figure 4.33. The mean water contact angle of the HNTs immediately (i.e. 0.1 s) after the droplet had been delivered to the surface), was found to be $(16 \pm 2)^\circ$, where the uncertainty is the standard deviation in the six measurements. This value is within the range of water contact angles expected for pristine HNTs, which has variously been reported in literature to be between about 10° and 20° .²³⁷

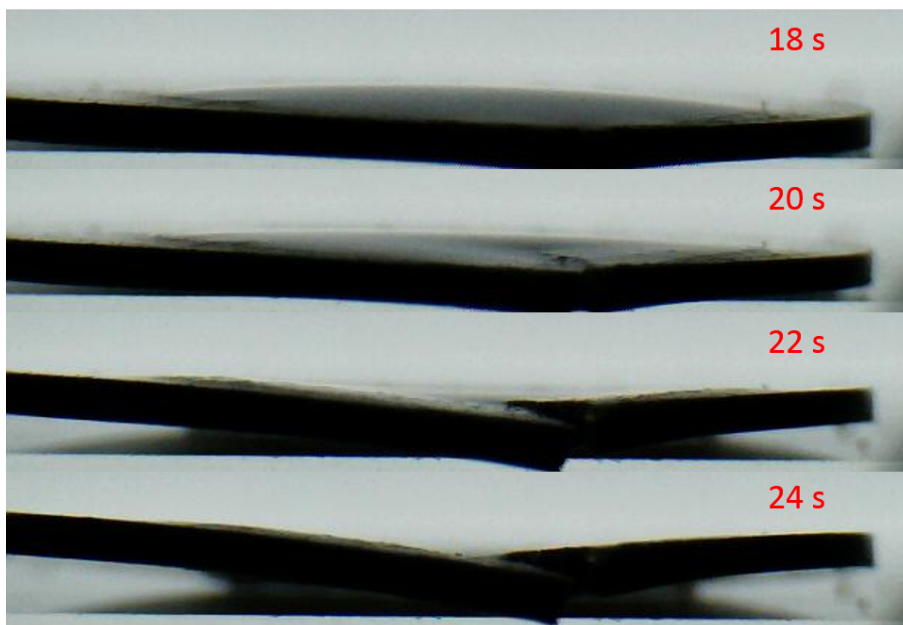


Figure 4.33: A figure illustrating how absorption of a water droplet by a pressed pellet of HNTs causes the pellet to undergo stresses which eventually lead to it breaking. This means that each sample can only be measured once.

The contact angles of the droplets were also measured as a function of time. As shown in figure 4.34, it was found the contact angle of a droplet of water on pure HNTs decreased linearly with time. This is consistent with Lucas-Washburn flow,²³⁸ which models the absorption of water by a porous medium with a network of cylindrical capillaries. The normal form of the Lucas-Washburn equation is given in equation 4.3, where l is the penetration length of the liquid, r is the pore radius in the substrate, γ is the surface tension of the liquid, η is the viscosity of the liquid, θ is the solid/liquid contact angle, and t is time. This can be rearranged to give equation 4.4, which demonstrates how the area over which the liquid front has diffused at a given time is a function of the contact angle. Assuming that only θ changes between different samples, it was thought that this might be a better way to quantify differences in wettability, i.e. using the gradient of the contact angle versus time slope, rather than the initial contact angle. For example, in figure 4.34, the average contact angle over the three discs is plotted versus time, and this can be fitted with a line of gradient $(-0.62 \pm 0.04)^\circ\text{s}^{-1}$, where the uncertainty is the standard error in the fit. This would potentially be a more accurate measure of wettability than simply using the initial contact angle, since it would rely on several data points rather than one, and may also reduce the uncertainty due to surface effects (e.g. surface roughness, variations in droplet delivery). Indeed, for pure HNTs, the relative uncertainty in the value of the slope of contact angle versus time is 6%, compared to the 13% relative uncertainty in the standard deviation of the value taken only from the initial contact angle.

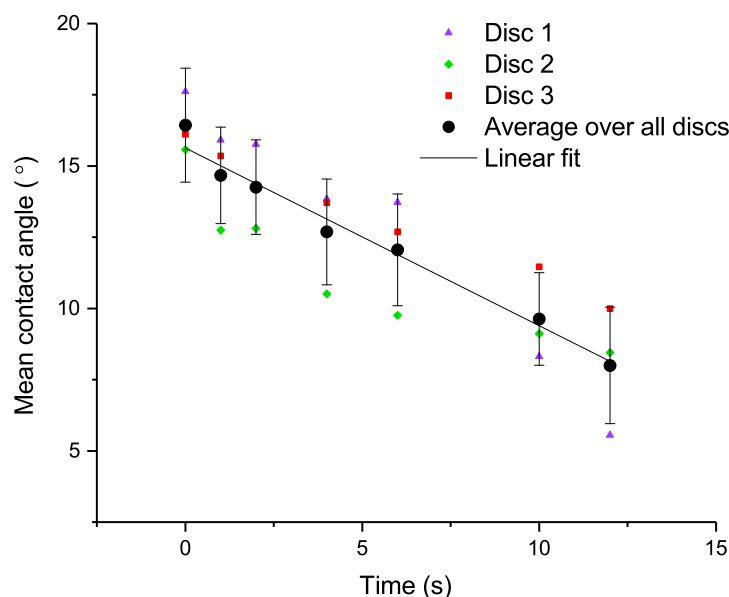


Figure 4.34: The water contact angle against time for three individual samples of HNTs, and the average of all three samples at these times. The contact angle appears to decrease linearly with time, which is consistent with Lucas-Washburn flow. Indeed, the change in average contact angle over time can be well-fitted with a straight line.

$$l = \left(\frac{\gamma r \cos \theta}{2\eta} \right)^{\frac{1}{2}} t^{\frac{1}{2}} \quad (4.3)$$

$$\frac{l^2}{t} = \frac{\gamma r \cos \theta}{2\eta} \quad (4.4)$$

The digital set-up was then used to study the behaviour of a water droplet on a sample of NH₂-HNTs. The initial water contact angle of the sample was found to be $(33 \pm 2)^\circ$, which is the same as Zhu *et al.* found for APTES coated silicon wafers.²¹¹ In contrast to the HNTs, the change in contact angle over time was not found to be purely linear, but rather was found to be non-linear at short times, before eventually reaching a linear regime after about 30 s (figure 4.35). In addition, the exact behaviour of the droplet was seen to vary between the pellets of the same sample. Nonetheless, taking an average across all three pellets still seemed to show a pattern, so it appeared that the gradient of the linear portion of the graph could indeed be used as an indicator of the wettability of the APTES coated HNTs. The gradient of this linear portion was found to be $(-0.14 \pm 0.03)^\circ \text{s}^{-1}$, which is lower than for the pure HNTs, as would be expected from equation 4.4 for a more hydrophobic sample. However, when this measurement was repeated for the other NH₂-HNTs, it was found that the rate of water uptake in the linear regime could vary extremely even between pellets of the same sample, which is shown in figure 4.36.

It was thought that this variation in droplet absorption rate could have been due to differences in pellet thicknesses, i.e. it may have been easier for the droplets to be absorbed by a thinner pellet, since the greater flexibility of a thinner pellet might mean there was

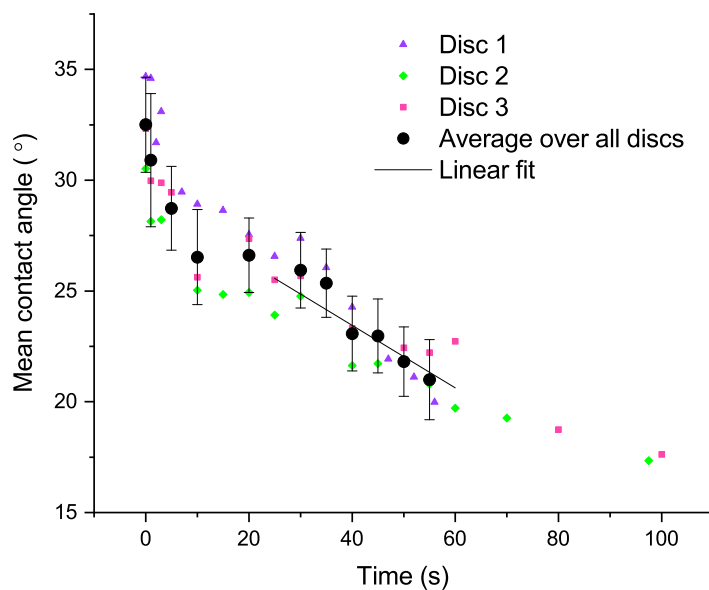


Figure 4.35: The water contact angle against time for three separate pellets of the same NH₂-HNTs. The behaviour of each sample is different, but an average across all three discs still seems to show a reasonable trend, with the contact angle starting to decrease linearly with time after about 30 s.

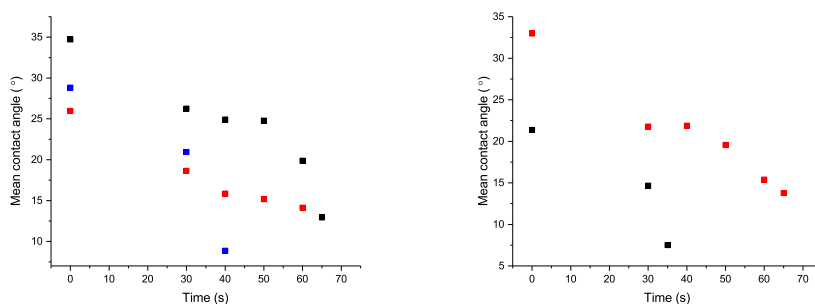


Figure 4.36: The contact angle versus time for several pellets of two different samples of NH₂-HNTs. The rate of absorption was seen to vary significantly even between pellets of the same sample, suggesting that the previous observation of a well-defined linear regime of water absorption by NH₂-HNTs may have been a coincidence.

less mechanical resistance to the reduction in size of the droplet. However, as shown in figure 4.37, plotting absorption time (i.e. the amount of time it took for the droplet of water to be completely absorbed) against disc thickness revealed no trend. The difference in the rate of absorption of the droplet must therefore instead be due to another factor, for example, random differences in droplet shape or surface topography somehow pinning and restricting the droplet, or the porous structure of each pellet somehow being different (despite the pellets being made in the same way). Regardless of the exact reason, it was concluded that the change in contact angle over time was an unreliable measure of wettability. Therefore, the initial water contact angle had to be used to quantify the wettability of the samples despite the relatively large uncertainty associated with this measurement.

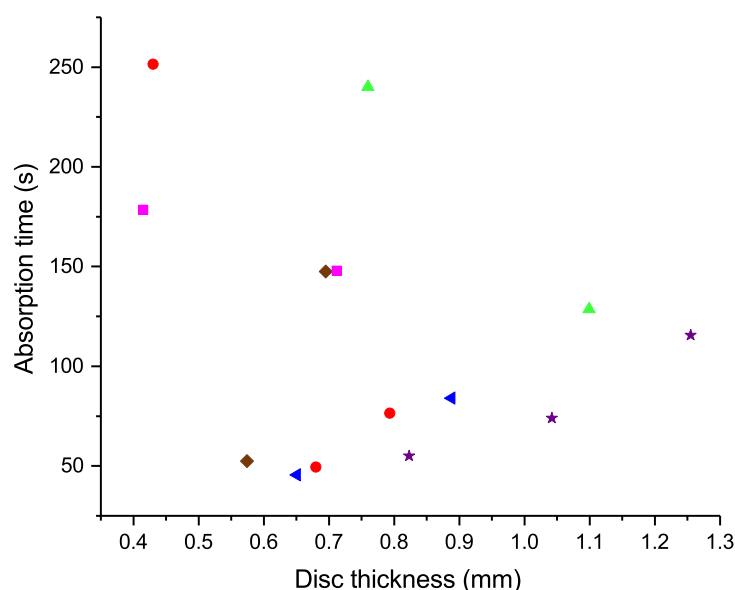


Figure 4.37: Absorption time (i.e. the amount of time for the water droplet to be fully absorbed) versus pellet thickness. Identical symbols indicate different pellets of the same sample. There was no clear trend between the speed of droplet absorption and disc thickness, so the differences in absorption time seen for discs of the same sample must be due to some other factor.

The water contact angles of all of the NH₂-HNTs are shown in figure 4.38. The uncertainty in each measurement is the standard deviation of several measurements, and the relative uncertainties range between 7% and 24%. The data appear to show that the water contact angle of the sample actually decreases as the amount of APTES coating increases. This is perhaps a surprising result, since it would indicate that the more of the (relative to pure HNTs) hydrophobic APTES that is grafted, the less hydrophobic the sample is. It would also mean that the variability of the APTES coating procedure used does in fact have a measurable impact on the chemical properties of the obtained coated material. A possible explanation for this trend would be that the differences in grafted amounts correspond to different multilayer structures of grafted silane, which have different wettability. However, the uncertainties in the data are relatively large (up to 24%), and overlap for all of the data points. Therefore, more samples and, ideally, a more precise measurement set-up would be needed to draw a concrete conclusion. Nonetheless, it can be concluded

that the 0.7 wt% variation seen in the grafted amount of APTES on the HNTs did affect their macroscopic wettability, which may in turn lead to differing degrees of reinforcement being provided by different batches of nanofiller were the NH₂-HNTs to be used as reinforcing fillers in an epoxy resin nanocomposite.

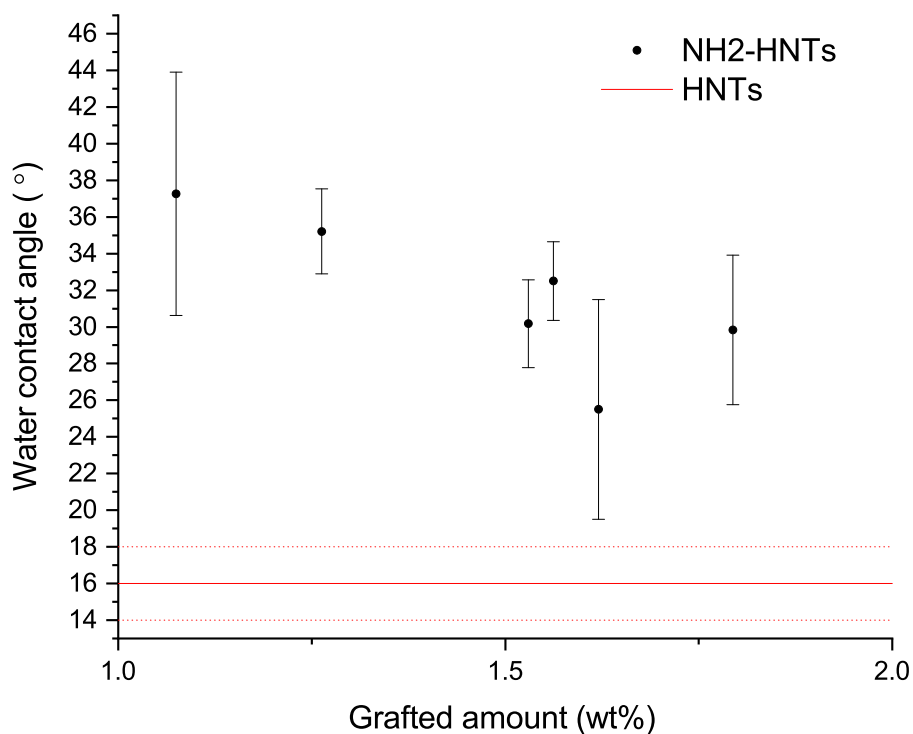


Figure 4.38: The mean initial water contact angles for all samples of NH₂-HNTs compared to untreated HNTs. All of the NH₂-HNTs show an increased contact angle in comparison to HNTs, but surprisingly the contact angle appears to decrease with a greater degree of coating. The solid red line is the initial water contact angle of untreated HNTs, and the dotted red lines are its associated uncertainty.

4.2.3 Piranha solution treatment of HNTs

General observations regarding the piranha solution treatment process

The published report by Sun *et al.* on piranha solution treatment of HNTs is vague with regards to experimental details; they do not even report reagent quantities for the process.⁷ Communication with the authors reveals that 30 g of HNTs were treated with about 100 mL of piranha solution, which had been left to cool slightly to allow for safer pouring from the vessel.²³⁹ They then heated the mixture of HNTs and piranha solution to 90 °C for 1 h. In this work, their procedure was compared to one where sulfuric acid was added to the HNTs, followed by the hydrogen peroxide (i.e. making the piranha solution in situ with the HNTs), and the reaction left for only 15 min. This was done to eliminate the hazard associated with pouring and heating piranha solutions (which increases the potential for spillages). In addition, 10 g of HNTs in 100 mL piranha solution was used here instead of 30 g, since the exact physical behaviour (exotherms, dispersion viscosity, etc.) of the system was unknown. From here on, the piranha solution treatment where the solution was generated in situ with the HNTs is referred to as p, and the treatment where the piranha solution was mixed before addition to the HNTs, followed by 1 h of heating at 90 °C, is referred to as 90p. The samples of treated HNTs obtained from either method are referred to as p-HNTs and 90p-HNTs, respectively.

The temperature was measured during both the p and 90p procedures. Figure 4.39 shows the temperature rise that occurs in the p procedure when sulfuric acid is added to HNTs, followed by the addition of aqueous hydrogen peroxide to make piranha solution. A temperature rise of around 2 °C is seen when the acid is added alone, but a rapid increase to about 90 °C is seen upon the addition of hydrogen peroxide, which is thought to mainly be due to the heat of hydration of the acid.⁶ The mixture cooled down slowly over the remaining treatment time, and was about 60 °C around 15 min after the formation of the piranha solution. It should be noted that this temperature range is within that at which Abdullayev *et al.* found that acid-etching of the HNTs' alumina interiors occurred at an appreciable rate.¹⁵⁵ The temperature of the 90p procedure was measured with an analogue thermometer. An exotherm to over 110 °C was seen upon heating, but the temperature was stable for most of the hour over which the mixture was heated. The temperature rise in both procedures is important to note with regards to safety, especially the exotherm in the case of the 90p procedure, as it suggests that there is a maximum safe volume that should be used, i.e. too large a volume would not be able to dissipate sufficient heat over its area, which could lead to rapid boiling and bumping of the mixture.

In both the p and 90p procedures, the dispersions were seen to foam significantly (figure 4.40), with the HNTs apparently able to stabilise the bubbles formed in the piranha solution. This is potentially very hazardous: foaming would have caused spillage out of the vessels were they to have been smaller in volume, and bursting bubbles have the potential to spit piranha solution out of the vessel. This is less of a problem in the p procedure; because no heating was required, a significantly oversized vessel could be used, meaning there was little chance of piranha solution being ejected. In the 90p procedure, a smaller vessel had to be used to allow for heating, and its contents came significantly closer to spilling out of the vessel. It is speculated that this potentially hazardous foaming would be exacerbated when using an increased concentration of HNTs, as Sun *et al.* did,⁷ i.e.

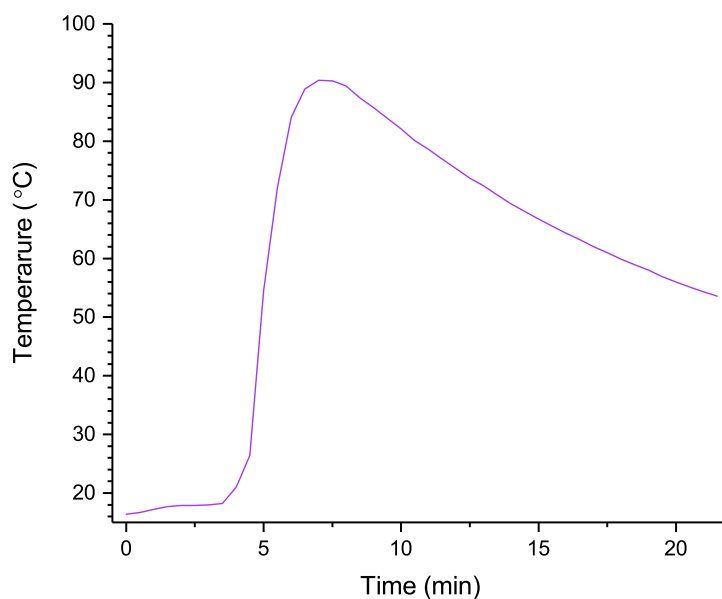
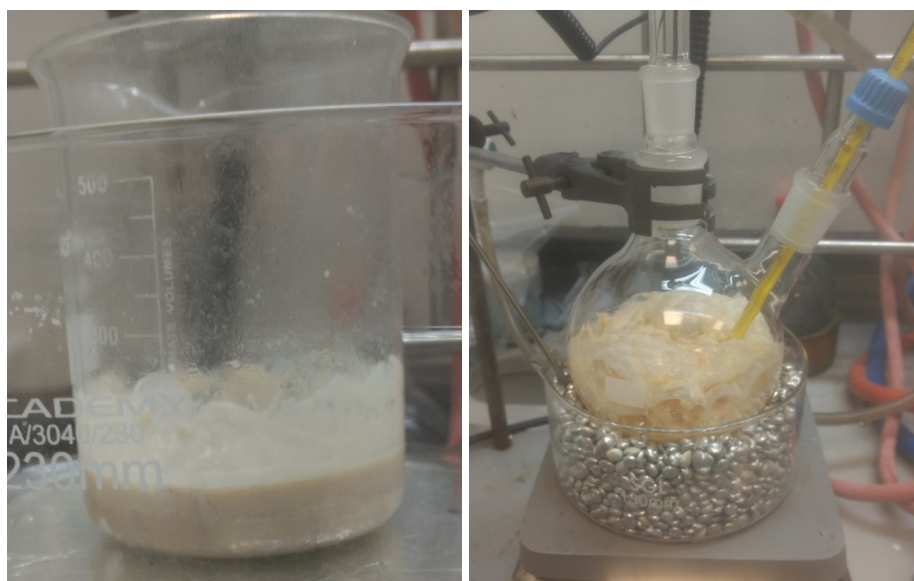


Figure 4.39: The temperature change seen when sulfuric acid is added to HNTs, followed by hydrogen peroxide to make piranha solution. The x axis is time from the addition of the sulfuric acid to the HNTs.

because increasing the concentration of HNTs would presumably lead to larger bubbles being stabilised. It is clear that the p procedure was safer than the 90p procedure, and that it is probably safer to use a lower concentration of HNTs in piranha solution than was used by Sun *et al.*²³⁹

It was also found that washing the piranha treated HNTs to neutral pH was difficult. Once the peroxide has decomposed, piranha solution is essentially a very concentrated solution of sulfuric acid, and a large volume of water is needed to return it to neutral pH (at least a 10^7 fold volume dilution is required, seeing as piranha solution has a pH below 0). Because HNTs form a gel at high concentrations in water, especially at low pH,¹³⁶ washing HNTs with water over a filter is impractical (i.e. because the water takes a long time to drain through the HNTs). The HNTs were instead washed using dialysis, i.e. a concentrated dispersion of the treated HNTs was placed in dialysis tubing, and suspended in a large amount of distilled water, with the water being changed frequently to maintain a pH gradient across the membrane.

The pH of the suspension inside the tubing was measured after each water change until it was neutral. Interestingly, it was found that using a pH meter to measure the washings gave an incorrect pH. Instead, using universal indicator paper was the best way to assess the pH of the washings. More specifically, although a pH meter measures a neutral pH for a dispersion of untreated HNTs in water, a reading of around 4.5 was repeatedly found for water containing a dispersion of p-HNTs, even though universal indicator paper showed a neutral pH for these dispersions. Additionally, when the p-HNTs were being washed by dialysis in distilled water, the pH meter would show a neutral pH in the water surrounding the dialysis tubing (which should contain no HNTs) and a pH of 4.5 inside the tube (where the p-HNTs were dispersed). Because pH meters work by measuring the conductivity



(a) p

(b) 90p

Figure 4.40: Pictures taken of the HNTs during the p and 90p piranha solution treatment processes. In both cases, the clay dispersion formed a foam, which is potentially hazardous as it could lead to spills of piranha solution.

of a solution, this suggests that there are some mobile, charged particles present in the dispersions of p-HNTs. These particles are presumably too large to diffuse through the dialysis tubing membrane (which had a molecular weight cut-off of 14 kDa, i.e. less than 5 nm^{240}). The identity of these particles is unknown, but they are speculated to be the Si-NPs that form as a consequence of etching of the alumina in HNTs by the acidic solution.¹⁵⁵ DLS on dispersions of HNTs and p-HNTs which had both been filtered twice through a $0.45 \mu\text{m}$ syringe filter to remove larger particles showed that HNTs remained in dispersion even after filtration, and also did not reveal a new population of small particles in the p-HNTs (figure 4.41). Indeed, the increased signal at longer delay times for the p-HNTs suggests that larger particles are present than in the HNTs. These are probably flocs of HNTs which form since the low pH lowers the energy barrier for flocculation (see Chapter 2). However, DLS is not necessarily evidence of absence of very small, mobile particles in the p-HNTs dispersion; small particles would be expected to scatter less light, and their autocorrelation functions would decay faster, so it is possible that the scattering from small particles would be swamped by the HNTs. In any case, universal indicator paper showed that the piranha treated HNTs could be washed to neutral pH by dialysis. This required a large volume of water: about 100-200 mL of an acidic dispersion of p-HNTs was initially suspended in the dialysis bag in 2 L of water, and >10 water changes were required to return the pH of the suspension to neutral.

Because of the difficulty of returning the piranha solution treated HNTs to neutral pH, a third sample was prepared by deliberately drying a sample of pure HNTs from water at about pH 1. This pH corresponds to a few hundred fold dilution of the piranha solution with water, which is a reasonable amount of washing solvent for someone to have used were they unaware of how much water was required to truly wash the HNTs back to neutral pH. The idea was to see whether any of the affects of piranha solution treatment of the HNTs were simply due to surface groups remaining protonated after inadequate

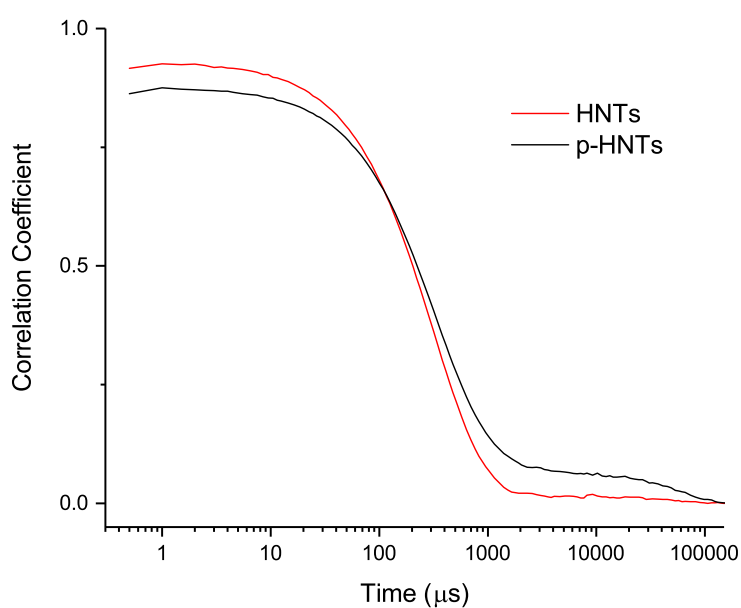


Figure 4.41: The correlation data from DLS for a dispersion of filtered p-HNTs vs filtered HNTs. Fitting the correlation data does not reveal a new population of smaller particles for the p-HNTs, which would be evidence of the small particles suspected to cause inaccurate pH meter readings in the dispersions of p-HNTs. Instead, the correlation data shows increased signal at longer times for the p-HNTs, suggesting the presence of larger particles, which are probably flocs of HNTs.

washing of the p-HNTs. These HNTs are referred to as pH1-HNTs.

Iron removal by piranha solution treatment

The most obvious change in the HNTs after piranha solution treatment is a colour change from light brown, to white, as shown in figure 4.42. Iron oxide is soluble in water at low pH,¹³⁷ so the colour change is probably due to dissolution of iron oxide in the extremely low pH piranha solution, which is subsequently washed away. This is confirmed by ICP-MS (table 4.1), which shows that the amount of iron in the sample is approximately halved after piranha solution treatment. The fact that any iron remains at all might be because the remaining iron is part of the HNTs' crystal structure (i.e. due to isomorphous substitution of Fe³⁺ for Al³⁺),⁵⁵ rather than a separate impurity. Piranha solution treatment is clearly an effective way to remove free iron oxide impurities from HNTs, which could be desirable in applications where colour is important, or where the presence of iron oxide would cause problems. However, it is probably the case that the same could be achieved just by rinsing HNTs with an acidic aqueous solution, rather than using the more hazardous piranha solution. The pH1-HNTs remained brown, so such a washing solution would have to be lower than pH 1.

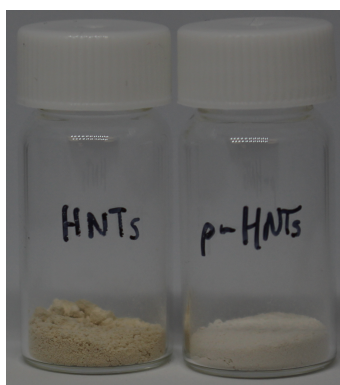


Figure 4.42: A side-by-side comparison of samples of untreated and piranha solution treated HNTs. Piranha solution treatment causes a colour change from light brown to white, which is thought to arise from dissolution and removal of iron oxide in the low pH solution.

Table 4.1: The concentration of iron in HNTs and p-HNTs as found by ICP-MS

Sample	Fe concentration/wt%
HNTs	1.00
p-HNTs	0.48

TEM imaging of piranha-solution treated HNTs

TEM images of the p-HNTs and 90p-HNTs (figure 4.43) appear to show that the nanotubes are largely intact after piranha solution treatment, which was also found by Sun *et al.*⁷ However, when compared to untreated HNTs (figure 4.44), there appears to be at

least some damage to the interiors of the piranha solution treated HNTs, which manifests as roughening of the interior surfaces of the nanotubes. This is consistent with the damage seen to HNTs after extensive acid digestion (figure 4.8), although it appears to occur to a much lesser extent in piranha solution treated HNTs than in deliberately acid-etched HNTs. The presence of the nanoparticles formed after acid dissolution of alumina from the HNTs might explain the incorrect pH readings given by the pH meter when washing the p-HNTs, i.e. these small particles may be charged and mobile enough to increase the conductivity of an aqueous suspension. These nanoparticles are about 5-10 nm in diameter, which is certainly large enough for them to be unable to pass through the dialysis membrane. However, while clearly abundant in acid-etched HNT samples (figure 4.8), these particles are not obviously present in the piranha treated samples.

Thermal degradation behaviour of piranha solution treated HNTs

TGA was carried out on the samples, and the masses lost by each sample are given in table 4.2. Both the p-HNTs and 90p-HNTs lost less mass than the HNTs (a difference of 0.14 wt% and 0.34 wt% respectively). This is consistent with dissolution and removal of alumina from the HNTs, as dehydroxylation of alumina is the main cause of weight loss as the HNTs are heated, i.e. a HNT sample containing less alumina would be expected to lose less mass upon heating. Interestingly, the pH1-HNTs lost 0.36 wt% more mass than the unmodified HNTs, and this increased mass loss was repeatable when the measurement was run again. It is unknown why this happens, but it could be that the aluminol groups on the interior of the HNTs remain protonated in the pH1-HNTs, and the extra hydrogen in the material is hence the cause of the extra mass loss upon dehydroxylation. However, it might be expected that this protonation would also change the kinetics of the decomposition, and it will be shown that the onset of dehydroxylation did not seem to change for the pH1-HNTs. In any case, it was clear that the differently treated HNT samples did lose different amounts of mass upon heating, and this has to be taken into account when determining grafted amounts in any subsequent coating reactions.

Table 4.2: The masses lost by treated and untreated samples of HNTs by 800 °C during TGA.

Sample	Mass lost at 800 °C/wt%	Difference relative to pure HNTs/wt%
HNTs	13.94	0.00
p-HNTs	13.80	-0.14
90p-HNTs	13.62	-0.34
pH1-HNTs	14.29	+0.36

The Differential Thermogravimetry (DTG) data, i.e. the rate of mass loss versus temperature, for the samples are noisy, but they all seem to show similar thermal decomposition behaviour, i.e. they all have one, similarly shaped peak (figure 4.45), which corresponds to dehydroxylation of alumina. The DTG peaks do have different heights and positions, and indeed, Sun *et al.* seem to take a lower DTG peak temperature for piranha-treated HNTs as an indication of lower thermal stability for this sample, which they attribute to the presence of more Si-OH groups on the HNTs.⁷ However, it is incorrect to use peak

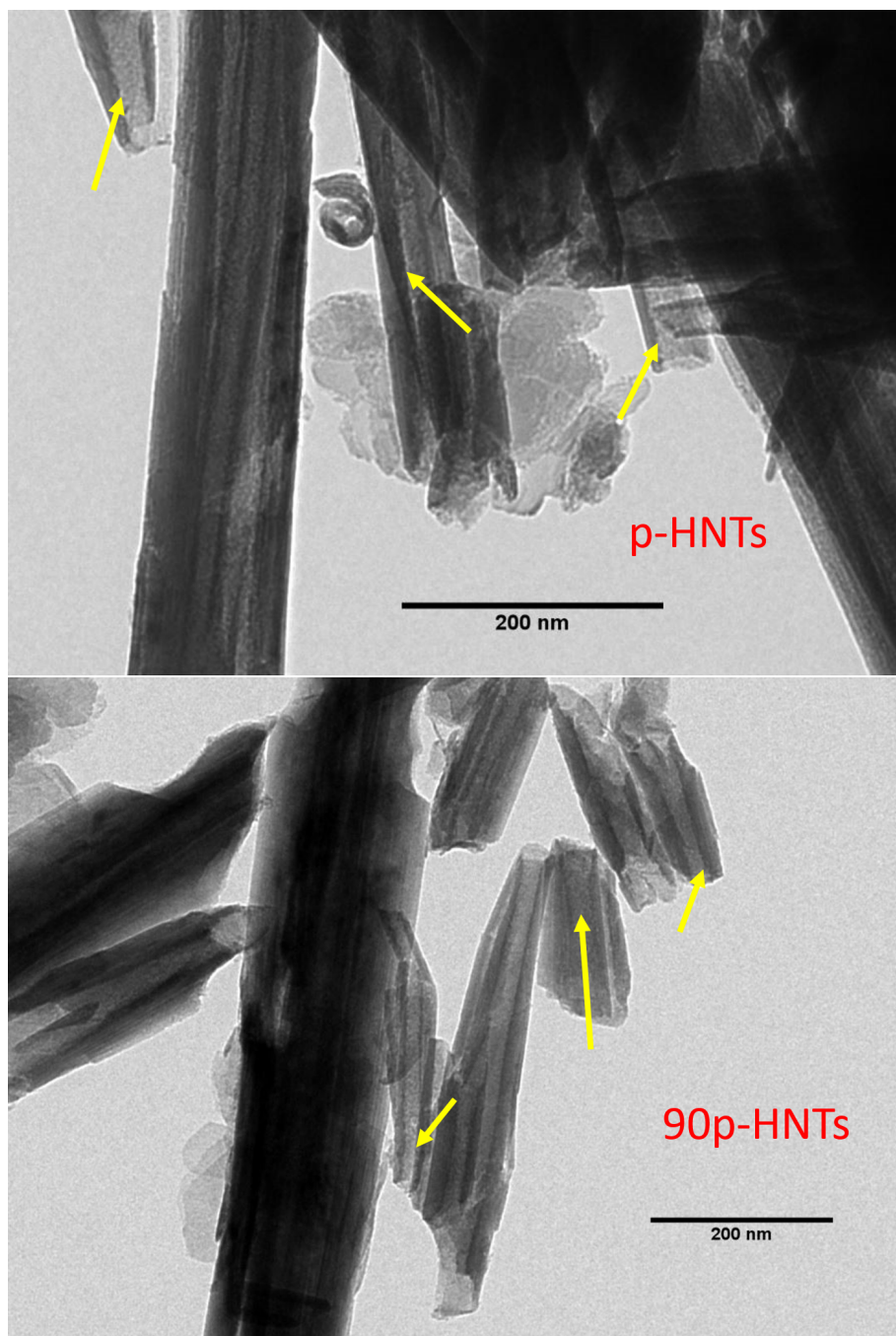


Figure 4.43: TEM images of piranha solution treated HNTs. There appear to be some initial signs of acid-damage having occurred to the p-HNTs and 90p-HNTs, which manifests as roughening of the interior surfaces of the nanotubes. Examples of these features are highlighted with yellow arrows.

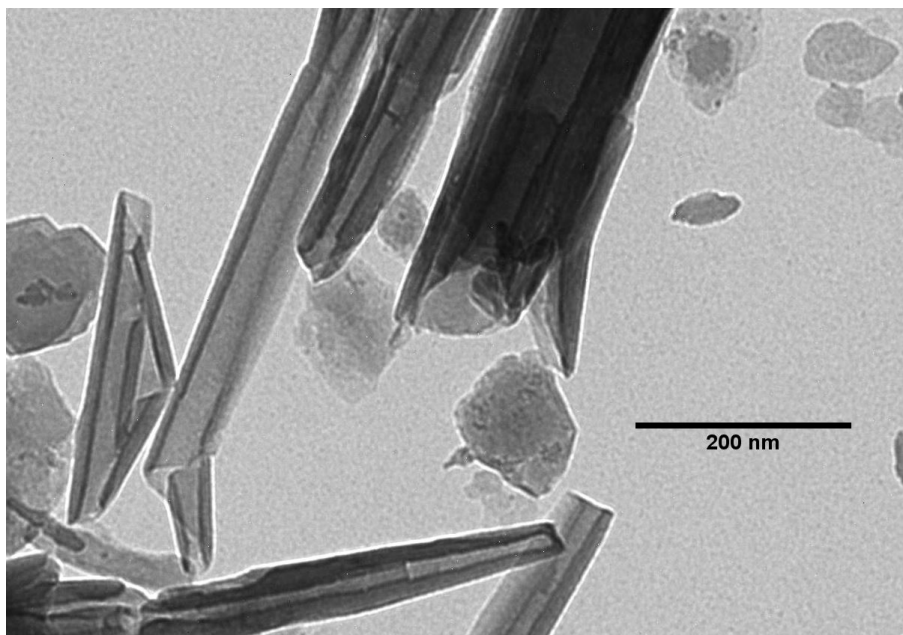


Figure 4.44: A magnified TEM image of untreated HNTs which illustrates the relatively smooth surface of the nanotube interiors.

centres in DTG data to draw conclusions about thermal stability, as their positions are influenced by the amount of sample that is being heated. Specifically, it will take longer for the whole of a larger sample to reach a given temperature, and once decomposition has started, it will take longer for decomposition products to diffuse from the centre of the sample and be evolved. For a larger sample, the DTG peak centre (i.e. the point of the maximum rate of mass loss) is hence shifted to a higher temperature.²⁴¹ Instead, the onset temperature of degradation should be used to compare thermal stabilities. The onset temperature is the temperature at which decomposition first starts to occur, which should not be as affected by sample amounts being measured.

However, quantifying thermal decomposition behaviour by means of the onset temperature is also not ideal. Methods for doing so are described in ASTM E2550-17,²⁴² which states that the onset temperature should be taken as the first temperature at which the data deviates from the baseline in either the raw data or the DTG data. The DTG data found here was too noisy, so the raw data had to be used. To find the onset temperature from the raw data, a slope was fitted to the baseline between 150 and 200 °C. The onset temperature was then taken as the first point that the data and fitted line deviated from one another. As per the ASTM guidance, this is done by subjective judgement after setting the full range of the y axis to only 1 wt%. However, this subjective method appeared to produce variable results. For example, when TGA of a sample of pH1-HNTs was repeated, the onset temperature was found to vary by almost 20 °C (between 227 and 245 °C), despite the mass remaining at 800 °C being repeatable (85.705 wt% and 85.707 wt%). This shows that onset temperature is not a reliable measurement, at least for these samples measured on this specific instrument. Nonetheless, onset temperatures found for the various HNT and treated HNTs are given in table 4.3 (note that only the pH1-HNTs were subject to a repeated onset temperature determination). All of the values are similar (within 10 °C of one another), and the p-HNTs in particular had an onset temperature only 3 °C away from the pure HNTs. Taking into account the unreliability of the measurement, this probably

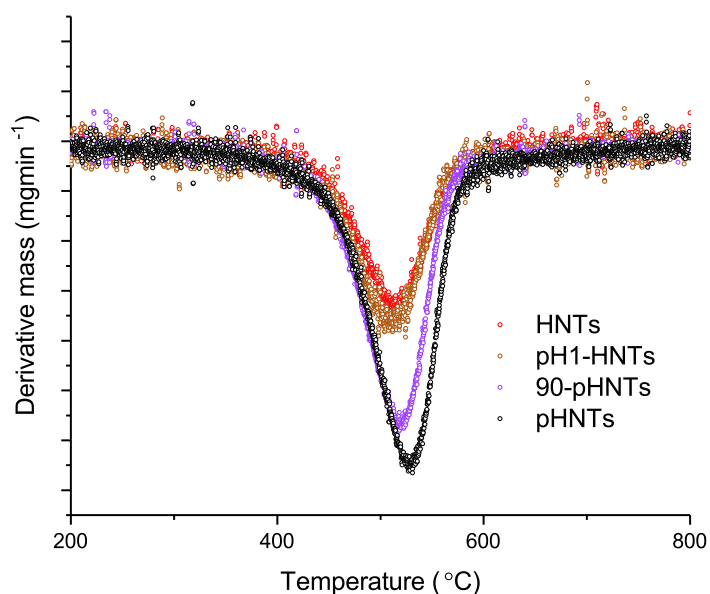


Figure 4.45: DTG curves for the various HNT and piranha-treated HNT samples. The data are noisy, but appear to show similar thermal decomposition behaviour (i.e. a similarly shaped peak) for all samples, at least superficially. The peak heights and centres differ, but these are influenced by the amount of sample used, so cannot be used to draw conclusions.

means that all of the samples had similar thermal decomposition temperatures. At the very least, TGA data almost certainly does not provide evidence of an increased concentration of Si-OH on the HNTs, as was postulated by Sun *et al.*⁷

Table 4.3: The temperatures at the onset of alumina decomposition for HNTs and treated HNTs.

Sample	Onset temperature/°C
HNTs	239
pH1-HNTs	227 - 245
p-HNTs	236
90p-HNTs	245

Characterisation of piranha-solution-treated HNTs using IR-spectroscopy

The piranha solution treated HNTs were characterised using IR spectroscopy. For the pH1-HNTs, IR spectroscopy seemed to indicate no significant chemical change, but for the p-HNTs and 90p-HNTs, a new shoulder on the Si-O-Si stretch peak at around 1250 cm^{-1} is observed, which is shown in figure 4.46. This was seen by Sun *et al.*,⁷ and is associated with the dissolution of alumina in the acidic conditions of piranha treatment.^{155,229} Sun *et al.* also found a new, broad peak at around 3450 cm^{-1} , which is important, as they attribute it to the presence of newly-formed Si-OH bonds.⁷ In this work, the broad ‘peak’ at 3450 cm^{-1} could be found for all the HNT samples, as shown in figure 4.47. Additionally, this peak seems more prominent if the sample was not dried immediately before the measurement (figure 4.48), which suggests that the absorption is actually due to physisorbed water. In correspondence, Sun *et al.* confirmed that they had not dried their samples immediately prior to measurement, so the variation they saw in this region could feasibly have been due to variations in ambient humidity.²³⁹ In summary, IR spectroscopy showed evidence of acid-etching of the alumina in the HNTs, but there was no evidence of the formation of new Si-OH groups.

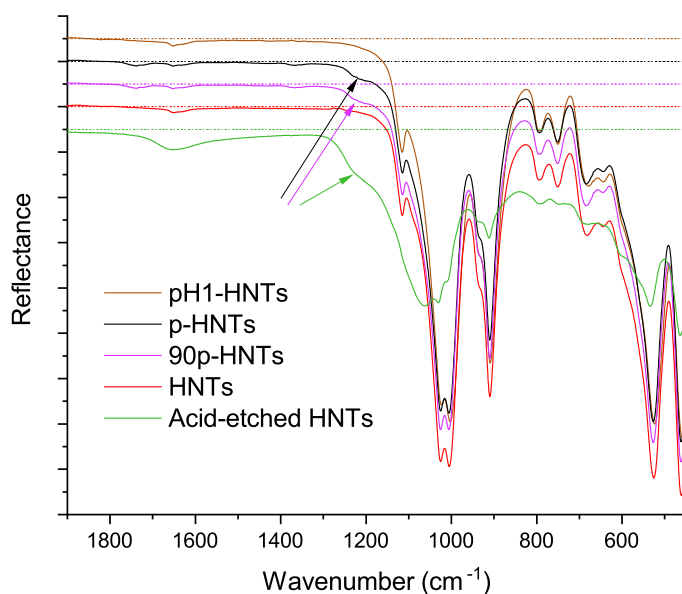


Figure 4.46: A close-up of the low frequency region of the IR spectra of HNTs, acid-etched HNTs, and piranha treated HNTs. The shoulder at about 1200 cm^{-1} is indicative of acid-etching of the nanotubes, and this has started to appear for both piranha-solution treated samples. The dotted lines are at 100% transmission for each sample.

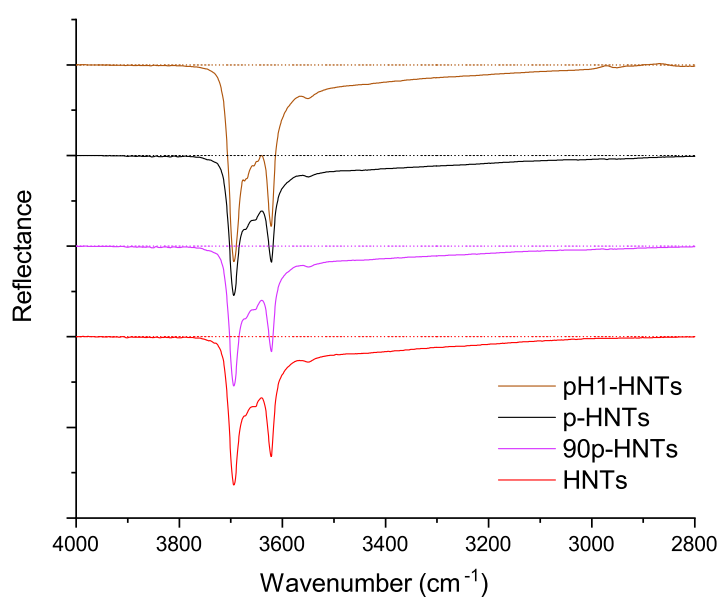


Figure 4.47: A close-up of the high frequency region of the IR spectra of HNTs and piranha treated HNTs. Sun et al. reported a new peak at 3450 cm^{-1} after piranha solution treatment, which they suggest is evidence of formation of new Si-OH groups.⁷ A broad absorption peak in this region was also found here, but it was found for untreated HNTs as well as piranha-treated HNTs, so it is not evidence of a change in the chemistry of the material. The dotted lines are at 100% transmission for each sample.

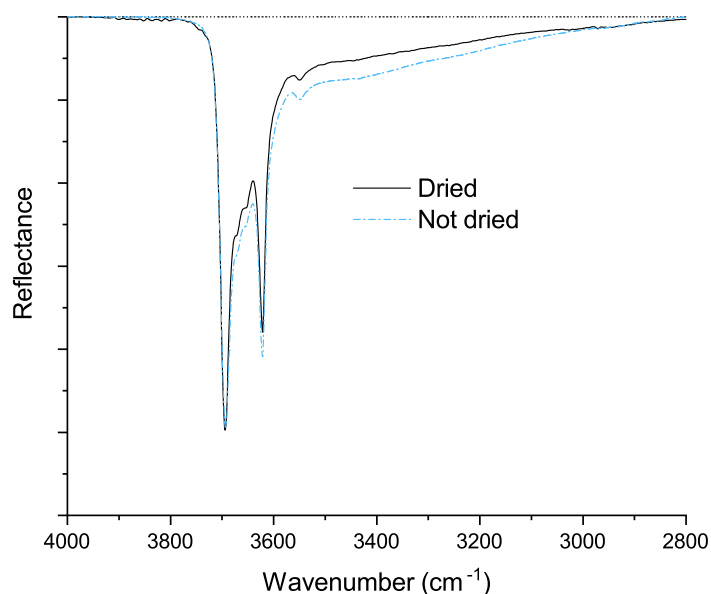


Figure 4.48: A close-up of the high frequency region of the IR spectra of *p*-HNTs that had and had not been dried immediately prior to measurement. Drying the samples reduces the intensity of the broad peak, suggesting that this peak is due to physisorbed water. To allow for comparison, the spectra have been adjusted using the ratio of the peak heights of the highest frequency Al-OH absorption (i.e. the peak at about 3700 cm⁻¹)

Introduction to XPS

XPS is a technique which allows the study of the chemical composition of surfaces. In XPS, samples are irradiated with X-rays which cause the ejection of electrons from atoms in the material via the photoelectric effect.²⁴³ The kinetic energy (E_k) of a resultant photoelectron depends on the energy of the incident radiation, the work function of the material (ϕ), and the binding energy of the electron (E_B), i.e. the energy of the orbital from which it was ejected. This relationship is described in equation 4.5.²⁴³ Therefore, the kinetic energy of a photoelectron can be used to calculate the energy of the electron orbital from which it was ejected. This energy is unique to a specific electron orbital in each element, and can also be affected by the element's exact chemical environment. This allows chemical information to be inferred from ejected photoelectrons. However, if a photoelectron undergoes a collision with another particle before it is detected, then its kinetic energy is no longer described by equation 4.5, and gives no information about the environment from which the electron came. The likelihood of a collision occurring as a photoelectron is emitted from a sample increases with increasing depth from the sample surface, which means that XPS gives information about the chemical composition of the surface alone, down to depths of a few nm.²⁴⁴

$$E_k = h\nu - E_B - \phi \quad (4.5)$$

In practice, an XPS instrument irradiates a sample with X-rays of a known wavelength,

and measures the intensity of detected photoelectrons as a function of their kinetic energy. Peaks in intensity correspond to the electron orbitals present, and the background intensity arises from photoelectrons which underwent collisions before being emitted from the sample. Each peak can be assigned to a specific element and chemical environment based on the binding energy at which it was measured. Taking into account the probability of an incident photon to cause ejection of an electron for each type of orbital (known as the sensitivity factor), the areas of these peaks can be used to find relative concentrations for each type of surface atom. This is typically done by applying a background subtraction to the regions containing each peak, then fitting them individually with one or more distributions (usually some kind of combined Gaussian/Lorentzian function). If multiple peaks are required for an acceptable fit of a region corresponding to a given element, it can be inferred that the element is present in multiple chemical environments within the sample.

During the XPS measurements, insulating samples (such as HNTs) have to be flooded with electrons using an electron gun in order to prevent cation build-up during the measurement.²⁴⁵ The flood of electrons slightly lowers the binding energies of the elements on the surface, so calibration is needed to find their true binding energies.²⁴⁵ Calibration is usually done by using the C 1s peak as an internal reference, i.e. the measured position of the C 1s peak is compared to an established true value, and the difference between the two is used to calibrate the binding energies for the rest of the elements. Carbon almost always provides a suitable calibration, since it is always present to some extent due to adventitious sources (e.g. adsorbed carbon dioxide).²⁴⁵

XPS measurements of HNT samples

In XPS measurements of treated HNTs, binding energy had to be calibrated differently to typical spectra. As previously mentioned, the C 1s peak is often used as reference for calibration, but in the case of the p-HNTs, 90p-HNTs, and pH1-HNTs, using the C 1s peak is problematic because the signal to noise ratio in the C 1s environment is low (illustrated in figure 4.49). While this low signal intensity might have been taken as an indication that piranha-solution treatment had removed organic impurities, the fact that it was also seen for the pH1-HNTs, which had not been piranha-treated, means that it is probably unrelated to sample preparation. Because the untreated HNTs were measured on a different day to the rest of the samples, the low C 1s signal intensity in the other samples is instead concluded to be due to a measurement-to-measurement difference in the operation of the instrument, specifically a reduced beam intensity. The low signal-to-noise ratio reduces the quality of the fit that can be made for the C 1s peak in p-HNTs, 90p-HNTs, and pH1-HNTs, which makes calibration based on this peak less reliable. It is also worth noting that Greczynski and Hultman questioned whether calibration using the C 1s peak was reliable at all.²⁴⁵ Therefore, the Al 2p peak was used to calibrate binding energy instead. This peak is relatively high intensity for all of the samples, and is known to be at 74.8 eV for halloysite.⁸ In aluminosilicates, this peak is also unchanged with changes in the aluminium coordination environment,²⁴⁶ so it is reasonable to assume it would not change after piranha solution treatment. Table 4.4 compares the position of the Si peak for each sample after calibration using either the C 1s or Al 2p peaks, and it can be seen that there is substantially less variation when the Al 2p is used; the variation seen when the Al 2p is used is within the instrument precision of ± 0.1 eV, whereas the peak

position varied by up to 0.4 eV when the C 1s was used. Therefore, it was concluded that calibration of the binding energies of HNT samples should be done using the Al 2p peak rather than the C 1s peak.

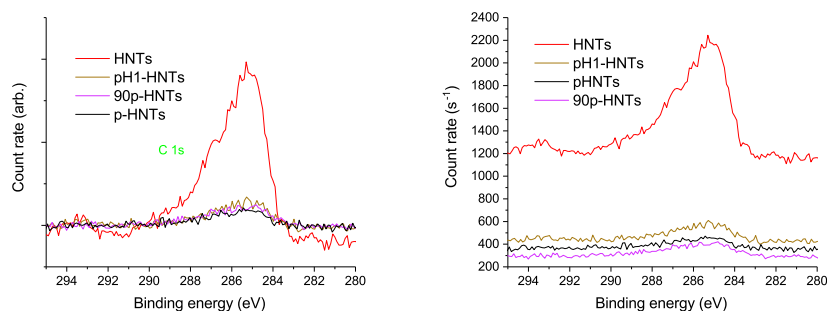


Figure 4.49: The C 1s region of HNTs, pH1-HNTs, and piranha-solution treated HNTs. The signal-to-noise ratio is poor for samples other than the pure HNTs, so it could not be used for calibration. The left-hand image illustrates the relative peak intensities when the background is adjusted to be the same for all four samples, while the right-hand image illustrates the absolute count rates for each sample.

Table 4.4: The position of the Si 2p peak when binding energy is calibrated using either the C 1s peak or Al 2p as a reference. Using the Al 2p produces much less variation, and so is preferred.

Sample	Si 2p (C 1s calibration)/eV	Si 2p (Al 2p calibration)/eV
HNTs	103.39	103.12
p-HNTs	103.51	103.13
90p-HNTs	103.47	103.15
pH1-HNTs	103.14	103.12

The binding energies of the elements (excluding iron) found in samples of HNTs and treated HNTs are given in table 4.5. The fitted peak positions for C 1s and O 1s were found to be variable. In the case of C 1s, this is due to low signal, as already mentioned. The fitting of the O 1s region will be discussed in more detail later. The positions of the Si 2p peak were found to be the same to within ± 0.1 eV, and were the same as the literature values of 103.18 eV⁸ and 103.2 eV.⁷

Table 4.5: The binding energies for the peaks fitted to XPS spectra of the HNTs and piranha-solution treated HNTs (calibrated by setting the Al 2p binding energy to 78.4 eV⁸).

Sample	Al 2p/eV	Si 2p/eV	C 1s/eV	O 1s/eV
HNTs	74.8	103.12	284.71, 286.23, 288.75	529.40, 532.20, 533.71
p-HNTs	74.8	103.13	284.66, 286.17, 286.35	531.86, 532.51, 532.59
90p-HNTs	74.8	103.15	285.24	531.68, 532.34, 532.59
pH1-HNTs	74.8	103.12	284.93, 286.59, 288.76	531.65, 532.18, 532.66

XPS measurements of the HNTs can be used to quantify the elemental composition of their surfaces. The absolute values of surface elements found by XPS are given in table

4.6, while the relative (to Si) concentrations of each element are given in table 4.7, and displayed visually in figure 4.50. In comparison to untreated HNTs and pH1-HNTs, the p-HNTs and 90p-HNTs were found to show depleted amounts of Al and C. The depletion of Al is consistent with dissolution and removal of the alumina from the sample. The surface concentrations of Al were similar for both p-HNTs and 90p-HNTs, but it is difficult to say whether this means a similar degree of acid-etching of the HNT interior occurred for both samples, since electron orbitals on the interior surface may be too far away from the nanotube surface to be able to be measured by XPS. The reduction in the intensity of the C peak relative to Si is consistent with oxidation and removal of at least some of the organic impurities from the HNTs by piranha solution. It is also worth noting that the lowest intensity C 1s was found for the p-HNTs rather than the 90p-HNTs, which might suggest that this method was more effective at removing organics as well as being safer. The enrichment of oxygen in p-HNTs and 90p-HNTs would be evidence of an increase in the number of surface hydroxyl groups on the HNTs after piranha solution treatment were it not for the fact that the pH1-HNTs, which had not been treated with piranha solution, were seen to have similar enrichment with oxygen. The reason for this oxygen enrichment is unknown, but it could possibly be due to adsorbed water on the samples, or some other difference in the ambient conditions of the measurement (e.g. reduced vacuum leading to more gas adsorption on the samples). In addition, no Fe was detectable for either the p-HNTs or 90p-HNTs, which is further evidence of the removal of iron oxide from the samples in the concentrated acid. On the basis of elemental analysis by XPS, it can be concluded that piranha solution treatment did remove iron and organic impurities from the HNTs, and that it removed Al from both the p-HNTs and 90p-HNTs via acid-etching.

Table 4.6: The concentrations of surface atoms as found in XPS spectra of the HNTs and piranha solution treated HNTs. The units are the percentage of total atoms, At%.

Sample	Al 2p/At%	Si 2p/At%	C 1s/At%	O 1s/At%	Fe 2p/At%
HNTs	14.83	18.46	5.15	61.26	0.29
p-HNTs	11.75	17.70	2.33	68.22	0.00
90p-HNTs	11.27	17.14	3.02	68.58	0.00
pH1-HNTs	13.28	16.79	4.07	65.4	0.46

Table 4.7: The relative (to Si) concentrations of surface atoms as found in XPS spectra of the HNTs and piranha-solution treated HNTs.

Sample	Al 2p	Si 2p	C 1s	O 1s	Fe 2p
HNTs	0.80	1	0.28	3.32	0.02
p-HNTs	0.66	1	0.13	3.85	0.00
90p-HNTs	0.66	1	0.18	4.00	0.00
pH1-HNTs	0.79	1	0.24	3.90	0.03

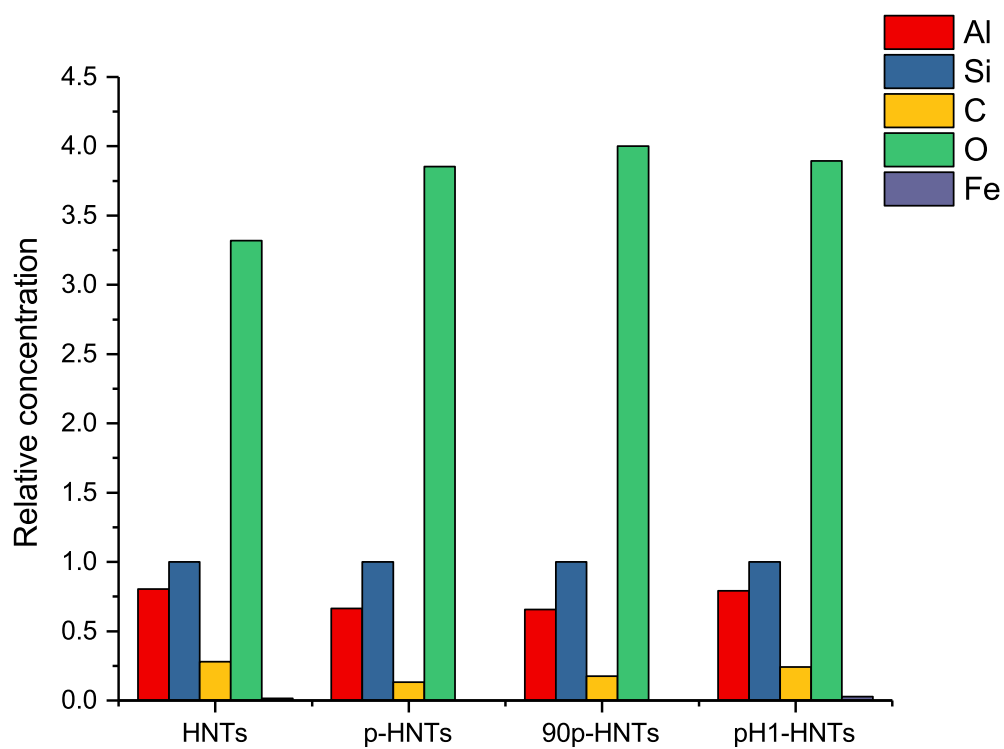


Figure 4.50: The concentration of elements in HNTs and piranha-solution treated HNTs relative to the concentration of silicon.

The lack of evidence from XPS for increased surface silanol concentration after piranha solution treatment

Sun *et al.* used the Si 2p peak in their XPS measurements of HNTs and piranha solution treated HNTs as further evidence of an increase in surface silanol concentration after piranha treatment.⁷ Their data for the Si 2p region is shown in figure 4.51. Specifically, they claimed that the Si 2p peak of HNTs could be fitted with one peak corresponding to the Si-O-Si silicon environment, but that the Si 2p peak of piranha solution treated HNTs should be resolved into two peaks representing the Si-O-Si and Si-OH silicon environments respectively.⁷

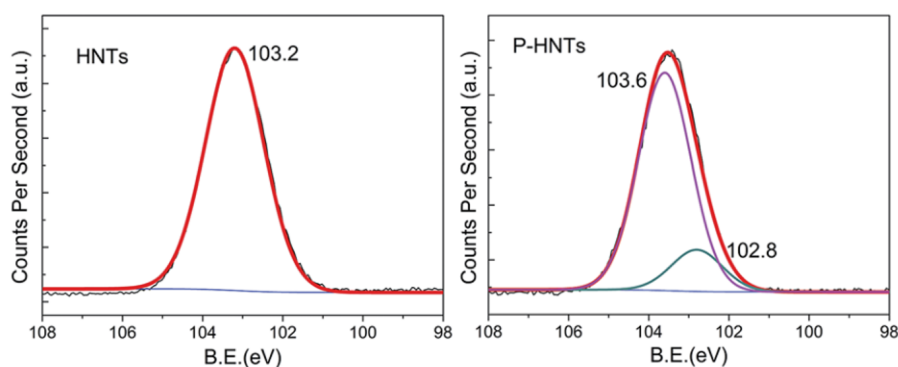


Figure 4.51: XPS data for the Si 2p region of HNTs and piranha solution treated HNTs, taken from work by Sun *et al.* (adapted with permission from *The Royal Society of Chemistry*).⁷ They fit the Si 2p region of their piranha solution treated HNTs with two peaks, and suggest that this is evidence of an increased concentration of silanol functional groups.

However, it was found here that both the HNTs and piranha solution treated HNTs could be fitted equally well with either one or two peaks. These fits are illustrated in figure 4.52. Table 4.8 lists the peak positions found for each sample using a one peak fit (1PF) or two peak fit (2PF), as well as the associated residual from the fit regression for both. Fitting with two peaks naturally leads to a lower residual, as it is always easier to more closely match the raw data with a larger number of peaks. However, from the fit residuals, there is no clear evidence that any of the samples should be fit with a different number of peaks to the others, i.e. because the difference between the 1PF and 2PF residuals is similar for each. In addition, automated fitting of two peaks to the Si 2p environment using XPS analysis software was found to give variable results depending on the exact order that fitting process was carried out. The fitting process can be constrained, e.g. by fixing the number of peaks and/or the positions of their centres, but at that point the user may start to artificially attribute meaning to the fitted peaks. Because the 2PF was not clearly more appropriate, and because the Si 2p peak for aluminosilicates like halloysite is only fitted with one peak elsewhere in the literature,⁸ the 1PF was deemed to be the correct one. The full width at half maximum (FWHM) for the Si 2p 1PF is also given in table 4.8, and was found to be the same to 0.1 eV for all of the samples, which is the instrument precision. Since the Si 2p region was so similar for all of the samples, it was concluded not to show any evidence for an increased number of silanol groups in HNTs after piranha solution treatment.

Kloprogge and Wood measured XPS spectra for several aluminosilicate minerals including halloysite.⁸ They fitted the O 1s region of their spectra with three peaks, as shown in

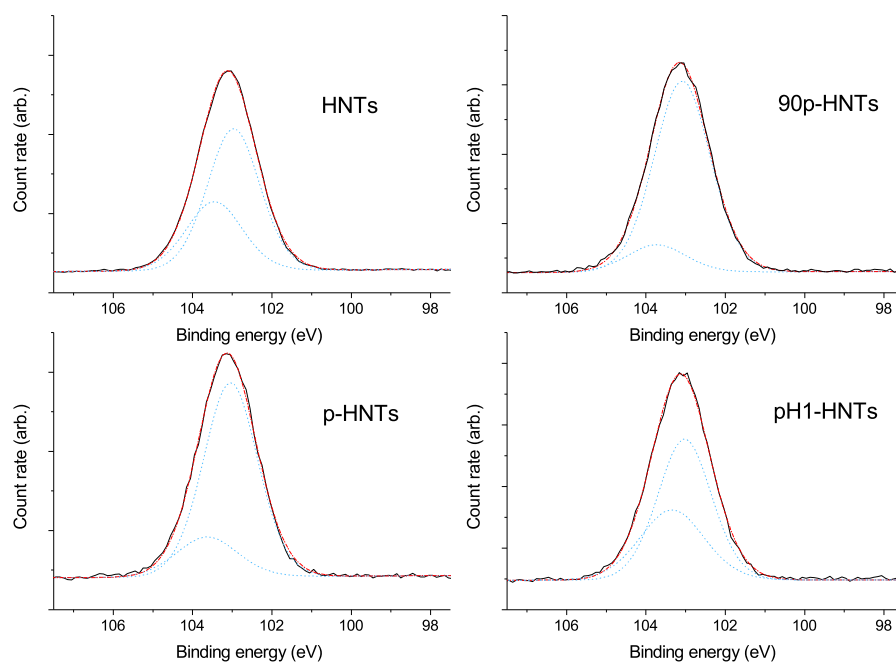


Figure 4.52: A comparison of one and two peak fits for XPS data in the Si 2p region of HNTs and treated HNTs. The black line is the data, the red dashed line is the 1PF, and the blue dotted lines represent the 2PF.

Table 4.8: A comparison of the peak positions and residuals found when fitting the Si 2p of the HNT and piranha-solution treated HNTs with either one peak (1PF) or two peaks (2PF).

Sample	1PF/eV	2PF/eV	1PF FWHM	1PF residual	2PF residual
HNTs	103.12	102.97, 103.45	1.68	1.15	0.90
p-HNTs	103.13	103.04, 103.63	1.71	1.06	0.89
90p-HNTs	103.15	103.08, 103.74	1.74	1.11	1.02
pH1-HNTs	103.12	103.03, 103.34	1.73	1.14	1.05

figure 4.53, with the two largest peaks corresponding to oxygen atoms in either of Si-O-Si or Si-O-Al, and oxygen atoms in hydroxyl groups (i.e. -O-H), respectively. They state that the ratio of these peaks can be used to quantify the relative amounts of oxygen in each environment. As such, analysis of the O 1s peak would theoretically be useful for determining whether piranha solution treatment had led to an increase in the number of surface hydroxyl groups in the HNTs. However, fitting the O 1s region with three peaks gave variable peak positions and areas between samples (figure 4.54), and none of the fits matched that described by Kloprogge and Wood.⁸ Even with extensive constraint of fitting parameters, it was difficult to achieve a satisfactory fit of the O 1s environment that was similar to that found in the literature.⁸ However, as can be seen in figure 4.55, the O 1s region does clearly require three peaks to be fit well, although it is difficult to give them physical meaning because they vary so much between samples. Fitting the O 1s region is therefore only used to obtain an overall concentration of oxygen in the samples, rather than to draw conclusions about different oxygen environments. Most importantly, it was not possible to draw any conclusions about the amount of hydroxyl groups on the HNT surface before and after piranha solution treatment.

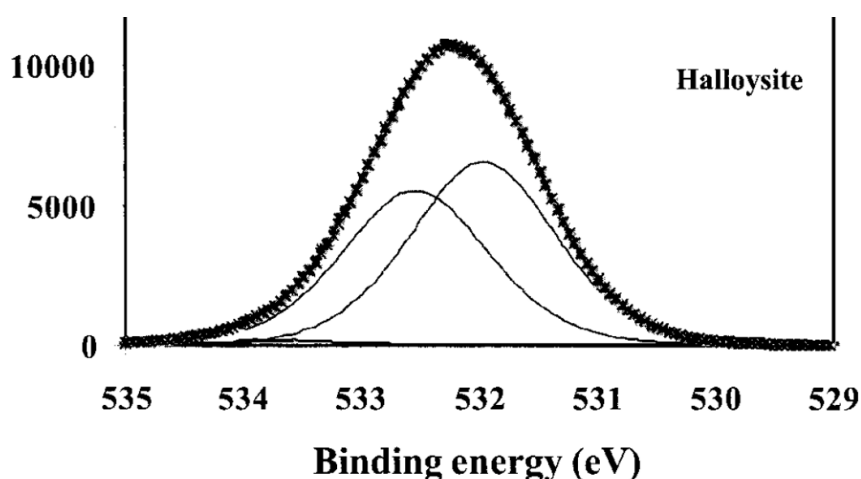


Figure 4.53: XPS data for the O 1s region of HNTs, adapted from work by Kloprogge and Wood.⁸ They fit the O 1s region of HNTs with three peaks, and suggest that the two largest peaks correspond to either Si-O-Si/Si-O-Al, or -O-H environments. Image adapted with permission.

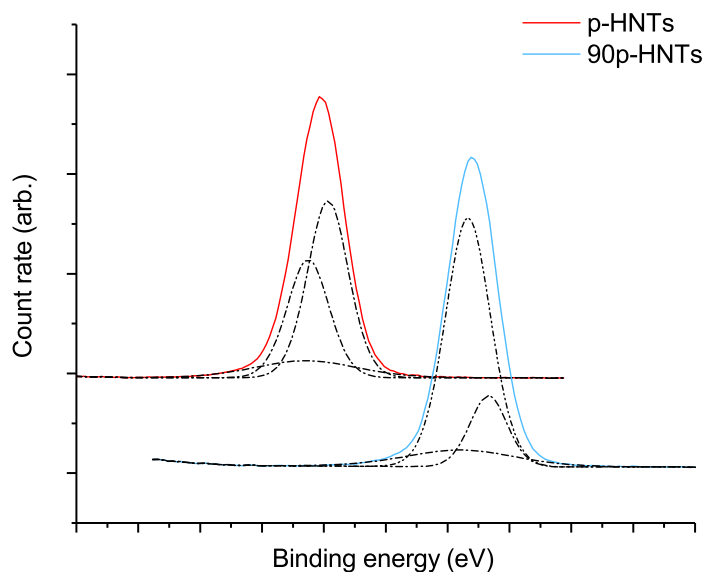


Figure 4.54: The O 1s region in XPS spectra of p-HNTs and 90p-HNTs. Between different samples, there was a lot of variation in how the O 1s peak could be fitted. It is therefore difficult to ascribe any physical meaning to the fitted curves.

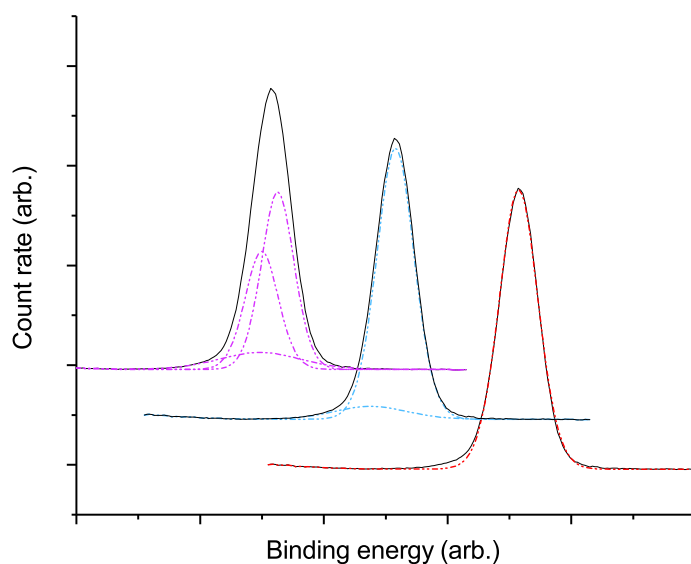


Figure 4.55: The raw data (black, solid lines) for the O 1s region of XPS spectra of HNTs can be fitted with one, two or three peaks (dashed lines). One peak clearly does not fit the edges of the peak, whereas two peaks produces a fit which is much closer to the raw data. Only using three peaks matches the data closely, but the three peaks do not match those described for halloysite by Kloprogge and Wood.⁸

The wettability of piranha solution treated HNTs

Finally, the water contact angles of p-HNTs and 90p-HNTs were measured. It should be noted that both of these samples were a different batch to those measured by the techniques discussed thus far, as the first batches were used up in the APTES coating described in the next section. However, they were made in exactly the same way as the first batch, so they would be expected to have the same properties. As can be seen in figure 4.56, the water contact angle of p-HNTs was essentially identical to that of HNTs, but the contact angle of the 90p-HNTs was only 75% that of the pure HNTs, i.e. the 90p-HNTs were measurably more hydrophilic than untreated HNTs. This is further evidence that the p-treatment caused no chemical change to the HNTs' surface chemistry; it certainly did not make the sample more hydrophilic, which had previously been suggested as an affect that piranha solution treatment has on silica surfaces.²²⁶ However, the 90p-treatment clearly had some effect. The increase in the hydrophilicity of the 90p-HNTs might be taken as evidence of an increased number of surface silanol groups, but this would contradict the findings from XPS and IR spectroscopy. An alternative explanation might be that the change in wettability is related to an increased amount of acid-etching products in the 90p-HNTs, i.e. the presence of more of the newly-formed Si-NPs may have had an impact. This is supported by TGA, which suggested that more alumina had been removed from the 90p-HNTs, although surface analysis by XPS suggested that both samples had similar amounts of surface Al.

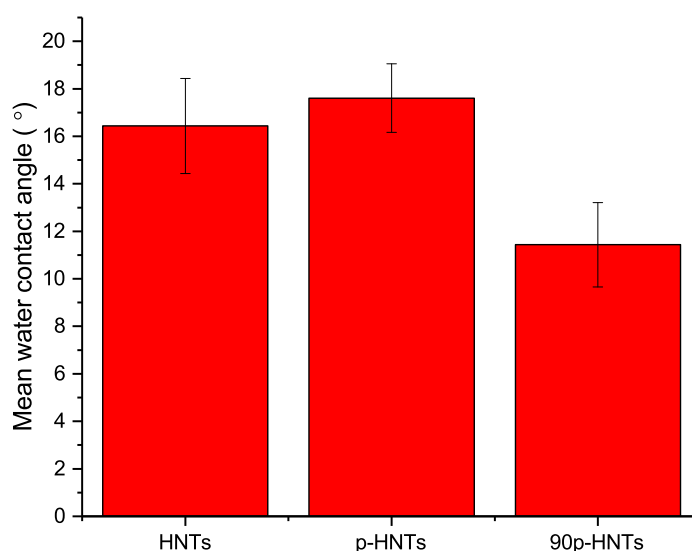


Figure 4.56: The water contact angle of untreated HNTs versus p-HNTs and 90p-HNTs. The HNTs and the p-HNTs have the same water contact angle, so it is concluded that the p-treatment does not change the HNT surface. However, the 90p-HNTs were measurably more hydrophilic; it is unknown why this is the case.

4.2.4 Summary of the effect of piranha solution treatment on HNTs

On the basis of IR spectroscopy, TGA, and XPS, it was concluded that piranha solution treatment led to no change in the concentration of surface silanol groups on HNTs, but these techniques, as well as TEM, also suggested that it did lead to acid-etching of the alumina from the interior of the HNTs. From water contact angle measurements, it can be concluded that p-treatment had no effect on the surface chemistry of the HNTs at all. However, the 90p-treatment made the HNTs measurably more hydrophilic; the exact reasons for this remain unknown, but it is speculated to be related to an increased degree of acid-etching of the HNTs in the 90p-treated sample compared to those in the p-treated sample.

4.2.5 APTES coating of piranha-solution-treated HNTs

The treated HNTs were coated with APTES in the same way as described in section 4.2.2. As can be seen in table 4.9, the grafted amounts of silane found by TGA on piranha solution treated and pH1-HNTs were within or close to the range found for untreated HNTs.

Table 4.9: The grafted amounts of APTES on HNTs and pre-treated HNTs.

Sample	Grafted amount of APTES/wt%
NH2-HNTs	1.07 - 1.79
NH2-p-HNTs	1.72
NH2-90p-HNTs	1.83
NH2-pH1-HNTs	1.40

Table 4.10 gives the relative (to Si) concentrations of surface elements found by XPS for the APTES-coated samples. Compared to the uncoated samples, the APTES-coated samples are all enriched with Si, C and N, which is consistent with the addition of the aminoalkoxysilane to the surface. The concentration of N is most important, as this is the only peak which is solely due to the grafting of APTES. This was found to be similar for each sample (note that the NH2-HNT sample measured by XPS had a grafted amount of 1.62 wt%), which in turn suggests that all of the samples had a similar thickness of coating of APTES on the exterior surface - since XPS is a surface measurement, a thicker coating of APTES would be expected to be reflected in a higher concentration of N, and vice versa. Similarly, the water contact angles of the coated pre-treated samples were found to be the same as coated untreated HNTs with similar grafted amounts of silane (figure 4.57). Therefore, TGA, XPS and contact angle measurements indicate that piranha solution pretreatment of the HNTs did not influence the outcome of subsequent coating with APTES. This is in contrast to the results of Sun *et al.*, who saw about an 80% increase in the amount of APTES that could be grafted after piranha solution treatment.⁷

Table 4.10: The relative (to Si) concentrations of surface atoms as found in XPS spectra of uncoated and APTES-coated HNT samples.

Sample	Al 2p	Si 2p	C 1s	O 1s	N 1s
NH2-HNTs	0.63	1	0.86	3.60	0.18
NH2-p-HNTs	0.57	1	0.80	3.27	0.17
NH2-90p-HNTs	0.51	1	0.93	3.07	0.18
NH2-pH1-HNTs	0.63	1	0.88	3.39	0.20
HNTs	0.80	1	0.28	3.32	0
p-HNTs	0.66	1	0.13	3.85	0
90p-HNTs	0.66	1	0.18	4.00	0
pH1-HNTs	0.79	1	0.24	3.90	0

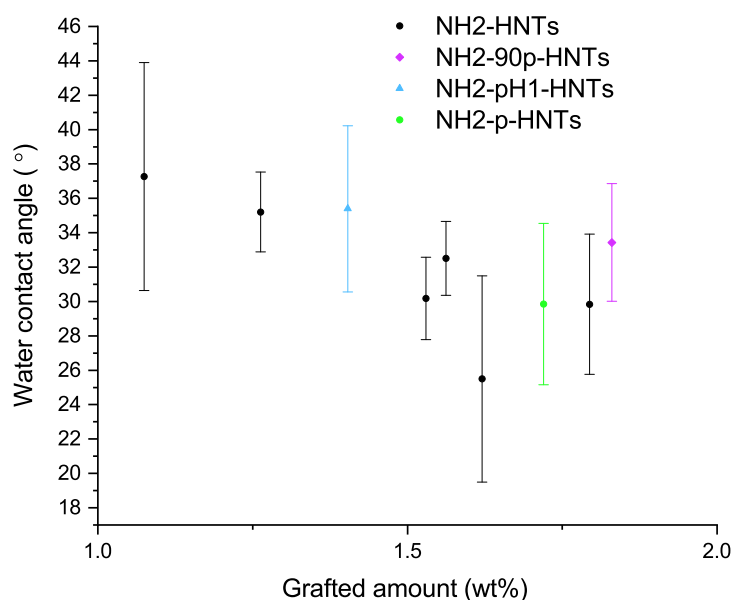


Figure 4.57: The water contact angles of all the APTES coated samples. None of the pre-treatments had an effect on the water contact angle of the obtained APTES-coated samples.

The pH1-HNTs had the lowest grafted amount as measured by TGA, but a similar surface concentration of N compared to the other samples. This might be because of a reduced amount of APTES coating on the interior alumina surface of the pH1-HNTs compared to the other samples. More specifically, it may be that the interior aluminol groups remained protonated after drying from pH 1 water, which might have meant that they were less able to undergo condensation with APTES, since the lone pair of electrons on the oxygen atom in $\text{Al-O}^+\text{H}_2$ would be unavailable for reaction. Imogolite, an aluminosilicate nanotube with an exterior of alumina groups (imogolite nanotubes essentially have the inverse structure of HNTs), has a large, positive zeta potential below about pH 8,²⁴⁷ so it is reasonable to assume that the alumina surface of HNTs would be extensively protonated at pH 1. The decreased amount of APTES on the interior surface would not necessarily

be seen by XPS if electrons from the this interior coating were not able to escape through the walls of the nanotubes without undergoing collisions that altered their kinetic energy.

There are several reasons why the results here may have differed from those of Sun *et al.*. Firstly, it could be that the differences in their procedure and the one used here were more important than expected. For example, ultrasonication of the HNTs into the toluene might be an important factor when coating piranha solution treated HNTs, as it is possible that flocculation of the particles in the low pH solution is never recovered from during washing, which would mean there was less surface area available for coating. Alternatively, it may be necessary to use the more rigorously dry conditions that they described, rather than the procedure used in this work. Since the grafted amounts of silane for untreated HNTs were similar in this work to those reported by Sun *et al.*,⁷ it seems unlikely that such differences were to blame. However, without knowing exact details of their experimental and analytical methods, it is difficult to isolate exactly why they saw such an increase in grafted amounts after piranha solution treatment.

4.3 Conclusions and future work

Through adapting procedures described in the literature, a method for silane coating of HNTs was established using the methacrylate-functional silane, TMPM. Specifically, two coating procedures using common reaction solvents seen in literature, toluene and ethanol, were compared. The successes of the coating reactions were confirmed by the appearance of new peaks in the IR spectra of the samples, a greater mass loss in TGA for samples after coating, and an increase in the water contact angle of the coated samples compared to untreated HNTs. TEM images appeared to show a new layer on the surface of HNTs coated with TMPM in toluene, suggesting that the procedure produced a multi- rather than mono-layer coating. It was found that using toluene rather than ethanol produced samples with a higher grafted amount of silane, and much greater water contact angle, so toluene was chosen as the better solvent. In addition, soxhlet extraction was compared to washing the samples by repeated rinsing and centrifugation, and it was found that soxhlet extraction was both less labour intensive, and, through TGA, appeared more effective at removing non-covalently bound silane. The knowledge gained in this process was used to inform future silane-coating procedures.

The HNTs were then coated with the amino-functional alkoxy silane, APTES, which should improve the performance of the HNTs when used as part of an epoxy resin nanocomposite. The success of the reactions were confirmed in a similar manner to those carried out previously. Repeating the reaction several times for various concentrations of HNTs and APTES showed that the results of the APTES coating were variable even when conditions were similar, with TGA indicating that grafted amounts of silane varied from around 1.1 wt% to around 1.8 wt%. This is consistent with the observation made by Zhu *et al.* that the outcome of the reaction was dependent on many factors, including variations in ambient humidity.²¹¹ However, it was also found that coating 40 g of HNTs with APTES led to grafted amounts within the range of those found when 10 g of HNTs was used, provided that the ratio [APTES]:[HNTs] was kept the same. This indicates that it should be possible to scale the coating process up to amounts relevant for producing a large number of nanocomposite parts without a significant change in the material. Because ex-

isting facilities at the University of Sheffield were not suitable for measuring the water contact angle of porous substrates, a new, digital contact angle measurement set-up was built. Using this, it was possible to show that the variation in grafted amount of silane on the various NH₂-HNT samples did lead to variation in the water contact angle. Surprisingly, the samples with the least amount of grafted APTES appeared to be the most hydrophobic. The variability in the results of APTES coating of HNTs may be important when considering the performance of different batches of NH₂-HNTs used in epoxy resin nanocomposites. Whether the variability does have an effect should be the subject of further investigation.

The effect of piranha solution treatment was also studied as a means of increasing the amount of APTES that can be grafted onto the HNTs. This was inspired by the work of Sun *et al.*, who found that piranha solution treatment of HNTs led to an increase in the number of hydroxyl groups on the surface, and a subsequent 80% increase in the amount of APTES that could be grafted to the nanotubes.⁷ Their piranha solution treatment was repeated, and compared to a shorter, safer one. In both cases, no evidence was found for an increased concentration of hydroxyl groups on the HNT surface, in contrast to their results. Subsequent APTES coating of the treated HNTs was found to yield similar results to using untreated HNTs. In addition, both piranha solution treatments led to damage of the nanotubes through acid-etching. Therefore, it was concluded that piranha solution was not effective for improving the amount of APTES that could be grafted onto HNTs.

It was, however, found that piranha solution treatment is an effective way of purifying the HNTs, since it appeared to reduce the concentration of both iron and carbon in the samples. However, if this is to be adopted as a purification method for HNTs, more work should be carried out to modify the procedure (e.g. shorter reaction time) to limit acid-etching of the nanotubes. Future work should also include repeating the silane coating reactions on untreated and piranha solution treated HNTs, but this time using the exact procedure that Sun *et al.* reported,⁷ and making sure that all of the samples were coated in a humidity-controlled environment. This should isolate the effect of the piranha solution pre-treatment, and prove conclusively whether or not it made any difference.

As a final note, it is acknowledged that it may be strange to dwell so much on the results of a single piece of literature as was done here, i.e. the work of Sun *et al.*⁷ However, their work remains the only published report about piranha solution treatment of HNTs (and indeed is the top search engine result for the phrase “piranha halloysite”), so it was felt to be important to study it in detail. In addition, the idea that piranha solution “hydroxylates” silica surfaces seems to be commonly repeated without citation, even though the chemistry of that hypothetical process does not make sense. As such, the result that the HNTs did not appear to have any more hydroxyl groups on their surfaces after piranha solution treatment is particularly important.

4.4 Materials and methods

4.4.1 Materials

A summary of the materials used in this chapter is given in table 4.11. Not included is deionised water, which was purified from the mains supply to a resistivity of 18.0 M Ω cm using a PureLab Option-Q water treatment unit.

Table 4.11: A list of the materials used in this chapter.

Material	Supplier	Purity and/or other comments
Halloysite nanotubes	I-Minerals Inc.	ULTRA HalloPure Halloysite (2015M)
3-(trimethoxysilyl)propyl methacrylate (TMPM)	Alfa Aesar	97%
Toluene	Fisher Scientific	$\geq 99\%$
Absolute Ethanol	Fisher Scientific	HPLC grade
(3-aminopropyl)-triethoxysilane (APTES)	Sigma-Aldrich	$\geq 98\%$
Nanomer I.44P (oMMT)	Sigma-Aldrich	35-45 wt% dimethyl dialkyl (C14-C18) amine
Sulfuric acid	Fisher Scientific	$\geq 95\%$
Hydrogen peroxide	Fisher Scientific	30% w/v stab., reagent grade

4.4.2 Synthetic methods

TMPM coating of HNTs (P1)

HNTs were dried in a vacuum oven at 100 °C for 1 h, then added to toluene (approx. 120 mL). The flask was fitted with a reflux condenser with a calcium chloride drying tube, and the mixture was heated to reflux with constant stirring. Once the toluene was boiling, TMPM was added rapidly to give an approximate alkoxysilane/HNT ratio of 0.3 wt/wt. The flask was quickly sealed, and the mixture was heated to reflux for 24 h with constant stirring. After this time, the mixture was allowed to cool. The solid was then washed using one of the two following methods:

1. The dispersion was poured into centrifuge tubes, and centrifuged for 10 min at 6000 rpm. The toluene was then carefully decanted, fresh toluene (about 40 mL in each centrifuge tube) was added, and the samples were centrifuged again. This was repeated five times before the final solid was obtained by decanting the toluene from the centrifuge tubes.
2. The dispersion was transferred to a cellulose soxhlet extraction thimble and soxhlet extracted with toluene for 48 h.

In both cases, the samples were subsequently dried overnight in a vacuum oven at 60 °C. The dry samples were then gently ground by hand to a fine powder.

TMPM coating of HNTs (P2)

About 5 g of HNTs were dispersed in 250 mL of absolute ethanol, and 17.5 g of TMPM was added. The mixture was heated to reflux with constant stirring for 24 h, then allowed to cool before being soxhlet extracted with ethanol for 48 h. After this time, the solid was dried overnight in a vacuum oven at 60 °C. The dry samples were then gently ground by hand to a fine powder.

TMPM coating of HNTs (P3)

P3 was carried out using the method described for P1 (with washing method 2), with the exception that ethanol was used as the reaction and washing solvent rather than toluene.

APTES coating of HNTs

The HNTs were coated using the same procedure described for P1 (with washing method 2), except APTES was used rather than TMPM.

Piranha solution treatment (90p)

In a beaker, 30% H₂O₂ (aq) (approx. 25 mL) was slowly and cautiously added to concentrated sulfuric acid (approx. 75 mL) with continuous stirring using a PTFE-coated magnetic follower. Once this solution had cooled enough to safely handle (several min), it was carefully poured into a flask containing HNTs (approx. 10 g). A thermometer and a reflux condenser were fitted to the flask, and the mixture was heated to 90 °C for 1 h with continuous stirring. Metal beads were used as the heating medium to prevent dangerous exothermic reactions occurring in case of spillage of the piranha solution out of the reaction vessel. During heating, the mixture was observed to foam and rise up the vessel walls; caution is therefore advised when carrying out this reaction.

After 1 h of heating, the piranha-solution/HNT mixture was left to cool, then carefully diluted with about a 4-fold excess of deionised water. The HNTs were then filtered out of the mixture under vacuum, before being re-dispersed in a minimum amount of water and placed in a cellulose dialysis tube with a molecular-weight-cut-off of 14 kDa. The HNTs were dialysed in about 2 L of water with regular water changes over 2-3 days, until the dispersion inside the tube was found using indicator paper to be neutral pH. This took >10 water changes. Once the dispersion was neutral pH, the HNTs were filtered out before being dried overnight in a vacuum oven at 60 °C. Once dry, the HNTs were gently ground by hand. The final 90p-HNTs were obtained as a fine, white powder.

Piranha solution treatment (p)

HNTs (approx. 10 g) were measured into an oversized beaker (500 mL capacity). Concentrated sulfuric acid (approx. 75 mL) was then added, and the mixture was gently stirred using a PTFE-coated magnetic follower to disperse the particles. Under continuous stirring, 30% H₂O₂ (aq) (approx. 25 mL) was slowly and cautiously added to the mixture. Once addition was completed, the mixture was left for 15 min with continuous stirring. When a thermocouple was taped to the underside of the beaker throughout mixing, it was found that temperature of the mixture rose rapidly to about 90 °C, before cooling to about 60 °C over the course of 15 min.

After this time, the mixture was carefully diluted with about a 4-fold excess of deionised water. The HNTs were then filtered out of the mixture under vacuum, before being re-dispersed in a minimum amount of water and placed in a cellulose dialysis tube with a molecular-weight-cut-off of 14 kDa. The HNTs were dialysed in about 2 L of water with regular water changes over 2-3 days, until the dispersion inside the tube was found using indicator paper to be neutral pH. This took >10 water changes. Once the dispersion was neutral pH, the HNTs were filtered out before being dried overnight in a vacuum oven at 60 °C. Once dry, the HNTs were gently ground by hand. The final p-HNTs were obtained as a fine, white powder.

Making pH1-HNTs

With magnetic stirring, about 1 g of conc. sulfuric acid was added to approx. 200 mL deionised water to give a solution of pH 0.8 (as measured by a pH probe). Approx. 13 g HNTs were added to this solution, which was stirred for 10 min to ensure that all of the solid had been wetted by the solution. The HNTs were then retrieved by 10 min of centrifugation at 6000 rpm, before being dried overnight in a vacuum oven at 60 °C. Once dry, the pH1-HNTs were gently ground to a fine powder by hand.

Acid-etching of HNTs

5.6 mL of conc. sulfuric acid was added to 100 mL deionised water to make a solution of about 1.05 M. To this solution, 0.9 g of HNTs were added, and the mixture was heated to 50 °C for 3 d with constant stirring. After this time, the solid was retrieved from solution by repeated centrifugation (10 min at 6000 rpm) and rinsing with deionised water (about 40 mL each cycle). The acid-etched HNTs were then retrieved by 10 min of centrifugation at 6000 rpm, before being dried overnight in a vacuum oven at 60 °C. Once dry, the pH1-HNTs were gently ground to a fine powder by hand.

4.4.3 Characterisation

TGA

About 10 - 20 mg of sample was measured using a Pyris TGA with a pure nitrogen atmosphere. The following heating program was used: hold for 5 min at 25 °C; heat from 25 °C to 60 °C at 10 °Cmin⁻¹; hold for 10 min at 60 °C; heat from 60 °C to 800 °C at 10 °Cmin⁻¹; hold at 800 °C for 5 min. The 10 min at 60 °C is included to remove physisorbed water from the sample surface. The percentage of sample remaining at a given temperature is then calculated by setting the sample mass at 100 °C as 100%, and comparing this to the mass of sample at the given temperature. The grafted amount was then calculated as the difference between the percentage mass remaining for pure HNTs at 800 °C and that of the sample at 800 °C, as shown in equation 4.6. For NH₂-p-HNTs etc., the mass of the pure HNTs is replaced with the mass of the appropriate treated HNTs (e.g. p-HNTs).

$$\text{Grafted amount (wt\%)} = (\text{Mass (pure HNTs) at 800 °C} - \text{Mass (sample) at 800 °C})\text{wt\%} \quad (4.6)$$

FT-IR spectroscopy

FT-IR measurements were taken using a PerkinElmer Spectrum Two spectrometer and a 'UATR Two' ATR sampling accessory. Samples were dried in a vacuum oven at 100 °C for at least 1 h before being taken for immediate measurement. After a background spectrum had been taken, small amounts of powdered sample (about a mg) were placed on the crystal for analysis, with the large "shoe" fitted, and the force gauge applied to a level of about 150. Spectra were collected as an average of 10 scans between 450 and 4000 cm⁻¹. The 'not dried' sample described in section 4.2.3, figure 4.48, was stored under ambient conditions before measurement.

TEM imaging

The samples were added to deionised water at a concentration of about 1 wt% HNTs, with vigorous shaking to disperse the solid. An approx. 10 μL portion of each dispersion was then dropped onto a carbon-coated TEM grid, and the excess liquid wicked away after approx. 1 min. The samples were then imaged using an FEI Tecnai transmission electron microscope.

Lab humidity measurements

The relative humidity of our lab was measured using a Files Thru The Air WIFI-TH+ High Accuracy Temperature and Humidity Sensor. This was kept on a shelf a few m

away from the fumehood, and logged relative humidity every 30 min over a period of 9 weeks. The data was collected by Stephen Knox.

Measurement of water contact angles

To obtain samples for water contact angle measurements, the HNT powders were pressed into circular pellets of about 1 cm in diameter using a hydraulic press, with pressure applied up to around 4000 psi, at which the samples were held for 30 s. The metal die used was one typically used for making KBr discs for IR spectroscopy. These pellets were then kept in a drying oven at 60 °C until immediately before measurement.

To obtain contact angle measurements, a 20 μ L droplet of water was placed on the pellet surface using a micro-pipette, and filmed as the droplet was absorbed using a generic digital microscope. Contact angles were found from images taken immediately after the introduction of the droplet by analysis using the DropSnake plug-in in ImageJ.²³⁴ The values reported here are the averages and standard deviations of 6 measurements for each sample (i.e. 2 measurements for each droplet, 3 pellets/droplets for each sample).

Measurements of pH

Measurements of pH were either made using a Mettler Toledo MP255 pH meter, or using universal indicator paper.

ICP-MS measurements of HNTs and p-HNTs

A few hundred mg of sample were digested using concentrated nitric acid, and analysed for Si, Al and Fe content on an Agilent 4500 ICP-MS. Samples were digested with acid and measured by Neil Bramall in the Department of Chemistry at the University of Sheffield.

XPS measurements

To obtain samples for XPS measurements, the HNT powders were pressed into circular pellets of about 1 cm in diameter using a hydraulic press, with pressure applied up to around 4000 psi, at which the samples were held for 30 s. The die was carefully cleaned between samples to limit cross-contamination. XPS data were collected by Dr. Deborah Hammond at the Sheffield Surface Analysis Centre using a Kratos Axis Supra X-ray Photoelectron spectrometer with an aluminium source.

Chapter 5

Conclusions and Future Work

5.1 Introduction

In this chapter, the conclusions from the preceding chapters will be summarised. These will then be placed in the context of the work as a whole; while the content and specific conclusions of each chapter are fairly disparate, there are still some general themes and conclusions which can be drawn. Finally, some recommendations and suggestions for future work will be discussed.

5.2 Summary of conclusions of each chapter

5.2.1 Chapter 2 - Characterisation of Halloysite Nanotubes

It was shown that the quantity and type of impurities in a sample of HNTs from I-Minerals did not always match the supplier data. Most importantly, it was illustrated using TEM that there are a significant number of non-tubular impurities in the samples, and that the HNT dimensions are both polydisperse, and different to the typical dimensions reported by the supplier. These facts serve to highlight that researchers should fully characterise a sample of HNTs independently, rather than relying on supplier or literature data.

A more important outcome of this chapter is the illustration of some of the difficulties associated with measuring the sizes and shapes of HNTs. More specifically, it was concluded that measuring values of size by hand from TEM images was susceptible to bias, as well as being time and labour intensive. It was found that scattering techniques (SAXS and DLS) could not be used to overcome these issues, since the polydispersity of the HNTs' dimensions, as well as the presence of morphological impurities, makes scattering data difficult to model. Automated image analysis of TEM images was suggested as a way of determining HNT sizes without bias. However, it was found to be difficult to automatically distinguish isolated HNTs from the large populations of agglomerated and non-tubular particles in the images. Some ways of reducing the population of agglomerated particles in the TEM images by changing sample preparation procedures were explored, but these were ultimately unsuccessful.

5.2.2 Chapter 3 - A Comparison of Mixing Methods for Dispersing Halloysite Nanotubes into an Epoxy Resin

In this chapter, ultrasonication was compared to the use of a three-roll mill (3RM) as a means of dispersing HNTs into an epoxy resin. It was found using optical and electron microscopy that the HNTs could be dispersed into the resin on the level of individual particles using both the 3RM in force mode and ultrasonication of a dispersion of HNTs in an epoxy/acetone solution, but not using the 3RM in gap mode, or with ultrasonication in the undiluted resin. TEM images showed that HNTs washed from the epoxy resin mixtures all had both a comparable mode length, and similar populations of longer tubes in comparison to each other and to the pure HNTs. Therefore, it was concluded that none of the mixing techniques damaged the nanotubes. This was in contrast to previous

literature, which had suggested that ultrasonication did reduce the length of HNTs.^{108,185}

Ultrasonication without dilution or cooling specifically caused an apparent chemical change in the resin, which was thought to be due to oxidation at the high temperature reached during the process. This chemical reaction seemingly increased the inherent viscosity of the resin/HNT mixture relative to the other mixing techniques, even after the difference in filler content in the mixtures was taken into account. This casts doubt on previous literature, which concluded that the increase in viscosity of an epoxy/HNT mixture upon ultrasonication was indicative of a greater degree of dispersion of the nanotubes in the resin.^{10,108} The reaction also led to an apparent coating on the surface of the HNTs, as seen by TEM, although the exact chemical nature of this coating is not known.

It was found that the filler content of the epoxy/HNT nanocomposites could be accurately determined by density measurements, and by burning off the resin in an air atmosphere (either by TGA or using a furnace). However, burning in low-oxygen atmospheres gave inaccurate results. It was seen that the actual measured filler content was often considerably less than the filler content expected considering the amount of HNTs initially added to the resin. This was especially true where ultrasonication had been used as the mixing technique. Therefore, an important conclusion of this chapter is that the filler content of epoxy/HNT nanocomposites should always be measured, rather than be calculated from the quantity added before mixing. As far as I am aware, the measurement of filler content has always been ignored in the literature for epoxy/HNT nanocomposites. Indeed, this may go some way to explaining the diversity of results seen in the literature.

Once filler contents had been determined, the flexural properties of epoxy/HNT nanocomposites made using the different mixing methods could be compared. Increases in flexural modulus relative to pure epoxy were seen for the highest filler content samples made by ultrasonication without dilution and by using the 3RM in force mode (up to 8% and 12%, respectively). However, flexural modulus was essentially unchanged for the other samples. No significant change in flexural strength relative to pure epoxy was seen for any of the samples.

It was found that epoxy/oMMT nanocomposites were difficult to make because of foaming of the mixtures, which could not be alleviated. Therefore, epoxy/HNT nanocomposites could only be compared to examples of epoxy/oMMT nanocomposites from literature. Doing so suggested that oMMT is more effective at increasing the stiffness of the epoxy at low filler contents,^{5,51} but HNTs can do so without causing any issues with processing. Such processing issues were seen in the literature to have a subsequent detrimental effect on the final strength of the epoxy/oMMT nanocomposites.^{5,51} This fact, and the fact that HNTs can clearly be well dispersed into epoxy resins without surface modification, are the main advantages of using HNTs rather than oMMT, since both are comparable in price and abundance.

5.2.3 Chapter 4 - Functionalisation of Halloysite Nanotubes with Alkoxysilane and Activation with Piranha Solution Pre-treatment

Coating of HNTs with 3-(trimethoxysilyl)propyl methacrylate was compared using three different procedures carried out in either toluene or ethanol. While all of the coating re-

actions were successful, it was determined that coating from refluxing toluene gave the best results, as indicated by a greater grafted amount of silane, and a greater water contact angle for this sample. Subsequently, soxhlet extraction rather than hand washing was determined to be the most effective means of removing the physisorbed silane from the HNT surface, which would be detrimental to mechanical performance in a nanocomposite.

It was then found that HNTs could effectively be coated with (3-aminopropyl)triethoxysilane (APTES) by the same reaction in toluene to give similar results to literature.⁷ However, repeating this reaction for several samples of HNTs led to variable grafted amounts of APTES as seen by TGA. This variation did not seem to correlate to reactant concentrations or aging of the silane in the bottle between reactions. The variability is instead concluded to be due to ambient humidity, as has previously been observed in literature.²¹¹ The analogue system for measuring water contact angles at the University of Sheffield was found to be unsuitable for these samples, so a new, digital set-up was developed. Using this digital set-up, the water contact angles of the APTES-coated samples could be found, and these also seemed to vary between batches. Indeed, the variation in wettability appeared to correlate to grafted amount of APTES, with a lower grafted amount leading to a higher water contact angle, and vice versa. Nonetheless, it was shown that the coating process could be scaled up from the 2 g scale reported in literature, to up to 40 g with the results remaining within the same range of variability. The degree of variability seen might have implications for the repeatability of performance between different batches of APTES-coated HNTs were they to be used as reinforcing fillers in epoxy resin nanocomposites.

Piranha solution pre-treatment of HNTs was attempted as a means of increasing the surface concentration of silanol groups, which would theoretically increase the amount of APTES that could be grafted to the HNT surface in subsequent reactions. This had previously shown to be effective in literature,⁷ despite the exact nature of the chemical interaction between the piranha solution and the HNT surface being unclear. A piranha solution pre-treatment for HNTs from literature⁷ (90p) was compared to a shorter, safer treatment (p). It was found that there was no evidence for an increased number of silanol groups on the HNT exterior surface after either piranha solution treatment process, although there was evidence for some degree of acid-etching of the HNTs' interior surfaces during treatment. However, while the p-treatment caused no change in the wettability of the HNTs, the 90p-treatment made them measurably more hydrophilic; the reasons for this are unknown, but are speculated to be related to an increased degree of acid-etching of this sample. Nonetheless, subsequent APTES coating of the piranha-treated HNTs gave results within the variability range of the untreated HNTs. Therefore, piranha solution pre-treatment was concluded not to be effective for improving the amount of APTES that could be grafted to the HNT surface. Piranha solution is hence not recommended as a pre-treatment step for HNTs, especially considering the risk involved in the process.

5.3 General conclusions

Variability of literature

An important general conclusion of this thesis is that existing literature regarding HNTs and HNT nanocomposites should be treated with some degree of scepticism. While it would be wrong to accuse authors of publishing intentionally misleading work, there are several important aspects which tend to be overlooked in literature, and could inadvertently be sources of confusion.

For example, the filler content of epoxy/HNT nanocomposites has, to best of my knowledge, never been reported in the literature. Instead, the reported values are generally either nominal, or calculated from the initial amount of HNTs added. However, in Chapter 3, it was shown that the actual filler content in epoxy/HNT nanocomposites was often lower than the expected value, especially when ultrasonication was used to make the samples. Since many nanocomposite properties are a function of filler content, this serves to shed doubt on the validity of comparisons between different nanocomposite samples in literature, especially in cases where differences in properties were seen to be small.

Similarly, it was found in Chapter 2 that measured values of HNT dimensions were significantly different to those listed in the supplier data sheet. In addition to that, it was found that these values were susceptible to bias when they were measured by hand in TEM images. Where HNT dimensions are reported in literature, they are usually based off supplier data,^{109,129,130} or obtained from a small number of manual measurements.^{131–134} It can be concluded that assuming either of these to be accurate is probably unwise.

Lastly, it was shown in Chapter 4 that no evidence could be found for an increase in surface silanol concentration on HNTs after piranha solution treatment. For HNTs, this is a direct contradiction of literature,⁷ but it also may cast doubt on the apparently-widely-held belief that piranha solution treatment increases silanol concentration on silica glass surfaces in general (specifically by hydroxylation).

Repeatability and inconsistency in literature

A second issue with the literature regarding HNTs and HNT nanocomposites is a lack of focus on consistency and repeatability. Indeed, there seems to be more focus on developing new and creative ways to modify and use HNTs than on improving existing techniques and technologies; many literature reports seek to functionalise HNTs in new ways or use them in a new application, rather than to “fill in the gaps” of existing literature.

For epoxy/HNT nanocomposites, one area in particular highlighted in Chapter 3 is the lack of consistency in the mixing techniques used in literature. More specifically, many different mixing procedures have been reported, and the reporting of mixing parameters in literature is often vague. However, in Chapter 3 it was shown that both the type of mixing and exact mixing parameters used have a significant impact on the quality of the obtained epoxy/HNT dispersion, which in turn can affect the properties of the final nanocomposites. It is therefore difficult to compare the results of different literature reports regarding epoxy/HNT nanocomposites which used different mixing techniques,

especially in the many cases where the degree of dispersion of the HNTs in the final nanocomposite is either not assessed, or seen to be poor. More consistency in mixing methods would be needed for it to be able to be established in literature which HNT properties (e.g. geographical origin, surface treatments etc.) lead to the best performing epoxy/HNT nanocomposites.

Another gap in the literature for HNT polymer nanocomposites is the repeatability of functionalisation. That is to say, the results of adding a functionalised HNT to a polymer are reported, but there is usually no indication of the repeatability of these results between different batches of functionalised HNTs. In Chapter 4, it was shown that there can be measurable differences between repeats of the same alkoxy silane coating process specifically. Surface functionalisation based on alkoxy silane chemistry is widely used for modifying HNTs, and it should therefore be established to what degree these differences between batches have implications for the application of HNTs before different alkoxy silane coatings are compared to one another, or to other types of surface modification.

5.4 Future Work

5.4.1 Chapter 2

One of the most obvious pieces of necessary future work would be the development of a method to measure the sizes of HNTs without bias, which would likely build on the automated analysis of TEM images of HNTs outlined in Chapter 2. The two main challenges associated with this are automatically distinguishing isolated HNTs from agglomerated and non-tubular particles, and producing TEM images in which there are very few agglomerated particles to begin with. In the former case, it is likely that machine learning would provide a solution. This would involve providing many images of the different types of object as training data, from which an appropriate algorithm may be able to recognise distinguishing patterns which are not obvious to the human eye. In the case of sample preparation, it is probable that cryo-TEM would need to be used to image samples in which the HNTs have not agglomerated during drying on the sample grid. Alternatively, a very low concentration of HNTs could be used, and the sample could be measured using by automated scanning of a large area of the TEM grid. This would both reduce the labour associated with imaging the nanotubes at low concentrations, and eliminate bias with regards to selecting which areas and nanotubes to image.

5.4.2 Chapter 3

The work outlined in Chapter 3 about measuring filler content in epoxy/HNT nanocomposites would be worth pursuing further. More specifically, epoxy/HNT nanocomposites could be prepared in a range of concentrations by ultrasonication without dilution, and their mechanical properties could be measured. Their mechanical properties could then be compared as a function of the expected value of filler concentration versus the actual value; doing so would quantify the extent to which relying on expected or nominal values of filler content is incorrect. Additionally, work could be carried out towards reducing the

uncertainty in the filler content measurements, specifically by replacing the mullite sample crucibles with another material (e.g. high-temperature steel), which would not suffer the same issue with moisture absorption increasing the uncertainty in the measurement.

The observation that ultrasonication of HNTs in epoxy resin without dilution or cooling causes a coating to form on the HNT surface is another interesting avenue for future work. It would be worth investigating the chemical nature of this coating, and initial characterisation could be carried out using the techniques outlined in Chapter 4. Whether or not this coating process can be controlled should also be explored, as this might provide an interesting functionalisation route for increasing the compatibility between HNTs and epoxy resin. However, it may be difficult to replicate the reaction, since it is unknown to what temperatures and pressures the epoxy was exposed during ultrasonication. That is to say, simply heating a mixture of epoxy and HNTs to the temperature achieved during ultrasonication may not recreate the same reaction conditions. Nonetheless, heating such mixtures at different temperatures for different reaction times would be a good place to start.

5.4.3 Chapter 4

The most important remaining work from Chapter 4 is investigating whether the variation in the APTES coating process leads to any differences in the mechanical properties of epoxy/NH₂-HNT nanocomposites between different batches of coated nanotubes. This could be investigated using the flexural testing outline in Chapter 3, but it would also be interesting to carry out further tests to measure other mechanical properties, such as fracture toughness and impact strength.

With regards to piranha solution pre-treatments, it would be worthwhile to replicate exactly the process described by Sun *et al.*⁷ Since the variation in APTES coating may well stem from day-to-day variations in ambient conditions (most importantly, humidity),²¹¹ it would be worth carrying out this experiment in a well-controlled environment. The use of an inert-atmosphere glove box would perhaps be the ideal solution, with all solvents and glassware being rigorously dried beforehand (the glassware specifically could be evacuated with inert gas while still hot from a glassware drying oven). Doing so would provide final, conclusive evidence as to whether or not piranha solution pre-treatment is effective for improving the amount of APTES that can be grafted to the HNT surface.

Appendix A

A.1 Appendix to Chapter 2

A.1.1 Supplier data sheet for HNTs

Figures A.1 to A.3 give relevant data for the HNTs used in this work, which is available directly from the supplier, I-Minerals Inc.. Figures A.1 and A.2 are taken from a presentation about the HalloPure product line, and figure A.3 is a standalone data sheet. Both documents were available from the company, and up-to-date, as of September 2019. They are reproduced here with permission.

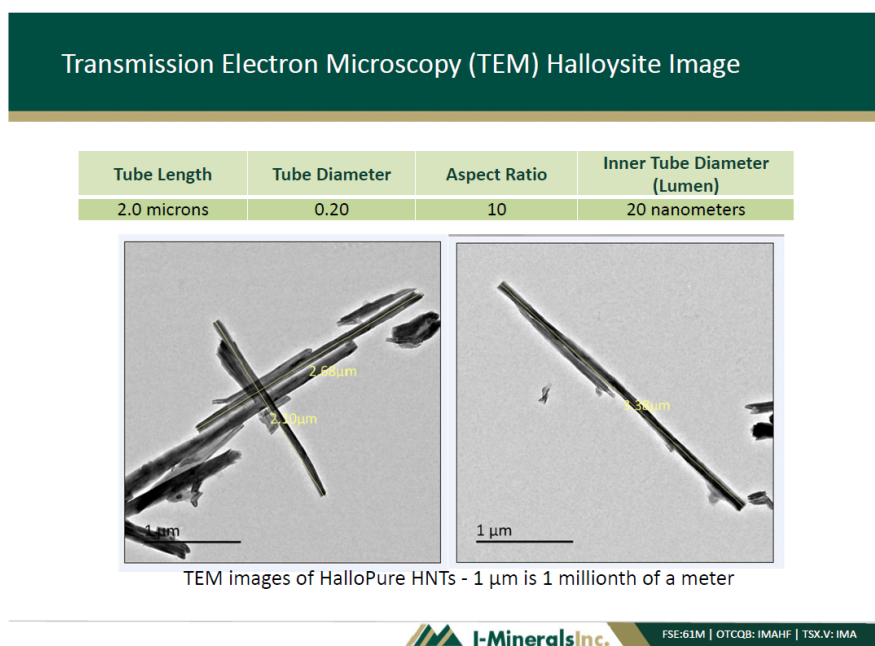


Figure A.1: TEM images of and size data for ULTRA HalloPure HNTs provided by I-Minerals Inc.

TYPICAL TRACE ELEMENTS. (total extraction in aqua regia; ppm)

Ag	As	Ba	Cd	Cr	Cu	Hg	Mo	Ni	Pb	Pt	Se	Zn	Ta
<0.02	1.03	115.6	<0.003	7.08	7.66	0.10	0.10	2.28	12.8	<0.02	<0.10	15.4	<0.10

Analysis by ICP by The James Hutton Institute (UKAS accredited)

Figure A.2: Trace elements in ULTRA HalloPure HNTs provided by I-Minerals Inc.



I-Minerals Inc.



HaloPure®
Halloysite Nanotubes (HNT)

product data

HaloPure®: 70%+ HNTs | ULTRA HalloPure®: 90%+ HNTs

Typical Tube Dimensions,
both grades

Tube Length	2 microns
Internal Tube Diameter	20 nanometers

HaloPure®

Particle size distribution,
cumulative % finer

µm	
20	100
10	99
5	97
2	80
1	67

ULTRA HalloPure®

Particle size distribution,
cumulative % finer

µm	
20	100
10	100
5	99
2	95
1	88

Typical Chemical Analysis

	SiO ₂	Al ₂ O ₃	Na ₂ O	K ₂ O	CaO	MgO	Fe ₂ O ₃	TiO ₂	LOI
HaloPure®	48.25	36.00	0.01	0.50	0.12	0.20	1.20	0.20	13.50
ULTRA HalloPure®	46.00	37.80	0.01	0.30	0.07	0.13	0.72	0.07	14.90

Typical Mineralogy by XRD (%)

	HaloPure®	ULTRA HalloPure®
Halloysite	78.0	90.0
Kaolinite	20.0	9.5
Quartz	0.9	0.5
Feldspar	1.1	-

Typical Physical Properties

ISO Brightness (%)	72.0	80.0
Oil Absorption (g/100g)	65.0	70.0
Moisture Content (% maximum)	1.0	1.0
Form	Powder	
Packaging	Sacks, IBCs, drums	

03.20.2018

For More Info: Linda Koep | Lkoep@imineralsinc.com | 208-659-8787

The information and data contained herein are believed to be accurate, but the manufacturer makes no warranty with respect thereto and disclaims responsibility for reliance thereon. These data relate only to the specific material described herein, and does not relate to use in connection with any other materials or in any process.

I-Minerals Inc. makes no warranties, express or implied, concerning this product. No warranty of fitness for any particular purpose is made and we assume no responsibility whatever for any use of this product. This product should be used by properly trained personnel, and in compliance with applicable health and safety laws and regulations.

Suite 880, 580 Hornby Street • Vancouver, BC Canada V6C 3B

www.imineralsinc.com

Figure A.3: The standalone data sheet for the properties of ULTRA HalloPure HNTs provided by I-Minerals Inc.

A.1.2 Comparison of all size data for HNTs

Figures A.4a and A.4b show the histograms and probability density functions (PDFs) for all of the HNT dimensions for both the first and second sets of measurements. These were referred to in section 2.6.3 of the main text.

A.1.3 MATLAB code

Code for filming using USB Microscope

The following MATLAB code takes images from a digital camera (“cam”) at a user defined frequency (“Pause”), for a user defined duration (“AcqTimeMin”). It returns JPEG format images with a time-stamp, starting at 0 s. This code was written by Ryan Seabright.

```
%Clears workspace to avoid overlaps
clear

%User to set Pause (s)
Pause = 0.1;
%Writes set pause as pause for the first iteration
SetPause = Pause;
%Sets initial average time to UI set time for initial iterative step
tAve = SetPause;

%User to set Acquisition time (minutes)
AcqTimeMin = 10;
%Converts acquisition time in minutes to number of frames
Frames = round((AcqTimeMin*60)/Pause);

%Selects webcam
cam = webcam(2);

%Starts the timer for naming purposes
tStart = tic;

%Starts Loop for image acquisition
for j = 1 : (Frames + 1);

    %Calculates time difference between set time and actual time
    DeltaT = Pause - tAve;
    %recalculates pause required to reach set pause
    SetPause = Pause + ((j-2)*DeltaT);
    %Pauses time that is set by measured time between loops
    pause(SetPause);
    %Calculates time in seconds elapsed each loop (s)
    TimeElap = toc(tStart);

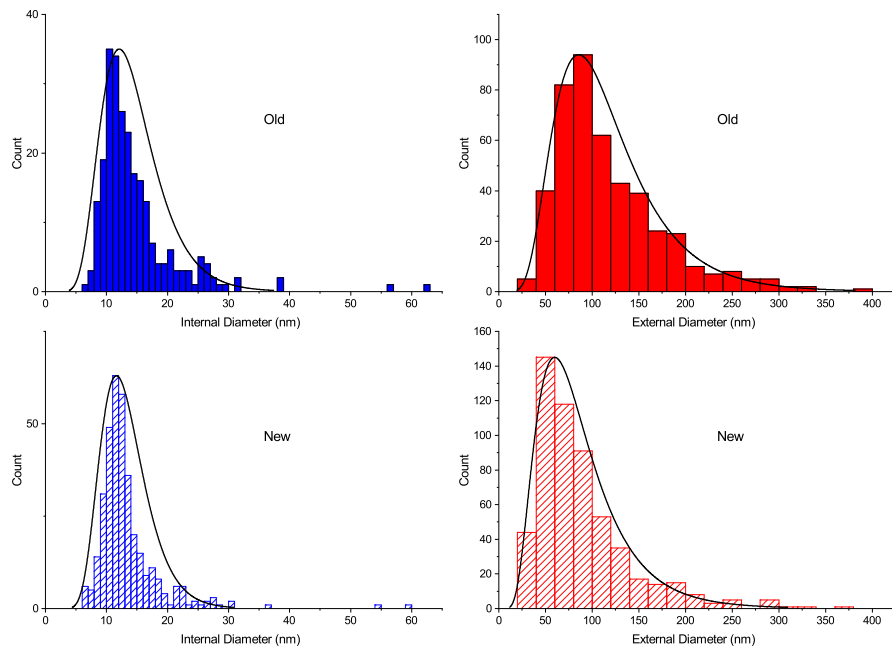
    %Creates an Array with data on the time of each acquisition
    T(j,:) = TimeElap;
    %Calculates time elapsed in seconds as a fraction of a Day
    DayFrac = TimeElap/86400;
    %Converts time elapsed in seconds to HH:MM:SS format
    HHMMSS = datestr(DayFrac, 'HH:MM:SS');
    %Compiles Tilde and HHMMSS into image text
    ImageText = [HHMMSS];
    %Snaps image from webcam selected
    img = snapshot(cam);
    %Combine image text and image into one image
    IMG = insertText(img, [10 10], ImageText, 'FontSize', 28, 'BoxOpacity', 0, 'TextColor', 'green');

    %Makes Filename
    Filename = num2str((j-1));
    %Writes each image to a file with the above set name
    imwrite(IMG, [Filename '.jpg']);
    %Displays images on subplot
    imshow(IMG);

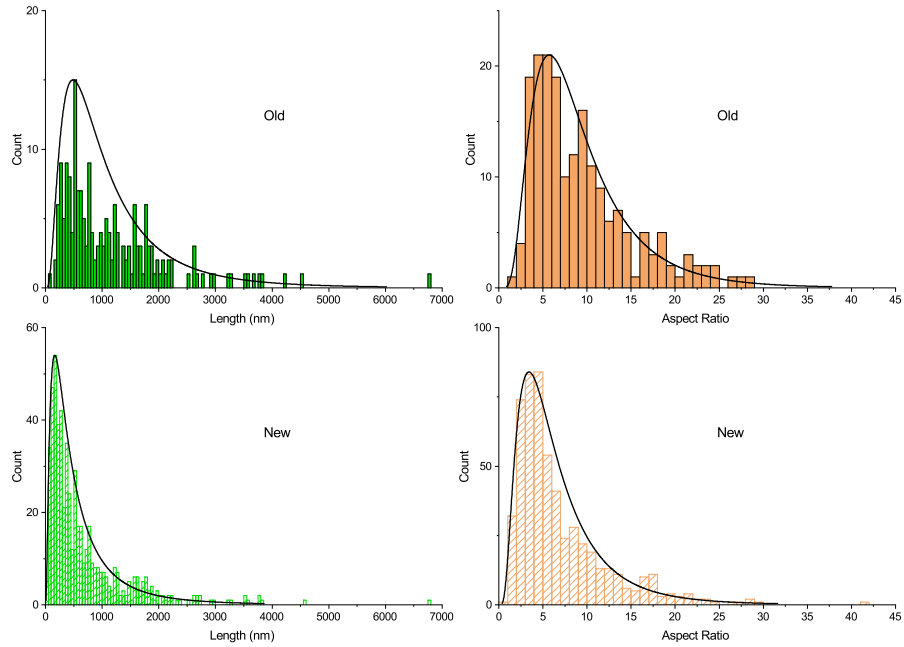
    %calculates avreage pause per frame since begining
    tAve = toc(tStart)/j;

end

%Writes time data to a text file
dlmwrite('Time_Data',T);
```



(a)



(b)

Figure A.4: Histograms and PDFs for the internal and external diameters (a), and lengths and aspect ratios (b) of HNTs measured in TEM images from the first (i.e. old) and second (i.e. new) sets of measurements

Code for fitting log-normal distributions to size data

This code takes a single column of data that has been imported into MATLAB by the user (e.g. “VarName1”) and fits the log-normal parameters μ (i.e. μ) and σ (i.e. σ) to the data, as well as the 95% confidence intervals of these values from the fit. A value of probability (y) is then calculated for each value of x, starting at “start”, then continuing at intervals of “step” until “stop” is reached. Start, step and stop are user-defined input parameters. Values of x and y can be exported for use in other software. Note that this code works in MATLAB 2016a, but not MATLAB 2019a.

```
%set 'data' to whatever name your input data has
data = VarName1;

%set the starting value, increment, and final value
%for the x axis in the logn plot

start = 0;
step = 0.01;
stop = 100;

%find mu and sigma of data, and 95% confidence
%intervals of both

[lognpar, conf] = lognfit(data);
mu = lognpar(1);
sigma = lognpar(2);

%sets x axis for logn plot

x = (start:step:stop);
%finds logn probability density function
y = lognpdf(x, mu, sigma);

%returns x and y as two columns

r = [x y]
pdf = r'
```

Code for automated image analysis

The following code identifies objects in TEM images of HNTs, fits them with ellipses, and filters them with the criteria outlined in section 2.6.4. It also returns values for circularity, and the ratios of, and differences between, the ellipse areas and object areas. The final image output is the original image with objects fitted with ellipses and indexed by object number.

```
%set image scale (input pixels/nm)
scale_pnm = 0.292;
scale = 1/scale_pnm;

% Read in image (must be in current folder).
Image = imread('HNTs_test_3.jpg');

% Convert image to greyscale.
I = rgb2gray(Image);

% Convert to binary with im2bw. Level is the threshold.
level = 0.6;
Ithresh = im2bw(I, level);

% Redraw the image with a square structuring element of 1 pixel.
se = strel('square', 1);
Imorph = imopen(Ithresh, se);

% Invert the binary image
Imorph = ~Imorph;

% Remove objects that cross the image borders
Imorph2 = imclearborder(Imorph, 8);

%turn into labelled image to allow ismember function to work later
labeled_Image = bwlabel(Imorph2, 8);
```

```

%Finds geometric properties of objects in the image
stats = regionprops(labeled_Image, 'Orientation', 'MajorAxisLength', 'MinorAxisLength', 'Eccentricity', 'Centroid',
'Area', 'Circularity');

%Define object properties, NB length and width being scaled to nm,
%area left as pixels
obj_Areas = [stats.Area]
obj_Ecc = [stats.Eccentricity]
obj_Width = [stats.MinorAxisLength]*scale
obj_Length = [stats.MajorAxisLength]*scale
obj_Circ = [stats.Circularity]

%Set filtering criteria, e.g. use minimum and maximum known tube
%dimensions obj_Width to be set using the distance in nm
allowableAreas = obj_Areas > 100;
allowableEccentricity = obj_Ecc > 0.7
allowableWidth = obj_Width < 500 & obj_Width > 20
keepTubes = find(allowableAreas & allowableEccentricity & allowableWidth);

%create image using only objects that fit the filtering criteria
keepTubesI = ismember(labeled_Image, keepTubes);

%create regionprops using only objects that already have been
%filtered
filtstats = regionprops(keepTubesI, 'Orientation', 'MajorAxisLength', 'MinorAxisLength', 'Eccentricity', 'Centroid',
'Area');

%find areas of ellipses, and the difference between
%ellipse and object area
for n = 1:length(filtstats)

    E_Area(n) = pi*[filtstats(n).MinorAxisLength]*[filtstats(n).MajorAxisLength]
    Empty = E_Area - [filtstats(n).Area]
    P_E_Space(n) = E_Area(n)/[filtstats(n).Area]

end

%Show original TEM image
figure, imshow(Image);

%hold to allow ellipses to be plotted without deleting image
hold on

%script for drawing ellipses
phi = linspace(0,2*pi,50);
cosphi = cos(phi);
sinphi = sin(phi);

for k = 1:length(filtstats)
    xbar = filtstats(k).Centroid(1);
    ybar = filtstats(k).Centroid(2);
    a = filtstats(k).MajorAxisLength/2;
    b = filtstats(k).MinorAxisLength/2;
    theta = pi*filtstats(k).Orientation/180;
    R = [ cos(theta)  sin(theta)
        -sin(theta)  cos(theta)];
    xy = [a*cosphi; b*sinphi];
    xy = R*xy;
    x = xy(1,:) + xbar;
    y = xy(2,:) + ybar;
    plot(x,y,'r','LineWidth',2);

    %plot the centroids of the ellipses
    centroids = cat(1, filtstats(k).Centroid);
    plot(centroids(:,1), centroids(:,2), 'r+');

    %Label each tube
    %shift label along x from centroid
    tex_x = xbar + 40;

    %turn obj num integer to text character
    label = int2str(k);
    text(tex_x, ybar, label, 'Color', 'y', 'fontSize', 28);

end

hold off

%Final dimensions of filtered objects in nm
Widths_nm = [filtstats.MinorAxisLength]*scale;
Lengths_nm = [filtstats.MajorAxisLength]*scale;
Aspect_R = Widths_nm/Lengths_nm;

```

Code for fitting the Beer-Lambert law to TEM images

This code was used to generate values of pixel intensity as a function of distance in two directions from a particles centre. The results were then fitted separately in the curve fitting app available with MATLAB. More specifically, the “Dooo” and “Intensity_o” (or “Diii” and “Intensity_i”, as appropriate) outputs from the MATLAB code were set as x and y in the curve fitting app.

```
%set image scale (input pixels/nm) (currently set to 1 since image scale
%is not known for the image)
scale_pnm = 1;
scale = 1/scale_pnm;

% Read in image (must be in current folder).
Image = imread('Single_Tube.jpg');

% Convert to greyscale.
I = rgb2gray(Image);

% Convert to binary with im2bw. Level is the threshold.
level = 0.6;
Ithresh = im2bw(I, level);

% Redraw the image with a square structuring element of 1 pixel.
se = strel('square', 1);
Imorph = imopen(Ithresh, se);

% Invert the binary image, as white pixels are the ones recognised as
% objects.
Imorph = ~Imorph;

% Remove objects that cross the image borders
Imorph2 = imclearborder(Imorph, 8);
Imorph3 = imfill(Imorph2, 'holes')

%turn into labelled image to allow ismember to work later
labeled_Image = bwlabel(Imorph3, 8);

%Finds geometric properties of objects in the image
stats = regionprops(labeled_Image, 'Orientation', 'MajorAxisLength', 'MinorAxisLength', 'Eccentricity',
'Centroid', 'Area');

%Define object properties, NB length and width being scaled to nm, area
%left as pixels
obj_Areas = [stats.Area]
obj_Ecc = [stats.Eccentricity]
obj_Width = [stats.MinorAxisLength]*scale
obj_Length = [stats.MajorAxisLength]*scale

%Set filtering criteria, e.g. use minimum and maximum known tube dimensions
%obj_Width to be set using the distance in nm
allowableAreas = obj_Areas > 1000;
allowableEccentricity = obj_Ecc > 0.7
allowableWidth = obj_Width < 500 & obj_Width > 50
keepTubes = find(allowableAreas & allowableEccentricity & allowableWidth);

%create image using only objects that fit the filtering criteria
keepTubesI = ismember(labeled_Image, keepTubes);

%Euclidean distance transform on the binary-inverted object
D = bwdist(~keepTubesI);

%Finds object skeleton
SK = bwskel(keepTubesI, 'MinBranchLength', 50);
%Distance transform of object skeleton
D_SK = bwdist(SK);
D_SK_Max = max(D_SK, [], 'all');

%Gives every pixel a direction away from the image skeleton
[Ig_Dm, Ig_Dd] = imgradient(D_SK, 'sobel');

%Finds the pixel furthest away from a 0 in the distance transform, i.e. the
%radius of a tube
D_Max = max(D, [], 'all');

%Find unique distances in the distance transform and the number of unique
%distances
D_U = unique(D);
DL = length(D_U);

%For loop finds the pixels corresponding to each distance in the distance
%transform and finds and averages their intensities in the original image.
%The distance from the centre, L, is taken from D_max.
for h = 1:DL

    %Finds distances in direction away from skeleton
    Dist_1 = find(D == D_U(h,1) & Ig_Dd < 0 & D_SK < ceil(D_Max));
    Dist_2 = find(D == D_U(h,1) & Ig_Dd > 0 & D_SK < ceil(D_Max));

    %This block handles data in direction 1
```

```

%
%Retrieves pixel intensities at a unique distance in the distance
%transformed image from the original image
Int_1 = Image(Dist_1);
%Averages all intensities at that distance
Mean_1(h) = mean(Int_1, 'all');
%Finds standard deviation of pixel intensity at that distance
Conv_1 = im2single(Int_1);
s_d_1(h) = std(Conv_1, 1, 'all', 'omitnan');
%Changes distances so minimum distance is now at the object centre
L_1(h) = -1*(D_U(h,1)-D_Max)*scale;
%Returns array of data (distance, intensity, std dev)
R_1 = [L_1; Mean_1; s_d_1];
%Transforms rows to columns for easy data handling
Results_1 = R_1';

%Repeats for direction 2
Int_2 = Image(Dist_2);
Mean_2(h) = mean(Int_2, 'all');
Conv_2 = im2single(Int_2);
s_d_2(h) = std(Conv_2, 1, 'all', 'omitnan');
L_2(h) = (D_U(h,1)-D_Max)*scale;
R_2 = [L_2; Mean_2; s_d_2];
Results_2 = R_2';

end

%Plots data in MATLAB figure for inspection (if desired)
P_d1 = Results_1(:,1)
P_I1 = Results_1(:,2)
P_d2 = Results_2(:,1)
P_I2 = Results_2(:,2)
figure, plot(P_d1, P_I1)
hold on
plot(P_d2, P_I2)
hold off

%Sets I_o
I_o = 200;
%Finds I_min to allow determination of R_i
I_min = min(Results_1(:,2));
%Determination of I_min
R_i_findlin = find(Results_1 == I_min);
[row,col] = ind2sub(size(Results_1), R_i_findlin);
R_i = Results_1(row,1);
%Determination of R_o
R_o = max(Results_1(:,1))
%Determination of k
k = (-0.5*log(I_min/I_o))/sqrt((R_o^2)-(R_i^2));

%Retrieve D from original image analysis code
D = Results_1(:,1);
D_U = unique(D);

%Find I vs. D for the tube walls
Intensity = Results_1(:,2);
Do = D < R_o & D > R_i
Doo = find(Doo == true);
Dooo = D(Doo);
Intensity_o = Intensity(Doo);

%Find I vs. D for tube interior
Di = D < R_i & D > 0;
Dii = find(Di == true);
Diii = D(Dii);
Intensity_i = Intensity(Dii);

%Calculates I for the fit using starting estimates of parameters
for h = 1:length(D);

    if D(h,1) > R_o
        Abs(h) = D(h,1)*0;

    elseif D(h,1) < R_o & D(h,1) > R_i
        Abs(h) = 2*k*R_o*sqrt((1-(D(h,1)/R_o)^2))

    else
        D(h,1) < R_i
        Abs(h) = 2*k*(R_o*sqrt((1-(D(h,1)/R_o)^2)) - R_i*sqrt((1-(D(h,1)/R_i)^2)))

    end

end

%Retrieves real values from the fit (ML automatically gives an i component
%to the fit).
Abs_real = real(Abs);
Abs_r = -1*Abs_real;
Abs_e = exp(Abs_r);

%Plots the BL function using the first estimates of parameters (plots over
%the original data)
I_fit = I_o*Abs_e;
figure, scatter(D,I_fit);
I_fit_col = I_fit';
F_D = [D;I_fit_col]
hold on
plot(P_d1, P_I1)

```

```
plot(P_d2, P_I2)  
hold off
```

A.2 Appendix to Chapter 3

A.2.1 General propagation of uncertainties

Propagation of uncertainties was carried out using the following general relationships:

If:

$$c = a + b \quad \text{or} \quad c = a - b \quad \text{etc.}$$

Then:

$$\delta_c^2 = \delta_a^2 + \delta_b^2$$

If:

$$c = ab \quad \text{or} \quad c = \frac{a}{b} \quad \text{etc.}$$

Then:

$$\left(\frac{\delta_c}{c}\right)^2 = \left(\frac{\delta_a}{a}\right)^2 + \left(\frac{\delta_b}{b}\right)^2$$

Here, c is a hypothetical variable calculated from two hypothetical measured values of a and b . The uncertainty in each variable is denoted δ , e.g. the uncertainty in b is δ_b .

In practice, propagation of uncertainties was done in several steps using a spreadsheet, rather than by simplifying an equation containing all of the relevant variables and uncertainties. These steps are summarised in the following sections.

A.2.2 Uncertainty in filler content determined by He pycnometry

The filler mass fraction in epoxy/HNT nanocomposites was determined from He pycnometry measurements using equations A.1 and A.2, which contain the variables explained in table A.1. Also included in the table are the densities of pure HNTs and the bulk epoxy resin polymer for reference.

$$\phi_f = \frac{\rho_s - \rho_b}{\rho_f - \rho_b} \quad (\text{A.1})$$

$$m_m = \frac{\phi_f \rho_f}{\rho_s} \quad (\text{A.2})$$

Equation A.2 can be derived as follows:

$$m_m = \frac{m_f}{m_s} = \frac{\rho_f V_f}{\rho_s V_s}$$

$$V_f = \phi_f V_s \quad \text{therefore} \quad m_m = \frac{\rho_f \phi_f V_s}{\rho_s V_s} = \frac{\rho_f \phi_f}{\rho_s}$$

Table A.1: Explanation of the variables contained in equations A.1 and A.2

Variable	Assignment	Value
ϕ_f	Volume fraction of filler	n/a
ρ_f	Density of filler (i.e. HNTs)	2.5479 ± 0.0022
ρ_b	Density of pure polymer	1.1884 ± 0.0002
ρ_s	Density of sample	n/a
m_m	Mass fraction of filler in sample	n/a
m_f	Mass of filler	n/a
m_s	Mass of sample	n/a
V_f	Volume of filler	n/a
V_s	Volume of sample	n/a

The uncertainty in the volume fraction of filler can be found by inputting the results of calculations A.3 and A.4 into equation A.5. The uncertainties in density are output by the pycnometer as the standard deviation of several measurements.

$$\delta_{(\rho_s - \rho_b)} = (\delta\rho_s^2 + \delta\rho_b^2)^{\frac{1}{2}} \quad (\text{A.3})$$

$$\delta_{(\rho_f - \rho_b)} = (\delta\rho_f^2 + \delta\rho_b^2)^{\frac{1}{2}} \quad (\text{A.4})$$

$$\delta_{\phi_f} = \phi_f \left(\left(\frac{\delta_{(\rho_s - \rho_b)}}{(\rho_s - \rho_b)} \right)^2 + \left(\frac{\delta_{(\rho_f - \rho_b)}}{(\rho_f - \rho_b)} \right)^2 \right)^{\frac{1}{2}} \quad (\text{A.5})$$

The uncertainty in the filler mass fraction is then given by equation A.6. When reporting filler fraction in wt%, δ_{m_m} simply needs to be multiplied by 100.

$$\delta_{m_m} = m_m \left(\left(\frac{\delta_{\phi_f}}{\phi_f} \right)^2 + \left(\frac{\delta_{\rho_f}}{\rho_f} \right)^2 + \left(\frac{\delta_{\rho_s}}{\rho_s} \right)^2 \right)^{\frac{1}{2}} \quad (\text{A.6})$$

A.2.3 Uncertainty in filler content determined by burn-off in a furnace

The initial filler content of a sample in which the resin had been burned off in a furnace was calculated using equation A.7, which contains the variables explained in table A.2.

$$\text{Filler mass fraction} = \frac{m_f - m_c + m_x}{lm_s} \quad (\text{A.7})$$

Table A.2: Explanation of the variables used in equation A.7

Variable	Assignment
m_f	The mass of the crucible + sample after heating.
m_c	The mass of the empty crucible.
m_x	The mass lost by the crucible lost during heating ($m_x = 0.00008m_c$).
m_s	The mass of the sample before heating.
l	The mass fraction of filler remaining after heating (for HNTs, this is 0.8580 ± 0.0006)

Equation A.8 gives the uncertainty in the mass lost by the crucible during heating. The uncertainty in the average mass fraction lost by the crucible is the standard deviation across several crucibles, and the uncertainty in m_c is the precision of the balance being used (either 0.01 g or 0.001 g).

$$\delta_{m_x} = m_x \left(\left(\frac{0.00003}{0.00008} \right)^2 + \left(\frac{\delta_{m_c}}{m_c} \right)^2 \right)^{\frac{1}{2}} \quad (\text{A.8})$$

The uncertainty in the mass remaining in the crucible after heating (denoted m_r) is given by equation A.9. The uncertainties δ_{m_f} and δ_{m_c} are equal, and are obtained from the precision of the balance being used.

$$\delta_{m_r} = (\delta_{m_f}^2 + \delta_{m_c}^2 + \delta_{m_x}^2)^{\frac{1}{2}} \quad (\text{A.9})$$

If one assumes that the mass remaining in the sample after heating is only from HNTs, then the mass of HNTs in the sample before heating (m_{HNTs}) can be given by equation A.10. The uncertainty in l is that obtained by propagating the precision of the TGA balance for the two measurements of mass required to work out the fraction of mass of HNTs remaining at 800 °C (i.e. initial mass, and mass at 800 °C). The uncertainty in m_{HNTs} is given by equation A.11.

$$m_{\text{HNTs}} = \frac{m_r}{l} \quad (\text{A.10})$$

$$\delta_{m_{\text{HNTs}}} = m_{\text{HNTs}} \left(\left(\frac{\delta_{m_r}}{m_r} \right)^2 + \left(\frac{0.0006}{0.08580} \right)^2 \right)^{\frac{1}{2}} \quad (\text{A.11})$$

The filler mass fraction in the sample, denoted m_m , can be simplified to equation A.12. The uncertainty in m_m is then given by equation A.13. Again, δ_{m_m} can be multiplied by 100 to give the uncertainty when filler fraction is being quoted in wt%.

$$m_m = \frac{m_{\text{HNTs}}}{m_s} \quad (\text{A.12})$$

$$\delta_{m_m} = m_m \left(\left(\frac{\delta_{m_{\text{HNTs}}}}{m_{\text{HNTs}}} \right)^2 + \left(\frac{\delta_{m_s}}{m_s} \right)^2 \right)^{\frac{1}{2}} \quad (\text{A.13})$$

Bibliography

- [1] B. Lecouvet, J. Horion, C. D'Haese, C. Bailly, and B. Nysten, "Elastic modulus of halloysite nanotubes," *Nanotechnology*, vol. 24, no. 10, p. 105704, 2013.
- [2] B. Lecouvet, M. Sclavons, S. Bourbigot, and C. Bailly, "Towards scalable production of polyamide 12/halloysite nanocomposites via water-assisted extrusion: Mechanical modeling, thermal and fire properties," *Polymers for Advanced Technologies*, vol. 25, no. 2, pp. 137–151, 2014.
- [3] C. Gommès, S. Blacher, K. Masenelli-varlot, C. Bossuot, E. Merae, and I. Nancy, "Image analysis characterization of multi-walled carbon nanotubes," *Carbon*, vol. 41, pp. 2561–2572, 2003.
- [4] S. Hillier, R. Brydson, E. Delbos, T. Fraser, N. Gray, H. Pendlowski, I. Phillips, J. Robertson, and I. Wilson, "Correlations among the mineralogical and physical properties of halloysite nanotubes (HNTs)," *Clay Minerals*, vol. 51, no. 3, pp. 325–350, 2016.
- [5] A. Yasmin, J. L. Abot, and I. M. Daniel, "Processing of clay/epoxy nanocomposites by shear mixing," *Scripta Materialia*, vol. 49, no. 1 SPEC., pp. 81–86, 2003.
- [6] C. W. Jones, *Applications of Hydrogen Peroxide and Derivatives*, p. 59. Royal Society of Chemistry, 1 ed., 1999.
- [7] P. Sun, G. Liu, D. Lv, X. Dong, J. Wu, and D. Wang, "Effective activation of halloysite nanotubes by piranha solution for amine modification via silane coupling chemistry," *RSC Adv.*, vol. 5, no. 65, pp. 52916–52925, 2015.
- [8] T. Klopogge, "Chemical bonding and electronic structures of the $\text{Al}_2\text{Si}_2\text{O}_5(\text{OH})_4$ polymorphs kaolinite, dickite, nacrite and halloysite by X-ray photoelectron spectroscopy," *Clay Science*, vol. 5, no. October, 2015.
- [9] B. Ellis, *Chemistry and Technology of Epoxy Resins*, p. 257. Springer-Science + Business Media, B.V., 1993.
- [10] V. Vahedi, P. Pasbakhsh, and S. P. Chai, "Toward high performance epoxy/halloysite nanocomposites: New insights based on rheological, curing, and impact properties," *Materials and Design*, vol. 68, pp. 42–53, 2015.
- [11] P. Sun, G. Liu, D. Lv, X. Dong, J. Wu, and D. Wang, "Simultaneous improvement in strength, toughness, and thermal stability of epoxy/halloysite nanotubes composites by interfacial modification," *Journal of Applied Polymer Science*, vol. 133, no. 13, 2016.

- [12] Y. Tang, S. Deng, L. Ye, C. Yang, Q. Yuan, J. Zhang, and C. Zhao, “Effects of unfolded and intercalated halloysites on mechanical properties of halloysite–epoxy nanocomposites,” *Composites Part A: Applied Science and Manufacturing*, vol. 42, no. 4, pp. 345–354, 2011.
- [13] H. Launay, C. M. Hansen, and K. Almdal, “Hansen solubility parameters for a carbon fiber/epoxy composite,” *Carbon*, vol. 45, pp. 2859–2865, dec 2007.
- [14] R. J. Young and P. A. Lovell, *Introduction to Polymers*, p. 384. CRC Press, 3 ed., 2011.
- [15] J. V. R. W. Jean-Pierre Pascault, Henry Sautereau, *Thermosetting Polymers*, pp. 1–4. Marcel Dekker, Inc., 2002.
- [16] B. Ellis, *Chemistry and Technology of Epoxy Resins*, p. 258. Springer-Science + Business Media, B.V., 1993.
- [17] T. A. Osswald and G. Menges, *Materials Science of Polymers for Engineers*, p. 7. Springer-Science + Business Media, B.V., 3 ed., 2010.
- [18] D. B. Miracle and S. L. Donaldson, *ASM Handbook, Volume 21: Composites*, pp. 3–18. ASM International, 2001.
- [19] R. J. Young and P. A. Lovell, *Introduction to Polymers*, pp. 600–602. CRC Press, 3 ed., 2011.
- [20] R. Rother, *Particulate-Filled Polymer Composites*, pp. 377–380. Rapra Technology Limited, 2 ed., 2003.
- [21] E. A. G. J. Brandrup, E. H. Immergut, *Polymer Handbook*, p. V/164. John Wiley and Sons, 4 ed., 1998.
- [22] M. Bar, R. Alagirusamy, and A. Das, “Flame retardant polymer composites,” *Fibers and Polymers*, vol. 16, no. 4, pp. 705–717, 2015.
- [23] P. R. Hornsby, “Fire Retardant Fillers for Polymers,” *International Materials Reviews*, vol. 46, no. 4, pp. 199–209, 2001.
- [24] B. Ellis, *Chemistry and Technology of Epoxy Resins*, p. 123. Springer-Science + Business Media, B.V., 1993.
- [25] D. B. Miracle and S. L. Donaldson, *ASM Handbook, Volume 21: Composites*, pp. 169–179. ASM International, 2001.
- [26] E. P. Plueddemann, *Composite Materials, Volume 6: Interfaces in Polymer Matrix Composites*, p. 2. Academic Press New York and London, 1974.
- [27] F. R. Jones, “A review of interphase formation and design in fibre-reinforced composites,” *Journal of Adhesion Science and Technology*, vol. 24, no. 1, pp. 171–202, 2010.
- [28] E. P. Plueddemann, *Composite Materials, Volume 6: Interfaces in Polymer Matrix Composites*, pp. 19–23. Academic Press New York and London, 1974.

- [29] M. Dey, J. M. Deitzel, J. W. Gillespie, and S. Schweiger, "Influence of sizing formulations on glass/epoxy interphase properties," *Composites Part A: Applied Science and Manufacturing*, vol. 63, pp. 59–67, 2014.
- [30] R. F. Minty, L. Yang, and J. L. Thomason, "The influence of hardener-to-epoxy ratio on the interfacial strength in glass fibre reinforced epoxy composites," *Composites Part A: Applied Science and Manufacturing*, vol. 112, no. May, pp. 64–70, 2018.
- [31] B. Ellis, *Chemistry and Technology of Epoxy Resins*, pp. 1–35. Springer-Science + Business Media, B.V., 1993.
- [32] B. Ellis, *Chemistry and Technology of Epoxy Resins*, pp. 72–80. Springer-Science + Business Media, B.V., 1993.
- [33] B. Ellis, *Chemistry and Technology of Epoxy Resins*, p. 270. Springer-Science + Business Media, B.V., 1993.
- [34] B. Ellis, *Chemistry and Technology of Epoxy Resins*, p. 2. Springer-Science + Business Media, B.V., 1993.
- [35] B. Ellis, *Chemistry and Technology of Epoxy Resins*, pp. 144–146. Springer-Science + Business Media, B.V., 1993.
- [36] B. Ellis, *Chemistry and Technology of Epoxy Resins*, pp. 290–297. Springer-Science + Business Media, B.V., 1993.
- [37] R. Rotheron, *Particulate-Filled Polymer Composites*, pp. 435–483. Rapra Technology Limited, 2 ed., 2003.
- [38] D. R. Paul and L. M. Robeson, "Polymer nanotechnology: Nanocomposites," *Polymer*, vol. 49, no. 15, pp. 3187–3204, 2008.
- [39] R. Kotsilkova, *Thermoset Nanocomposites for Engineering Applications*, pp. 1–3. Smithers Rapra Technology Limited, 2007.
- [40] C. O. Blattmann and S. E. Pratsinis, "Nanoparticle Filler Content and Shape in Polymer Nanocomposites," *KONA Powder and Particle Journal*, no. August, pp. 1–30, 2018.
- [41] M. A. Ashraf, W. Peng, Y. Zare, and K. Y. Rhee, "Effects of Size and Aggregation/Agglomeration of Nanoparticles on the Interfacial/Interphase Properties and Tensile Strength of Polymer Nanocomposites," *Nanoscale Research Letters*, vol. 13, 2018.
- [42] S. Kango, S. Kalia, A. Celli, J. Njuguna, Y. Habibi, and R. Kumar, "Progress in Polymer Science Surface modification of inorganic nanoparticles for development of organic – inorganic nanocomposites — A review," *Progress in Polymer Science*, vol. 38, no. 8, pp. 1232–1261, 2013.
- [43] J. Helmlinger, C. Sengstock, C. Groß-Heitfeld, C. Mayer, T. A. Schildhauer, M. Köller, and M. Epple, "Silver nanoparticles with different size and shape: equal cytotoxicity, but different antibacterial effects," *RSC Adv.*, vol. 6, no. 22, pp. 18490–18501, 2016.

- [44] J. A. De Volder, Michael F. L.; Tawfick, Sameh H.; Baughman, Ray H.; Hart, “Carbon nanotubes: present and future commercial applications,” *Science*, vol. 339, no. 6119, pp. 535–539, 2013.
- [45] F. Liu, P. Ming, and J. Li, “Ab initio calculation of ideal strength and phonon instability of graphene under tension,” *Physical Review B - Condensed Matter and Materials Physics*, vol. 76, no. 6, pp. 1–7, 2007.
- [46] S. Bergin, Z. Sun, D. Rickard, and P. Streich, “Multicomponent solubility parameters for single-walled carbon nanotube- solvent mixtures,” *Acs Nano*, vol. 3, no. 8, pp. 2340–2350, 2009.
- [47] M. Ellenbecker, S. J. Tsai, M. Jacobs, M. Riediker, T. Peters, S. Liou, A. Avila, and S. FossHansen, “The difficulties in establishing an occupational exposure limit for carbon nanotubes,” *Journal of Nanoparticle Research*, vol. 20, no. 5, 2018.
- [48] G. W. Beall and C. E. Powell, *Fundamentals of Polymer-Clay Nanocomposites*, pp. 1–3. Cambridge University Press, 2007.
- [49] G. W. Beall and C. E. Powell, *Fundamentals of Polymer-Clay Nanocomposites*, pp. 4–22. Cambridge University Press, 2007.
- [50] G. W. Beall and C. E. Powell, *Fundamentals of Polymer-Clay Nanocomposites*, pp. 68–74. Cambridge University Press, 2007.
- [51] A. Yasmin, J. L. Abot, and I. M. Daniel, “Processing of Clay/Epoxy Nanocomposites with A Three-Roll Mill Machine,” *Materials Research Society Symposium Proceedings*, vol. 740, pp. 75–80, 2002.
- [52] G. W. Beall and C. E. Powell, *Fundamentals of Polymer-Clay Nanocomposites*, pp. 35–46. Cambridge University Press, 2007.
- [53] B. Biswas, L. N. Warr, E. F. Hilder, N. Goswami, M. M. Rahman, J. G. Churchman, K. Vasilev, G. Pan, and R. Naidu, “Biocompatible functionalisation of nanoclays for improved environmental remediation,” *Chemical Society Reviews*, vol. 48, no. 14, pp. 3740–3770, 2019.
- [54] M. Kotal and A. K. Bhowmick, “Polymer nanocomposites from modified clays: Recent advances and challenges,” *Progress in Polymer Science*, vol. 51, pp. 127–187, 2015.
- [55] E. Joussein, S. Petit, J. Churchman, B. Theng, D. Righi, and B. Delvaux, “Halloysite clay minerals – a review,” *Clay Minerals*, vol. 40, no. 4, pp. 383–426, 2005.
- [56] P. Yuan, D. Tan, and F. Annabi-Bergaya, “Properties and applications of halloysite nanotubes: recent research advances and future prospects,” *Applied Clay Science*, vol. 112-113, pp. 75–93, 2015.
- [57] M. Liu, Z. Jia, D. Jia, and C. Zhou, “Recent advance in research on halloysite nanotubes-polymer nanocomposite,” *Progress in Polymer Science*, vol. 39, no. 8, pp. 1498–1525, 2014.

- [58] P. Pasbakhsh and G. J. Churchman, *Natural Mineral Nanotubes: Properties and Applications*, pp. 97–99. Apple Academic Press, 2015.
- [59] G. Kenne and C. Detellier, “Applied Clay Science Functional nanohybrid materials derived from kaolinite,” *Applied Clay Science*, vol. 130, pp. 33–39, 2016.
- [60] P. Pasbakhsh and G. J. Churchman, *Natural Mineral Nanotubes: Properties and Applications*, pp. 99–101. Apple Academic Press, 2015.
- [61] B. K. G. Theng, G. J. Churchman, J. S. Whitton, and G. G. C. Claridge, “Comparison of Intercalation Methods for Differentiating Halloysite From Kaolinite,” *Clays and Clay Minerals*, vol. 32, no. 4, pp. 249–258, 1984.
- [62] B. Singh, “Why Does Halloysite Roll?—A New Model,” *Clays and Clay Minerals*, vol. 44, no. 2, pp. 191–196, 1996.
- [63] F. Ferrante, N. Armata, and G. Lazzara, “Modeling of the Halloysite Spiral Nanotube,” *The Journal of Physical Chemistry C*, vol. 119, no. 29, pp. 16700–16707, 2015.
- [64] Y. Kuroda, K. Ito, K. Itabashi, and K. Kuroda, “One-step exfoliation of kaolinites and their transformation into nanoscrolls,” *Langmuir*, vol. 27, no. 5, pp. 2028–2035, 2011.
- [65] D. A. Prishchenko, E. V. Zenkov, V. V. Mazurenko, R. F. Fakhrullin, Y. M. Lvov, and V. Mazurenko, “Molecular dynamics of the halloysite nanotubes,” *Physical Chemistry Chemical Physics*, 2018.
- [66] S. Cuenot, C. Fretigny, S. Demoustier-Champagne, and B. Nysten, “Surface tension effect on the mechanical properties of nanomaterials measured by atomic force microscopy,” *Physical Review B*, vol. 69, no. 16, pp. –, 2004.
- [67] L. Reijnders, “Human health hazards of persistent inorganic and carbon nanoparticles,” *Journal of Materials Science*, vol. 47, no. 13, pp. 5061–5073, 2012.
- [68] Y. Ding, T. A. Kuhlbusch, M. Van Tongeren, A. S. Jiménez, I. Tuinman, R. Chen, I. L. Alvarez, U. Mikolajczyk, C. Nickel, J. Meyer, H. Kaminski, W. Wohlleben, B. Stahlmecke, S. Clavaguera, and M. Riediker, “Airborne engineered nanomaterials in the workplace—a review of release and worker exposure during nanomaterial production and handling processes,” *Journal of Hazardous Materials*, vol. 322, pp. 17–28, 2017.
- [69] Y. Lvov, W. Wang, L. Zhang, and R. Fakhrullin, “Halloysite Clay Nanotubes for Loading and Sustained Release of Functional Compounds,” *Advanced Materials*, vol. 28, no. 6, pp. 1227–1250, 2016.
- [70] V. Vergaro, E. Abdullayev, Y. M. Lvov, A. Zeitoun, R. Cingolani, R. Rinaldi, and S. Leporatti, “Cytocompatibility and uptake of halloysite clay nanotubes,” *Biomacromolecules*, vol. 11, no. 3, pp. 820–826, 2010.
- [71] M. Kryuchkova, A. Danilushkina, Y. Lvov, and R. Fakhrullin, “Evaluation of toxicity of nanoclays and graphene oxide in vivo: a *Paramecium caudatum* study,” *Environ. Sci.: Nano*, vol. 3, pp. 442–452, 2016.

- [72] Z. Long, Y. P. Wu, H. Y. Gao, J. Zhang, X. Ou, R. R. He, and M. Liu, "In vitro and in vivo toxicity evaluation of halloysite nanotubes," *Journal of Materials Chemistry B*, vol. 6, no. 44, pp. 7204–7216, 2018.
- [73] G. I. Fakhrullina, F. S. Akhatova, M. Lvov, and R. F. Fakhrullin, "Environmental Science Nano Toxicity of halloysite clay nanotubes in vivo : a *Caenorhabditis elegans* study †," *Environmental Science: Nano*, vol. 2, pp. 54–59, 2015.
- [74] P. Pasbakhsh and G. J. Churchman, *Natural Mineral Nanotubes: Properties and Applications*, pp. 421–423. Apple Academic Press, 2015.
- [75] X. Lai, M. Agarwal, Y. M. Lvov, C. Pachpande, K. Varahramyan, and F. A. Witzmann, "Proteomic profiling of halloysite clay nanotube exposure in intestinal cell co-culture," *Journal of Applied Toxicology*, vol. 33, no. 11, pp. 1316–1329, 2013.
- [76] R. Rong, Y. Zhang, Y. Zhang, Y. Hu, W. Yang, and X. Hu, "Inhibition of inhaled halloysite nanotube toxicity by trehalose through enhanced autophagic clearance of p62," *Nanotoxicology*, vol. 13, no. 3, pp. 354–368, 2019.
- [77] K. Archontogeorgis, P. Steiropoulos, A. Tzouvelekis, E. Nena, and D. Bouros, "Lung Cancer and Interstitial Lung Diseases: A Systematic Review," *Pulmonary Medicine*, vol. 2012, p. 11, 2012.
- [78] K. Steenland, "One agent, many diseases: Exposure-response data and comparative risks of different outcomes following silica exposure," *American Journal of Industrial Medicine*, vol. 48, no. 1, pp. 16–23, 2005.
- [79] A. J. Koivisto, A. B. Bluhme, K. I. Kling, A. S. Fonseca, E. Redant, F. Andrade, K. S. Hougaard, M. Krepker, O. S. Prinz, E. Segal, A. Holländer, K. A. Jensen, U. Vogel, and I. K. Koponen, "Occupational exposure during handling and loading of halloysite nanotubes – A case study of counting nanofibers," *NanoImpact*, vol. 10, no. April, pp. 153–160, 2018.
- [80] S. R. Levis and P. B. Deasy, "Use of coated microtubular halloysite for the sustained release of diltiazem hydrochloride and propranolol hydrochloride," *International Journal of Pharmaceutics*, vol. 253, pp. 145–157, 2003.
- [81] D. Tan, P. Yuan, F. Annabi-Bergaya, D. Liu, L. Wang, H. Liu, and H. He, "Loading and in vitro release of ibuprofen in tubular halloysite," *Applied Clay Science*, vol. 96, pp. 50–55, 2014.
- [82] L. Li, H. Fan, L. Wang, and Z. Jin, "Does halloysite behave like an inert carrier for doxorubicin?," *RSC Advances*, vol. 6, no. 59, pp. 54193–54201, 2016.
- [83] G. Cavallaro, G. Lazzara, M. Massaro, S. Milioto, R. Noto, F. Parisi, and S. Riela, "Biocompatible poly(N -isopropylacrylamide)-halloysite nanotubes for thermoresponsive curcumin release," *Journal of Physical Chemistry C*, vol. 119, no. 16, pp. 8944–8951, 2015.
- [84] M. S. Alkathiri, J. Palasuk, G. J. Eckert, J. A. Platt, and M. C. Bottino, "Halloysite nanotube incorporation into adhesive systems - effect on bond strength to human dentin," *Clinical Oral Investigations*, vol. 19, no. 8, pp. 1905–1912, 2015.

- [85] W. Wei, E. Abdullayev, A. Hollister, D. Mills, and Y. M. Lvov, "Clay Nanotube/Poly(methyl methacrylate) Bone Cement Composites with Sustained Antibiotic Release," *Macromolecular Materials and Engineering*, vol. 297, no. 7, pp. 645–653, 2012.
- [86] G. Cavallaro, G. Lazzara, S. Milioto, G. Palmisano, and F. Parisi, "Halloysite nanotube with fluorinated lumen: Non-foaming nanocontainer for storage and controlled release of oxygen in aqueous media," *Journal of Colloid and Interface Science*, vol. 417, pp. 66–71, 2014.
- [87] H. Jing, Y. Higaki, W. Ma, H. Wu, W. O. Yah, H. Otsuka, Y. M. Lvov, and A. Takahara, "Internally Modified Halloysite Nanotubes as Inorganic Nanocontainers for a Flame Retardant," *Chemistry Letters*, vol. 42, no. 2, pp. 121–123, 2013.
- [88] O. Owoseni, Y. Zhang, S. J. Adams, V. T. John, E. Nyankson, R. B. Gupta, J. He, G. L. McPherson, and A. Bose, "Release of surfactant cargo from interfacially-active halloysite clay nanotubes for oil spill remediation," *Langmuir*, vol. 30, no. 45, pp. 13533–13541, 2014.
- [89] S. M. Lee and D. Tiwari, "Organo and inorgano-organo-modified clays in the remediation of aqueous solutions: An overview," *Applied Clay Science*, vol. 59-60, pp. 84–102, 2012.
- [90] G. Kiani, "High removal capacity of silver ions from aqueous solution onto Halloysite nanotubes," *Applied Clay Science*, vol. 90, pp. 159–164, 2014.
- [91] W. He, Y. Chen, W. Zhang, C. Hu, J. Wang, and P. Wang, "Removal of UO₂²⁺ from aqueous solution using halloysite nanotube-Fe₃O₄ composite," *Korean Journal of Chemical Engineering*, vol. 32, no. 3, pp. 1–8, 2015.
- [92] J. Matusik and A. Wóscisło, "Enhanced heavy metal adsorption on functionalized nanotubular halloysite interlayer grafted with aminoalcohols," *Applied Clay Science*, vol. 100, pp. 50–59, 2014.
- [93] D. Bielska, A. Karewicz, T. Lachowicz, K. Berent, K. Szczubiałka, and M. Nowakowska, "Hybrid photosensitizer based on halloysite nanotubes for phenol-based pesticide photodegradation," *Chemical Engineering Journal*, vol. 262, pp. 125–132, 2015.
- [94] V. M. Abbasov, T. A. Mamedova, E. G. Ismailov, E. N. Askerova, K. S. Teyubov, N. V. Gasankhanova, and S. K. Alieva, "Catalytic production of olefins using natural halloysite nanotubes," *Catalysis in Industry*, vol. 6, no. 3, pp. 170–175, 2014.
- [95] P. Liu and M. Zhao, "Silver nanoparticle supported on halloysite nanotubes catalyzed reduction of 4-nitrophenol (4-NP)," *Applied Surface Science*, vol. 255, no. 7, pp. 3989–3993, 2009.
- [96] Q. Wei, R. Shi, D. Lu, and Z. Lei, "In situ formation of gold nanoparticles on magnetic halloysite nanotubes via polydopamine chemistry for highly effective and recyclable catalysis," *RSC Adv.*, vol. 6, no. 35, pp. 29245–29253, 2016.

- [97] M. Massaro, C. G. Colletti, G. Buscemi, S. Cataldo, S. Guernelli, G. Lazzara, L. F. Liotta, F. Parisi, A. Pettignano, and S. Riela, "Palladium nanoparticles immobilized on halloysite nanotubes covered by a multilayer network for catalytic applications," *New Journal of Chemistry*, vol. 42, no. 16, pp. 13938–13947, 2018.
- [98] B. Mu, W. Wang, J. Zhang, and A. Wang, "Superparamagnetic sandwich structured silver/halloysite nanotube/Fe₃O₄ nanocomposites for 4-nitrophenol reduction," *RSC Adv.*, vol. 4, no. 74, p. 39439, 2014.
- [99] S. Hillier, "The rise and rise of halloysite," *Clay Minerals*, vol. 51, no. 3, pp. 303–308, 2016.
- [100] E. Abdullayev and Y. Lvov, "Halloysite Clay Nanotubes for Controlled Release of Protective Agents," *ACS Nano*, vol. 2, no. 5, pp. 814–820, 2008.
- [101] E. Gutiérrez and F. Bono, "Review of industrial manufacturing capacity for fibre-reinforced polymers as prospective structural components in Shipping Containers," tech. rep., European Commission, 2013.
- [102] A. Jenifer, N. Rasana, and K. Jayanarayanan, "Synergistic effect of the inclusion of glass fibers and halloysite nanotubes on the static and dynamic mechanical, thermal and flame retardant properties of polypropylene," *Materials Research Express*, vol. 5, no. 6, 2018.
- [103] B. Guo, Q. Zou, Y. Lei, and D. Jia, "Structure and Performance of Polyamide 6/Halloysite Nanotubes Nanocomposites," *Polymer Journal*, vol. 41, no. 10, pp. 835–842, 2009.
- [104] U. A. Handge, K. Hedicke-Höchstötter, and V. Altstädt, "Composites of polyamide 6 and silicate nanotubes of the mineral halloysite: Influence of molecular weight on thermal, mechanical and rheological properties," *Polymer*, vol. 51, no. 12, pp. 2690–2699, 2010.
- [105] Y. Lin, K. M. Ng, C. M. Chan, G. Sun, and J. Wu, "High-impact polystyrene/halloysite nanocomposites prepared by emulsion polymerization using sodium dodecyl sulfate as surfactant," *Journal of Colloid and Interface Science*, vol. 358, no. 2, pp. 423–429, 2011.
- [106] D. Pedrazzoli, A. Pegoretti, R. Thomann, J. Kristöf, and J. Karger-Kocsis, "Toughening linear low-density polyethylene with halloysite nanotubes," *Polymer Composites*, vol. 36, pp. 869–883, may 2015.
- [107] J. Guo, J. Qiao, and X. Zhang, "Effect of an alkalized-modified halloysite on PLA crystallization, morphology, mechanical, and thermal properties of PLA/halloysite nanocomposites," *Journal of Applied Polymer Science*, vol. 44272, pp. 1–9, 2016.
- [108] T. V. Brantseva, S. O. Ilyin, I. Y. Gorbunova, S. V. Antonov, Y. M. Korolev, and M. L. Kerber, "Epoxy reinforcement with silicate particles: Rheological and adhesive properties - Part II: Characterization of composites with halloysite," *International Journal of Adhesion and Adhesives*, vol. 68, pp. 248–255, 2016.

- [109] T. Kim, S. Kim, D. K. Lee, B. Seo, and C.-S. Lim, "Surface treatment of halloysite nanotubes with sol-gel reaction for the preparation of epoxy composites," *RSC Adv.*, vol. 7, no. 75, pp. 47636–47642, 2017.
- [110] H. Vahabi, M. R. Saeb, K. Formela, and J. M. L. Cuesta, "Flame retardant epoxy/halloysite nanotubes nanocomposite coatings: Exploring low-concentration threshold for flammability compared to expandable graphite as superior fire retardant," *Progress in Organic Coatings*, vol. 119, no. December 2017, pp. 8–14, 2018.
- [111] S. Zeng, C. Reyes, J. Liu, P. A. Rodgers, S. H. Wentworth, and L. Sun, "Facile hydroxylation of halloysite nanotubes for epoxy nanocomposite applications," *Polymer (United Kingdom)*, vol. 55, no. 25, pp. 6519–6528, 2014.
- [112] Y. Ye, H. Chen, J. Wu, and L. Ye, "High impact strength epoxy nanocomposites with natural nanotubes," *Polymer*, vol. 48, no. 21, pp. 6426–6433, 2007.
- [113] Z. Vuluga, M. Corobea, C. Elizetxea, M. Ordonez, M. Ghiurea, V. Raditoiu, C. Nicolae, D. Florea, M. Iorga, R. Somoghi, and B. Trica, "Morphological and Tribological Properties of PMMA/Halloysite Nanocomposites," *Polymers*, vol. 10, no. 8, p. 816, 2018.
- [114] C. E. Tas, S. Hendessi, M. Baysal, and S. Unal, "Halloysite Nanotubes / Polyethylene Nanocomposites for Active Food Packaging Materials with Ethylene Scavenging and Gas Barrier Properties," *Food and Bioprocess Technology*, 2017.
- [115] P. Krishnaiah, C. T. Ratnam, and S. Manickam, "Development of silane grafted halloysite nanotube reinforced polylactide nanocomposites for the enhancement of mechanical, thermal and dynamic-mechanical properties," *Applied Clay Science*, vol. 135, pp. 583–595, 2017.
- [116] Y. Dong, J. Marshall, H. J. Haroosh, S. Mohammadzadehmoghadam, D. Liu, X. Qi, and K. T. Lau, "Polylactic acid (PLA)/halloysite nanotube (HNT) composite mats: Influence of HNT content and modification," *Composites Part A: Applied Science and Manufacturing*, vol. 76, pp. 28–36, 2015.
- [117] M. Raji, M. E. M. Mekhzoum, D. Rodrigue, A. el kacem Qaiss, and R. Bouhfid, "Effect of silane functionalization on properties of polypropylene/clay nanocomposites," *Composites Part B: Engineering*, vol. 146, no. April, pp. 106–115, 2018.
- [118] P. Kubade and P. Tambe, "Influence of halloysite nanotubes (HNTs) on morphology, crystallization, mechanical and thermal behaviour of PP/ABS blends and its composites in presence and absence of dual compatibilizer," *Composite Interfaces*, vol. 23, no. 5, pp. 433–451, 2016.
- [119] M. Du, B. Guo, and D. Jia, "Thermal stability and flame retardant effects of halloysite nanotubes on poly(propylene)," *European Polymer Journal*, vol. 42, no. 6, pp. 1362–1369, 2006.
- [120] Y. Guo, K. Yang, X. Zuo, Y. Xue, C. Marmorat, Y. Liu, C.-C. Chang, and M. H. Rafailovich, "Effects of clay platelets and natural nanotubes on mechanical properties and gas permeability of poly(lactic acid) nanocomposites," *Polymer*, vol. 83, pp. 246–259, 2016.

- [121] M. Wu and H.-X. Huang, “Structural Interpretations on Tensile Fracture Mechanism and Elongational Rheology of Poly(Vinylidene Fluoride)/Halloysite Nanotubes Nanocomposites,” *Polymer Engineering and Science*, 2017.
- [122] S. Deng, J. Zhang, L. Ye, and J. Wu, “Toughening epoxies with halloysite nanotubes,” *Polymer*, vol. 49, no. 23, pp. 5119–5127, 2008.
- [123] J. Zhang, D. Zhang, A. Zhang, Z. Jia, and D. Jia, “Dendritic polyamidoamine-grafted halloysite nanotubes for fabricating toughened epoxy composites,” *Iranian Polymer Journal (English Edition)*, vol. 22, no. 7, pp. 501–510, 2013.
- [124] K. Wang, L. Chen, J. Wu, M. L. Toh, C. He, and A. F. Yee, “Epoxy nanocomposites with highly exfoliated clay: Mechanical properties and fracture mechanisms,” *Macromolecules*, vol. 38, no. 3, pp. 788–800, 2005.
- [125] P. Vijayan P, A. Tanvir, M. Mrlik, M. Urbanek, and M. Al-Maadeed, “TiO₂/Halloysite hybrid filler reinforced epoxy nanocomposites,” *Polymer Composites*, 2018.
- [126] Z. Li, L. Liu, A. Jiménez González, and D.-Y. Wang, “Bioinspired polydopamine-induced assembly of ultrafine Fe(OH)₃ nanoparticles on halloysite toward highly efficient fire retardancy of epoxy resin via an action of interfacial catalysis,” *Polymer Chemistry*, vol. 8, no. 26, pp. 3926–3936, 2017.
- [127] P. Pasbakhsh, G. J. Churchman, and J. L. Keeling, “Characterisation of properties of various halloysites relevant to their use as nanotubes and microfibre fillers,” *Applied Clay Science*, vol. 74, pp. 47–57, 2013.
- [128] H. Liu and L. C. Brinson, “Reinforcing efficiency of nanoparticles : A simple comparison for polymer nanocomposites,” *Composites Science and Technology*, vol. 68, pp. 1502–1512, 2008.
- [129] E. Shchukina, D. Grigoriev, T. Sviridova, and D. Shchukin, “Comparative study of the effect of halloysite nanocontainers on autonomic corrosion protection of polyepoxy coatings on steel by salt-spray tests,” *Progress in Organic Coatings*, vol. 108, no. March, pp. 84–89, 2017.
- [130] K. Fujii, A. N. Nakagaito, H. Takagi, and D. Yonekura, “Sulfuric acid treatment of halloysite nanoclay to improve the mechanical properties of PVA/halloysite transparent composite films,” *Composite Interfaces*, vol. 21, no. 4, pp. 319–327, 2014.
- [131] H. Mo, K. Yang, S. Li, and P. Jiang, “High thermal conductivity and high impact strength of epoxy nanodielectrics with functionalized halloysite nanotubes,” *RSC Adv.*, vol. 6, no. 73, pp. 69569–69579, 2016.
- [132] T. V. Brantseva, S. O. Ilyin, I. Y. Gorbunova, S. V. Antonov, Y. M. Korolev, and M. L. Kerber, “Epoxy reinforcement with silicate particles: Rheological and adhesive properties - Part II: Characterization of composites with halloysite,” *International Journal of Adhesion and Adhesives*, vol. 68, pp. 248–255, 2016.
- [133] H. Kang, X. Liu, S. Zhang, and J. Li, “Functionalization of halloysite nanotubes (HNTs) via mussel-inspired surface modification and silane grafting for

- HNTs/soy protein isolate nanocomposite film preparation,” *RSC Adv.*, vol. 7, no. 39, pp. 24140–24148, 2017.
- [134] P. Zheng, Y. Du, and X. Ma, “Selective fabrication of iron oxide particles in halloysite lumen,” *Materials Chemistry and Physics*, vol. 151, pp. 14–17, 2015.
- [135] R. T. D. Silva, P. Pasbakhsh, K. L. Goh, and L. Mishnaevsky, “3-D computational model of poly (lactic acid)/ halloysite nanocomposites : Predicting elastic properties and stress analysis,” *Polymer*, vol. 55, no. 24, pp. 6418–6425, 2014.
- [136] Z. Luo, H. Song, X. Feng, M. Run, H. Cui, L. Wu, J. Gao, and Z. Wang, “Liquid crystalline phase behavior and sol-gel transition in aqueous halloysite nanotube dispersions,” *Langmuir*, vol. 29, pp. 12358–12366, 2013.
- [137] W. Stumm and G. F. Lee, “The chemistry of aqueous iron,” *Schweizerische Zeitschrift fuer Hydrologie*, vol. 22, no. 1, pp. 295–319, 1960.
- [138] S. C. Pang, S. F. Chin, and M. A. Anderson, “Redox equilibria of iron oxides in aqueous-based magnetite dispersions: Effect of pH and redox potential,” *Journal of Colloid and Interface Science*, vol. 311, no. 1, pp. 94–101, 2007.
- [139] S. Gårdebjer, M. Andersson, J. Engström, P. Restorp, M. Persson, and A. Larsson, “Using Hansen solubility parameters to predict the dispersion of nano-particles in polymeric films,” *Polym. Chem.*, vol. 7, no. 9, pp. 1756–1764, 2016.
- [140] J. K. Whitmer and E. Luijten, “Sedimentation of aggregating colloids,” *Journal of Chemical Physics*, vol. 134, no. 3, pp. 1–10, 2011.
- [141] C. M. Hansen, “The Three Dimensional Solubility Parameter and Solvent Diffusion Coefficient. Their Importance in Surface Coating Formulation,” *J. Paint Technology*, p. 104, 1967.
- [142] J. B. Petersen, J. Meruga, J. S. Randle, W. M. Cross, and J. J. Kellar, “Hansen solubility parameters of surfactant-capped silver nanoparticles for ink and printing technologies,” *Langmuir*, vol. 30, no. 51, pp. 15514–15519, 2014.
- [143] S. H. Wang, J. H. Liu, C. T. Pai, C. W. Chen, P. T. Chung, A. S. T. Chiang, and S. J. Chang, “Hansen solubility parameter analysis on the dispersion of zirconia nanocrystals,” *Journal of Colloid and Interface Science*, vol. 407, pp. 140–147, 2013.
- [144] J. N. Israelachvili, *Intermolecular and Surface Forces*, p. 299. Elsevier Academic Press, 3 ed., 2011.
- [145] J. N. Israelachvili, *Intermolecular and Surface Forces*, p. 292. Elsevier Academic Press, 3 ed., 2011.
- [146] J. N. Israelachvili, *Intermolecular and Surface Forces*, pp. 326–327. Elsevier Academic Press, 3 ed., 2011.
- [147] J. N. Israelachvili, *Intermolecular and Surface Forces*, p. 291. Elsevier Academic Press, 3 ed., 2011.

- [148] P. Moulin and H. Roques, "Zeta potential measurement of calcium carbonate," *Journal of Colloid and Interface Science*, vol. 261, no. 1, pp. 115–126, 2003.
- [149] Y. Joo, J. H. Sim, Y. Jeon, S. U. Lee, and D. Sohn, "Opening and blocking the innerpores of halloysite.," *Chemical communications (Cambridge, England)*, vol. 49, no. 40, pp. 4519–21, 2013.
- [150] R. K. Iler, *The Chemistry of Silica: Solubility, Polymerisation, Colloid and Surface Properties, and Biochemistry*, p. 356. John Wiley and Sons, Inc., 1979.
- [151] P. Atkins and J. de Paula, *Atkins' Physical Chemistry*, pp. 700–702. Oxford University Press, ninth ed., 2010.
- [152] S. Fawcett, T. G. Needham, F. Crowder, C. Kabekkodu, "No Title," in *Proceedings of the 10th National Conference on X-ray Diffraction and ICDD Workshop*, (Shanghai), pp. 1–3, 2009.
- [153] R. M. Carr, "Intercalation of salts in halloysite," *Clays and Clay Minerals*, vol. 26, no. 2, pp. 144–152, 1978.
- [154] S. W. P. W. Jonathan Clayden, Nick Greeves, *Organic Chemistry*, pp. 65–69. Oxford University Press, 2009.
- [155] E. Abdullayev, A. Joshi, W. Wei, Y. Zhao, and Y. Lvov, "Enlargement of halloysite clay nanotube lumen by selective etching of aluminum oxide," *ACS Nano*, vol. 6, no. 8, pp. 7216–7226, 2012.
- [156] P. Yuan, P. D. Southon, Z. Liu, M. E. R. Green, J. M. Hook, S. J. Antill, and C. J. Kepert, "Functionalization of halloysite clay nanotubes by grafting with 3-aminopropyltriethoxysilane," *Journal of Physical Chemistry C*, vol. 112, no. 40, pp. 15742–15751, 2008.
- [157] J. Madejová, "FTIR techniques in clay mineral studies," *Vibrational Spectroscopy*, vol. 31, no. 1, pp. 1–10, 2003.
- [158] E. Limpert, W. a. Stahel, and M. Abbt, "Log-normal Distributions across the Sciences: Keys and Clues," *BioScience*, vol. 51, no. 5, p. 341, 2001.
- [159] F. Vogt, "A self-guided search for good local minima of the sum-of-squared-error in nonlinear least squares regression," *Journal of Chemometrics*, vol. 29, no. 2, pp. 71–79, 2015.
- [160] A. N. Spiess and N. Neumeyer, "An evaluation of R2 as an inadequate measure for nonlinear models in pharmacological and biochemical research: A Monte Carlo approach," *BMC Pharmacology*, vol. 10, pp. 1–11, 2010.
- [161] "Evaluating Goodness of Fit." <https://uk.mathworks.com/help/curvefit/evaluating-goodness-of-fit.html>. Accessed: 2019-09-02.
- [162] P. Gans, *Data Fitting in the Chemical Sciences*, pp. 124–125. John Wiley and Sons, 1992.

- [163] M. Liu, B. Guo, M. Du, Y. Lei, and D. Jia, "Natural inorganic nanotubes reinforced epoxy resin nanocomposites," *Journal of Polymer Research*, vol. 15, no. 3, pp. 205–212, 2008.
- [164] R. F. Thompson, M. Walker, C. A. Siebert, S. P. Muench, and N. A. Ranson, "An introduction to sample preparation and imaging by cryo-electron microscopy for structural biology," *Methods*, vol. 100, pp. 3–15, 2016.
- [165] O. Glatter and O. Kratky, *Small Angle X-ray Scattering*, pp. 3–7. Academic Press, 1982.
- [166] O. Glatter and O. Kratky, *Small Angle X-ray Scattering*, p. 21. Academic Press, 1982.
- [167] H. Schnablegger and Y. Singh, *The SAXS Guide*, p. 24. Anton Parr GmbH, 4 ed., 2017.
- [168] H. Schnablegger and Y. Singh, *The SAXS Guide*, p. 30. Anton Parr GmbH, 4 ed., 2017.
- [169] H. Schnablegger and Y. Singh, *The SAXS Guide*, pp. 12–13. Anton Parr GmbH, 4 ed., 2017.
- [170] G. Cavallaro, L. Chiappisi, P. Pasbakhsh, M. Gradzielski, and G. Lazzara, "Applied Clay Science A structural comparison of halloysite nanotubes of different origin by Small- Angle Neutron Scattering (SANS) and Electric Birefringence," *Applied Clay Science*, no. August, pp. 0–1, 2017.
- [171] S. Zhang, H. Yang, and L. Singh, "Dynamic Light Scattering Measurement of Nanometer Particles in Liquids," *Journal of Nanoparticle Research*, vol. 2, no. 2, pp. 123–131, 2000.
- [172] T. Liu and Z. Xiao, "Dynamic light scattering of rigid rods - A universal relationship on the apparent diffusion coefficient as revealed by numerical studies and its use for rod length determination," *Macromolecular Chemistry and Physics*, vol. 213, no. 16, pp. 1697–1705, 2012.
- [173] M. Massaro, S. Riela, C. Baiamonte, J. L. J. Blanco, C. Giordano, P. Lo Meo, S. Milioto, R. Noto, F. Parisi, G. Pizzolanti, and G. Lazzara, "Dual drug-loaded halloysite hybrid-based glycocluster for sustained release of hydrophobic molecules," *RSC Adv.*, vol. 6, no. 91, pp. 87935–87944, 2016.
- [174] S. Jafarzadeh, V. Haddadi-Asl, and H. Roghani-Mamaqani, "Nanofibers of poly (hydroxyethyl methacrylate)-grafted halloysite nanotubes and polycaprolactone by combination of RAFT polymerization and electrospinning," *Journal of Polymer Research*, vol. 22, no. 7, p. 123, 2015.
- [175] M. Massaro, C. G. Colletti, G. Lazzara, S. Guernelli, R. Noto, and S. Riela, "Synthesis and Characterization of Halloysite-Cyclodextrin Nanosponges for Enhanced Dyes Adsorption," *ACS Sustainable Chemistry and Engineering*, vol. 5, no. 4, pp. 3346–3352, 2017.

- [176] Y. Joo, Y. Jeon, S. U. Lee, J. H. Sim, J. Ryu, S. Lee, H. Lee, and D. Sohn, "Aggregation and stabilization of carboxylic acid functionalized halloysite nanotubes (HNT-COOH)," *Journal of Physical Chemistry C*, vol. 116, pp. 18230–18235, aug 2012.
- [177] P. P. Vijayan, Y. M. Hany El-Gawady, and M. A. S. Al-Maadeed, "Halloysite Nanotube as Multifunctional Component in Epoxy Protective Coating," *Industrial and Engineering Chemistry Research*, vol. 55, no. 42, pp. 11186–11192, 2016.
- [178] M. Liu, B. Guo, M. Du, X. Cai, and D. Jia, "Properties of halloysite nanotube-epoxy resin hybrids and the interfacial reactions in the systems," *Nanotechnology*, vol. 18, no. 45, 2007.
- [179] M. Kim, S. Kim, T. Kim, D. K. Lee, B. Seo, and C.-s. Lim, "Mechanical and Thermal Properties of Epoxy Composites Containing Zirconium Oxide Impregnated Halloysite Nanotubes," *Coatings*, vol. 7, no. 12, p. 231, 2017.
- [180] P. P. Vijayan, Y. M. H. El-Gawady, and M. A. S. Al-Maadeed, "A comparative study on long term stability of self-healing epoxy coating with different inorganic nanotubes as healing agent reservoirs," *Express Polymer Letters*, vol. 11, no. 11, pp. 863–872, 2017.
- [181] J. Zhang, D. Zhang, a. Zhang, Z. Jia, and D. Jia, "Poly (methyl methacrylate) grafted halloysite nanotubes and its epoxy acrylate composites by ultraviolet curing method," *Journal of Reinforced Plastics and Composites*, vol. 32, no. 10, pp. 713–725, 2013.
- [182] T. J. Mason, "Ultrasound in synthetic organic chemistry," *Chemical Society Reviews*, vol. 26, no. 6, pp. 443–451, 1997.
- [183] D. Victor, A. Ceretti, L. Caetano, M. Carmo, and D. J. Carastan, "The Role of Dispersion Technique and Type of Clay on the Mechanical Properties of Clay / Epoxy Composites," *Macromolecular Symposia*, vol. 1800055, pp. 1–10, 2019.
- [184] Y. Li, H. Zhang, E. Bilotti, and T. Peijs, "Optimization of Three-Roll Mill Parameters for In-Situ Exfoliation of Graphene," *MRS Advances*, vol. 1, no. 19, pp. 1389–1394, 2016.
- [185] R. Rong, X. Xu, S. Zhu, B. Li, X. Wang, and K. Tang, "Facile preparation of homogeneous and length controllable halloysite nanotubes by ultrasonic scission and uniform viscosity centrifugation," *Chemical Engineering Journal*, vol. 291, pp. 20–29, 2016.
- [186] B. Ellis, *Chemistry and Technology of Epoxy Resins*, p. 3. Springer-Science + Business Media, B.V., 1993.
- [187] S. Knox, *A Fundamental Understanding of the Factors Controlling the Chemical Performance of Model Polymer Networks*. PhD thesis, The University of Sheffield, 2018.
- [188] N. Jouault, F. Dalmas, F. Boue, and J. Jestin, "Multiscale characterization of filler dispersion and origins of mechanical reinforcement in model nanocomposites," *Polymer*, vol. 53, no. 3, pp. 761–775, 2012.

- [189] N. Jouault, D. Zhao, and S. K. Kumar, "Role of casting solvent on nanoparticle dispersion in polymer nanocomposites," *Macromolecules*, vol. 47, no. 15, pp. 5246–5255, 2014.
- [190] G. W. Beall and C. E. Powell, *Fundamentals of Polymer-Clay Nanocomposites*, pp. 23–27. Cambridge University Press, 2007.
- [191] E. J. Vandenberg, "Epoxide Polymers: Synthesis, Stereochemistry, Structure, and Mechanism*," *Journal of Polymer Science Part A*, vol. 7, no. 1462, pp. 525–567, 1969.
- [192] P. Pustkova, J. M. Hutchinson, F. Roman, and S. Montserrat, "Homopolymerization Effects in Polymer Layered Silicate Nanocomposites Based Upon Epoxy Resin: Implications for Exfoliation," *Journal of Applied Polymer Science*, vol. 114, no. 2, pp. 1040–1047, 2009.
- [193] A. L. Motyka, "An Introduction to Rheology with an Emphasis on Application to Dispersions," *Journal of Chemical Education*, vol. 73, no. 4, p. 374, 2009.
- [194] R. Wagener and T. J. Reisinger, "A rheological method to compare the degree of exfoliation of nanocomposites," *Polymer*, vol. 44, no. 24, pp. 7513–7518, 2003.
- [195] D. J. Carastan, "Private communication," 2019.
- [196] R. J. Young and P. A. Lovell, *Introduction to Polymers*, p. 300. CRC Press, 3 ed., 2011.
- [197] M. R. Loos, L. A. F. Coelho, S. H. Pezzin, and S. C. Amico, "The effect of acetone addition on the properties of epoxy," *Polímeros*, vol. 18, no. 1, pp. 76–80, 2008.
- [198] G. W. Beall and C. E. Powell, *Fundamentals of Polymer-Clay Nanocomposites*, pp. 49–51. Cambridge University Press, 2007.
- [199] G. W. Beall and C. E. Powell, *Fundamentals of Polymer-Clay Nanocomposites*, p. 56. Cambridge University Press, 2007.
- [200] H.-w. He, W. Huang, and F. Gao, "International Journal of Polymer Analysis and Comparison of four methods for determining fiber content of carbon fiber / epoxy composites," *International Journal of Polymer Analysis and Characterization*, vol. 21, no. 3, pp. 251–258, 2016.
- [201] N. Grassie, M. I. Guy, and N. H. Tennent, "Degradation of epoxy polymers: Part 4—Thermal degradation of bisphenol-A diglycidyl ether cured with ethylene diamine," *Polymer Degradation and Stability*, vol. 14, no. 2, pp. 125–137, 2003.
- [202] J. H. Petropoulos, K. Tsimillis, C. Savvakis, and V. Havredaki, "Simple sensitive techniques for absolute and differential helium pycnometry," *Journal of Physics E: Scientific Instruments*, vol. 16, no. 11, pp. 1112–1115, 1983.
- [203] R. J. Young and P. A. Lovell, *Introduction to Polymers*, p. 384. CRC Press, 3 ed., 2011.

- [204] J. Jancar, J. F. Douglas, F. W. Starr, S. K. Kumar, P. Cassagnau, A. J. Lesser, S. S. Sternstein, and M. J. Buehler, "Current issues in research on structure-property relationships in polymer nanocomposites," *Polymer*, vol. 51, no. 15, pp. 3321–3343, 2010.
- [205] "Plastics – determination of flexural properties," standard, British Standards Institution, London, England, 2013.
- [206] V. Nigam, D. K. Setua, G. N. Mathur, and K. K. Kar, "Epoxy-montmorillonite clay nanocomposites: Synthesis and characterization," *Journal of Applied Polymer Science*, vol. 93, no. 5, pp. 2201–2210, 2004.
- [207] Y. Zhou, F. Pervin, M. A. Biswas, V. K. Rangari, and S. Jeelani, "Fabrication and characterization of montmorillonite clay-filled SC-15 epoxy," *Materials Letters*, vol. 60, no. 7, pp. 869–873, 2006.
- [208] H. Ishida and G. Kumar, *Molecular Characterization of Composite Interfaces*, pp. 2–5. Plenum Press, 1985.
- [209] C.J.Brinker, "Hydrolysis and Condensation of Silicates: Effects on Structure," *Journal of Non-Crystalline Solids*, vol. 100, no. 1-3, pp. 31–50, 1988.
- [210] G. Tesoro and Yulong Wu, "Silane coupling agents: the role of the organofunctional group," *Journal of Adhesion Science and Technology*, vol. 5, no. 10, pp. 771–784, 1991.
- [211] M. J. Zhu, M. Z. Lerum, and W. Chen, "How To Prepare Reproducible, Homogeneous, and Hydrolytically Stable Aminosilane-Derived Layers on Silica," *Langmuir*, vol. 28, no. 1, pp. 416–423, 2012.
- [212] R. K. Iler, *The Chemistry of Silica: Solubility, Polymerisation, Colloid and Surface Properties, and Biochemistry*, pp. 648–650. John Wiley and Sons, Inc., 1979.
- [213] H. Ishida and G. Kumar, *Molecular Characterization of Composite Interfaces*, pp. 34–35. Plenum Press, 1985.
- [214] L. Y. Yu, H. M. Shen, and Z. L. Xu, "PVDF–TiO₂ Composite Hollow Fiber Ultrafiltration Membranes Prepared by TiO₂ Sol–Gel Method and Blending Method," *Journal of Applied Physics*, vol. 113, pp. 1763–1772, 2009.
- [215] Y. Zhang, Y. Xie, A. Tang, Y. Zhou, J. Ouyang, and H. Yang, "Precious-Metal Nanoparticles Anchored onto Functionalized Halloysite Nanotubes," *Industrial & Engineering Chemistry Research*, vol. 53, no. 13, pp. 5507–5514, 2014.
- [216] S. Jana, S. Das, C. Ghosh, A. Maity, and M. Pradhan, "Halloysite Nanotubes Capturing Isotope Selective Atmospheric CO₂," *Scientific Reports*, vol. 5, pp. 1–8, 2015.
- [217] N. Nishiyama, R. Shick, and H. Ishida, "Adsorption Behavior of a Silane Coupling Agent on Colloidal Silica Studied by Gel Permeation Chromatography Determination of Chemisorbed Amount of Silane onto Colloidal Silica Surface," *Journal of Colloid and Interface Science*, vol. 143, no. 1, pp. 146–156, 1990.

- [218] M. Albdiry and B. Yousif, "Morphological structures and tribological performance of unsaturated polyester based untreated/silane-treated halloysite nanotubes," *Materials & Design*, vol. 48, pp. 68–76, 2013.
- [219] Q. Chen, Y. Zhao, W. Wu, T. Xu, and H. Fong, "Fabrication and evaluation of Bis-GMA/TEGDMA dental resins/composites containing halloysite nanotubes," *Dental Materials*, vol. 28, no. 10, pp. 1071–1079, 2012.
- [220] H. Zhang, X. Zhu, Y. Wu, H. Song, and X. Ba, "High-efficiency grafting of halloysite nanotubes by using π -conjugated polyfluorenes via "click" chemistry," *Journal of Materials Science*, pp. 4387–4395, 2015.
- [221] "Piranha solution explosions." <https://cenblog.org/the-safety-zone/2015/01/piranha-solution-explosions/>. Accessed: 2019-09-16.
- [222] "Piranha solution." <https://www.chemistryworld.com/podcasts/piranha-solution/3007809.article>. Accessed: 2019-09-16.
- [223] C. W. Jones, *Applications of Hydrogen Peroxide and Derivatives*, pp. 245–251. Royal Society of Chemistry, 1 ed., 1999.
- [224] C. W. Jones, *Applications of Hydrogen Peroxide and Derivatives*, pp. 117–144. Royal Society of Chemistry, 1 ed., 1999.
- [225] K. Shirai, Y. Yoshida, Y. Nakayama, M. Fujitani, H. Shintani, K. Wakasa, M. Okazaki, J. Snauwaert, and B. Van Meerbeek, "Assessment of decontamination methods as pretreatment of silanization of composite glass fillers," *Journal of Biomedical Materials Research*, vol. 53, no. 3, pp. 204–210, 2000.
- [226] K. J. Seu, A. P. Pandey, F. Haque, E. A. Proctor, A. E. Ribbe, and J. S. Hovis, "Effect of surface treatment on diffusion and domain formation in supported lipid bilayers," *Biophysical Journal*, vol. 92, no. 7, pp. 2445–2450, 2007.
- [227] P. Frantz and S. Granick, "Surface Preparation of Silicon for Polymer Adsorption Studies," *Langmuir*, vol. 8, no. 4, pp. 1176–1182, 1992.
- [228] R. K. Iler, *The Chemistry of Silica: Solubility, Polymerisation, Colloid and Surface Properties, and Biochemistry*, pp. 40–42. John Wiley and Sons, Inc., 1979.
- [229] R. D. White, D. V. Bavykin, and F. Walsh, "The stability of halloysite nanotubes in acidic and alkaline aqueous suspensions," *Nanotechnology*, vol. 23, p. 065705, 2012.
- [230] A. B. Zhang, L. Pan, H. Y. Zhang, S. T. Liu, Y. Ye, M. S. Xia, and X. G. Chen, "Effects of acid treatment on the physico-chemical and pore characteristics of halloysite," *Colloids and Surfaces A: Physicochemical and Engineering Aspects*, vol. 396, pp. 182–188, 2012.
- [231] H. Ishida and G. Kumar, *Molecular Characterization of Composite Interfaces*, p. 27. Plenum Press, 1985.
- [232] J. N. Israelachvili, *Intermolecular and Surface Forces*, pp. 201–203. Elsevier Academic Press, 3 ed., 2011.

- [233] J. N. Israelachvili, *Intermolecular and Surface Forces*, pp. 434–441. Elsevier Academic Press, 3 ed., 2011.
- [234] A. F. Stalder, G. Kulik, D. Sage, L. Barbieri, and P. Hoffmann, “A snake-based approach to accurate determination of both contact points and contact angles,” *Colloids and Surfaces A: Physicochemical and Engineering Aspects*, vol. 286, no. 1-3, pp. 92–103, 2006.
- [235] L. A. Savaş and S. Savaş, “Interrelation between Contact Angle and Interlayer Spacing of Montmorillonite Clay Used in Polymer Nanocomposites,” *Polymers and Polymer Composites*, vol. 21, no. 3, pp. 129–132, 2018.
- [236] A. Pegoretti, A. Dorigato, M. Brugnara, and A. Penati, “Contact angle measurements as a tool to investigate the filler-matrix interactions in polyurethane-clay nanocomposites from blocked prepolymer,” *European Polymer Journal*, vol. 44, no. 6, pp. 1662–1672, 2008.
- [237] P. Bhagabati, T. K. Chaki, and D. Khastgir, “One-Step in Situ Modification of Halloysite Nanotubes: Augmentation in Polymer–Filler Interface Adhesion in Nanocomposites,” *Industrial & Engineering Chemistry Research*, vol. 54, no. 26, pp. 6698–6712, 2015.
- [238] K. Sarah and H. Ulrich, “Short timescale wetting and penetration on porous sheets measured with ultrasound, direct absorption and contact angle,” *RSC Advances*, vol. 8, no. 23, pp. 12861–12869, 2018.
- [239] G. Liu, “Private communication,” 2019.
- [240] “Pore Size Chart for Different types of filtration.” <https://www.repligen.com/resources/knowledge-base/references/mabselectsure-1>. Accessed: 2019-08-22.
- [241] M. R. Schilling, “Effects of Sample Size and Packing in the Thermogravimetric Analysis of Calcium Montmorillonite STx-1,” *Clays and Clay Minerals*, vol. 38, no. 5, pp. 556–558, 1990.
- [242] “Standard test method for thermal stability by thermogravimetry,” standard, ASTM International, West Consohocken, PA, United States, 2017.
- [243] D. Briggs and M. P. Seah, *Practical Surface Analysis, Volume 1: Auger and X-ray Photoelectron Spectroscopy*, p. 112. John Wiley & Sons, second ed., 1996.
- [244] D. Briggs and M. P. Seah, *Practical Surface Analysis, Volume 1: Auger and X-ray Photoelectron Spectroscopy*, p. 151. John Wiley & Sons, second ed., 1996.
- [245] G. Greczynski and L. Hultman, “C 1s Peak of Adventitious Carbon Aligns to the Vacuum Level: Dire Consequences for Material’s Bonding Assignment by Photoelectron Spectroscopy,” *ChemPhysChem*, vol. 18, no. 12, pp. 1507–1512, 2017.
- [246] P. R. Anderson and W. E. Swartz, “X-Ray photoelectron spectroscopy of some aluminosilicates,” *Inorganic Chemistry*, vol. 13, no. 9, pp. 2293–2294, 1974.

- [247] M. Bonini, A. Gabbani, S. Del Buffa, F. Ridi, P. Baglioni, R. Bordes, and K. Holmberg, “Adsorption of Amino Acids and Glutamic Acid-Based Surfactants on Imogolite Clays,” *Langmuir*, vol. 33, no. 9, pp. 2411–2419, 2017.